



저작자표시-비영리-변경금지 2.0 대한민국

이용자는 아래의 조건을 따르는 경우에 한하여 자유롭게

- 이 저작물을 복제, 배포, 전송, 전시, 공연 및 방송할 수 있습니다.

다음과 같은 조건을 따라야 합니다:



저작자표시. 귀하는 원저작자를 표시하여야 합니다.



비영리. 귀하는 이 저작물을 영리 목적으로 이용할 수 없습니다.



변경금지. 귀하는 이 저작물을 개작, 변형 또는 가공할 수 없습니다.

- 귀하는, 이 저작물의 재이용이나 배포의 경우, 이 저작물에 적용된 이용허락조건을 명확하게 나타내어야 합니다.
- 저작권자로부터 별도의 허가를 받으면 이러한 조건들은 적용되지 않습니다.

저작권법에 따른 이용자의 권리는 위의 내용에 의하여 영향을 받지 않습니다.

이것은 [이용허락규약\(Legal Code\)](#)을 이해하기 쉽게 요약한 것입니다.

[Disclaimer](#)

공학박사 학위논문

Fabrication and mechanical response
of nanoscale metallic glasses

나노 스케일 비정질 합금의 제조 및
기계적 변형 거동 분석에 대한 연구

2016년 8월

서울대학교 대학원

재료공학부

김진우

Fabrication and mechanical response of
nanoscale metallic glasses

나노 스케일 비정질 합금의 제조 및
기계적 변형 거동 분석에 대한 연구

지도교수 박 은 수

이 논문을 공학박사 학위논문으로 제출함
2016년 7월

서울대학교 대학원
재료공학부
김진우

김진우의 공학박사 학위논문을 인준함
2016년 7월

위원장 김 영 운

부위원장 박 은 수

위원 한 흥 남

위원 김 도 향

위원 장 동 찬



Abstract

Fabrication and mechanical response of nanoscale metallic glasses

Jinwoo Kim

Department of Materials Science and Engineering

College of Engineering

Seoul National University

The extrinsic size reduction of metallic glasses into nanoscale is a unique route for enhancing the plasticity of metallic glasses with avoiding the general propensity of strength-ductility trade-off. However, the origins of the unique deformation behaviors in nanoscale metallic glasses are still in veil. The lack of explainable origins and the several inconsistencies among the reports depending on alloy system and sample preparation history cause controversies over the mechanical behaviors of nanoscale metallic glass. In addition, the dimensional limitation hinders nanoscale metallic glasses from practical applications despite their exceptional mechanical properties by sample size effect, ironically.

In this study, comprehensive investigations on the mechanical response of metallic glass nanoparticles and nanofoams were conducted in order to clarifying the origin of unique mechanical behaviors of nanoscale metallic glasses and extending their applications. A single metallic glass nanoparticle with near-perfectly spherical morphology minimizing surface flaws is a proper material for investigating the

genuine size-dependent behaviors of nanoscale metallic glass without extrinsic effects such as ion irradiation and surface roughness induced by focused ion beam. The metallic glass nanoparticles and nanofoams handled in this study were prepared through the dealloying process of phase-separating metallic glass precursors. The precise control of alloy composition and cooling rate based on thermodynamic assessments enables to fabricate phase separating metallic glass precursors with a desirable size distribution of secondary phases for preparing metallic glass nanoparticles or nanofoams. From this, Ti-based metallic glass nanoparticles and nanofoams were fabricated by dealloying of phase separating metallic glass precursors with droplet-structure and interconnected structure, respectively, and their compressive deformation behaviors were systematically investigated by *in situ* compression tests inside a scanning electron microscope.

The compressive test results of the particles were analyzed based on contact mechanics, considering their spherical morphology unusual for mechanical testing. The results suggest that the stress distribution inside the compressed particle changes from highly concentrated state at near contact center to uniformly distributed state during the increase of strain. Then, interestingly, the metallic glass particle exhibit steady-state plastic flow with nearly-constant flow stress at the plastic-dominant stage with high strain condition. Through the estimation of the critical stress for shear banding using an extended relation analogous to the Griffith's crack equation, the steady-state plastic flow at high strain condition is confirmed to be the homogeneous deformation by the activation of distributed shear transformation zones in entire sample volume rather than inhomogeneous shear banding. In addition, the flow stress and viscosity dependences on strain rate in metallic glass nanoparticles reveal the steady-state homogeneous flow of the particles obviously follows non-Newtonian

flow behavior regardless of sample sizes.

In order to elucidate the origin of the non-Newtonian homogeneous flow behavior of metallic glass nanoparticles, a novel deformation map for metallic glasses is constructed in this study, which covers the size-dependent mechanical behaviors of metallic glasses. The correlations among the boundaries constituting the deformation map provide illuminating insights on the deformation of metallic glass. Based on the novel deformation map, it is suggested that the detectable homogeneous deformation of nanoscale metallic glass at room temperature originates from the continuous viscosity decrease induced by shear stress into under $\sim 10^{12}$ Pa·s (termed to “mechanically-induced glass transition”). The detectable homogeneous deformation of nanoscale metallic glass at room temperature with GPa-scale flow stress can have only non-Newtonian flow characteristic.

These unique mechanical properties of nanoscale metallic glasses have a limitation for structural application due to their extremely small size scale. To overcome this drawback, the properties of nanoscale metallic glasses can be transferred to the intrinsic properties of materials with larger scale, such as metallic glass-based materials with architected or hierarchical structure. As a candidate of the novel metallic glass-based materials, metallic glass nanofoams is suggested in this study. The results of their compression tests suggest that the unique deformation behavior of nanoscale metallic glass can be applied to extended scales by designing metallic glass-based materials with multi-scale structure such as nanofoams consisting of nanoscale metallic glasses as intrinsic scale components.

Keywords : Metallic glass, Nanoparticle, Nanofoam, Nanomechanics.
Deformation map, Mechanically-induced glass transition

Student Number : 2010-20592

Table of Contents

Abstract	i
Table of Contents.....	iv
List of Figures	viii
List of Tables.....	xx
List of Abbreviations	xxi
List of Symbols.....	xxii
Chapter 1. Introduction	1
1.1. Deformation of metallic glasses.....	1
1.1.1. Fundamental mechanisms of deformation.....	4
1.1.2. Homogeneous deformation.....	8
1.1.3. Inhomogeneous deformation and shear banding	12
1.1.4. Deformation map for metallic glasses	15
1.2. Nanomechanical behavior of metallic glasses	19
1.2.1. Size effect on strength.....	19
1.2.2. Size effect on deformation mode transition	24
1.2.3. Extrinsic factors affecting nanomechanical behaviors of metallic glasses	27
1.3. Phase separation in metallic glasses	30
1.3.1. Thermodynamic background of phase separation	34
1.3.2. Mechanisms of phase separation	38
1.4. Thesis motivation and scopes	41

Chapter 2. Experimental procedures	43
2.1. Sample preparation	43
2.1.1. Arc melting	43
2.1.2. Melt spinning	43
2.1.3. Chemical dealloying	44
2.1.4. Micro-pillar fabrication.....	45
2.2. Microstructural characterization	47
2.2.1. Scanning electron microscopy	47
2.2.2. Three-dimensional microstructure analysis	47
2.2.3. Transmission electron microscopy	48
2.3. Thermal analysis.....	49
2.3.1. Differential scanning calorimetry	49
2.3.2. Thermomechanical analysis.....	49
2.4. Mechanical analysis.....	50
2.4.1. Nanocompression test in electron microscope.....	50
2.4.2. High temperature tensile creep test.....	50
2.4.3. Nanoindentation test	51
Chapter 3. Fabrication and microstructure control of metallic glass	
nanoparticles and nanofoams.....	54
3.1. Introduction.....	54
3.2. Microstructure control of precursor alloys	58
3.2.1. Effect of alloy composition.....	58
3.2.2. Effect of cooling rate	66
3.2.3. Three-dimensional microstructure analysis	70

3.3. Microstructure of metallic glass nanoparticles	74
3.4. Microstructure of metallic glass nanofoams	80
3.5. Summary	85
Chapter 4. Deformation behavior of metallic glass nanoparticles.....	86
4.1. Introduction.....	86
4.2. Analysis on compressive deformation behavior of individual metallic glass nanoparticles	89
4.2.1. Contact diameter-strain relation.....	91
4.2.2. Contact pressure-strain relation and deformation stages during compression	95
4.2.3. Critical stress analysis for shear banding and homogeneous deformation at high strain condition	102
4.2.4. Molecular dynamic simulations	109
4.3. Non-Newtonian homogeneous flow behavior of metallic glass nanoparticles	113
4.4. Brittle fracture of crystallized nanoparticles.....	119
4.5. Summary	121
Chapter 5. Deformation map for nanoscale metallic glasses.....	123
5.1. Introduction.....	123
5.2. Steady-state flow analysis near glass transition temperature.....	125
5.3. Boundaries constituting the deformation map	132
5.3.1. Boundary of non-Newtonian and Newtonian flow	132
5.3.2. Iso-viscosity contours in a stress-temperature plot.....	135

5.3.3. Critical stress curve for shear localization	140
5.4. Construction of deformation map	144
5.5. Interpretation of homogeneous deformation of metallic glass nanoparticles on deformation map	146
5.6. Summary	149
Chapter 6. Deformation behavior of metallic glass nanofoams	151
6.1. Introduction.....	151
6.2. Compressive deformation behavior of nanoporous metallic glass micropillar.....	156
6.3. Ligament size effect on hardness of metallic glass nanofoams	165
6.4. Deformation mode transition depending on ligament size	168
6.5. Summary.....	171
Chapter 7. Conclusions	173
Bibliography.....	I
Abstract in Korean	XII

List of Figures

Figure 1.1. (a) Schematic illustration for the comparison of atomic structure in crystalline metals and metallic glasses. (b) Solidification path of metallic glass in Time-temperature-transformation (TTT) diagram.

Figure 1.2. Ashby map of fracture toughness versus strength of materials. Reprinted from ref. 8 with permission through "Copyright Clearance Center".

Figure 1.3. Schematic illustration of atomic shear transformations in metallic glasses. (a) Free volume model¹⁰. (b) Shear transformation zone (STZ) model¹¹. Recomposed from ref. 9 with permission through "Copyright Clearance Center".

Figure 1.4. (a) Volume-temperature relation in transformations among liquid, glass and crystal. (b) A La-Al-Ni metallic glass deformed homogeneously to 20000% in the supercooled liquid region. (b) is recomposed from ref. 26 and 31 with permission through "Copyright Clearance Center".

Figure 1.5. (a) Stress-strain curves of homogeneous deformation of Zr-based metallic glass at 623 K²⁸. (b) Steady-state homogeneous flow data for Zr-based metallic glass at high temperatures near the glass transition temperature^{9,28}. Recomposed from ref. 9 with permission through "Copyright Clearance Center".

Figure 1.6. (a) Schematic illustration of the initiation process of a shear band. (b) (HR)TEM images of a shear band formed during the bend test of Fe_{79.3}B_{16.4}Si₄C_{0.3} metallic glass ribbon, recomposed from ref. 45 with permission under the terms of the "Creative Commons Attribution Non-Commercial License". (c) SEM images showing shear steps associated with shear bands in a bent strip of Zr₅₇Nb₅Al₁₀Cu_{15.4}Ni_{12.6} metallic glass, reprinted from ref. 46 with permission through "Copyright Clearance Center".

Figure 1.7. A first deformation map for metallic glasses based on the free volume theory, suggested by Spaepen¹⁰. Reprinted from ref. 14 with permission through "Copyright Clearance Center".

Figure 1.8. Deformation maps for metallic glasses in (a) stress-temperature and (b) strain rate-temperature axes, suggested by Schuh et al.⁹. The absolute values shown are for the specific glass $Zr_{41.2}Ti_{13.8}Cu_{12.5}Ni_{10}Be_{22.5}$. Reprinted from ref. 9 with permission through "Copyright Clearance Center".

Figure 1.9. (a) Schematic stress-strain curve for the definitions of σ_l and σ_f . (b) Schematic illustration of a cylindrical sample and the penetrating path of a shear band.

Figure 1.10. (a) Normalized strength versus sample size plot of experimental data. The solid line is a fitting line using the relation of Eq. 1-4. (b) Strength and strain limit of Cu-Zr metallic glasses in different size scale (bulk- and submicron-scale). Reprinted from ref. 54 and 63 with permission through "Copyright Clearance Center".

Figure 1.11. Homogenous deformation of nanoscale metallic glass at room temperature. (a) Compressive deformation of pillar-type Pd-Si metallic glass samples. The clear transition is observed from localized shear banding in microscale samples to homogeneous deformation in nanoscale samples. (b) Tensile deformation of a Zr-based metallic glass nanorod showing necking behavior and unusual strain hardening. Reprinted from ref. 55 and 58 with permission through "Copyright Clearance Center".

Figure 1.12. Schematic representation of the applied stresses required to shear band initiation⁵⁴ versus homogeneous deformation as a function of sample size^{55,58}. The insets are recomposed from ref. 31 with permission through "Copyright Clearance Center".

Figure 1.13. Influence of ion irradiation on the deformation of metallic glass nanorod.

(a) Deformation map showing the influence of ion fluence and irradiated volume fraction on the amount of plastic strain. (b–d) Typical force–time curves and fracture morphologies for the shear banding (b), intermediate (c) and ductile-type deformation (d), respectively. Reprinted from ref. 72 with permission through “Copyright Clearance Center”.

Figure 1.14. TEM images of phase separating metallic glasses (a) $\text{La}_{27.5}\text{Zr}_{27.5}\text{Cu}_{10}\text{Ni}_{10}\text{Al}_{25}$. (b) $\text{Nd}_{30}\text{Zr}_{30}\text{Co}_{30}\text{Al}_{10}$. (c) $\text{Ni}_{54}\text{Nb}_{23}\text{Y}_{23}$. (d) $\text{Zr}_{35}\text{Gd}_{20}\text{Al}_{23}\text{Ni}_{22}$. The image of (b) is a dark-field image while the others are all bright-field images. The insets are selected area diffraction patterns (SADP) corresponding to each of observed regions. Reprinted from ref. 83,84,88 and 89 with permission through “Copyright Clearance Center”.

Figure 1.15. Schematic description of (a) Gibbs free energy change by mixing (ΔG^{mix}), (b) miscibility gap in binary system and (c) microstructures formed by phase separation depending on the compositions of alloy melt.

Figure 1.16. Schematic diagrams showing spatial variations in concentration variation and morphology evolution ($t_1 < t_2 < t_3$) during phase separation by two different mechanisms⁷⁴. (a) Nucleation and growth. (b) Spinodal decomposition. Reprinted from ref. 74 with permission through “Copyright Clearance Center”.

Figure 2.1. (a) The overview of arc melting apparatus. (b) Setup inside the chamber of arc melting apparatus. (c) The overview of melt-spinning apparatus. (b) Setup inside the chamber of melt-spinning apparatus.

Figure 2.2. (a) SEM image of Ti-based metallic glass nanoparticles dispersed individually on a Si substrate. (b) The overview of an in-situ indentation tester (Hysitron PI-85 Picoindenter) for testing inside SEM.

Figure 2.3. (a) A sample gripped by grabs for high-temperature creep test in TMA apparatus. (b) Schematic illustration of TMA tensile mode testing in this study. (c) The sample and grabs loaded on quartz stage for tensile mode

testing inside TMA apparatus.

Figure 3.1. Fabrication of metallic glass nanoparticles (a) and nanofoams (b) by dealloying process of phase separating metallic glass precursors.

Figure 3.2. (a, b) The atomic sizes of constituent elements¹²¹ and the relationships of mixing enthalpy¹²⁰ among them in (a) Y-Ti-Al-Co and (b) Gd-Ti-Al-Co alloy systems. (c, d) Pseudo-binary miscibility gaps of (c) Y-Ti-Al-Co and (d) Gd-Ti-Al-Co alloy systems estimated by thermodynamic calculations^{87,94}.

Figure 3.3. SEM images of (Y,Gd)-Ti-Al-Co metallic glass as-spun ribbons at the center region of cross-section, obtained using in-lens secondary electron detector. (a) $Y_{19}Ti_{36}Al_{25}Co_{20}$. (b) $Y_{25}Ti_{30}Al_{25}Co_{20}$. (c) $Y_{27.5}Ti_{27.5}Al_{25}Co_{20}$. (d) $Y_{30}Ti_{25}Al_{25}Co_{20}$. (e) $Gd_{19}Ti_{36}Al_{25}Co_{20}$. (f) $Gd_{25}Ti_{30}Al_{25}Co_{20}$. (g) $Gd_{27.5}Ti_{27.5}Al_{25}Co_{20}$. (h) $Gd_{30}Ti_{25}Al_{25}Co_{20}$.

Figure 3.4. Bright-field TEM images of (Y,Gd)-Ti-Al-Co as-spun ribbon samples and (inset) corresponding selected area diffraction patterns. (a) $Y_{27.5}Ti_{27.5}Al_{25}Co_{20}$. (b) $Gd_{27.5}Ti_{27.5}Al_{25}Co_{20}$ (c) $Y_{19}Ti_{36}Al_{25}Co_{20}$. (d) $Gd_{19}Ti_{36}Al_{25}Co_{20}$.

Figure 3.5. DSC heat flow spectrum of as-spun ribbon with selected compositions in (Y, Gd)-Ti-Al-Co alloy systems and three monolithic metallic glass ribbons, $Y_{55}Al_{25}Co_{20}$, $Ti_{55}Al_{25}Co_{20}$ and $Gd_{55}Al_{25}Co_{20}$.

Figure 3.6 (a) Schematic illustration of melt-spinning process showing the definition of ‘wheel side’ and ‘free side’ of a ribbon sample. (b, c) Cross-section SEM images of $Y_{27.5}Ti_{27.5}Al_{25}Co_{20}$ alloy ribbon at the positions near free side edge (b) and wheel side edge (c), obtained using in-lens secondary electron detector.

Figure 3.7 Cross-section SEM images of Y-Ti-Al-Co metallic glass as-spun ribbons covering wide range from wheel side to free side of ribbon, obtained using in-lens secondary electron detector. (a) $Y_{30}Ti_{25}Al_{25}Co_{20}$. (b)

$Y_{27.5}Ti_{27.5}Al_{25}Co_{20}$. (c) $Y_{25}Ti_{30}Al_{25}Co_{20}$. (d) $Y_{19}Ti_{36}Al_{25}Co_{20}$.

Figure 3.8. Three-dimensional microstructure analysis of $Gd_{30}Ti_{25}Al_{25}Co_{20}$ as-spun ribbon. (a-h) The selected images among ~ 660 images obtained by serial sectioning-imaging process using FIB/SEM dual-beam equipment. (i) Combined 2-D and 3-D images showing the stacking direction of 2-D images. (j) The constructed 3-D microstructure of an entire observed volume. (k) An enlarged part of (i) at near free side.

Figure 3.9. Three-dimensional microstructure analysis of $Y_{19}Ti_{25}Al_{25}Co_{20}$ as-spun ribbon. (a-f) The selected images among ~ 90 images obtained by serial sectioning-imaging process using FIB/SEM dual-beam equipment. (g) Combined 2-D and 3-D images showing the stacking direction of 2-D images. (h) The constructed 3-D microstructure of an entire observed volume.

Figure 3.10. Metallic glass nanoparticles fabricated by dealloying process of $Y_{27.5}Ti_{27.5}Al_{25}Co_{20}$ (a) and $Gd_{27.5}Ti_{27.5}Al_{25}Co_{20}$ (b) precursor PS-MG alloys.

Figure 3.11. EDS line profile with HAADF-STEM imaging. (a,b) EDS line profile (a) and HAADF image (b) of $Y_{27.5}Ti_{27.5}Al_{25}Co_{20}$ precursor alloy. (c,d) EDS line profile (c) and HAADF image (d) of a nanoparticle fabricated by dealloying of the precursor alloy. A yellow line in (b) and (d) is the direction of EDS line scan (a) and (c), respectively.

Figure 3.12. Ellingham diagram¹²⁴ for metal-oxide formation. Reprinted from ref. ¹²⁵ with permission through "Copyright Clearance Center"..

Figure 3.13. EDS line profile across the phase boundary in $Gd_{27.5}Ti_{27.5}Al_{25}Co_{20}$ precursor alloy (a) and at the edge of a particle fabricated by dealloying of the precursor alloy.

Figure 3.14. SEM image of $Y_{19}Ti_{36}Al_{25}Co_{20}$ precursor alloy before dealloying (a) and a metallic glass nanofoam (b) fabricated by dealloying of the

precursor alloy.

Figure 3.15. (a) Cross-section SEM image of a Ti-based metallic glass nanofoam dealloyed from $Y_{19}Ti_{36}Al_{25}Co_{20}$ precursor alloy. (b) ligament size distribution inside the nanofoam depending as a function of distance from wheel side edge.

Figure 3.16. Metallic nanofoam with a hierarchical nanoporous structure fabricated by multi-stage dealloying process of $Y_{19}Ti_{36}Al_{25}Co_{20}$ precursor alloy. (a) low-magnification image showing the uniform porous structure in large scale (pore size : 200 ~ 300 nm) (b) An enlarged part of (a). (c) High-magnification image showing the nanoporous structure in smaller scale inside the ligaments in larger scale.

Figure 4.1. (a) SEM image of a single MG-NP observed from the direction nearly-parallel to the surface of the substrate (tilt angle = 2°). (b) Diffraction pattern of a MG-NP obtained by TEM. (c, d) Bright-field TEM images of MG-NPs with different sizes.

Figure 4.2. (a-f) A series of SEM images of a compressed MG-NP with $d = 310$ nm, at strain of 0 (a), 0.14 (b), 0.28 (c), 0.42 (d), 0.56 (e), 0.7 (f). (g) $d_c - \varepsilon$ relation in the compression test of MG-NPs. The black dots with error bars are measured d_c values from SEM video analysis, and the colored solid line is a fitting line obtained by the combination of three different contact diameter models. (h) Schematic illustrations of the geometric relations in the three contact diameter models¹³³.

Figure 4.3. (a) F and p_c versus ε relations obtained from the compression test of a MG-NP with $d = 410$ nm under beam-off condition. The upper inset is the first derivative curve ($dp_c/d\varepsilon$) of the $p_c - \varepsilon$ curve. The red solid line is a critical stress for shear localization (σ_{SB}) estimated by Eq. 4-13. (b) Schematic illustrations describing pressure (p) distributions on the contact surface of a compressed MG-NP in the corresponding deformation stages¹³³.

Figure 4.4. (a) An enlarged part of Figure 4.3 (a) showing the transition from elastic dominant(I) to elastic-plastic(II) deformation. (b) Schematic description with axis definitions and the position under the maximum shear stress. (c) Stress distribution along the x direction on the contact surface at the first pop-in event. (d) Distribution of the normal stress (σ_x , σ_z) and maximum shear stress (τ_{max}) along the z axis inside a particle, based on Hertzian contact theory^{130,131}.

Figure 4.5. The other enlarged part of Figure 4.3 (a) showing transition from elastic-plastic (II) to plastic-dominant (III) deformation. The pop-ins with rapid strain burst are marked with red arrows.

Figure 4.6. Schematic illustration of a geometric relation for the shear banding area which penetrates a whole MG-NP.

Figure 4.7. (a) Compressive shear deformation patterns of a Zr-based metallic glass sample with an aspect ratio of 0.67. (b) Magnified image of the sample in (a). (c) Schematic illustrations of the confining effect in the region near contact plane and the formation of shear bands depending on the aspect ratio of samples. Reproduced from ref. ¹³⁷ with permission through "Copyright Clearance Center".

Figure 4.8. (a) an enlarged part of the steady state flow region in the $p_c - \varepsilon$ curve of Figure 4.3 (a). (b) Schematic illustration of the possible origins of minor p_c fluctuations in steady-state flow of a compressed MG-NP.

Figure 4.9. (a) A series of images of a compressed $\text{Cu}_{64}\text{Zr}_{36}$ MG-NP with $d = 20$ nm in MD simulation, depending on strain. (b) Cooling curve of solidification for the MG-NP. The inset is a radial distribution function (RDF) curves after solidification. (c) Contact diameter (d_c) versus strain (ε) relation in the compression of the MG-NP. The dotted lines correspond to the three different contact diameter models.

Figure 4.10. MD-simulated compressive deformation of a $\text{Cu}_{64}\text{Zr}_{36}$ MG-NP with $d = 20$ nm (a) $F - \varepsilon$ curve of the MG-NP during compression. (b) p_c versus

ε response of the MG-NP. (c-d) Atomic local shear strain (η^{Mises}) distribution inside the particle at different strains, showing the atomic position under relatively high strain of $\eta^{Mises} > 0.6$ (c) and on a cross-sectional plane (d).

Figure 4.11. (a-b) Schematic description of the difference between Newtonian and Non-Newtonian flow in viscosity (a) and flow stress (b) change depending on strain rate, generally observed in metallic glasses. (c-d) Viscosity change (c) and flow stress variation (d) of La-Al-Ni bulk metallic glass depending on strain rate and temperature. (c) and (d) are recomposed from ref. ¹²⁷ with permission through "Copyright Clearance Center".

Figure 4.12. Contact pressure (p_c) - strain (ε) curves obtained from the compression tests of MG-NPs. (a) p_c - ε curves from the MG-NPs with different sizes but under same strain rate. (c) p_c - ε curves from the MG-NPs with similar sizes under different strain rates.

Figure 4.13. (a) Steady-state flow stress at $\varepsilon = 0.4$ from the compression deformation of MG-NPs with different diameters under various strain rate conditions. The average stress value is marked as a black dotted line. σ_{SB} at $\varepsilon = 0.4$ depending on particle diameter is plotted as a green dotted line based on Eq. 4-13. (b) Viscosity versus strain rate relation showing a clear dependency of viscosity on strain rate (non-Newtonian flow behavior).

Figure 4.14. Compression test result of a crystallized nanoparticle with $d = 425$ nm. (a) Load-strain curve of the crystallized nanoparticle. (b-c) SEM images of the particle morphology before (b) and after (c) compression test.

Figure 5.1. Heat flow spectrum in a DSC measurement and strain-temperature response in an isochronal TMA measurement of $Ti_{55.8}Co_{30.4}Al_{11.7}Gd_{2.1}$ as-spun ribbon sample. The heating rate in the both measurement is 10 K/min.

Figure 5.2. High-temperature tensile creep test results of $Ti_{55.8}Co_{30.4}Al_{11.7}Gd_{2.1}$ as-

spun ribbon samples. (a) Strain, strain rate and heat flow versus time plot from the result under the condition of $\sigma = 250$ MPa and $T = 723$ K. Each colored vertical axis corresponds to the curve with the same color. (b) Strain rate versus time curves obtained at the different temperatures under $\sigma = 250$ MPa. The inset table is the list of strain rate in steady-state flow region for each test condition.

Figure 5.3. Steady-state flow stress versus strain rate relation for $\text{Ti}_{55.8}\text{Co}_{30.4}\text{Al}_{11.7}\text{Gd}_{2.1}$ as-spun ribbon samples, at the temperatures near glass transition temperature (713 ~ 753 K).

Figure 5.4. The transition boundary between non-Newtonian and Newtonian flow in stress-temperature plot (uniaxial case) for $\text{Ti}_{55.8}\text{Co}_{30.4}\text{Al}_{11.7}\text{Gd}_{2.1}$ metallic glass.

Figure 5.5. Stress-temperature scaling relation for a constant viscosity in steady-state flow. (a) Stress-temperature plot normalized by $T_0(\eta_0)$ and $\sigma_0(\eta_0)$, where $\log_{10}\eta_0 = 5$. (b) Plot of normalized stress and temperature with various shear strain rate, demonstrating the scaling relationship of Eq. 5-9. Note that σ of horizontal axis in the figures (a) and (b) means shear stress, while the symbol means normal uniaxial stress in the body text. Reprinted from ref. 145 with permission through "Copyright Clearance Center".

Figure 5.6. (a) Viscosity-temperature plot obtained from the combination of Eq. 5-2 and Eq. 5-11. The inset shows a procedure for searching stress-temperature points for a constant viscosity. (b) Iso-viscosity contours in uniaxial stress-temperature plot, delineated by fitting the positions of same viscosity (obtained from (a)) with Eq. 5-10.

Figure 5.7. Experimental shear strength normalized by shear modulus (or shear strain at yielding) versus temperature normalized by glass transition temperature. The colored solid curves are fitting curves based on the universal relations^{9,51} of Eq. 5-12 (yellow) and Eq. 5-13 (navy). The data points from experiments were collected by Johnson and Samwer in ref.

51 for a variety of metallic glasses.

Figure 5.8. The critical stress curves for shear banding in the alloy composition of the MG-NPs ($\text{Ti}_{55.8}\text{Co}_{30.4}\text{Al}_{11.7}\text{Gd}_{2.1}$) depending on the diameter of particle, based on Eq. 4-13 and Eq. 5-13.

Figure 5.9. Deformation map for metallic glasses in stress-temperature axes encompassing their nanoscale mechanical behavior. The absolute values in the map is based on the metallic glass of the same composition with the MG-NPs ($\text{Ti}_{55.8}\text{Co}_{30.4}\text{Al}_{11.7}\text{Gd}_{2.1}$).

Figure 6.1. (a) Schematic demonstration for the extension of materials properties in micro/nanoscale as a ‘extrinsic size scale’ into the intrinsic properties of large-scale materials (e.g. micro/nano-truss structure). (b) Hollow Cu-Zr metallic glass nanolattice as an example of (a). (c) An enlarged view of the nanolattice (b) showing the hollow structure. (d) Deformation map for the metallic glass nanolattice in the temperature-wall thickness space. Recomposed from ref. ¹⁵⁸ and ¹⁵⁹ with permission through “Copyright Clearance Center”.

Figure 6.2. Schematic compressive stress-strain curves for foams¹⁶⁰. (a) an elastomeric foam. (b) an elastic-plastic foam. (c) an elastic-brittle foam.

Figure 6.3. Compressive deformation of Zr-based metallic glass foams¹⁶¹. (a-c) low-magnification SEM images of the compressed metallic glass foams after unloading from applied macroscopic strains of 4% (a), 24% (b), 43% (c). (d-g) SEM images of deformed ligaments in the foam sample, after unloading from the strain of 4% (d), 9% (e), 14% (f), 19% (g). (h-i) Engineering stress-strain curves of the foam samples as a function of relative density for a constant pore size 230 μm (h), and as a function of pore size for near-constant relative density ($\sim 23\%$). Recomposed from ref. ¹⁶¹ with permission through “Copyright Clearance Center”.

Figure 6.4. Fabrication of a nanoporous metallic glass micropillar from $\text{Y}_{19}\text{Ti}_{36}\text{Al}_{25}\text{Co}_{20}$ precursor alloy. (a-b) SEM images of the partially-

dealloyed precursor alloy for micropillar fabrication. (c-e) SEM images after ion beam milling for micropillar fabrication. (c) upper view. (d) lateral view in low magnification. (e) lateral view in higher magnification with tilt angle ~ 52 degrees.

Figure 6.5. Compressive deformation of a nanoporous metallic glass micropillar. (a) Engineering stress-strain curve. (b-g) SEM images observed after each corresponding loading-unloading cycle.

Figure 6.6. Image analysis for the estimation of relative density of metallic glass nanofoam. (a) SEM images of $Y_{19}Ti_{36}Al_{25}Co_{20}$ precursor alloy with the boundary of contrast threshold between two amorphous phases. (b) Contrast spectrum in the image of (a)

Figure 6.7. An enlarged part of the deformation map for metallic glass, with the critical stress (σ_{SB}) curves for shear banding depending on sample diameter in the case of cylindrical sample.

Figure 6.8. (a) SEM image of nanoporous metallic glass pillar after unloading from applied macroscopic strains of $\sim 30\%$. (b) von Mises stress distribution inside nanoporous gold at the onset of yielding, analyzed by finite element modeling. Arrows denotes the region of stress concentration. (b) is recomposed from ref. ¹⁶² with permission through "Copyright Clearance Center".

Figure 6.9. (a) SEM image of the indented cross-section of metallic glass nanofoam by nanoindentation technique. (b) Hardness of metallic glass nanofoam depending on the ligament size. Horizontal bars on data points shows the ligament size range covered by a single indent corresponding to each data point.

Figure 6.10. (a) Engineering compressive stress-strain curves of nanoporous metallic glass micropillar with different ligament sizes. (b-d) SEM images of the pillars before and after compressive deformation, with average ligament sizes of ~ 270 nm (b), ~ 180 nm (c), ~ 60 nm (d). (e-g) Magnified surface

morphology of the compressed pillars with average ligament sizes of ~270 nm (e), ~180 nm (f), ~60 nm (g).

Figure 6.11. A diagram showing the transference of the excellent mechanical properties of nanoscale metallic glass to intrinsic scale properties in the extended scale materials (such as metallic glass nanofoam).

List of Tables

Table 1.1. Alloy systems forming phase separating metallic glasses by rapid quenching.

Table 5.1. The parameters of $T_0(\eta)$ and $\sigma_0(\eta)$ corresponding to a viscosity value η , obtained from the fitting process using Eq. 5-10 in Figure 5.6 (b).

List of Abbreviations

3-D	Three-dimensional
CSM	Cooperative shear model
DSC	Differential scanning calorimetry
EDS	Energy dispersive spectroscopy
FIB	Focused ion beam
GFA	Glass-forming ability
HAADF	High-angle annular dark field
MD simulation	Molecular dynamic simulation
MG	Metallic glass
MG-NP	Metallic glass nanoparticle
PS-MG	Phase separating metallic glass
RDF	Radial distribution function
RT	Room temperature
SADP	Selected area diffraction pattern
SB	Shear band
SEM	Scanning electron microscopy
STEM	Scanning transmission electron microscopy
STZ	Shear transformation zone
TEM	Transmission electron microscopy
TMA	Thermomechanical analysis
TTT diagram	Time-temperature-transformation diagram

List of Symbols

A	Proportional constant, or shear band area
a	Aspect ratio ($=h/d$), or contact radius
D	Cross-sectional diameter of cylinder, or dimensionless constant
d	Diameter of spherical particle
d_c	Contact diameter
d_{hertz}	Hertzian contact diameter
d_{geo}	Geometric contact diameter
d_{cyl}	Cylindrical contact diameter
$d_{ligament}$	Thickness (size) of ligament in foam
Δd_c	Difference between d_{cyl} and measured d_c
E	Young's modulus
E_r	Reduced elastic modulus
F	Applied load
G	Gibbs free energy
G_m	Molar Gibbs free energy
ΔG^{mix}	Gibbs free energy change of mixing
H	Hardness
H_{bulk}	Hardness of bulk scale material with $\rho_{rel} = 1$
H_{foam}	Hardness of foam
$H_{ligament}$	Hardness of ligament in foam
ΔH^{mix}	Enthalpy change of mixing
h	Height of sample
Δh	Compressed depth ($= \delta$)
i	A component of multi-component system

k	Boltzmann constant
n_i	A number of moles of component i
p_c	Contact pressure
p_{max}	Maximum pressure on contact surface
p_y	Micro-yield strength
Q	Characteristic activation energy
r	Radius of spherical particle
r_{SB}	Radius of the shear band area
ΔS^{mix}	Entropy change of mixing
T	Temperature
T_g	Glass transition temperature
T_g^*	$T_0(\eta)$ when $\eta = 10^{12}$ Pa·s
T_x	crystallization onset temperature
$T_0(\eta)$	Temperature where the viscosity reaches η when stress is zero
t_{SB}	Thickness of shear band
U_{el}	(Released) elastic strain energy
U_{SB}	Shear band formation energy
V	Characteristic volume, or sample volume
ΔV	Expansion of macroscopic volume
X_i	Mole fraction of component i
Γ	Shear band energy per unit area
γ	Shear strain
γ_c	Universal shear elastic limit
γ_0	Characteristic strain
$\dot{\gamma}$	Shear strain rate
$\dot{\gamma}_s$	Characteristic shear strain rate

δ	Displacement ($=\Delta h$)
ε	Normal strain
ε'	Equal to $1 - \varepsilon + \sqrt{2\varepsilon - \varepsilon^2}$ for spherical particle
$\dot{\varepsilon}$	Normal strain rate
$\dot{\varepsilon}_{steady-state}$	Normal strain rate at steady-state
η	Viscosity
η^{Mises}	Atomic local shear strain
μ	Shear modulus
ν	Poisson's ratio
ρ_{rel}	Relative density of foam
σ	Normal uniaxial stress ($=\sigma_z$)
σ_f	Flow stress
σ_l	Onset stress of shear band initiation
σ_{SB}	Critical stress for shear band formation ($\sim\sigma_l$)
σ_0	Bulk strength
$\sigma_0(\eta)$	Normal stress where viscosity reaches η when T is 0 K
σ_x	Normal stress of x direction
σ_{pl}^*	Plastic collapse strength of elastic-plastic foam
$\sigma_{ligament}$	Strength of ligament in foam
τ	Shear stress
τ_{max}	Maximum shear stress
$\tau_0(\eta)$	Shear stress where the viscosity reaches η when T is 0 K
ϕ	Porosity of foam
Ψ	Equal to $2\sqrt{2}E\Gamma/a$
ψ	Stability function
Ω	Characteristic STZ volume

Chapter 1.

Introduction

1.1. Deformation of metallic glasses

Metallic glasses (also often referred to as amorphous alloys or glassy alloys) are a special class of metallic solid materials, having a disordered atomic structure unlike crystalline metals with long-range atomic order^{1,2} (Figure 1.1 (a)). A metallic glass is generally fabricated by quenching a metallic melt rapidly over a critical cooling rate to avoid crystallization and be solidified into amorphous state through glass transition (Figure 1.1 (b)). Since the discovery of the first metallic glass³ in 1960, numerous multi-component alloys with low critical cooling rate have been developed in various alloy systems for securing high glass-forming ability (GFA) even in bulk scale over 1mm (i.e. bulk metallic glasses)⁴. With overcoming the dimensional constraint, metallic glasses have attracted tremendous interests for structural applications due to their excellent mechanical properties, such as (i) high strength much closer to the theoretical limit than their crystalline counterparts, (ii) large elastic strain limit of $\sim 2\%$ as compared with $\sim 0.2\%$ for crystalline materials and (iii) exceptional fracture toughness ranging from highly brittle to extremely tough^{1,5-7}. From the unusual combinations of the mechanical properties, metallic glasses possess a unique status among various structural materials, as briefly summarized in Figure 1.2. In this section, the general nature of mechanical deformation of metallic glasses will be discussed based on accumulated precedent researches.

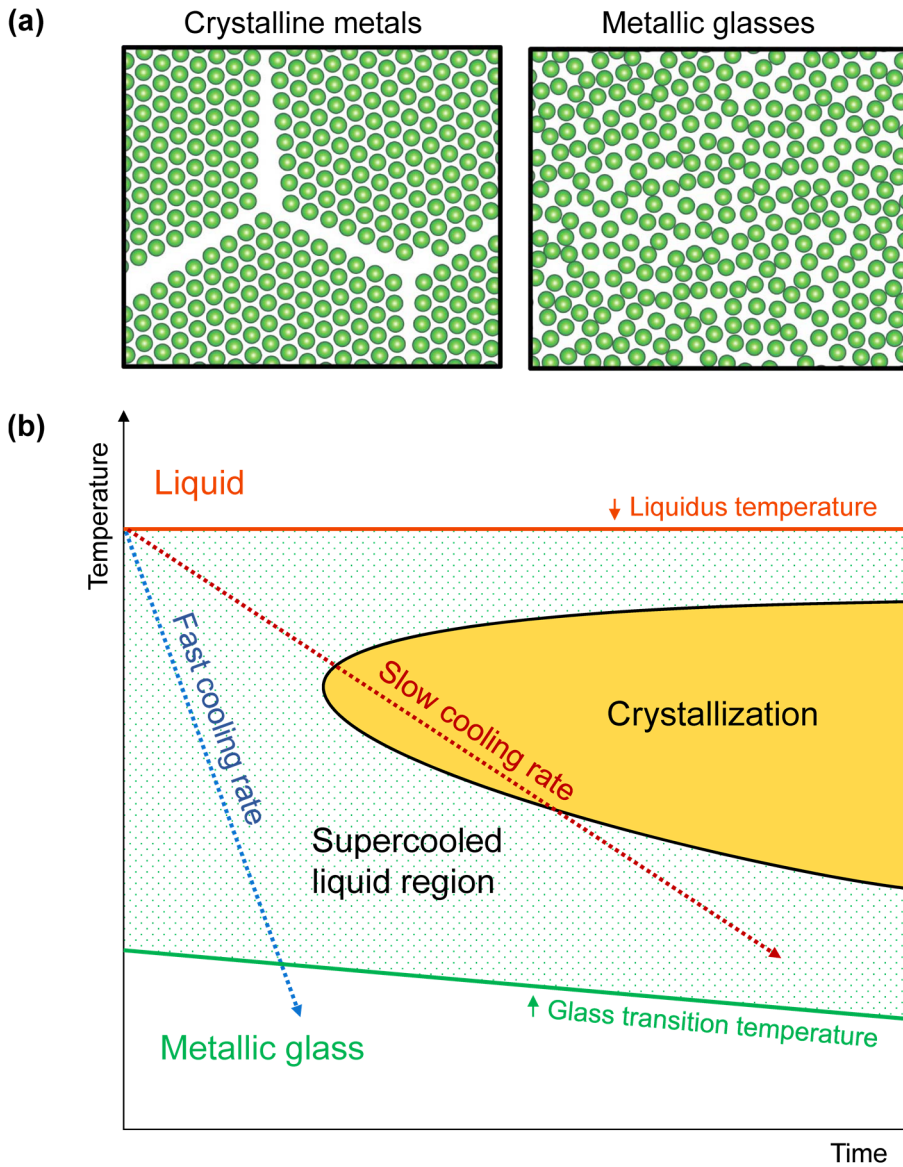


Figure 1.1. (a) Schematic illustration for the comparison of atomic structure in crystalline metals and metallic glasses. (b) Solidification path of metallic glass in Time-temperature-transformation (TTT) diagram.

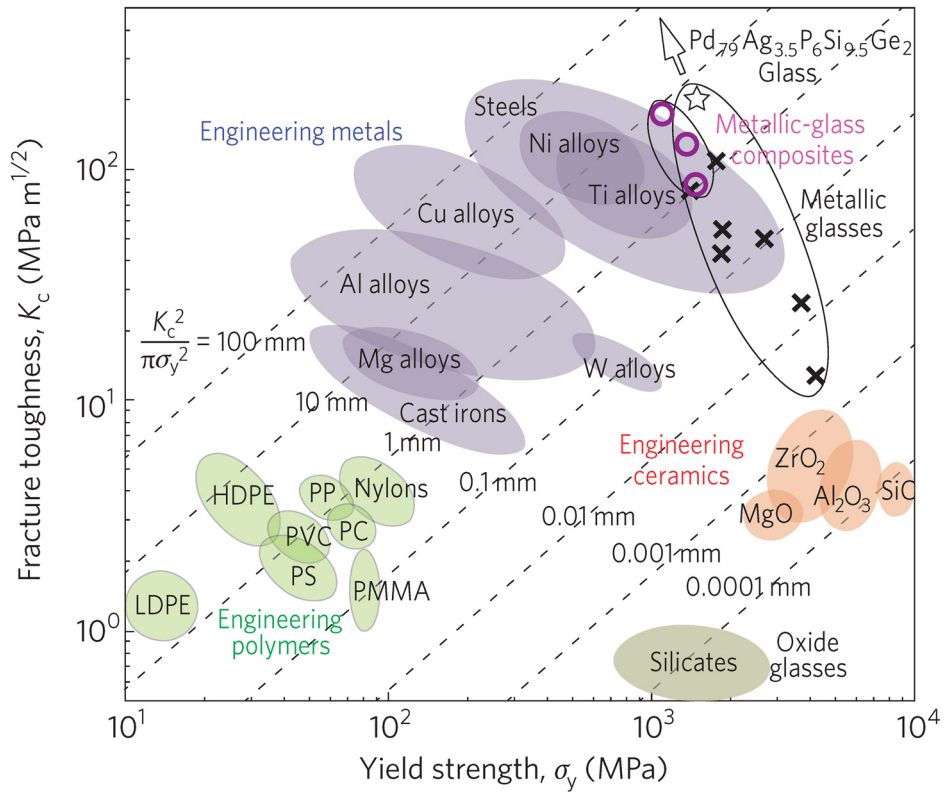


Figure 1.2. Ashby map of fracture toughness versus strength of materials. Reprinted from ref. 8 with permission through “Copyright Clearance Center”.

1.1.1. Fundamental mechanisms of deformation

In conventional crystalline metals with long-range ordered atomic structure, plastic deformation is mediated by their well-defined defects such as dislocations which drive the deformation to be initiated at low energy level. However, the deformation of metallic glasses without long-range translational symmetry is mediated by local atomic rearrangement, the direct process of breaking and rebuilding the atomic bonds⁹. The exact nature of this local atomic motion accommodating shear strain in metallic glasses is not completely comprehended yet, but the fundamental unit of the local atomic rearrangement have been suggested by two different model, free volume theory¹⁰ and shear transformation zone (STZ) theory¹¹. The metallic bonding character in metallic glasses enables their atomic structures to be considered as a simplified hard-sphere model suggested by Bernal¹², as compared to the complex bonding nature in covalent or ionic glasses. In this model, the atomic structure of metallic glass (or metallic liquid) is described as dense random packing of atomic hard-spheres. From this, the schematic illustration depicting the fundamental unit models for local shear transformation is shown in Figure 1.3.

In the atomistic view in metallic glasses, the total volume of a metallic glass can be separated into the volume occupied by the atomic spheres and the vacant volume among the spheres ('free volume'¹³). In the free volume theory¹⁰ on the deformation of metallic glasses, a nearest neighbor environment with relatively large free volume close to atomic volume is the potentially preferred site for the diffusive jump of atoms, as described in Figure 1.3 (a). The diffusive atomic jumps induced by shear stress leaves behind flow defects with a relatively low packing density,

resulting deformation-induced strain softening by mechanical dilatation. Although the follow-up researches¹⁴⁻¹⁶ suggest that the deformation motion of metallic glasses involves cooperative motion of multiple atoms instead of a single-atom motion in this model, the free volume model provides a clear insight into the strain softening and shear localization of metallic glasses at low temperature, and also quantitative analysis on the dilation of metallic glasses from the flow defect creation and annihilation process^{14,17}.

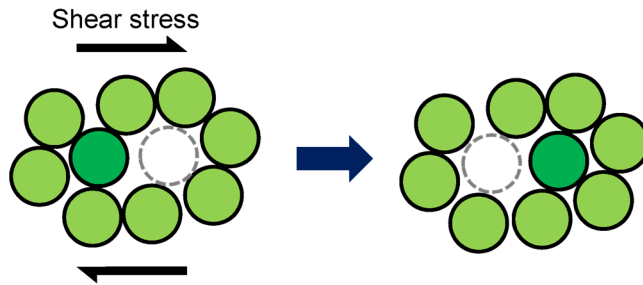
Unlike a single-atomic diffusive jump in the free volume theory, a local cluster of atoms undergoing inelastic shear distortion (STZ) is regarded as a fundamental unit for the deformation of metallic glasses in STZ theory^{9,11}, as described in Figure 1.3 (b). Based on atomistic simulations and sheared bubble raft experiments¹⁸, Argon introduced the concept of STZ as spontaneous and cooperative reorganization of a small cluster of randomly close-packed atoms. According to this view, STZ is not an instant event defined in a local volume rather than a structural defect in metallic glasses⁹. The computational modeling^{16,19,20} and experimental investigations²¹⁻²⁴ provided the estimation of STZ size to be a few tens to a few hundred atoms, varying with simulated (or tested) alloy compositions and testing methods. Analogous to the diffusive jumps in free volume theory, the operation of STZ is also significantly affected by local atomic configuration (or the distribution of free volume).

Although the free volume model and STZ model adopt different atomic motions as an underlying mechanism for the deformation of metallic glasses, these two distinct models share many common features which provide fruitful insights on the macroscopic deformation of metallic glasses⁹. The general flow equations of macroscopic flow in the both models can be expressed in a form of Eq. 1-1, though the specific factors in the expression are slightly different depending on the models.

$$\dot{\gamma} = A \cdot \exp\left(-\frac{Q}{kT}\right) \sinh\left(\frac{\tau V}{kT}\right) \quad \text{Eq. 1-1}$$

Here, $\dot{\gamma}$, τ , k and T are shear strain rate, applied shear stress, Boltzmann constant and temperature, respectively. A is a proportional constant bearing the influences of the attempt frequency, the characteristic strain (γ_0) and the fraction of material deforming via the activated process (diffusive jumps or STZ operation). Q is the characteristic activation energy for the corresponding processes in the models, and V is the characteristic volume, equal to ‘the product of the characteristic strain and STZ volume’ for STZ operation and ‘the half of atomic volume’ for diffusive atomic jump, respectively. The hyperbolic sine term in Eq. 1-1 originates from the consideration of forward operations of the processes competing with backward ones, implying the anelastic response and cyclic deformation of metallic glass in the both mechanisms of the two models. The exponential term implies that the both mechanisms are thermally activated so the stress and flow characteristics of the deformation is significantly influenced by temperature. The both mechanism also results in the increase of free volume (dilatational process) in the local volume where the processes is activated, then the accumulation of local dilatation leads to macroscopic mechanical behaviors such as strain softening and shear localization in metallic glasses. In contrast to various atomistic mechanisms on external conditions underlying the deformation of crystalline materials, the deformation of metallic glass is regarded to be governed by a single mechanism, whether it is diffusive atomic jump or STZ operation.

(a) Free volume theory



(b) Shear transformation zone (STZ) theory

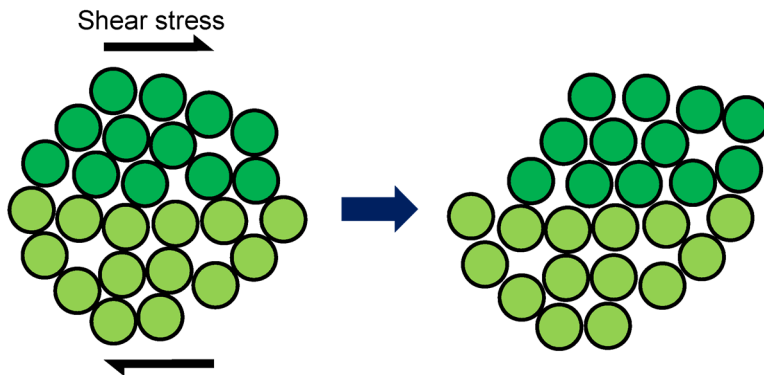


Figure 1.3. Schematic illustration of atomic shear transformations in metallic glasses. **(a)** Free volume model¹⁰. **(b)** Shear transformation zone (STZ) model¹¹. Recomposed from ref. 9 with permission through "Copyright Clearance Center".

1.1.2. Homogeneous deformation

The homogeneous deformation of a metallic glass occurs when the operations of flow defects (diffusive atomic jump or STZ operation) is distributed homogeneously throughout the whole volume of the alloy, and is typically observed at temperatures near the glass transition temperature (T_g) of the alloy⁹. As described in Figure 1.4 (a), a metallic glass at elevated temperature have the expansion of macroscopic volume (ΔV) which involves the influence of primary(α)- or secondary(β)-relaxations²⁵. The thermally-activated relaxation behaviors lead to the accumulation of locally dilatated volume, and the metallic glass at the temperatures near T_g has sufficient population of highly dilatated local regions distributed homogeneously in the sample. This enables the spontaneous and homogeneous activations of flow defects throughout the whole sample and macroscopic homogeneous plastic flow. Through the homogeneous deformation at elevated temperature, the alloy can be elongated even in excess of 10000%²⁶ as shown in Figure 1.4 (b). The exceptional processability of metallic glasses at elevated temperature (especially in the supercooled liquid region) is applied as thermoplastic forming technique for the precise processing of metallic glasses from macroscale to nanoscale²⁷.

The homogeneous deformation near or in the supercooled liquid region (the temperature region between T_g and T_x where T_x is the crystallization onset temperature; Figure 1.4 (a)) have a clear transition between Newtonian flow (with strain rate-independent viscosity) and non-Newtonian flow (strain rate-dependent viscosity) behavior. Figure 1.5 (a) and (b) shows a representative results on the transition behavior obtained by the compression tests of $Zr_{41.2}Ti_{13.8}Cu_{12.5}Ni_{10}Be_{22.5}$

bulk metallic glass samples²⁸. At relatively low strain rate (e.g. $1 \times 10^{-3} \text{ s}^{-1}$ in the results of Figure 1.5 (a)), the compressed sample rapidly enter into the steady-state flow condition with a constant flow stress, which regarded as a balance state between flow defect creation and annihilation⁹. In contrast, the samples compressed with relatively high strain rate have a stress overshoot behavior before approaching the steady-state conditions. The stress overshoot phenomena originate from unbalanced condition of free volume creation and annihilation^{17,29} in non-Newtonian flow. The hasty and excessive creation of free volume at the initial deformation stage until a peak stress induces softening (flow stress decrease) and gradually approach to the steady-state conditions.

The relation between steady-state flow stress and strain rate in the Zr-based metallic glass depending on temperature is displayed in Figure 1.5 (b). The linear relation between the stress and strain rate implies the constant viscosity ($\eta = \tau/\dot{\gamma}$) independent to strain rate at relatively high temperature and low strain rate conditions, which correspond to the definition of Newtonian flow behavior. In contrast, the relation become out of the linearity (i.e. non-Newtonian flow behavior) at relatively low temperature and high strain rate conditions. The transition between non-Newtonian to Newtonian flow behavior and the application of flow stress-strain relation in steady-state conditions of metallic glasses will be discussed in detail in Chapter 5. In addition, the homogeneous deformation of metallic glass is also observed even at room temperature, from nanoscale metallic glass samples³⁰. The unique deformation behavior of metallic glasses will be discussed briefly in Section 1.2, and be intensively investigated in Chapter 4 and Chapter 5.

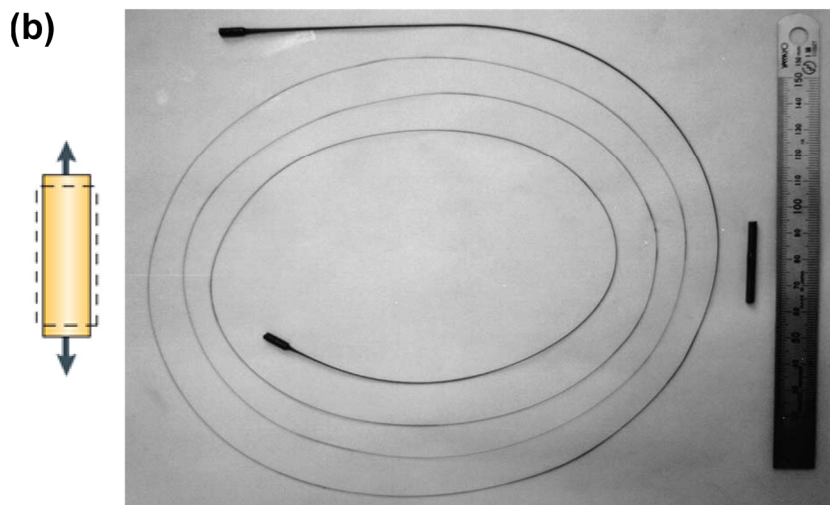
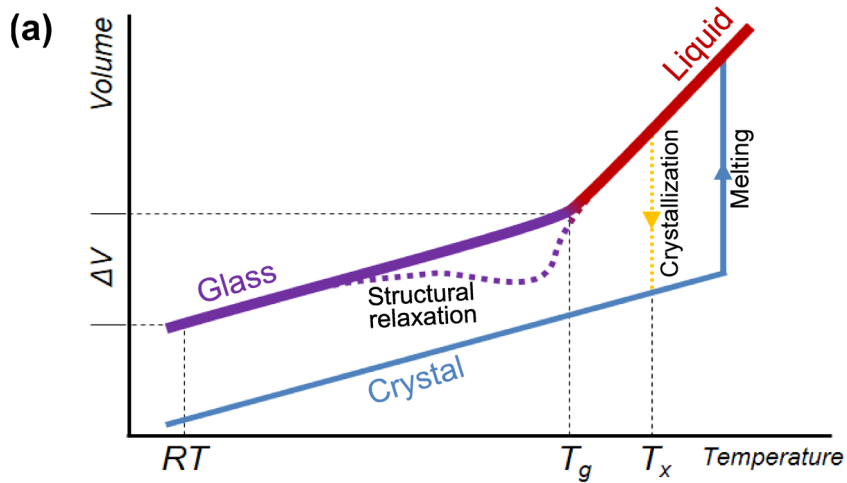


Figure 1.4. (a) Volume-temperature relation in transformations among liquid, glass and crystal. (b) A La-Al-Ni metallic glass deformed homogeneously to 20000% in the supercooled liquid region. (b) is recomposed from ref. 26 and 31 with permission through “Copyright Clearance Center”.

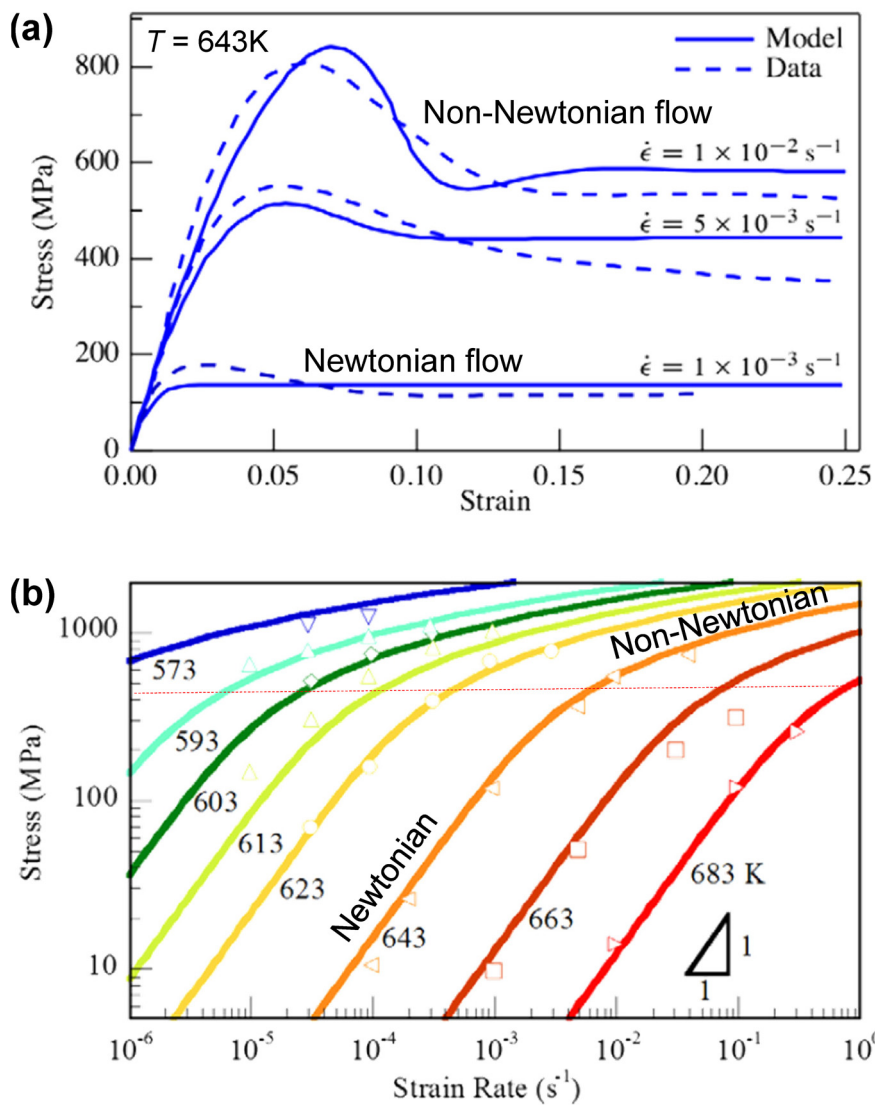


Figure 1.5. (a) Stress-strain curves of homogeneous deformation of Zr-based metallic glass at 623 K²⁸. (b) Steady-state homogeneous flow data for Zr-based metallic glass at high temperatures near the glass transition temperature^{9,28}. Recomposed from ref. 9 with permission through "Copyright Clearance Center".

1.1.3. Inhomogeneous deformation and shear banding

In contrast to the homogeneous deformation of metallic glasses at elevated temperature discussed in the previous section, the macroscopic plastic deformation of metallic glasses at low temperatures near room temperature is mediated by thin band-shape instabilities accommodating largely-concentrated shear strains, termed ‘shear bands’. The spontaneous shear localization to form shear bands in metallic glasses originate from the shear softening nature of the alloys. If a local volume in a metallic glass is plastically deformed through local shear transformation, it suffers accompanying dilatation and become softer than the surrounding undeformed regions, which eventually results in the self-focusing concentration of plastic strains into a thin shear band in the direction of maximum shear stress². After the initiation, shear bands generally operate very rapidly and can accommodate displacement apparently up to nearly the millimeter scale^{9,32}, generally being a main cause of extremely limited plasticity of metallic glasses. Therefore, the control of shear bands for inducing their multiple nucleation and blocking their rapid propagation have been attracted enormous research interests in order to improve the plasticity of metallic glasses^{2,31,33}.

Various scenarios of shear band formation have been suggested by theoretical considerations and computational simulations³⁴⁻³⁶. One of them is introduced here, focusing on the intrinsic structural inhomogeneity of metallic glasses as an origin of the shear band initiation³⁵, rather than the pre-existing extrinsic flaws or casting defects³⁴. When a sufficiently large population of STZs is homogeneously activated in a metallic glass matrix under high stress, the STZs would eventually exceed the percolation limit and the percolated STZs forms a thin band of intensively dilatated

state along the direction of maximum shear stress (Figure 1.6 (a)). Then, shear strains would be highly concentrated to the softened band-shape region rather than relatively dense and hard surrounding regions, resulting in its rapid development to a mature shear band with thickness of a few tens of nanometers (Figure 1.6 (b)).

Compared to conventional crystalline metals, metallic glasses exhibit lower values of Young's modulus and higher elastic strain limit (~2%), which means the remarkably higher capability for storing elastic strain energy per unit volume (i.e. resilience). The enormous elastic strain energy stored in a metallic glass during loading until the yield point is released with yielding through the small volume fraction of the alloy with in shear bands, causing substantial temperature rise. The evidences of the temperature rise in shear bands are often observed in metallic glasses as vein patterns from liquid-like shear flow on the fracture surface³⁷, fracture accompanied by sparking³⁸, and are also suggested by direct thermographic measurements^{39,40}. However, the alternative concept of 'cold' shear bands was suggested recently in contrast to 'hot' shear bands with substantial temperature rise^{41,42}. From a precisely displacement-controlled test of compressive deformation of bulk metallic glasses, it is reported that the dominant shear band can operate in a stick-slip manner and this acceleration-deceleration cycles of shear band sliding causes only negligible rise of temperature^{36,43,44}. As the hot shear bands generally develop in a runaway instability, the controlled and serrated sliding of the major shear band is also an important condition for multiple shear bands to have the opportunity to contribute to the plastic deformation. Thus, understanding cold shear bands as well as hot shear bands provides physical insights into the shear instability processes and offers useful information for improving the plasticity of metallic glasses⁴⁵.

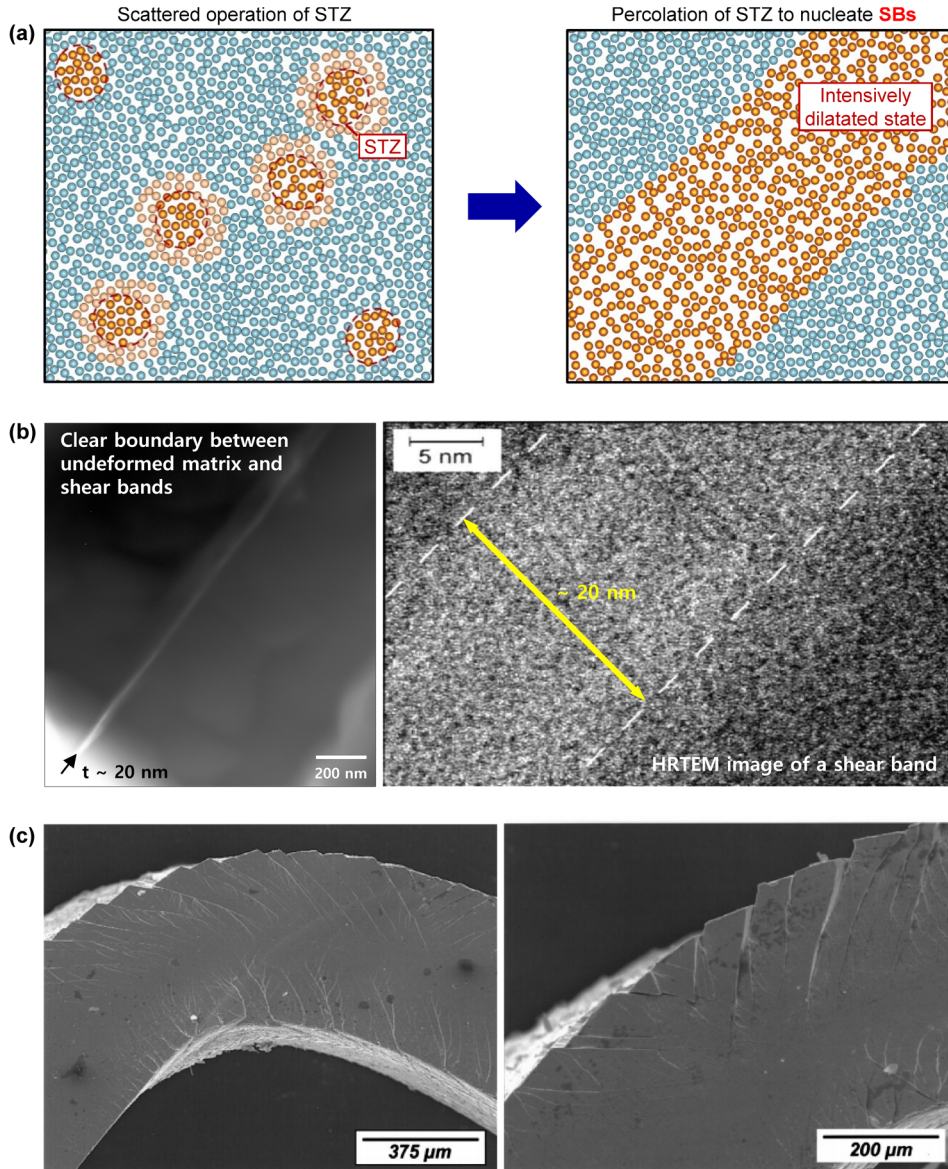


Figure 1.6. (a) Schematic illustration of the initiation process of a shear band. (b) (HR)TEM images of a shear band formed during the bend test of $Fe_{79.3}B_{16.4}Si_4C_{0.3}$ metallic glass ribbon, recomposed from ref. 45 with permission under the terms of the “Creative Commons Attribution Non-Commercial License”. (c) SEM images showing shear steps associated with shear bands in a bent strip of $Zr_{57}Nb_5Al_{10}Cu_{15.4}Ni_{12.6}$ metallic glass, reprinted from ref. 46 with permission through “Copyright Clearance Center”.

1.1.4. Deformation map for metallic glasses

Deformation-mechanism maps of materials display the dominant deformation mechanisms of materials under external conditions such as stress, temperature, or strain rate⁴⁷. These two-dimensional diagrams provide intuitively understandable information on the deformation of materials, and fruitful assistance in the selection of proper materials suitable for practical applications. A deformation-mechanism map is composed of mechanism transition boundaries, delineated from the model-based constitutive equations and the experimental data obtained under external conditions corresponding to the ordinates and abscissas of the map^{47,48}. Meanwhile, for metallic glasses (MGs), the ‘deformation maps’ (without the term ‘mechanism’)⁹ have been suggested representing the phenomenologies of deformation (or deformation mode) depending on external conditions, since the plastic deformation of MG is governed by a single mechanism, or an elementary plastic unit of shear transformation (i.e. diffusive atomic jump¹⁰ or shear transformation zone (STZ) operation¹¹). The first deformation map of MG proposed by Spaepen¹⁰ shows deformation mode variation under stress-temperature conditions based on free volume theory (Figure 1.7). The map with stress and temperature axes displays two basic deformation modes of homogeneous flow and inhomogeneous flow by shear banding, and strain rate contours. Since then, the intensive researches on the deformation of MGs have advanced the deformation map of MG^{28,29,49-51}, represented by the work of Schuh and his coworkers⁹ (Figure 1.8).

Schuh and his co-workers suggested two complementary maps in a stress-temperature space and a strain rate-temperature space, respectively, with the absolute values obtained experimentally from the specific glass $Zr_{41.2}Ti_{13.8}Cu_{12.5}Ni_{10}Be_{22.5}$.

The stress-temperature space in Figure 1.8 (a), as in the work of Spaepen, are primarily classified to two regions; homogeneous deformation and inhomogeneous shear localization. The boundary between the two primary deformation modes (displayed with thick solid line) directly indicates the yield strength of a metallic glass regulated by the onset of shear banding, which declines slightly with temperature. The effect of applied pressure on the temperature-dependent yield stress is also illustrated as a dotted line. The homogeneous regime is divided into the sub regions of elastic deformation, Newtonian and non-Newtonian flow. The elastic deformation region is defined as the region only with negligible flow with extremely low strain rate under $\sim 10^{12} \text{ s}^{-1}$, because, strictly speaking, there is no regime where the homogeneous flow may be avoided.

In the strain rate-temperature map in Figure 1.8 (b), the boundary between homogeneous and inhomogeneous deformation is also shown and the effect of applied strain rate upon shear banding events and serrated flows is intensively displayed in inhomogeneous deformation regime, which have been systematically investigated by nanoindentation studies⁵⁰. The vertical contours of constant stress are also displayed inside the non-Newtonian homogeneous regime. The dashed arrows at strain rates over $\sim 10^3 \text{ s}^{-1}$ denotes the softening effect due to adiabatic shear localization (the formation of hot shear bands). The deformation maps of MGs, comparably to deformation-mechanism maps, provide fruitful and straightforward information on mechanical behaviors of MG under external conditions.

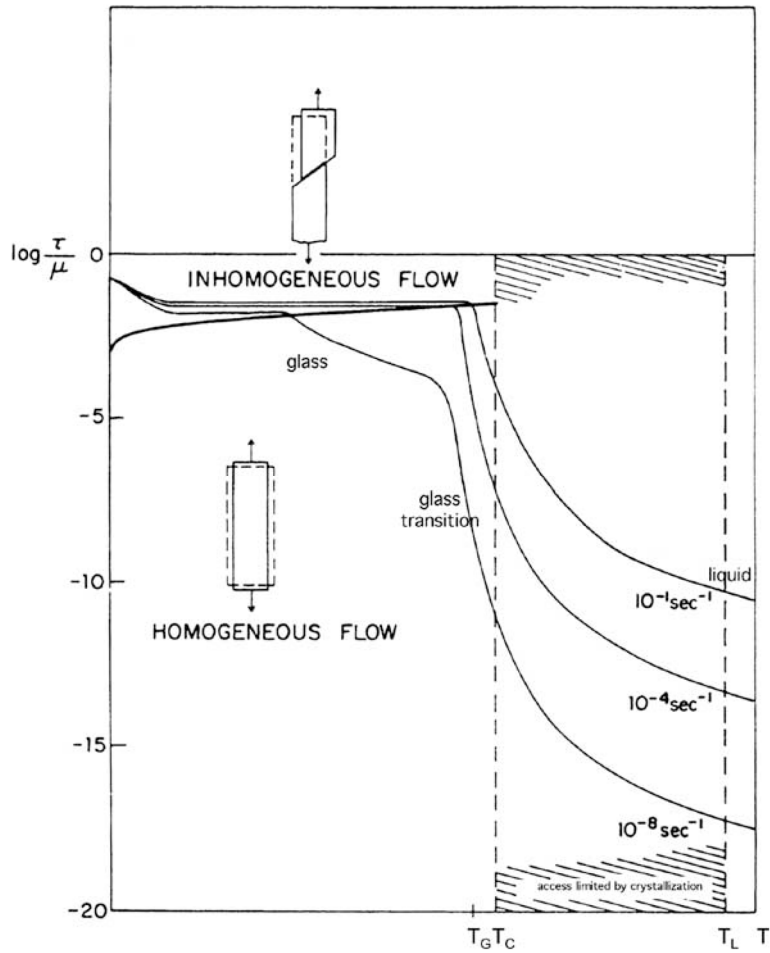


Figure 1.7. A first deformation map for metallic glasses based on the free volume theory, suggested by Spaepen¹⁰. Reprinted from ref. 14 with permission through "Copyright Clearance Center".

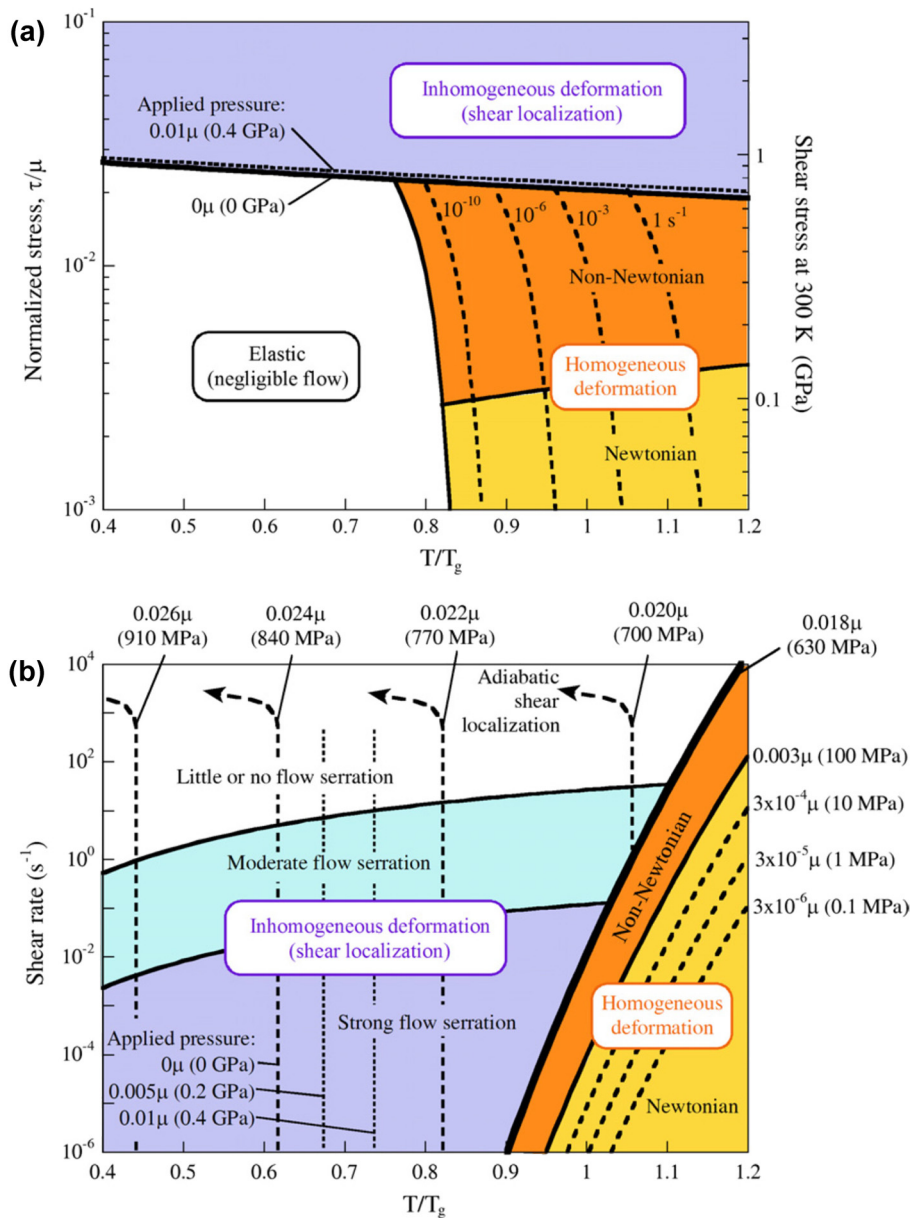


Figure 1.8. Deformation maps for metallic glasses in (a) stress-temperature and (b) strain rate-temperature axes, suggested by Schuh et al.⁹. The absolute values shown are for the specific glass $\text{Zr}_{41.2}\text{Ti}_{13.8}\text{Cu}_{12.5}\text{Ni}_{10}\text{Be}_{22.5}$. Reprinted from ref. 9 with permission through “Copyright Clearance Center”.

1.2. Nanomechanical behavior of metallic glasses

With the extrinsic size reduction into micro- or nanoscale, materials exhibit unique mechanical behaviors clearly distinct from that of bulk scale samples. In the case of crystalline metals, the sample size reduction induces interesting mechanical behaviors such as strengthening by dislocation starvation in nanoscale⁵² and surface-controlled dislocation multiplication in microscale⁵³. Although metallic glasses do not possess the crystalline defects such as dislocations, recent studies in a past decade demonstrated that nanoscale metallic glasses also show size-dependent deformation behaviors distinguishable from those in bulk scale. The interesting tendencies of size effect on the deformation of metallic glasses are not only “the smaller is the stronger” under shear banding regime⁵⁴⁻⁵⁶ but also the mode transition of plastic deformation from brittle-inhomogeneous to ductile-homogeneous manner⁵⁵⁻⁵⁹, while the both still be controversial subjects. In this section, the prevailing trends among precedent studies on size-dependent deformation behavior of metallic glasses will be introduced based on both qualitative and quantitative explanations for the sample size effects, and the extrinsic factors significantly affecting the nanomechanical behaviors will be also briefly summarized.

1.2.1. Size effect on strength

The variety results from uniaxial mechanical tests of samples with different sizes and alloy compositions have been reported for investigating sample size dependence of yield strength in metallic glasses, and can be roughly categorized into two groups; a group of results showing the trend of increased strength with size reduction^{54-56,60-63} and the other with no clear size dependence of strength⁶⁴⁻⁶⁶. In

order to resolve this dispute, a normalized relation enabling the comparison among the results from different alloy systems was suggested by Wang et al.⁵⁴, from the extension of an energy balance model⁵⁸ analogous to Griffith crack propagation criterion.

For the derivation of the normalized relation of size-dependent strength⁵⁴, the situation of a uniaxial compression test of metallic glass is assumed and its stress-strain curve is illustrated schematically in Figure 1.9 (a). After the initiation of a shear band at the onset stress of σ_I , the stress required become the flow stress σ_f which maintains the propagation/sliding of the shear band. Assuming adiabatic conditions, the released elastic energy (U_{el}) from the sample volume by shear band formation is equal to the elastic strain energy difference between the stress state of σ_I and σ_f , which is expressed as

$$U_{el} = \left(\frac{\sigma_I^2}{2E} - \frac{\sigma_f^2}{2E} \right) \times \frac{\pi D^2 h}{4} \quad , \quad \text{Eq. 1-2}$$

where E , D and h is Young's modulus, cross-sectional diameter and height, respectively, of the metallic glass sample. If the sample size is large enough to ignore the size effect (i.e. bulk scale), σ_f approaches the bulk strength (σ_0). The required energy for shear band formation (U_{SB}) can be estimated from the multiplying the area of shear band (A) and its unit energy per area ($\Gamma = t_{SB}\mu\gamma_c$ (ref. ⁶⁷), where t_{SB} is the shear band thickness and γ_c is the universal shear elastic limit⁹).

$$U_{SB} = A \cdot \Gamma \quad . \quad \text{Eq. 1-3}$$

Here, A is equal to $\sqrt{2}\pi D^2/4$ by assuming a shear band penetrating entire sample and its angle to be ~ 45 degrees, as described in Figure 1.9 (b). The reduced relation

from the equality between Eq. 1-2 and Eq. 1-3 can be expressed as,

$$\sigma_l^2 - \sigma_0^2 = 2\sqrt{2}E \frac{\Gamma}{aD} = \frac{\Psi}{D} \quad \text{Eq. 1-4}$$

where is $a = h/D$ is the aspect ratio of the sample and $\Psi = 2\sqrt{2}E\Gamma/a$ is constant for a particular metallic glass.

Figure 1.10 (a) summarizes the reported data from samples of various alloy systems and compositions in the plot of the normalized stress and sample diameter. The shear band initiation stress (~yield strength) values depending on sample diameter is normalized by the bulk strength (σ_0) of the corresponding metallic glass and Ψ , and the normalized stress-sample diameter data collapse well onto a single universal curve corresponding to the relation of Eq. 1-4. This results reveals that the trend of increased strength by sample size reduction seems to prevail regardless of alloy chemistry, while the underlying origin of the trend is still somewhat unclear.

In addition to the size-dependent strength, the elastic strain limit of metallic glasses would be also affected by sample size if the elastic modulus is independent to the size. Tian et al.⁶³ have reported that the elastic strain limit and the corresponding strength of submicron-sized metallic glasses are approximately twice as high as those of bulk metallic glasses (Figure 1.10 (b)), by employing a precise strain evaluation technique with nanoscale markers and *in situ* transmission microscope. The results suggest that Young's modulus of a metallic glass is independent (or has only a minor effect) to the extrinsic size reduction of the sample down to tens of nanometer scale, and its elastic strain limit can be increased proportionally to the degree of strengthening by sample size reduction.

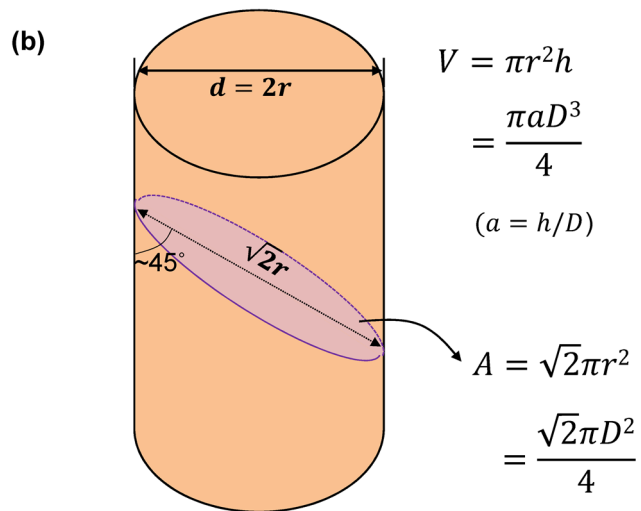
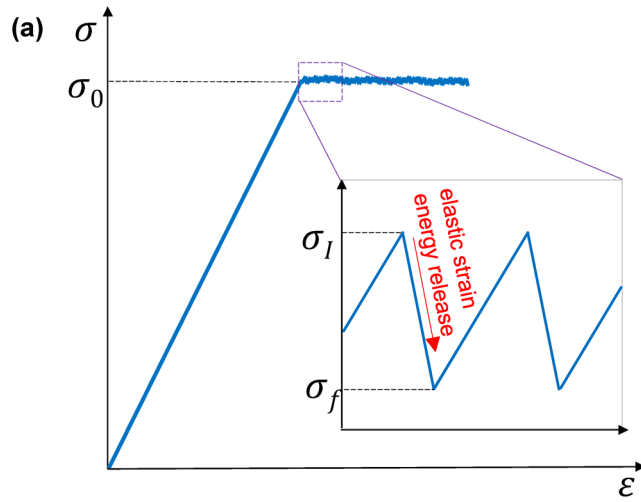


Figure 1.9. (a) Schematic stress-strain curve for the definitions of σ_l and σ_f . (b) Schematic illustration of a cylindrical sample and the penetrating path of a shear band.

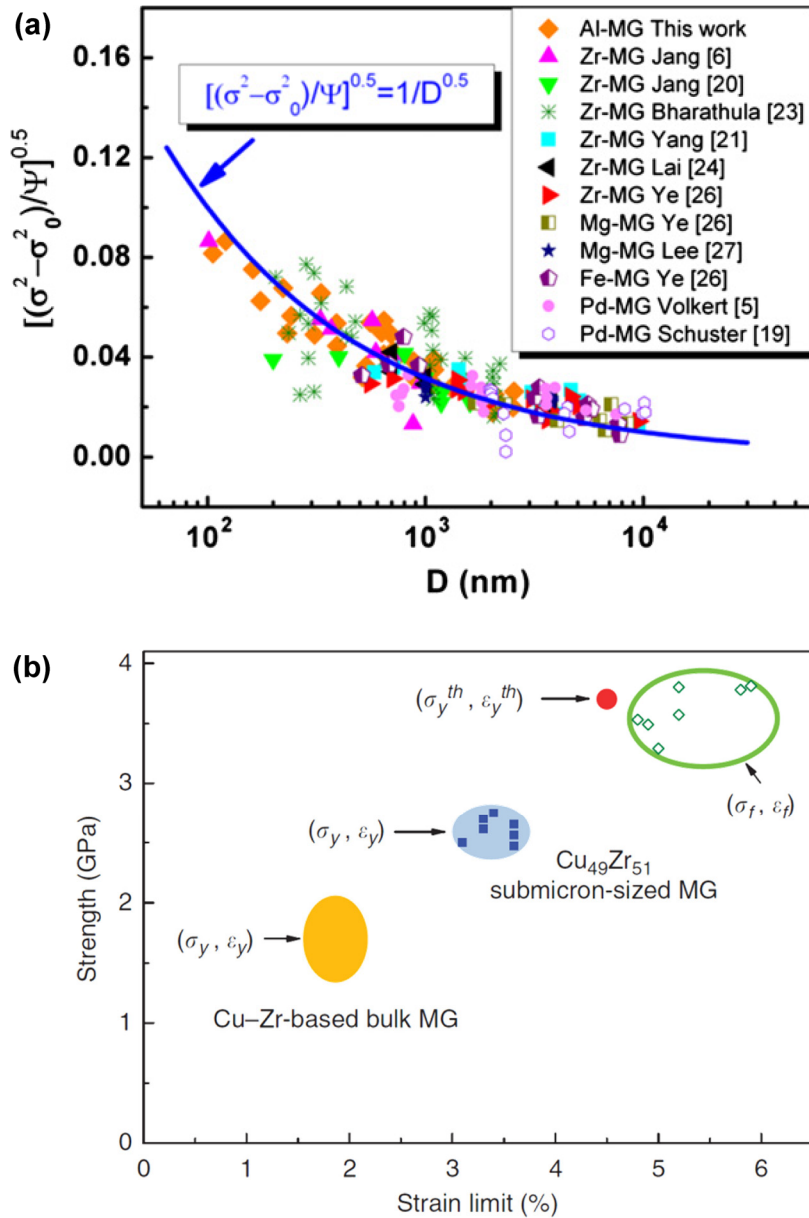


Figure 1.10. (a) Normalized strength versus sample size plot of experimental data. The solid line is a fitting line using the relation of Eq. 1-4. **(b)** Strength and strain limit of Cu-Zr metallic glasses in different size scale (bulk- and submicron-scale). Reprinted from ref. 54 and 63 with permission through “Copyright Clearance Center”.

1.2.2. Size effect on deformation mode transition

Volkert et al. first reported the transition from shear band-mediated inhomogeneous deformation in bulk/microscale metallic glasses to homogeneous deformation in a few hundreds of nanometer-sized metallic glasses⁵⁸ (Figure 1.11 (a)), from the compression tests of pillar-type samples prepared by FIB milling. Since then, similar phenomena have been reported by follow-up researches^{54-57,59,60,64,66,68-71}. Interestingly, Jang et al.⁵⁵ reported the obvious necking behavior from homogeneous deformation even in tensile deformation of Zr- based metallic glass nanorod samples, accompanying the unusual work-hardening behavior after yielding (Figure 1.11 (b)). The emergence of deformation mode transition by sample size reduction in metallic glasses is often interpreted via the correlation between the stress required for homogeneous deformation and for shear band formation^{54,55,58} (Figure 1.12). As discussed in the previous section, the stress required for shear band formation is predicted to have the relation of Eq. 1-4 as displayed in blue solid line in Figure 1.12. In contrast, the stress required to initiate room-temperature homogeneous deformation is often regarded to be independent of sample size, and bounded by the ideal strength (upper limit) and the room-temperature elastic limit (lower limit). In this view, a sample size at the intersection of the two stress required for each of deformation modes would be critical size for deformation mode transition, and the sample with a size under the critical value can exhibit homogeneous deformation priorly at stress level lower than the stress required for shear band formation. However, the origin of homogeneous deformation at room temperature and the scientific meaning of size-independence in the stress required for the homogeneous deformation is still in a veil, for nanoscale metallic glasses.

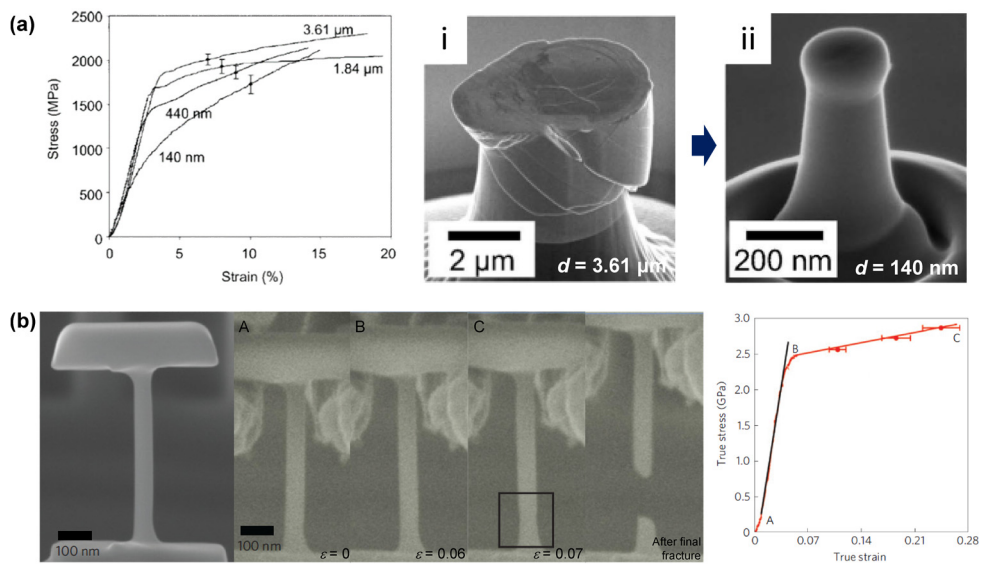


Figure 1.11. Homogeneous deformation of nanoscale metallic glass at room temperature. **(a)** Compressive deformation of pillar-type Pd-Si metallic glass samples. The clear transition is observed from localized shear banding in microscale samples to homogeneous deformation in nanoscale samples. **(b)** Tensile deformation of a Zr-based metallic glass nanorod showing necking behavior and unusual strain hardening. Reprinted from ref. 55 and 58 with permission through “Copyright Clearance Center”.

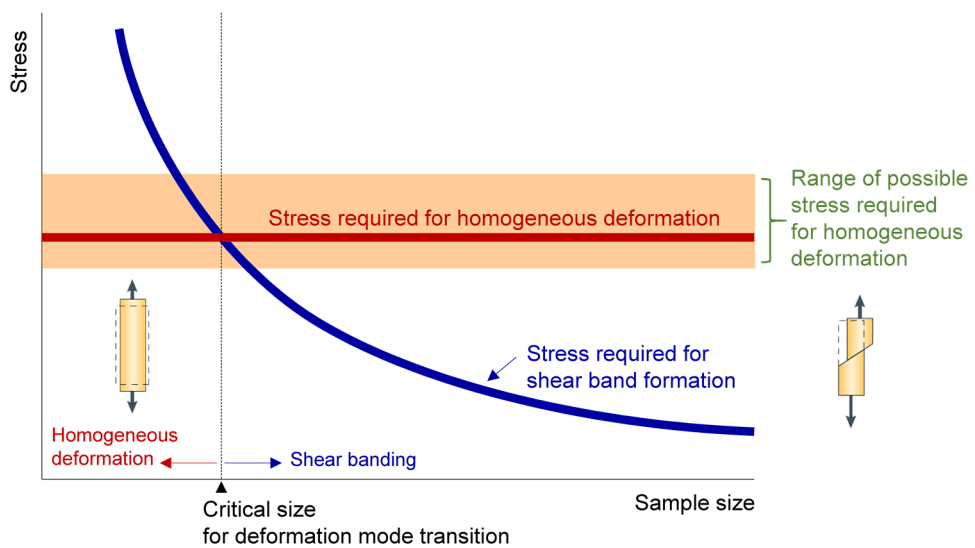


Figure 1.12. Schematic representation of the applied stresses required to shear band initiation⁵⁴ versus homogeneous deformation as a function of sample size^{55,58}. The insets are recomposed from ref. 31 with permission through “Copyright Clearance Center”.

1.2.3. Extrinsic factors affecting nanomechanical behaviors of metallic glasses

The size effects on the mechanical behavior of metallic glasses, introduced in the previous sections, are still controversial subjects due to inconsistent results depending on not only alloy system but also sample preparation history³⁰. The majority of nanoscale metallic glasses tested in previous studies were fabricated by focused ion beam (FIB), which uses high intensity Ga⁺ ion beam for etching the surface of a sample and fabricating nanopillar- or nanorod-shaped samples suitable for uniaxial mechanical testing. FIB-fabricated samples cannot avoid the Ga⁺ ion irradiation not only on the surface but also in the certain sample volume depending on the intensity of ion beam applied for etching process⁷². Such Ga⁺ ion irradiation effect on the mechanical behavior of metallic glasses have been largely overlooked in numerous researches on nanomechanical testing of metallic glasses, before a systematical investigation by Gianola et al.⁷² showing that the irradiation volume fraction and ion fluence by FIB clearly induce a transition from brittle-like to ductile-like tensile behavior accompanying a reduction of yield stress in molded metallic glass nanowires (Figure 1.8).

In addition, the surface roughness of nanoscale metallic glass also significantly affects the plastic deformation mode of nanoscale metallic glasses^{71,73}. Adibi et al.⁷³ employed molecular dynamic simulations for investigating the influence of surface roughness on the tensile deformation of metallic glass nanorods, from the comparison of deformation behavior between nanorods with near-perfectly smooth surface and the others with rough surface resembling the sample surface exposed to FIB irradiation. The results reveals that nanoscale metallic glasses with atomistically

smooth surfaces exhibit catastrophic failure via obviously localized shear band propagation, while the others with surface imperfections exhibit a clear transition from shear banding to necking instability above a critical roughness ratio of $\zeta \sim 1/20$, defined as the ratio between the average surface imperfection size and sample diameter.

However, it is worth noting that the size dependence on the strength and deformation mode transition from FIB-prepared specimens reported in previous studies cannot be attributed solely to the influence of ion irradiation or pre-existing surface flaws, because a metallic glass nanorod prepared by a FIB-less electroplating method can also be deformed homogeneously⁷¹ and the yield strength increase of metallic glasses by sample size reduction were observed in FIB-fabricated pillar samples⁵⁴ in contrast to the strength drop in highly-irradiated metallic glasses⁷². Therefore, in order to probe into genuine size effects on the deformation behaviors of metallic glass, nanomechanical studies using metallic glass specimens with a smooth and clean surface prepared by FIB-less process are necessary.

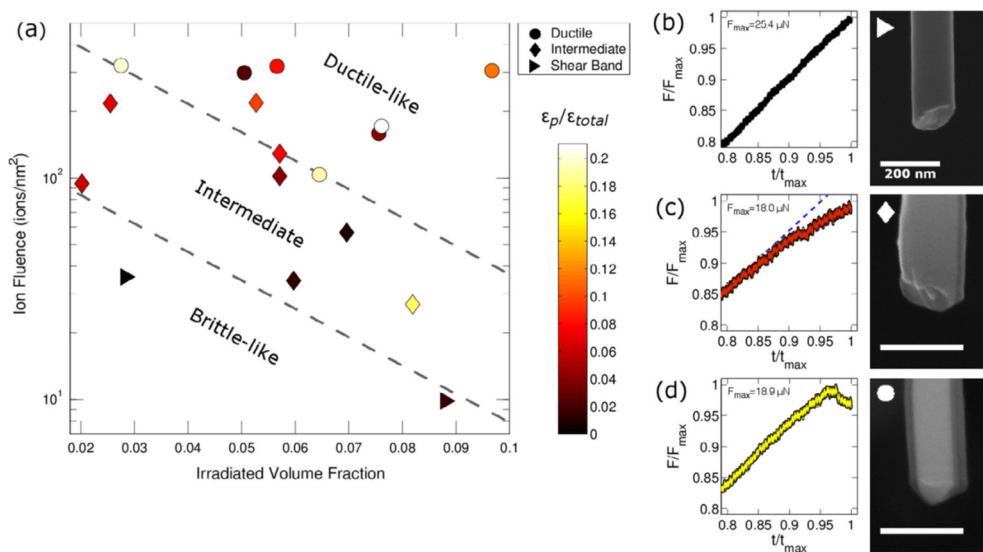


Figure 1.13. Influence of ion irradiation on the deformation of metallic glass nanorod. **(a)** Deformation map showing the influence of ion fluence and irradiated volume fraction on the amount of plastic strain. **(b–d)** Typical force–time curves and fracture morphologies for the shear banding (b), intermediate (c) and ductile-type deformation (d), respectively. Reprinted from ref. 72 with permission through “Copyright Clearance Center”.

1.3. Phase separation in metallic glasses

Since metallic glasses are thermodynamically unstable, they undergo structural changes during cooling from the liquid melts or during heating from the frozen-in glassy state⁷⁴. From this point of view, phase separation in metallic glasses can occur by (i) liquid–liquid separation during cooling from the liquid melts or (ii) by solid-state separation in frozen-in glass during heating. Earlier reports⁷⁵⁻⁸⁰ on phase separation in metallic glasses mostly deal with the latter, while the occurrence of phase separation in frozen-in glass (having only the negative mixing enthalpies among the constituent) during heating may be questionable⁷⁴. In contrast of the separation in frozen-in glass, clearly-separated two-glass structures in metallic glasses have been widely reported in the alloy systems with an intentionally-included atomic pair of a large positive enthalpy of mixing^{74,81-90}.

It is well known that an atomic pair with a large positive enthalpy of mixing relation forms a miscibility gap with high critical temperatures (~binodal line) in the equilibrium binary system and liquid-state phase separation can occur at temperatures over liquidus temperature when the composition of a melt is in the miscibility gap. However, the relations of large negative mixing enthalpy among constituent elements are generally favorable for stabilizing liquid phase and securing high glass-forming ability (GFA) in an alloy⁹¹. An alloy with an atomic pair with a large positive enthalpy of mixing relation should struggle with deterioration of the GFA, and phase separating metallic glasses can be designed by enhancing the GFA of each separated liquid phase by the aid of additional alloying elements. Kündig et al.⁸⁹ first reported a two-amorphous-phase structure formed by liquid–liquid phase separation during cooling from the liquid melts in La-Zr-Al-Cu-Ni system with a

large mixing enthalpy relation between La and Zr. Two quaternary systems inside the quinary system, La-Al-Cu-Ni and Zr-Al-Cu-Ni, have good glass-forming abilities, and their combination enables the liquid-state phase separation during cooling from the melt into La-rich and Zr-rich phase with sufficient glass-forming ability for solidified into amorphous state by rapid quenching (e.g. melt-spinning). An example of La-Zr-Al-Cu-Ni as-spun ribbon sample is shown in Figure 1.14 (a) and the phase-separated amorphous structure can be directly observed by electron microscopy. From the analogous alloy designs with this, various phase separating metallic glasses have been reported in the alloy systems such as Y-Ti-Al-Co^{87,92}, Cu-Zr-Al-Y⁹⁰, Nd-Zr-Al-Co⁸⁸, Ni-Nb-Y^{84,93}, Gd-Ti-Al-Co⁹⁴, Gd-Hf-Co-Al⁸¹, Cu-Zr-Al-Gd⁸², Gd-Zr-Al-Ni⁸³ and Zr-Gd-Co-Al⁸⁶.

The phase separating metallic glasses exhibit some unique characteristic from their unusual dual-amorphous structure with distinct chemistry. Park et al.⁹⁰ reported a precise control of amorphous heterogeneity in Cu-Zr-Al-Y phase separating metallic glasses into atomic scale can enhance the plasticity of the alloys by affecting local viscous flow behavior during shear deformation. Nd-Zr-Al-Co⁸⁸ and Gd-(Hf,Ti,Y)-Co-Al⁹⁵ phase separating metallic glasses were reported to have some unique magnetic behavior depending on the shape of separated amorphous phase. Besides, the phase separating metallic glass glasses can be used as the precursor materials for dealloying process (selective dissolution) for fabricating multi-component amorphous nanoparticle⁹⁶ and nanofoam materials⁹⁷, which is also the main concern in this study among the applications of phase separating metallic glass.

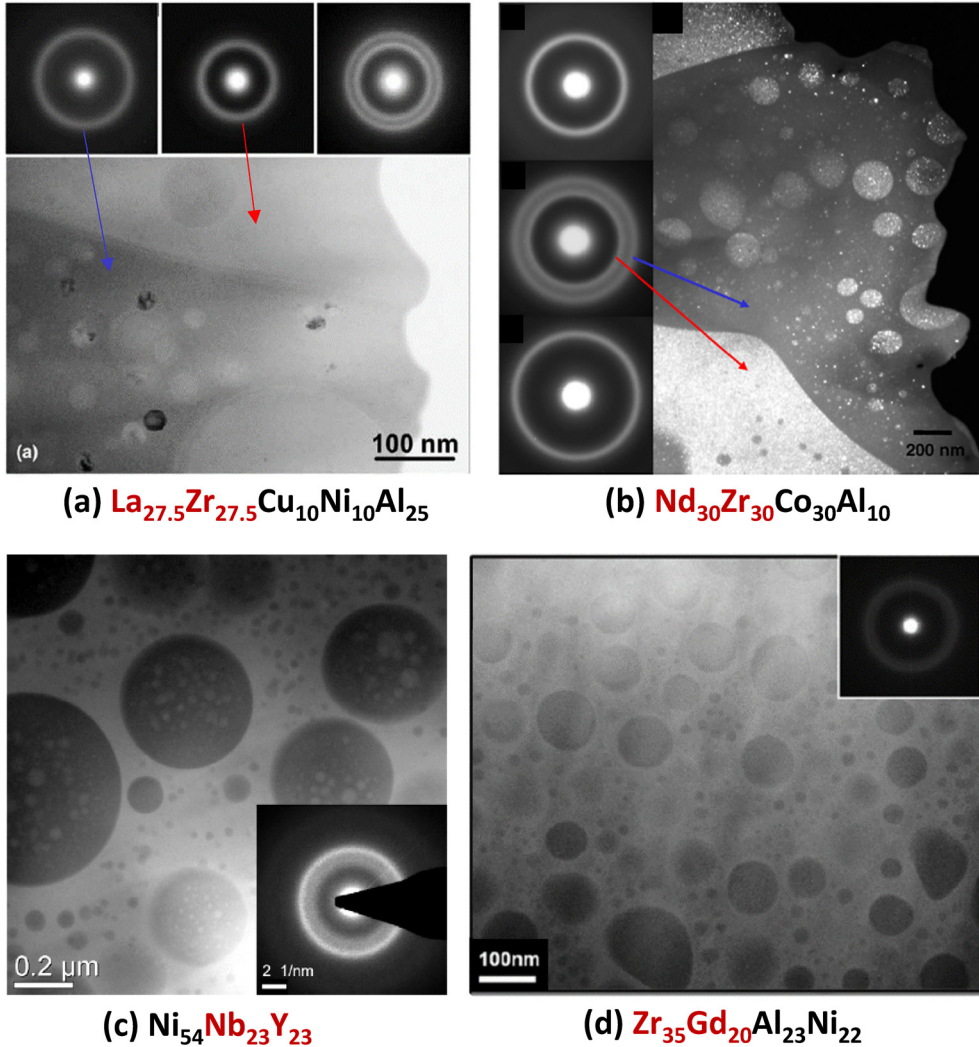


Figure 1.14. TEM images of phase separating metallic glasses (a) $\text{La}_{27.5}\text{Zr}_{27.5}\text{Cu}_{10}\text{Ni}_{10}\text{Al}_{25}$. (b) $\text{Nd}_{30}\text{Zr}_{30}\text{Co}_{30}\text{Al}_{10}$. (c) $\text{Ni}_{54}\text{Nb}_{23}\text{Y}_{23}$. (d) $\text{Zr}_{35}\text{Gd}_{20}\text{Al}_{23}\text{Ni}_{22}$. The image of (b) is a dark-field image while the others are all bright-field images. The insets are selected area diffraction patterns (SADP) corresponding to each of observed regions. Reprinted from ref. 83,84,88 and 89 with permission through “Copyright Clearance Center”.

Table 1.1. Alloy systems forming phase separating metallic glasses by rapid quenching.

Alloy system	A pair with $\Delta H^{mix} \gg 0$ (J/mol)		Compositions	Ref.
La-Zr-Al-Cu-Ni	La-Zr	(+13)	$\text{La}_{27.5}\text{Zr}_{27.5}\text{Cu}_{10}\text{Ni}_{10}\text{Al}_{25}$	89
Zr-(Nd,Pr,Ce)-Al-Ni	Zr-(Nd,Pr)	(+10)	$\text{Zr}_x(\text{Nd,Pr,Ce})_{60-x}\text{Al}_{15}\text{Ni}_{25}$	98
	Zr-Ce	(+12)		
Y-Ti-Al-Co	Y-Ti	(+15)	$\text{Y}_x\text{Ti}_{56-x}\text{Al}_{24}\text{Co}_{20}$	87,92
Cu-Zr-Al-Y	Zr-Y	(+9)	$\text{Cu}_{46}\text{Zr}_{47-x}\text{Al}_7\text{Y}_x$	90
Cu-Zr-Al-Gd	Gd-Zr	(+9)	$\text{Cu}_{46}\text{Zr}_{47-x}\text{Al}_7\text{Gd}_x$	82
Nd-Zr-Al-Co	Nd-Zr	(+10)	$\text{Nd}_{60-x}\text{Zr}_x\text{Co}_{30}\text{Al}_{10}$	88
Ni-Nb-Y	Nb-Y	(+30)	$\text{Ni}_{100-x}\text{Nb}_x\text{Y}_x$	84,93
Gd-Ti-Al-Co	Gd-Ti	(+15)	$\text{Gd}_x\text{Ti}_{55-x}\text{Al}_{25}\text{Co}_{20}$	94
Gd-Hf-Co-Al	Gd-Hf	(+11)	$\text{Gd}_{55-x}\text{Hf}_x\text{Co}_{25}\text{Al}_{20}$	81
Gd-Zr-Al-Ni	Gd-Zr	(+9)	$\text{Zr}_{35}\text{Gd}_{20}\text{Al}_{25-x}\text{Ni}_{20+x}$	83
Zr-Gd-Co-Al	Gd-Zr	(+9)	$\text{Zr}_{56-x}\text{Gd}_x\text{Co}_{28}\text{Al}_{16}$	86

1.3.1. Thermodynamic background of phase separation

In this section, a thermodynamic description of the stability condition for a multicomponent system^{74,99} (as general phase separating metallic glasses) will be briefly discussed. For a closed system at constant temperature T and pressure P , the criterion of equilibrium is given by minimization of Gibbs free energy.

$$(\delta G)_{P,T,n_i} \geq 0 \quad . \quad \text{Eq. 1-5}$$

n_i is a number of moles of component i in a multi-component system. Hancock¹⁰⁰ demonstrated that the criterion of stability of the multicomponent liquid with respect to infinitesimal composition fluctuations at constant T and P can be expressed by the conditions of following diagonal determinants:

$$G_{11} \geq 0 \quad \text{Eq. 1-6}$$

$$\begin{vmatrix} G_{11} & G_{12} \\ G_{21} & G_{22} \end{vmatrix} \geq 0 \quad \text{Eq. 1-7}$$

$$\begin{vmatrix} G_{11} & G_{12} & \cdots & G_{1m} \\ G_{21} & G_{22} & \cdots & G_{2m} \\ \vdots & \vdots & \ddots & \vdots \\ G_{m1} & G_{m2} & \cdots & G_{mm} \end{vmatrix} \geq 0 \quad . \quad \text{Eq. 1-8}$$

The last condition is trivial, because the determinant in Eq. 1-8 associated with the G_{ij} matrix is always null by applying Gibbs-Duhem equation,

$$n_1 G_{1i} + n_2 G_{2i} + \cdots + n_m G_{mi} = 0 \quad . \quad \text{Eq. 1-9}$$

The stability condition also can be expressed by using the stability function ψ , in terms of molar Gibbs free energy G_m of the system and mole fraction of component i ($X_i = n_i / \sum n_i$) as follows,

$$\psi = \begin{vmatrix} \frac{\partial^2 G^m}{\partial X_2^2} & \cdots & \frac{\partial^2 G^m}{\partial X_2 \partial X_i} & \cdots & \frac{\partial^2 G^m}{\partial X_2 \partial X_m} \\ \vdots & & \vdots & & \vdots \\ \frac{\partial^2 G^m}{\partial X_i \partial X_2} & \cdots & \frac{\partial^2 G^m}{\partial X_i^2} & \cdots & \frac{\partial^2 G^m}{\partial X_i \partial X_m} \\ \vdots & & \vdots & & \vdots \\ \frac{\partial^2 G^m}{\partial X_m \partial X_2} & \cdots & \frac{\partial^2 G^m}{\partial X_m \partial X_i} & \cdots & \frac{\partial^2 G^m}{\partial X_m^2} \end{vmatrix} \geq 0 \quad \text{Eq. 1-10}$$

If $\psi > 0$, the liquid is stable and any small composition fluctuations will decay back reversibly with time. If $\psi < 0$, however, the liquid is unstable and cannot be persistent against infinitesimal composition fluctuations, then will undergo phase separation by spinodal decomposition. The spinodal composition can be determined by the criterion $\psi = 0$. If the G_m of a system is given in terms of mole fraction, by using the stability function, it can be determined whether the liquid is stable against an infinitesimal fluctuation in composition (spinodal decomposition) or not.

For a simplified binary system of the components A and B, the molar Gibbs free energy can be written as

$$G_m = X_A G_A^0 + X_B G_B^0 + \Delta G^{mix} \quad . \quad \text{Eq. 1-11}$$

$$\Delta G^{mix} = \Delta H^{mix} - T \Delta S^{mix} \quad . \quad \text{Eq. 1-12}$$

When $\Delta H^{mix} \gg 0$, the region of instability (range between the point a and d in Figure 1.15 (a)) appears at the low temperature (e.g. $T = T_2$) where the ΔH^{mix} term become more dominant than the $T \Delta S^{mix}$ term, while the region of immiscibility vanishes at high temperatures over a critical temperature T_c . The stability function in the binary solution can be expressed by the reduction of Eq. 1-12 as follows:

$$\psi = \frac{\partial^2 G^m}{\partial X_2^2} \geq 0 \quad . \quad \text{Eq. 1-13}$$

This means the spinodal decomposition occurs between the inflection points (between the point b and c in Figure 1.15 (a)). The miscibility gap (binodal curve) and spinodal curve in a temperature-composition space (Figure 1.15 (b)) can be delineated from the equilibrium compositions and inflection points in the ΔG^{mix} curve, respectively, depending on temperature. The practical shapes of miscibility gaps are generally asymmetrical, different with the idealized case in Figure 1.15 (b). In order to express the molar Gibbs free energy and Gibbs free energy change with mixing in multi-component system with immiscibility near practical cases, various solution models have been suggested with extended considerations for complex configuration in the system⁹⁹, and can be adopted to thermodynamic calculation of miscibility gap.

Chang et al.⁹⁴ assessed the existence of miscibility gap and spinodal curve in Gd-Ti-Al-Co quaternary system, through the description of Gibbs free energies of the liquid solution phases by the sub-regular solution model using the Redlich–Kister formula¹⁰¹. They succeeded in evaluating the Gibbs free energy surface of the multi-component system at the partial compositional sections of quaternary phase tetrahedron, and suggested the pseudo-binary section of miscibility gap between two ternary compositions of Gd-Al-Co and Ti-Al-Co. The thermodynamic assessment of miscibility gap and spinodal line in phase separating metallic glasses provides fruitful information for controlling the phase-separated structure through the manipulation of the compositional and kinetic variables in alloying and casting process, which will be intensively investigated in Chapter 3.

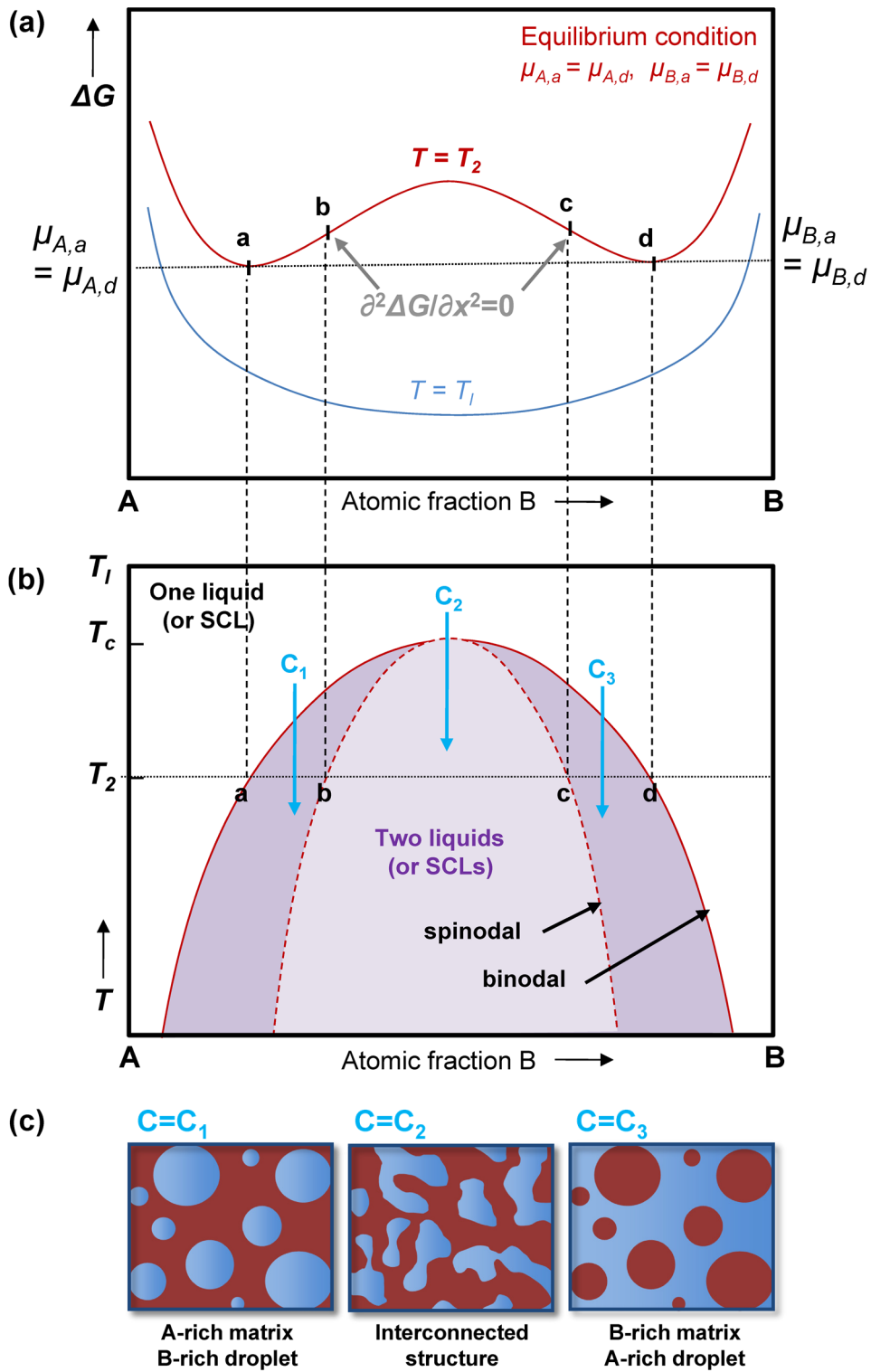


Figure 1.15. Schematic description of (a) Gibbs free energy change by mixing (ΔG^{mix}), (b) miscibility gap in binary system and (c) microstructures formed by phase separation depending on the compositions of alloy melt.

1.3.2. Mechanisms of phase separation

If a stable alloy melt at high temperature over $\sim T_c$ enters into the miscibility gap by cooling, the mixture of two liquid phase can be more stable than a homogeneous single liquid phase and some of these fluctuations can grow irreversibly to reduce free energy, as described in Figure 1.15 (a) and (b). The miscibility gap can be divided into two regions, a region between binodal and spinodal lines (metastable) and the other inside spinodal line (unstable). In the metastable region, $\psi > 0$, an infinitesimal composition fluctuation is accompanied by an increase in free energy and will decay reversibly. In order to separate a homogenous liquid phase into two liquid phase with equilibrium compositions for minimizing Gibbs free energy, the process should overcome the energy barrier for nucleation. Thus, the typical phase-separation mechanism in this metastable region is the “nucleation and growth” (Figure 1.16 (a)). In this mechanism, phase separation initiates by forming energetically stable solute rich domains (nuclei), which requires large thermal fluctuation to overcome the nucleation energy barrier. The energy barrier originates from the formation of a distinct interface between nuclei and matrix by nucleation. After the formation of nuclei over critical size, the phase separation proceeds by growth of those nuclei by diffusion of solute from matrix solution. From the beginning (nucleation) of phase separation process, droplet phases have largely different compositions from matrix composition. The resulting microstructure (“droplet structure”) shows a homogeneous distribution of spherical droplet phases in matrix phase.

In unstable liquid region where $\psi < 0$ within a spinodal line, phase separation takes place by spinodal decomposition process (Figure 1.16 (b)). The infinitesimal

fluctuations do not decay reversibly. Instead, they extend spatially and irreversibly without energy barriers to overcome. Therefore, spinodal decomposition does not experience thermally activated state, and proceeds spontaneously as a continuous growth of composition fluctuation through inverse (“up-hill”) diffusion against the concentration gradient to reduce free energy. The probability of the infinitesimal fluctuation is distributed homogeneously in the entire alloy melt and the amplitude of composition fluctuation grows continuously. According to the Cahn’s linearized theory¹⁰², especially in the early stage of decomposition, the concentration fluctuation with a particular dominant wavelength, corresponding to maximum growth rate, grows exponentially with time only in amplitude⁷⁴. Depending mainly on the undercooling and diffusivity of the constituting elements, only a single Fourier component among the various fluctuation wavelengths survives especially at early stage of spinodal decomposition and this component dominates the characteristic scale length of the domains. At this stage, the phase domains have no distinct interface and show continuous network structure with hyperbolic interfaces, characterized by negative Gaussian curvature having both convex and concave curvature. With an increase of concentration difference between the two phase domains, the interfacial energy corresponding to gradient energy increases. In order to reduce the total interfacial energy, coarsening of the domain structure takes place to reduce interfacial energy of the system. Depending on viscosity and diffusivity of the material, different growth mechanism is expected to dominate the coarsening kinetics, resulting in change in morphologies of phase separated metallic glass. The well-defined interconnected structure of the spinodal decomposition is a transient structure, which coarsens self-similarly for a limited duration of time and then breaks up into fragmented structures.

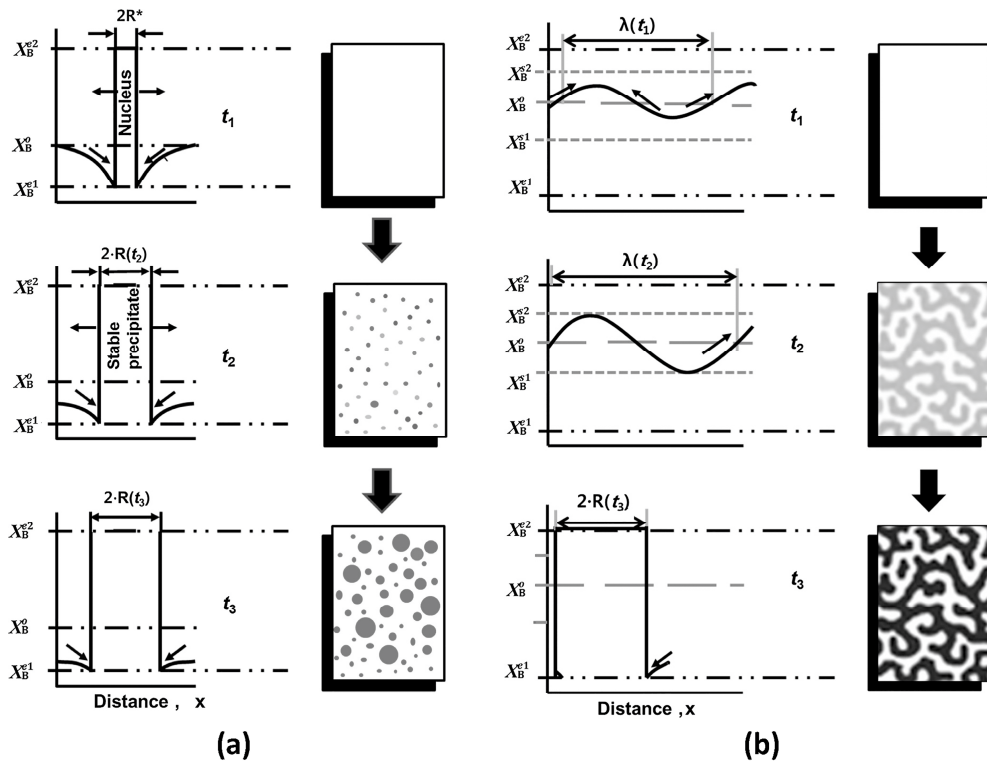


Figure 1.16. Schematic diagrams showing spatial variations in concentration variation and morphology evolution ($t_1 < t_2 < t_3$) during phase separation by two different mechanisms⁷⁴. **(a)** Nucleation and growth. **(b)** Spinodal decomposition. Reprinted from ref. 74 with permission through "Copyright Clearance Center".

1.4.Thesis motivation and scopes

Nanoscale metallic glasses possess exceptional mechanical properties, which cannot be described based on current deformation maps for metallic glasses, such as excellent strength much higher than the already high strength of bulk samples, accompanying large elastic limit much over 2% and improved ductility through the homogeneous deformation. Thus, the extrinsic size reduction of metallic glasses into the nanoscale is a unique route for enhancing the plasticity of metallic glasses with avoiding the general propensity of strength-ductility trade-off. However, the origins of the unique deformation behaviors in nanoscale metallic glasses are still in veil. The lack of explainable origins and the several inconsistencies among the results depending on alloy system and sample preparation history cause controversies over the mechanical behaviors of nanoscale metallic glass.

From the precedent views on the homogeneous deformation of nanoscale metallic glasses at room temperature, the increased stress required for shear band initiation and the suppression of localized shear banding by sample size reduction lead to the occurrence of homogeneous deformation of which the stress required is regarded as being independent to sample size. However, the causality between ‘suppression of localized shear bands’ and ‘homogeneous deformation at room temperature’ is still ambiguous, and the scientific signification of ‘the critical stress for homogeneous deformation’ is also obscure. In addition, the dimensional limitation hinders nanoscale metallic glasses from practical applications despite their exceptional mechanical properties by sample size effect, ironically.

From the views mentioned above, a few questions on the mechanical behavior of nanoscale metallic glasses are emerged as follow:

Q1) Is the homogeneous deformation of nanoscale metallic glasses at room temperature induced dominantly by the influence of sample preparation methods, such as ion irradiation effect and surface roughness?

Q2) Can the nanoscale metallic glasses at room temperature flow as the high-temperature supercooled liquid state, through homogeneous deformation? If there is a difference, what is the main difference in the flow characteristics of both states?

Q3) How can the internal state of nanoscale metallic glasses suffering homogeneous deformation be described qualitatively or quantitatively?

Q4) What is the scientific signification of the stress required for homogeneous deformation of nanoscale metallic glass at room temperature? Does it remain constant independent to sample size?

Q5) How can the exceptional mechanical properties of nanoscale metallic glasses be applied to the materials in larger scale for extended applications?

In this study, comprehensible solutions will be suggested to the questions above, through the comprehensive analysis on the mechanical response of metallic glass nanoparticles and nanofoams. The samples are fabricated by dealloying process of phase separating metallic glass precursors, which will be discussed intensively in Chapter 3. The systematical investigations on the deformation of metallic glass nanoparticles will be discussed in Chapter 4. Based on the findings in Chapter 4, A novel deformation map for metallic glasses covering the mechanical behavior of nanoscale metallic glasses will be suggested in Chapter 5. The extended applications of the mechanical properties of nanoscale metallic glasses will be introduced through the compressive deformation of metallic glass nanofoams, in Chapter 6.

Chapter 2.

Experimental procedures

2.1. Sample preparation

2.1.1. Arc melting

For preparing the master alloy buttons, arc melting of high-purity elements were employed. The mixtures of high-purity elements (99.9% or higher) of the desired compositions in (Y,Gd)-Ti-Al-Co system were prepared by precise weighing in 0.1 mg-scale. The mixtures of elements were placed on a water-cooled copper hearth inside the chamber of arc-melting apparatus (SAMHAN Vacuum development Co. Ltd.; Figure 2.1 (a) and (b)). Then, the chamber was evacuated into a high vacuum state under 1.5×10^{-5} torr and was backfilled with high purity (5N) Ar gas. Prior to the melting the mixture of elements, a pure Ti button was melted, which act as a getter for remaining oxygen in high-purity Ar atmosphere. The mixtures of elements were melted with arc plasma from a tungsten electrode, and re-melted at least 4 times after flipping, for achieving homogeneously alloyed buttons. Weight loss by melting process was controlled to be less than 1% of the initial weight.

2.1.2. Melt spinning

The alloy buttons prepared by arc melting were cut in to proper size for putting inside a quartz tube with an inner diameter ~ 12 mm. The quart tube was placed

inside the chamber of melt-spinning apparatus (SAMHAN Vacuum development Co. Ltd.; Figure 2.1 (c) and (d)). The chamber was also evacuated into a high vacuum state under 1.5×10^{-5} torr and was backfilled with high purity (5N) Ar gas. Then, the alloy button was re-melted by induction heating and the melt was injected through the nozzle of the quartz tube (nozzle diameter < 1 mm) onto a rotating copper wheel with surface velocity ~ 40 m/s. For the injection, high-purity (5N) Ar gas was applied with an over pressure of 50 kPa. The product of this process was thin ribbon-shape with the thickness ~ 25 μm and width ~ 2 mm. The alloy compositions of fabricated alloy ribbons were $\text{Y}_{19}\text{Ti}_{36}\text{Al}_{25}\text{Co}_{20}$, $\text{Y}_{25}\text{Ti}_{30}\text{Al}_{25}\text{Co}_{20}$, $\text{Y}_{27.5}\text{Ti}_{27.5}\text{Al}_{25}\text{Co}_{20}$, $\text{Y}_{30}\text{Ti}_{25}\text{Al}_{25}\text{Co}_{20}$ (Y-Ti-Al-Co phase separating metallic glasses), $\text{Gd}_{19}\text{Ti}_{36}\text{Al}_{25}\text{Co}_{20}$, $\text{Gd}_{25}\text{Ti}_{30}\text{Al}_{25}\text{Co}_{20}$, $\text{Gd}_{27.5}\text{Ti}_{27.5}\text{Al}_{25}\text{Co}_{20}$, $\text{Y}_{30}\text{Ti}_{25}\text{Al}_{25}\text{Co}_{20}$ (Gd-Ti-Al-Co phase separating metallic glasses), $\text{Ti}_{55}\text{Al}_{25}\text{Co}_{20}$, $\text{Y}_{55}\text{Al}_{25}\text{Co}_{20}$, $\text{Gd}_{55}\text{Al}_{25}\text{Co}_{20}$ (Ternary monolithic metallic glasses for comparison), and $\text{Ti}_{55.8}\text{Co}_{30.4}\text{Al}_{11.7}\text{Gd}_{2.1}$ (Metallic glass ribbon with the average composition of metallic glass nanoparticles fabricated by dealloying of $\text{Gd}_{27.5}\text{Ti}_{27.5}\text{Al}_{25}\text{Co}_{20}$ ribbon).

2.1.3. Chemical dealloying

For the fabrication of Ti-based metallic glass nanoparticles and nanofoams, chemical dealloying process was employed with (Y,Gd)-Ti-Al-Co phase separating metallic glass ribbons. For the fabrication of nanoparticles, the ribbons with droplet-type phase-separated structure (e.g. $\text{Y}_{27.5}\text{Ti}_{27.5}\text{Al}_{25}\text{Co}_{20}$, $\text{Gd}_{27.5}\text{Ti}_{27.5}\text{Al}_{25}\text{Co}_{20}$) were immersed in 0.1M nitric acid solution after crushing the ribbons into small pieces for securing large reactive surface area. Ultrasonication was applied to the solution to accelerate the reaction rate. In order to prevent excessive heating effect from

ultrasonication, the solution was cooled in cold water bath for 5 minutes after ultrasonication process for 5 minutes. The ultrasonication-cooling cycles were repeated for 6~8 times to complete dissolution of (Y,Gd)-rich amorphous phases, and the products after dealloying reaction were separated from the solution by centrifugation with rotating speed of 3000 rpm. The separated nanoparticles were kept in high-purity (99.9%) ethanol, in order to prevent powder explosion.

For the fabrication of metallic glass nanofoams, the ribbons with interconnected-type phase-separated structure (e.g. $Y_{19}Ti_{36}Al_{25}Co_{20}$) were immersed in 0.1M nitric acid solution without crushing process. For the clear observation of cross-section, the cross-section of some ribbons was fine-polished using diamond lapping films and MultiPrep™ system (Allied High Tech) before dealloying process. The dealloyed depth in the ribbons can be controlled by immersion time. For $Y_{19}Ti_{36}Al_{25}Co_{20}$ ribbon in 0.1M nitric acid solution, the dissolution rate was ~ 4 $\mu\text{m/hr}$ from the free side edge. In order to obtain completely dealloyed ribbons without Y-rich phase, the ribbon was immersed in the nitric acid solution for 24 hrs.

2.1.4. Micro-pillar fabrication

Micropillars of a metallic glass nanofoam were prepared by focused ion beam-scanning electron microscope (FIB-SEM) dual beam system (FEI Nova 600). The pillars were fabricated into parallelepiped or cylindrical shape with taper angle under 2 degrees. In order to minimize the influence of Ga ion beam irradiation inside the sample, the multi-step milling with step-by-step decrease of beam current was employed with approaching the final milling stage. The aspect ratios (height/width) of the fabricated micropillars were controlled to be ~ 2.5.

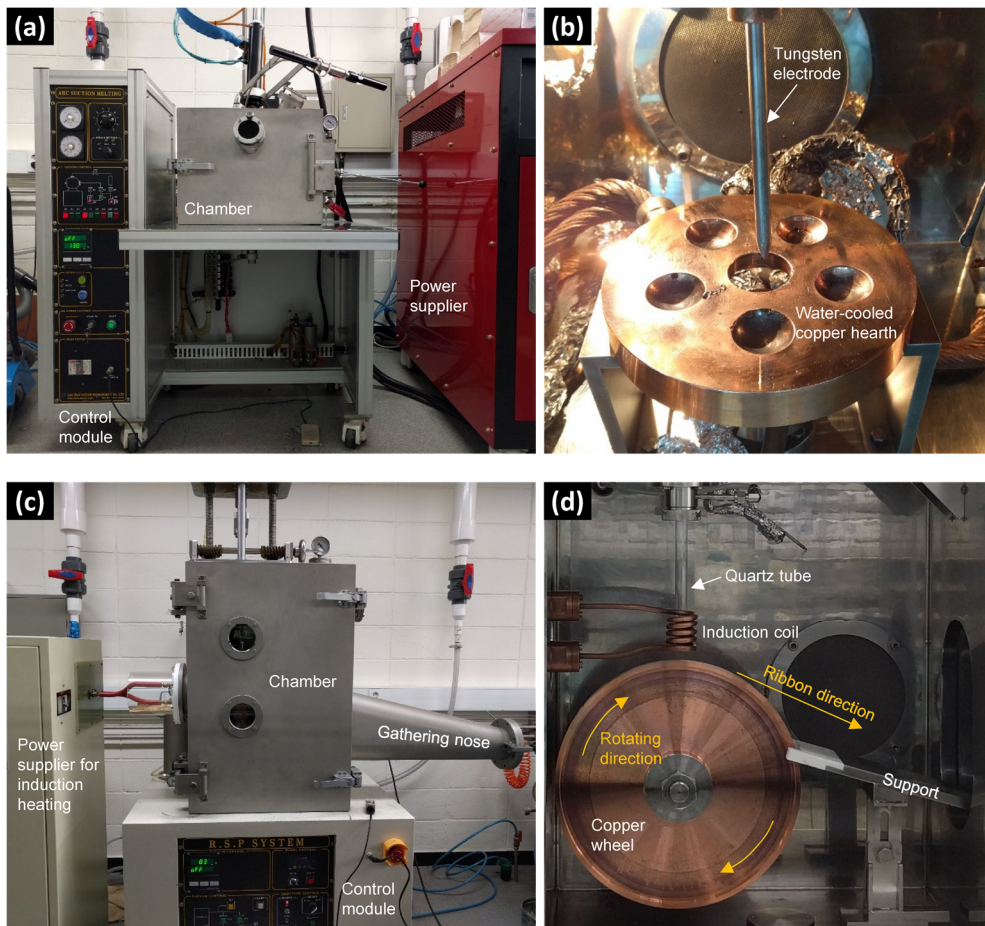


Figure 2.1. (a) The overview of arc melting apparatus. (b) Setup inside the chamber of arc melting apparatus. (c) The overview of melt-spinning apparatus. (d) Setup inside the chamber of melt-spinning apparatus.

2.2. Microstructural characterization

2.2.1. Scanning electron microscopy

The SEM observations were performed to characterize the microstructure of the phase separating metallic glass ribbons and the morphology of nanoparticles and nanofoams. The phase separating metallic glass ribbons, especially their (Y,Gd)-rich phases, have a large oxygen affinity to form oxide layer from the contact with water-based solutions, which hinders the ribbon sample prepared by with normal mechanical polishing methods from clear microstructural observation in SEM. Rather than the mechanical methods, the cross-section of the ribbons were fine-polished by Ga ion beam and directly observed through in-lens secondary electron detector in FIB/SEM dual beam system (Carl Zeiss 1540EsB Crossbeam system). The in-lens detector (or Through-the-lens detector in FEI Nova 600) provides high-intensity and high-contrast secondary electron images from dominantly SE1-type signals, which enables a clear distinction of separated amorphous phases in the high resolution images of the ribbons.

2.2.2. Three-dimensional microstructure analysis

The 3-D microstructure of the selected ribbon samples were obtained by serial sectioning and imaging method, automatically conducted by FIB/SEM dual beam system (Carl Zeiss 1540EsB Crossbeam system). A single cycle of sectioning-imaging contains a short ion beam milling process in depth of 20nm and a following imaging process by in-lens detector. Approximately ~ 660 and ~90 serial images were obtained from $\text{Gd}_{30}\text{Ti}_{25}\text{Al}_{25}\text{Co}_{20}$ and $\text{Y}_{19}\text{Ti}_{36}\text{Al}_{25}\text{Co}_{20}$ alloy ribbons, respectively.

The images were re-aligned (due to the drift in the sectioning-imaging process) and the 3-D microstructures were constructed from the stacking of aligned images using Avizo Fire 6 software (FEI software).

2.2.3. Transmission electron microscopy

The thin disc samples for transmission electron microscopy (TEM) were prepared from the ribbon samples. The ribbon samples were punched into 3mm-diameter-disc, and were polished into the thickness $< 10 \mu\text{m}$ by mechanical polishing. The further thinning of the samples was conducted by ion-milling process using Precision Ion Polishing System (Gatan PIPS II model 695) with liquid nitrogen cooling. The thin disc sample was cleaned by plasma cleaner (Fischione Model 1020) before TEM observation. In the case of nanoparticles, spraying process were employed for preparing TEM samples. The nanoparticles were placed on thin wedge with the top thickness of $1 \mu\text{m}$ by spraying the nanoparticles after dispersing them in ethanol by ultrasonication.

For the observation of bright-field TEM images and the corresponding diffraction patterns, TEM equipment operated at 200 kV (Tecnai F20) and operated at 300 kV (JEOL 3000F, JEOL 3010 and Philips CM300FEG) were used. The chemical variation between the ribbon before dealloying and the nanoparticle after dealloying was investigated by energy dispersive spectroscopy (EDS, EDAX Octane Silicon Drift Detector) linked with TEM (Tecnai F20), with high-angle annular dark field (HAADF) imaging in scanning transmission electron microscope (STEM) mode.

2.3. Thermal analysis

2.3.1. Differential scanning calorimetry

The differential scanning calorimeter (Perkin Elmer DSC 8500) with intracooler system which has an operable temperature range of 223 ~ 1023 K was utilized to measure heat flow spectrum and analyze crystallization reaction of amorphous phases during isochronal heating and isothermal heating process. The samples were enclosed in Al or Cu pan for the measurement. An empty pan was used as a reference. Pt-based heating cell was purged with high purity argon gas with a flow rate of 20 ml/min to minimize sample oxidation. The system was calibrated using high purity In and Zn standards before sample measurements. The temperature scan measurements were performed with a heating rate of 10 K/min or 20 K/min, depending on samples. In isothermal measurement, the sample temperature is raised to the preset temperature with a heating rate of 10 K/min and kept isothermally.

2.3.2. Thermomechanical analysis

The temperature-dependent strain responses of ribbon samples were investigated to detect the softening point (glass transition region) of the ribbon samples. After removing spikes at the side of ribbons by mechanical fine-polishing, the ribbon samples were gripped tightly by sample grabs for tensile mode testing. Then, the sample with the grabs was loaded in thermomechanical analyzer (TA instruments TMA Q400) The heating rate for temperature scan was 10 K/min and the applied force was 0.1 N. The experimental procedures for steady-state flow analysis at a constant stress and temperature will be discussed in Section 2.4.2.

2.4. Mechanical analysis

2.4.1. Nanocompression test in electron microscope

For the compression test of metallic glass nanoparticles, the particles were placed on a flat silicon substrate by spraying the particles dispersed in ethanol after ultrasonication. An example of dispersed Ti-based nanoparticles on a Si substrate is shown in Figure 2.2 (a). The individually-dispersed particles (dealloyed from $\text{Gd}_{27.5}\text{Ti}_{27.5}\text{Al}_{25}\text{Co}_{20}$ ribbons) were compressed by in-situ nanomechanical tester (Hysitron PI-85 picoindenter) in a SEM (FEI Quanta 250 FEG). The instrument was equipped with a flat diamond punch with 1 μm -diameter circular end, and the sample is loaded as described in Figure 2.2 (b). After then, the entire device of in-situ tester is inserted inside the SEM chamber. The particles were compressed between the diamond punch and the substrate in the displacement-controlled mode with drift correction. Except the result with an in-situ recorded SEM movie for contact diameter measurement, the compression tests were conducted under beam-off condition. For the compression test of micropillar-type samples, the instrument was equipped with a flat diamond punch with 10 μm -diameter circular end and the procedure is same as described above except the particle dispersion process.

2.4.2. High temperature tensile creep test

In order to investigate the steady-state homogeneous flow of metallic glass ribbons, the high temperature tensile creep tests were conducted with $\text{Ti}_{55.8}\text{Co}_{30.4}\text{Al}_{11.7}\text{Gd}_{2.1}$ alloy ribbons using thermo-mechanical analyzer (TA instruments TMA Q400) under the load-controlled condition. The ribbons were

prepared to have a dimension of width ~ 0.2 mm, thickness ~ 25 μm and initial gauge length ~ 8 mm by precise mechanical polishing (Allied High Tech MultiPrepTM Polishing System). The precise values of width and thickness were measured by optical microscope observation before the creep tests. The prepared samples were gripped tightly by sample grabs for tensile mode testing (Figure 2.2 (a)). In order to prevent the damage on the sample grabs during high-temperature measurements, thin copper films with thickness ~ 100 μm were inserted between a sample and the grabs. The sample with the grabs was loaded on quartz stage for tensile mode testing, as shown in Figure 2.2 (b) and (c). The upper stage and grabs are at a fixed position, while the lower parts are forced downwards by actuator. The temperature range for the creep tests was determined by differential scanning calorimetry and thermo-mechanical analysis with constant heating rate of 10 K/min, as discussed in Section 2.3.1 and 2.3.2. The sample temperature is raised to the preset temperature by the precise feedback control with furnace temperature. The heating rate to a target temperature was 10 K/min and kept isothermally at a desirable testing temperature.

2.4.3. Nanoindentation test

The nanoindentation tests (Hysitron TriboLab 750) were performed in order to obtain the elastic moduli (E and μ) and hardness of the ribbon. The fine-polished cross-section of the ribbon was tested by Berkovich-type diamond tip in load-controlled mode at a constant loading rate of 1 mN/s up to a maximum load of 5 mN. The values of E and μ is obtained by averaging the results of 30 repeated tests and assuming the Poisson's ratio of the alloy ~ 0.35 which is a general value for Ti-based metallic glasses.

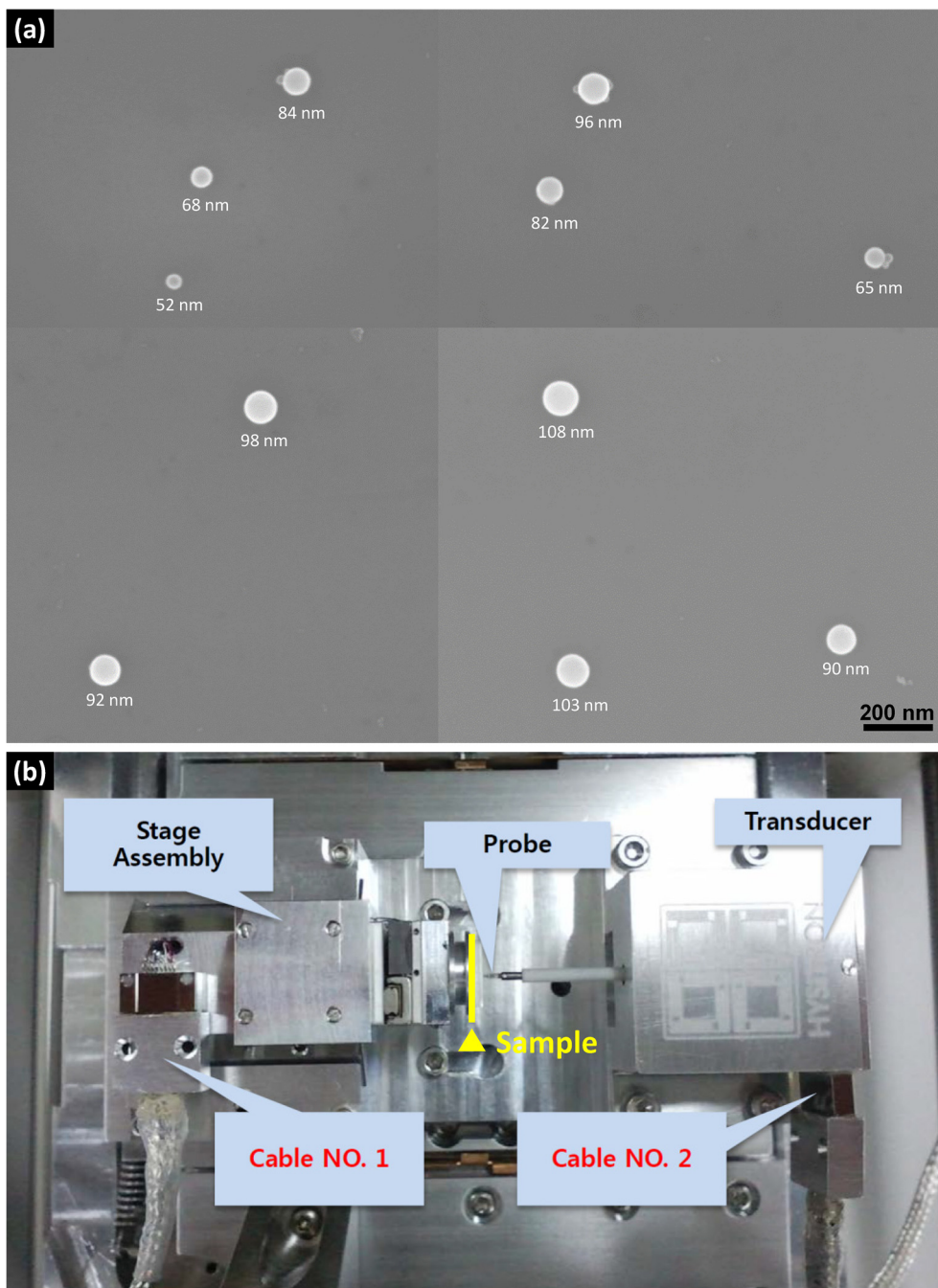


Figure 2.2. (a) SEM image of Ti-based metallic glass nanoparticles dispersed individually on a Si substrate. (b) The overview of an in-situ indentation tester (Hysitron PI-85 Picoindenter) for testing inside SEM.

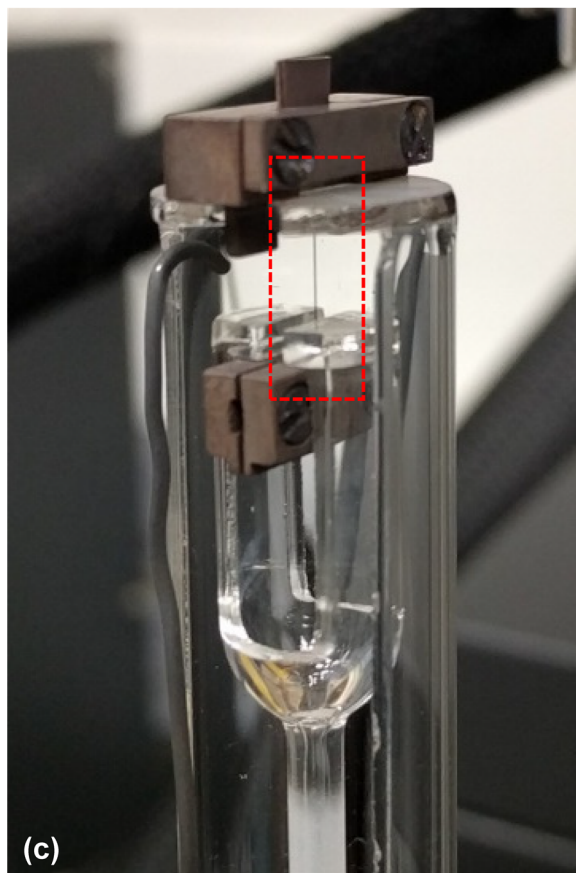
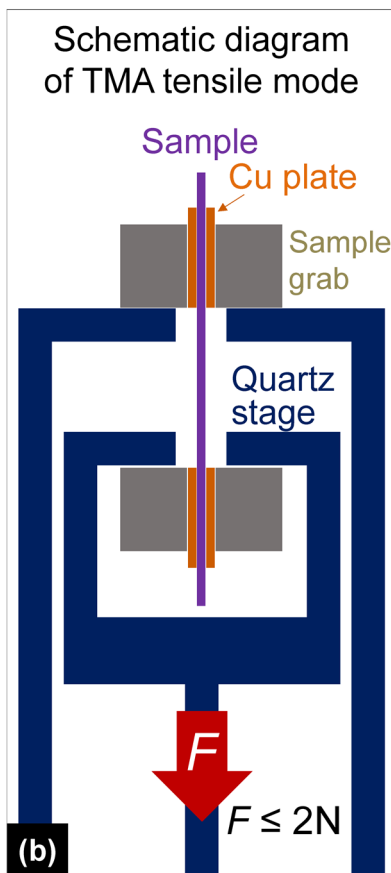
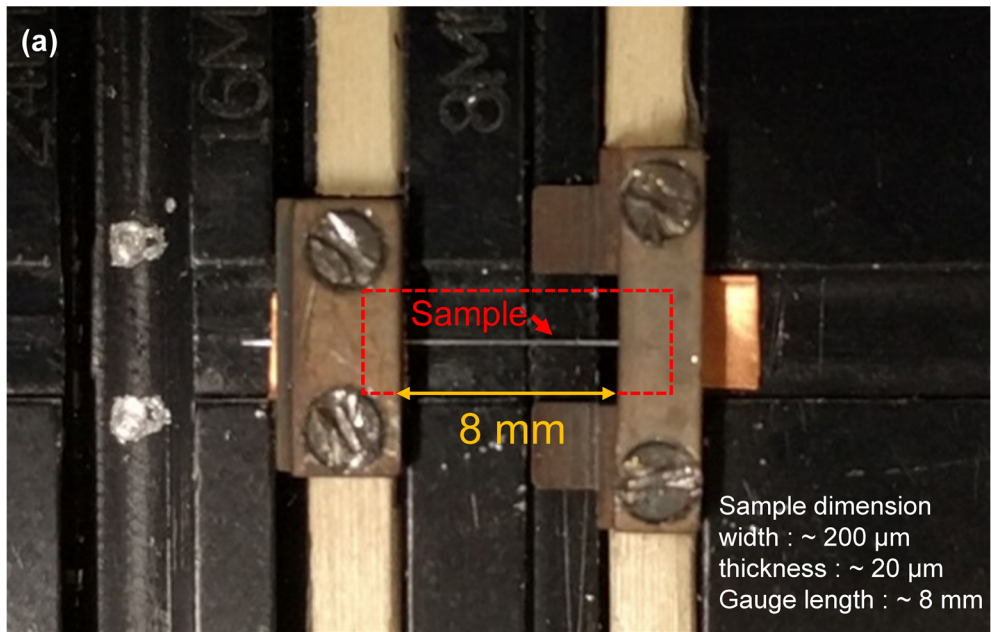


Figure 2.3. (a) A sample gripped by grabs for high-temperature creep test in TMA apparatus. (b) Schematic illustration of TMA tensile mode testing in this study. (c) The sample and grabs loaded on quartz stage for tensile mode testing inside TMA apparatus.

Chapter 3.

Fabrication and microstructure control of metallic glass nanoparticles and nanofoams

3.1. Introduction

Micro- to nano-structured metallic glasses have attracted wide interests of researchers due to their functional and structural specialties. Among them, metallic glass particles (i.e. powders) have been developed for structural applications after sintering into bulk size^{103,104}, and also for functional applications in chemistry¹⁰⁵ and magnetic materials^{106,107}. Gas atomization technique is a technique generally applied for fabricating metallic glass particles^{108,109}. The technique is a useful for fabricating a large amount of microparticles over gram-scale, while the size of the fabricated particles is normally over a few micrometers. Although a recent study suggested that a small portion of nanoparticles (with diameter under 1 micron) can be fabricated by precise temperature control of alloy melt in gas atomization¹⁰⁹, the technique is normally not proper process for metallic glass nanoparticles. Metallic glass nanoparticles having diameter in a few tens to a few hundred nanometers can be synthesized through mechanical alloying¹¹⁰ or wet-chemical reaction^{105,106}. However, the nanoparticles from these (mechano-)chemical process have uneven surface morphology and extremely small size under 100 nm, which is out of size range for mechanical investigation in this study.

On the other hand, metallic glass foams (i.e. porous metallic glasses) have been

also actively developed for structural applications by supplementing poor ductility of metallic glass and achieving high mechanical energy absorption¹¹¹⁻¹¹⁵. The first metallic glass foam was developed by Schroers et al. in Pd-Cu-Ni-P alloy system using inactive gas-expansion method using gas-releasing agents¹¹⁶. Since then, various metallic glass foams were fabricated in various alloy systems using the similar gas-expansion methods^{112,114,115}, placeholders (to be leached out for leaving pores)^{113,117}, hollow microspheres¹¹⁸ and powder metallurgical methods¹¹⁹. These metallic glass foams have microscale pores and irregular porous structure due to the difficulty in controlling gas expansion and dispersion of additive materials in metallic glass matrix.

Differentiating from the method mentioned above, the metallic glass nanoparticles and nanofoams handled in this study are fabricated through the dealloying process of phase separating metallic glass (PS-MG)^{96,97} (Figure 3.1). The alloy design considering mixing enthalpy relations among constituent elements, the unique metallic glass with two chemically-different amorphous phases can be fabricated through phase separation phenomena during quenching from melt state. Due to the distinct chemical compositions of separated phases, they have different reactivity against a certain chemical solution, which enables to dissolve more reactive one selectively with the solution while the other remains without reaction (dealloying process). Depending on the separated structure of the amorphous phases, the inactive remaining phase after dealloying process forms metallic glass nanoparticles or nanofoams. Therefore, the initial structure of PS-MG precursor alloy significantly affects the product of dealloying process. By the precise control of alloy composition and cooling rate, PS-MG alloy with nanoscale secondary amorphous phases can be fabricated, which can be applied as a precursor of

dealloying process for nanoscale metallic glass particles or metallic glass foams with nanometer-sized pores.

In this chapter, the fabrication process and microstructural investigation of metallic glass nanoparticles and nanofoam is described. The morphology of the nanoparticles and nanofoams is projected from the microstructure of secondary phases in precursor alloys. Thus, the microstructure control of PS-MG precursor alloys will be discussed first, for manipulating the product of dealloying process. The compositional effect and kinetic effect on the formation of phase-separated microstructure in PS-MGs is systematically investigated through intensive microstructure analysis including three-dimensional microstructural analysis. The microstructures of the metallic glass nanoparticles and nanofoams are also investigated by an intensive characterization method on imaging and chemical analysis.

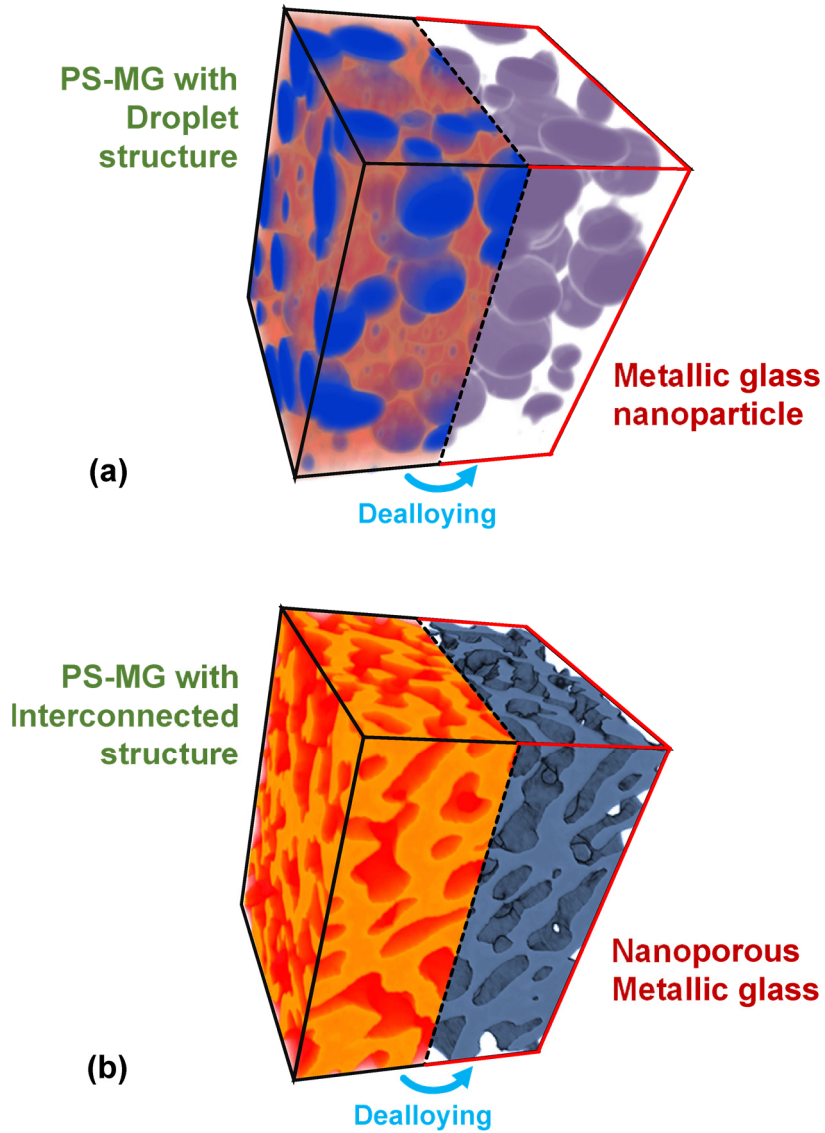


Figure 3.1. Fabrication of metallic glass nanoparticles (a) and nanoporous metallic glass (b) by dealloying process of phase separating metallic glass precursors.

3.2. Microstructure control of precursor alloys

In dealloying process of PS-MG precursor alloy, a reactive phase is selectively dissolved by a proper solution (generally acid) and the other inactive phase remains its morphology formed at the casting process of the precursor. Therefore, the structure of PS-MG precursor dominantly determines the morphology of the product after dealloying, and the microstructural control of the precursor is a key issue for manipulating the metallic glass nanoparticles and nanofoams used in this study.

Among various alloy systems forming PS-MGs with clearly separated two-phase microstructure (see Section 1.3 for the detailed information), Y-Ti-Al-Co⁸⁷ and Gd-Ti-Al-Co⁹⁴ alloy system were selected for proper PS-MG precursors in this study, due to their easiness to control their secondary amorphous phase in nanoscale and large reactivity difference between the separated (Ti-rich and (Y,Gd)-rich) amorphous phases. In this section, the microstructure control of the PS-MG precursor alloys in the two alloy systems was systematically investigated especially focused on the effect of their chemical composition and cooling rate in quenching process.

3.2.1. Effect of alloy composition

The empirical rules for high glass-forming ability includes the relations of large negative mixing enthalpy among alloying elements⁹¹. However, PS-MG is formed from unique alloy design intentionally including a pair of constituents having a large positive mixing enthalpy. Figure 3.2 (a) and (b) shows the mixing enthalpy relations and the atomic size of constituent elements in (Y,Gd)-Ti-Al-Co alloy systems. Ti and (Y,Gd) have a relation of large positive mixing enthalpy¹²⁰, which causes liquid-

state phase separation between them. However, each divided ternary alloy system, Ti-Al-Co and (Y,Gd)-Al-Co (grouped by dotted ellipse in Figure 3.2 (a) and (b)), in the two quaternary systems satisfy the empirical rule for high-glass forming ability, by large negative mixing enthalpy relations¹²⁰ and considerable atomic size¹²¹ difference among the constituent elements. Thus, Co and Al enhance the glass-forming ability of each liquid phase separated by liquid-state phase separation. As a result, (Y,Gd)-Ti-Al-Co alloy can be separated to Ti-rich and Gd-rich liquid phase with sufficient GFAs during cooling from the melt state, then the each separated phases can be solidified to the individual amorphous phases by rapid quenching.

The pseudo-binary miscibility gaps of (Y,Gd)-Ti-Al-Co alloy systems were derived from thermodynamic calculations in preceding studies^{87,94} (Figure 3.2 (c) and (d)). Based on the two ternary compositions of (Y,Gd)-Al-Co and Ti-Al-Co systems, binodal (red curve) and spinodal line (purple dotted curve) are delineated in pseudo-binary section. If phase separation process initiates under the temperature-composition condition in a red region between binodal and spinodal curves, the alloy melt will be separated to form droplet structure by nucleation and growth mechanism. Whereas the phase separation occurs through spinodal decomposition if the initial condition is in a purple region below spinodal curve, resulting in interconnected structure of the separated phases (the inset image of Figure 3.2 (c), see Section 1.3.2 for detailed information). From the pseudo-binary diagrams, the microstructure after phase separation can be predicted depending on the initial composition of alloy melt.

The microstructure of alloy samples with selected compositions in (Y,Gd)-Ti-Al-Co alloy systems are summarized in Figure 3.3. The samples were prepared in the form of thin ribbon by melt-spinning process. The as-spun ribbons have a clear phase-separated microstructure with Ti-rich amorphous phases (dark contrast) in

Gd-rich amorphous phase (bright contrast). Close to the predictions from Figure 3.2 (c) and (d), the alloys with a composition near $(Y,Gd)_{19}Ti_{36}Al_{25}Co_{20}$ have interconnected structure by spinodal decomposition, while the alloys with higher Ti contents have droplet structure with Ti-rich amorphous droplet phase in (Y,Gd)-rich amorphous matrix phase. Binodal curve in pseudo-binary diagram (or binodal surface in ternary or higher) represents the critical temperature of phase separation depending on alloy composition. Increase of (Y,Gd) contents from $(Y,Gd)_{19}Ti_{36}Al_{25}Co_{20}$ composition leads to the decrease of critical temperature for phase separation (binodal curve in Figure 3.2 (c) and (d)), while the glass transition temperature has only minor change depending on alloy composition. Thus, the temperature range between the critical temperature and glass transition temperature (solidification), enabling the growth of separated phases, decreases with increasing (Y,Gd) contents from $(Y,Gd)_{19}Ti_{36}Al_{25}Co_{20}$. From this reason, the clear size decrease of separated (secondary) amorphous phase is observed with increasing (Y,Gd) contents in the ribbon samples of Figure 3.3. In addition, Gd-Ti-Al-Co system has a miscibility gap at much higher temperature as compared to that of Y-Ti-Al-Co system. This results in the microstructure with relatively larger secondary phases in the ribbons of Gd-Ti-Al-Co system (Figure 3.3 (a-d)) than that of Y-Ti-Al-Co system (Figure 3.3 (e-f)).

The amorphous structure of the separated phases in the ribbon samples is confirmed by transmission electron microscope (Figure 3.4). The images show the clear separation between two phases with sharp phase-interfaces. The selective area diffraction patterns (the inset images of Figure 3.4 (a-d)) corresponding to each observed region have two distinguishable diffuse halo ring, which present the existence of two amorphous phase with different chemistry. The inner ring

corresponds to (Y,Gd)-rich amorphous phase and the outer to Ti-rich amorphous phase. Inside the separated amorphous phases (both secondary and matrix phases) with relatively large phase size, the product of secondary separation is observed as a small droplet phases with the diameter of 10 ~ 30 nm (Figure 3.4 (c) and (d)). Due to the high cooling rate of melt-spinning process, the phases separated by primary separation does not have sufficient time to equilibrate and be supersaturated. In this situation, a driving force develops secondary separation process, which leads to a complex hierarchical structure⁸⁷.

Due to the distinct chemistry of Ti-rich and (Y,Gd)-rich amorphous phases, their thermal stabilities (or crystallization behaviors) are also dissimilar. Figure 3.5 is heat flow spectrum of the selected ribbon samples in (Y,Gd)-Ti-Al-Co system and three monolithic metallic glass ribbons ((Ti,Y,Gd)₅₅Al₂₅Co₂₀), obtained by differential scanning calorimetry. The PS-MG ribbons shows clearly two exothermic reactions corresponding to crystallization reactions of each amorphous phase. From the comparison with the crystallization peak of the monolithic glass samples, the exothermic peaks at relatively lower temperature correspond to the crystallization of (Y,Gd)-rich amorphous phase (shaded with blue (Y-rich) or orange (Gd-rich) in Figure 3.5), while those at relatively higher temperature correspond to the crystallization of Ti-rich amorphous phases (shaded with green in Figure 3.5).

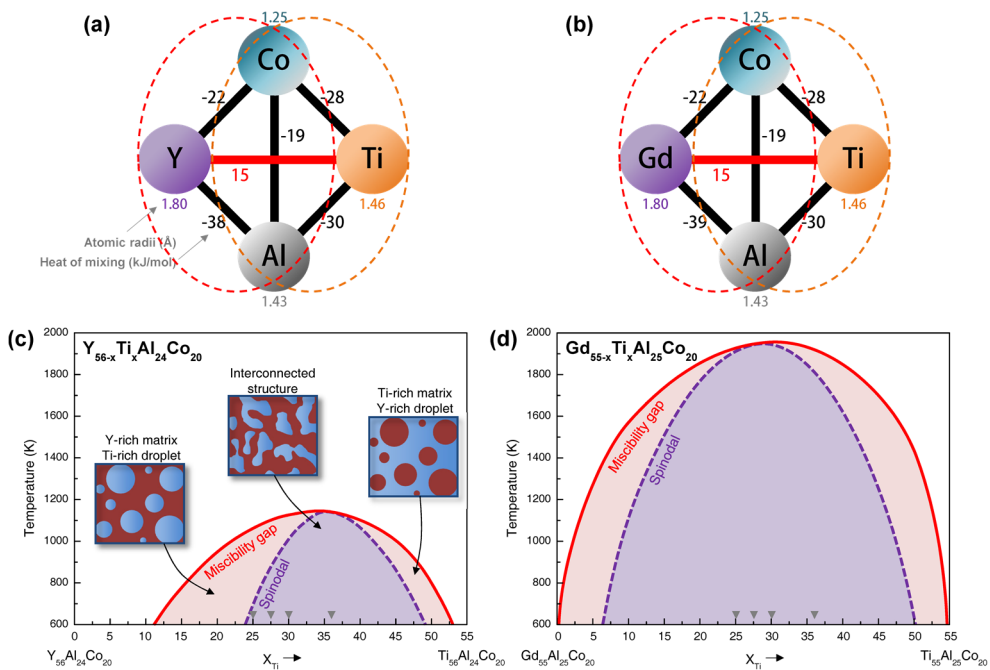


Figure 3.2. (a, b) The atomic sizes of constituent elements¹²¹ and the relationships of mixing enthalpy¹²⁰ among them in (a) Y-Ti-Al-Co and (b) Gd-Ti-Al-Co alloy systems. (c, d) Pseudo-binary miscibility gaps of (c) Y-Ti-Al-Co and (d) Gd-Ti-Al-Co alloy systems estimated by thermodynamic calculations^{87,94}.

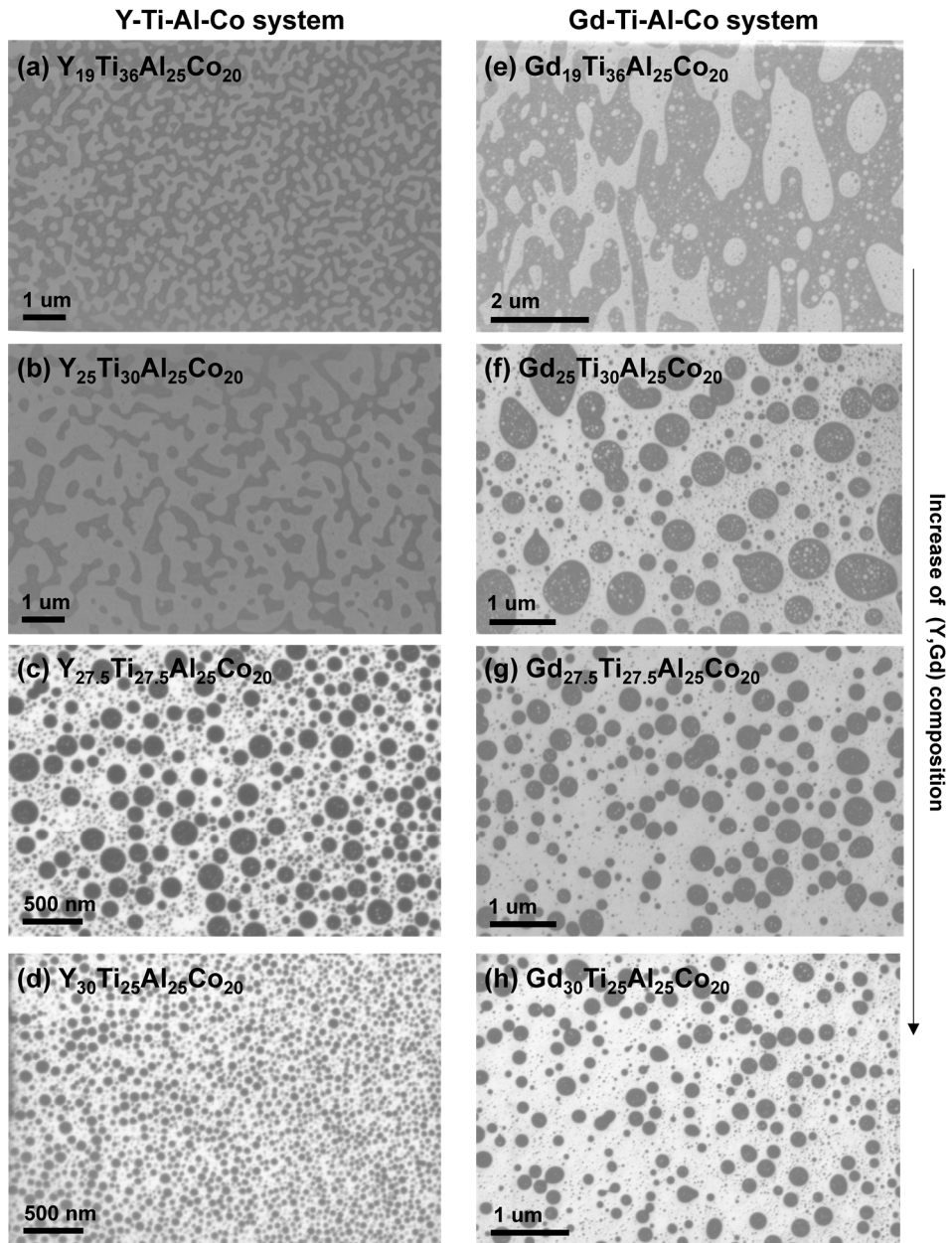


Figure 3.3. SEM images of (Y,Gd)-Ti-Al-Co metallic glass as-spun ribbons at the center region of cross-section, obtained using in-lens secondary electron detector.

(a) $\text{Y}_{19}\text{Ti}_{36}\text{Al}_{25}\text{Co}_{20}$. (b) $\text{Y}_{25}\text{Ti}_{30}\text{Al}_{25}\text{Co}_{20}$. (c) $\text{Y}_{27.5}\text{Ti}_{27.5}\text{Al}_{25}\text{Co}_{20}$. (d) $\text{Y}_{30}\text{Ti}_{25}\text{Al}_{25}\text{Co}_{20}$.

(e) $\text{Gd}_{19}\text{Ti}_{36}\text{Al}_{25}\text{Co}_{20}$. (f) $\text{Gd}_{25}\text{Ti}_{30}\text{Al}_{25}\text{Co}_{20}$. (g) $\text{Gd}_{27.5}\text{Ti}_{27.5}\text{Al}_{25}\text{Co}_{20}$. (h) $\text{Gd}_{30}\text{Ti}_{25}\text{Al}_{25}\text{Co}_{20}$.

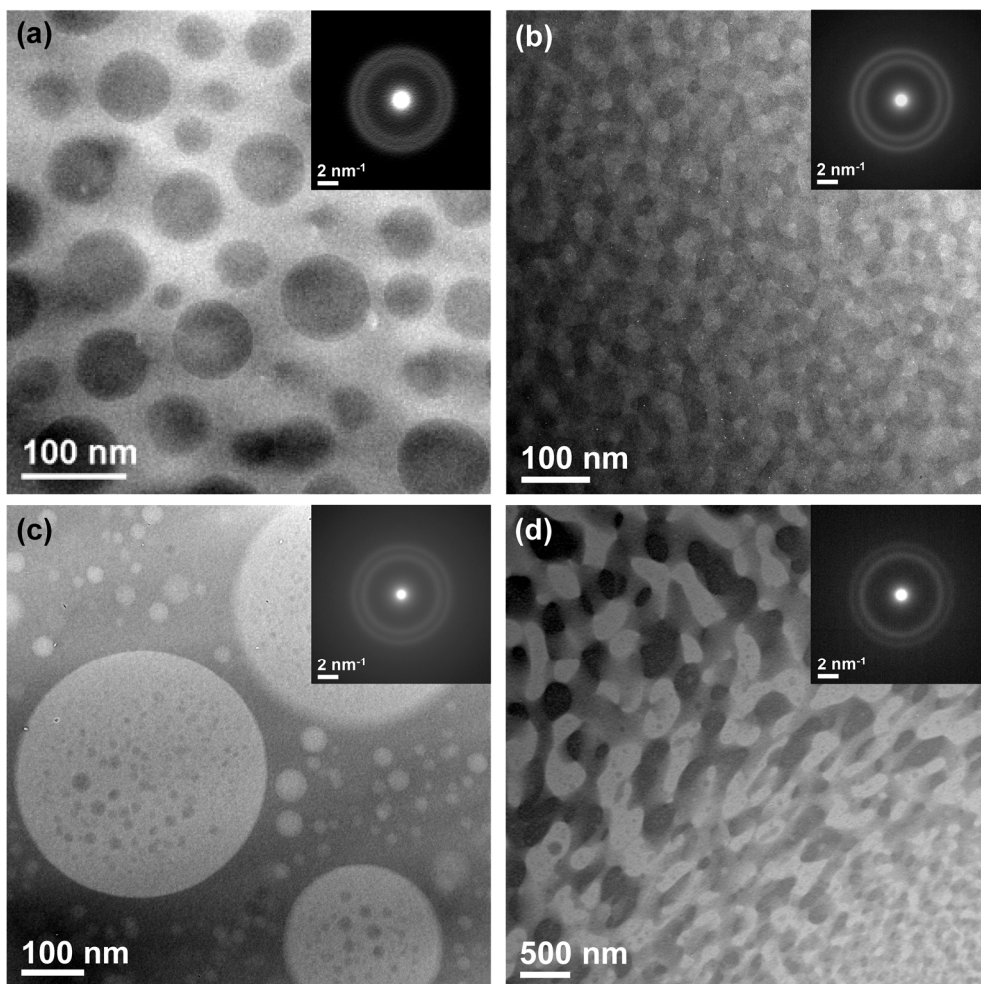


Figure 3.4. Bright-field TEM images of (Y,Gd)-Ti-Al-Co as-spun ribbon samples and (inset) corresponding selected area diffraction patterns.

(a) $\text{Y}_{27.5}\text{Ti}_{27.5}\text{Al}_{25}\text{Co}_{20}$. **(b)** $\text{Gd}_{27.5}\text{Ti}_{27.5}\text{Al}_{25}\text{Co}_{20}$ **(c)** $\text{Y}_{19}\text{Ti}_{36}\text{Al}_{25}\text{Co}_{20}$. **(d)** $\text{Gd}_{19}\text{Ti}_{36}\text{Al}_{25}\text{Co}_{20}$.

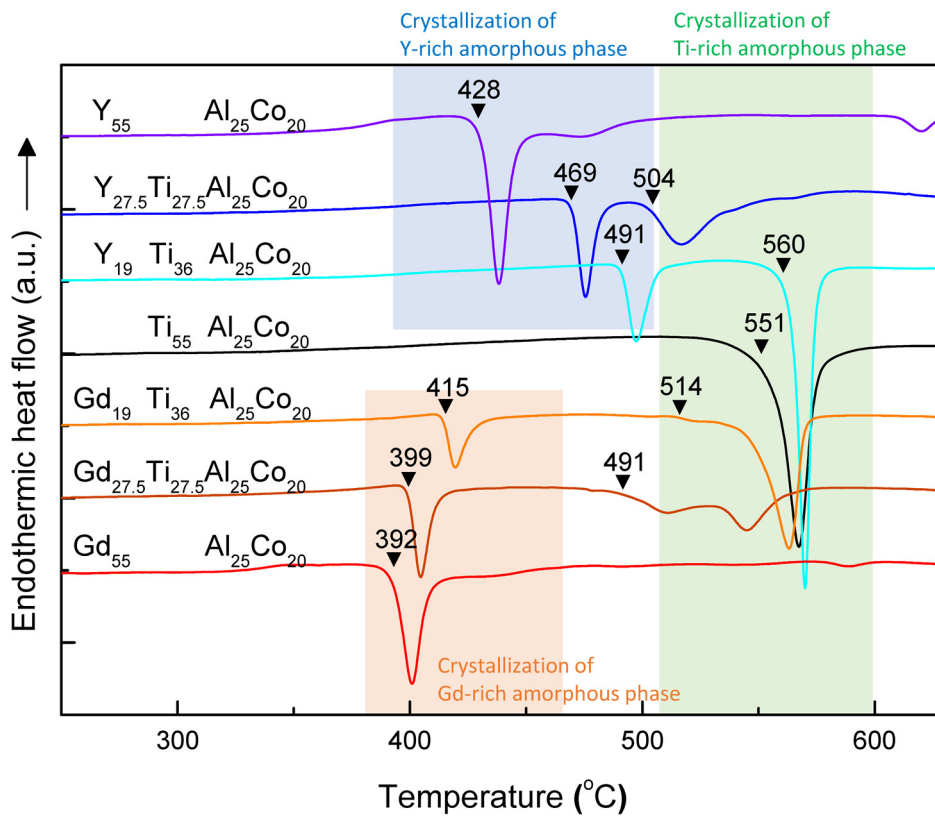


Figure 3.5. DSC heat flow spectrum of as-spun ribbon with selected compositions in (Y, Gd)-Ti-Al-Co alloy systems and three monolithic metallic glass ribbons, $Y_{55}Al_{25}Co_{20}$, $Ti_{55}Al_{25}Co_{20}$ and $Gd_{55}Al_{25}Co_{20}$.

3.2.2. Effect of cooling rate

The size of amorphous phases in PS-MG is significantly affected by kinetic factors of phase separation process. The effect of temperature range between the critical point of phase separation and glass transition temperature was highlighted by assuming that the ribbons solidified under a same cooling rate in the previous section, the effect of cooling rate should be considered to control the microstructure of PS-MG precursors, even in a single as-spun ribbons from melt-spinning process. The process of melt-spinning technique is described in Figure 3.6 (a). The master alloy button is melted in a quartz tube by induction heating, then the melt is injected through the nozzle of the quartz tube to the surface of a rotating copper wheel. The thin stream of melt after collision on the wheel surface is rapidly quenched into a ribbon. In this situation, the ribbon has two different faces. One is directly contacted with the chilled copper wheel, and the other is contacted only with Ar atmosphere. The former is called 'wheel side' and the latter 'free side' of ribbon. The wheel side of a ribbon has a relatively higher cooling rate due to the contact with the copper wheel, while the free side is cooled with a relatively slow rate. This leads to the difference of phase size inside a PS-MG ribbon depending on the distance from the wheel side edge.

For example, the droplet-structured $Y_{27.5}Ti_{27.5}Al_{25}Co_{20}$ as-spun ribbons shows a clear difference in the size of Ti-rich droplet phases between at near free side (Figure 3.6 (a)) and at near wheel side (Figure 3.6 (b)). The trend is comparably observed in PS-MG ribbon samples regardless of the alloy composition and the type of separated microstructure (whether droplet or interconnected structure), as shown in Figure 3.7. The results reveal an obvious trend that the average phase size of separated phases

becomes larger at the position with farther distance from wheel side edge. Note that the region close to free side edge does not always have the largest average phase size, because the influence of heat transfer by Ar atmosphere at free side is noticeable as the thickness of ribbon increases. Figure 3.7 (a) and (d) show the influence, where the position with the largest average phase size appears at near the center of cross-section, rather than the free side edge of the ribbons.

The size distribution in a wide range by the cooling rate gradient in a single PS-MG ribbon sample enables to fabricate metallic glass nanoparticles with various sizes or metallic glass nanofoams with pore size gradient by a single dealloying process. This unique feature in the dealloying process of PS-MG ribbons provides a great advantage in the investigation of size-dependent deformation behaviors in nanoscale metallic glasses, which will be discussed in Chapter 4.

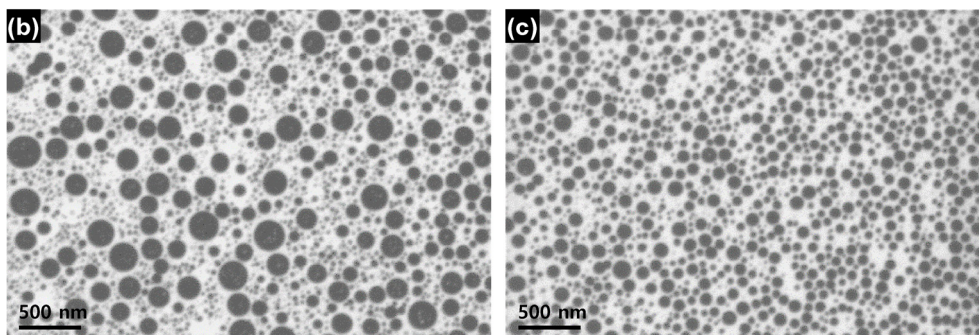
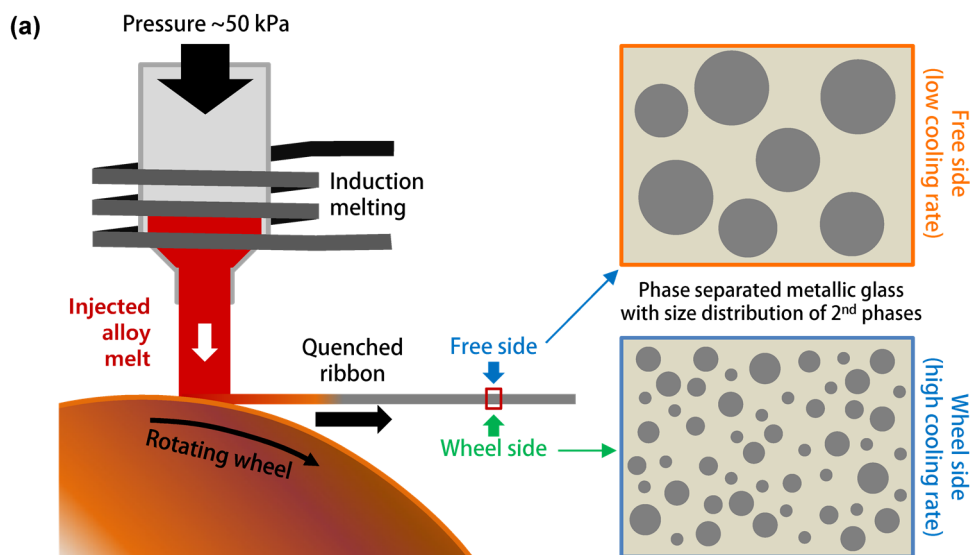


Figure 3.6 (a) Schematic illustration of melt-spinning process showing the definition of ‘wheel side’ and ‘free side’ of a ribbon sample. (b, c) Cross-section SEM images of $Y_{27.5}Ti_{27.5}Al_{25}Co_{20}$ alloy ribbon at the positions near free side edge (b) and wheel side edge (c), obtained using in-lens secondary electron detector.

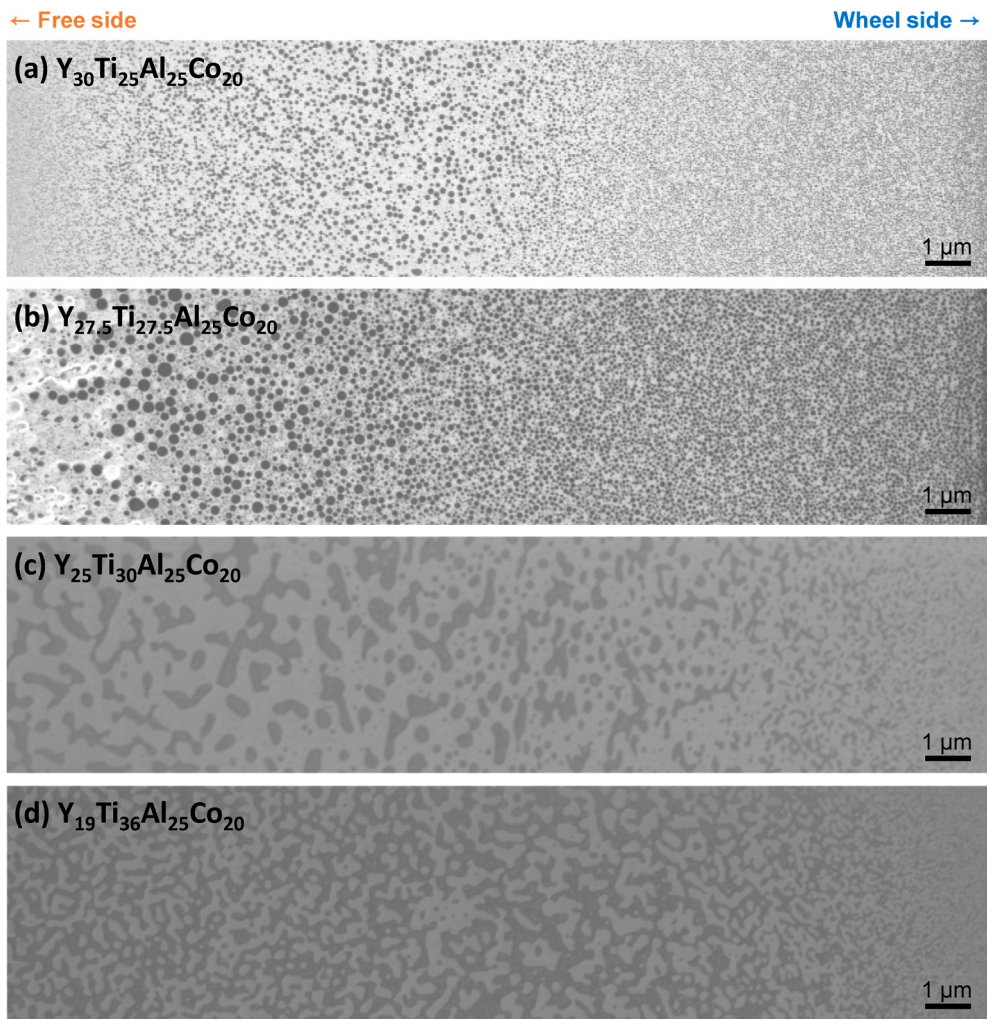


Figure 3.7 Cross-section SEM images of Y-Ti-Al-Co metallic glass as-spun ribbons covering wide range from wheel side to free side of ribbon, obtained using in-lens secondary electron detector. (a) $Y_{30}Ti_{25}Al_{25}Co_{20}$. (b) $Y_{27.5}Ti_{27.5}Al_{25}Co_{20}$. (c) $Y_{25}Ti_{30}Al_{25}Co_{20}$. (d) $Y_{19}Ti_{36}Al_{25}Co_{20}$.

3.2.3. Three-dimensional microstructure analysis

Three-dimensional (3-D) characterization of material microstructure provides ‘truly’ quantitative measurement of geometric properties that cannot be obtained using a 2-D analysis, such as the number of features (secondary phases, precipitates, etc.) per unit volume, feature connectivity, real feature shapes and volumetric sizes, and spatial distribution information¹²². The 3-D microstructural information of a material can be used as a direct basis for the prediction of mechanical response of the material (e.g. finite element analysis (FEA)). Depending on the purpose and observable volume scale (voxel dimension), various tomographic methods has been developed and applied for 3-D microstructure characterization, such as 3-D atom probe tomography, electron microscope tomography, focused ion beam (FIB) tomography, X-ray tomography and mechanical serial sectioning combined with optical imaging.

In order to characterize the 3-D microstructure of PS-MGs, serial sectioning-imaging method using FIB/SEM dual-beam equipment was performed with two PS-MG as-spun ribbons; $\text{Gd}_{30}\text{Ti}_{25}\text{Al}_{25}\text{Co}_{20}$ and $\text{Y}_{19}\text{Ti}_{36}\text{Al}_{25}\text{Co}_{20}$ having droplet and interconnected structure, respectively. The FIB/SEM-based tomography has the voxel-scale appropriate for the characterization of a few-hundred nm-sized features in material microstructure. For $\text{Gd}_{30}\text{Ti}_{25}\text{Al}_{25}\text{Co}_{20}$ droplet-structured ribbon, the planes observed by SEM are parallel to the free side face. The imaging process was started near the free side face and gradually approached close to wheel side by serial sectioning by FIB, as shown with some selected images in Figure 3.8 (a-h). The total number of the serial images is ~660, and a 3-D microstructure was constructed by stacking them in the direction described in Figure 3.8 (i), after alignment and

cropping of the images. Figure 3.8 (j) shows an entire volume of constructed 3-D microstructure. Gd-rich matrix phase is expressed as a transparent region inside a rectangular parallelepiped bounding box. Ti-rich phases (orange) formed by primary phase separation in the region near free side have clear spherical morphology which is expected by strong surface tension of separated phases, while those in the region near wheel side have irregular morphologies which may come from (i) strong flow turbulence effect at the moment of collision with a rotating copper wheel or (ii) the intermediate mechanism of phase separation between nucleation-growth and spinodal decomposition induced by high cooling rate at wheel side. An enlarged part of the 3-D microstructure (Figure 3.8 (k)) shows the existence of small Gd-rich phases inside a larger Ti-rich droplets, formed by secondary phase separation.

Similarly, the 3-D microstructure of $Y_{19}Ti_{36}Al_{25}Co_{20}$ interconnected-structured sample was also investigated, as shown in Figure 3.9. For this sample, the observed planes are perpendicular to both free side and wheel side face of the ribbon. The selected images among the total ~90 images are shown in Figure 3.9 (a-f), and a 3-D microstructure (Figure 3.9 (h)) was constructed by stacking them in the direction described in Figure 3.9 (g). The 3-D microstructure exhibit an obvious change of phase size induced by cooling rate gradient from wheel side to free side of the ribbon. The 3-D microstructures obtained from FIB/SEM tomography provides the direct geometrical model necessary for finite element analysis predicting the mechanical response of PS-MGs, while the finite element analysis and experimental investigation for the mechanical behaviors of PS-MG remains for future works.

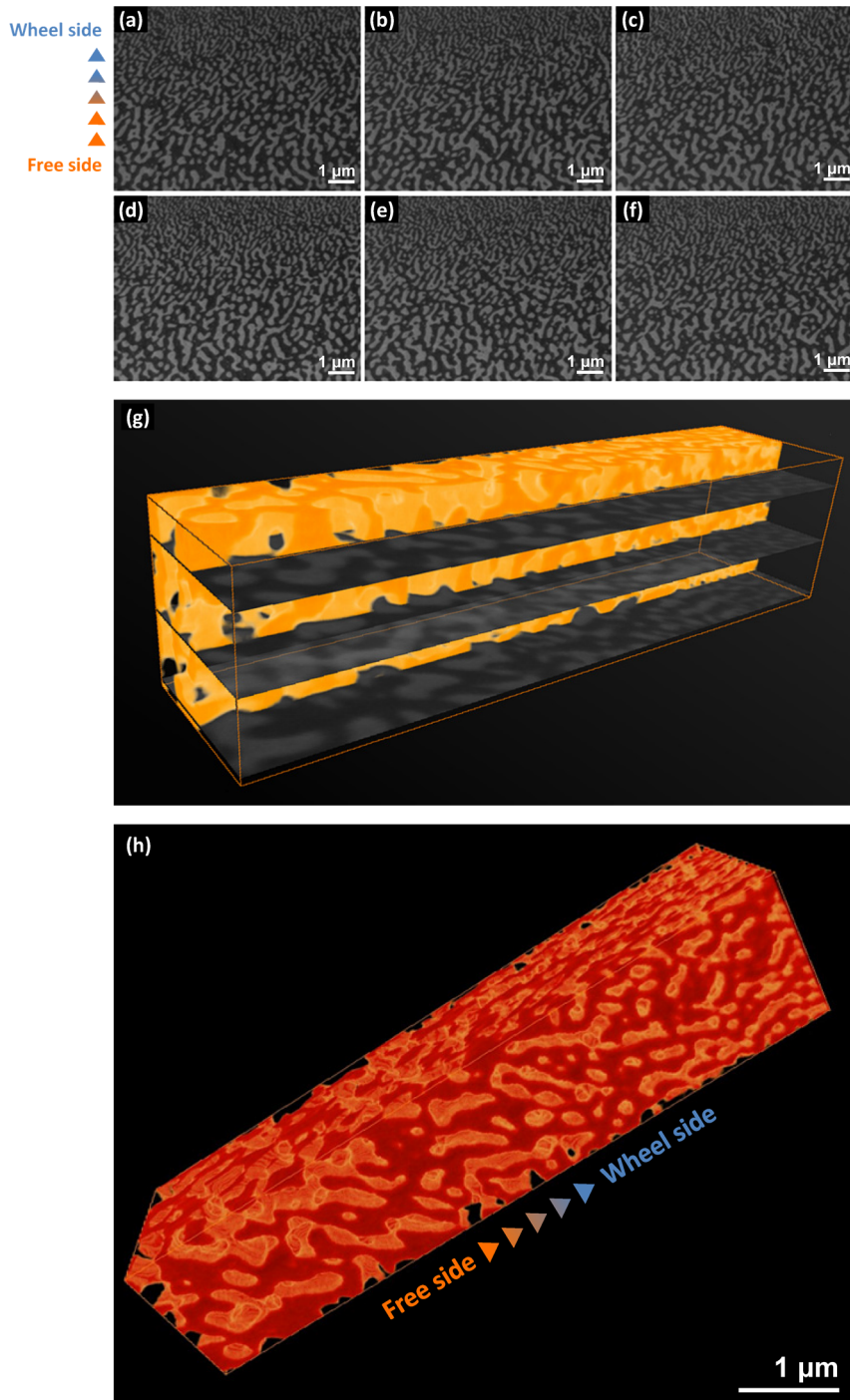


Figure 3.9. Three-dimensional microstructure analysis of $Y_{19}Ti_{25}Al_{25}Co_{20}$ as-spun ribbon. **(a-f)** The selected images among ~ 90 images obtained by serial sectioning-imaging process using FIB/SEM dual-beam equipment. **(g)** Combined 2-D and 3-D images showing the stacking direction of 2-D images. **(h)** The constructed 3-D microstructure of an entire observed volume.

3.3. Microstructure of metallic glass nanoparticles

Metallic glass nanoparticles can be fabricated by dealloying process (selective dissolution) of PS-MG precursors with droplet-structure. Due to the distinct chemical compositions of separated phases in PS-MG, they have different reactivity against a certain chemical solution. In the case of (Y,Gd)-Ti-Al-Co alloys, (Y,Gd) is rapidly dissolved in nitric acid solution, while Ti forms a strong passivating layer with thickness under a few nm (to be discussed later). By immersion of the precursor alloy in a dilute nitric acid solution, the Gd-rich matrix phase is selectively dissolved and the Ti-rich spherical phases maintains their morphology and chemistry. The droplet structure with nanometer-scale secondary amorphous phases can be obtained by compositional control depending on alloy systems, as described in 3.2.1.

Figure 3.10 shows the morphology of metallic glass nanoparticles fabricated by dealloying of $Y_{27.5}Ti_{27.5}Al_{25}Co_{20}$ and $Gd_{27.5}Ti_{27.5}Al_{25}Co_{20}$ precursor alloy in 0.1 M nitric acid solution. The particles generally have nearly-perfect spherical morphology, while a small portion of relatively large particles (diameter over ~ 500 nm) has slightly distorted shape from sphere due to the flow turbulence effect and agglomeration with adjacent spherical phases. The particle from $Y_{27.5}Ti_{27.5}Al_{25}Co_{20}$ precursor (Figure 3.10 (a)) have a size distribution smaller than that from $Gd_{27.5}Ti_{27.5}Al_{25}Co_{20}$ precursor (Figure 3.10 (b)), clearly reflecting the microstructure of the precursor alloys (Figure 3.3 (c) and (g)). The average chemical compositions of the Ti-based nanoparticles of Figure 3.10 (a) and (b) are $Ti_{54.4}Co_{32.0}Al_{10.2}Y_{3.4}$ and $Ti_{55.8}Co_{30.4}Al_{11.7}Gd_{2.1}$, respectively.(analyzed by energy dispersive spectroscopy in SEM.

In order to investigate the chemical change between the precursor alloy before

dealloying and the nanoparticle after dealloying, intensive microstructural analysis was performed using high-angle annular dark-field (HAADF) imaging of scanning transmission electron microscope (STEM) and accompanied energy dispersive spectroscopy (EDS). Figure 3.11 shows line profile analysis results across the phase boundary of precursor $Y_{27.5}Ti_{27.5}Al_{25}Co_{20}$ alloys and the edge of a nanoparticle obtained from the precursor. At the phase boundary of the precursor alloy (Figure 3.11 (a) and (b)), a narrow transition region (B) between Y-rich matrix phase (A) and Ti-rich droplet phase is observed with a Co-enrich shell layer (thickness ~ 4 nm), which can be attributed to the effect of critical wetting as previously suggested^{85,123}. After dealloying the precursor alloy (Figure 3.11 (c) and (d)), the nanoparticle has Ti oxide layer (thickness ~ 3 nm) which acts as a passivating layer (E) against etching by the nitric acid solution. In addition, an abnormal Ti-Co-rich oxide thin layer (F) exists between the Ti oxide layer (E) and Ti-rich amorphous phase (F). This can be understood from the correlation with the Ti oxide layer (E) formation. The Ellingham diagram¹²⁴ of oxide formation (Figure 3.12) suggests that the standard free energy for the formation of Ti oxide is lower than that of Co oxide, which means Ti oxide can be formed easily with low potential energy as compared to Co oxide. Despite the existence of Co-enrich shell layer at the edge of Ti-rich droplet before dealloying, Ti is priorly consumed to form the Ti oxide passivating layer during dealloying process, resulting slight decrease of Ti contents in the inner region and the unsolicited increase of Co composition in the region F. The similar layered structure is observed also in the nanoparticle from $Gd_{27.5}Ti_{27.5}Al_{25}Co_{20}$ precursor alloy (Figure 3.13). The existence of the abnormal Ti-Co-enrich oxide layer in the multi-component amorphous nanoparticles lead to the unique magnetic behaviors, which will be will be reported in the forthcoming report.

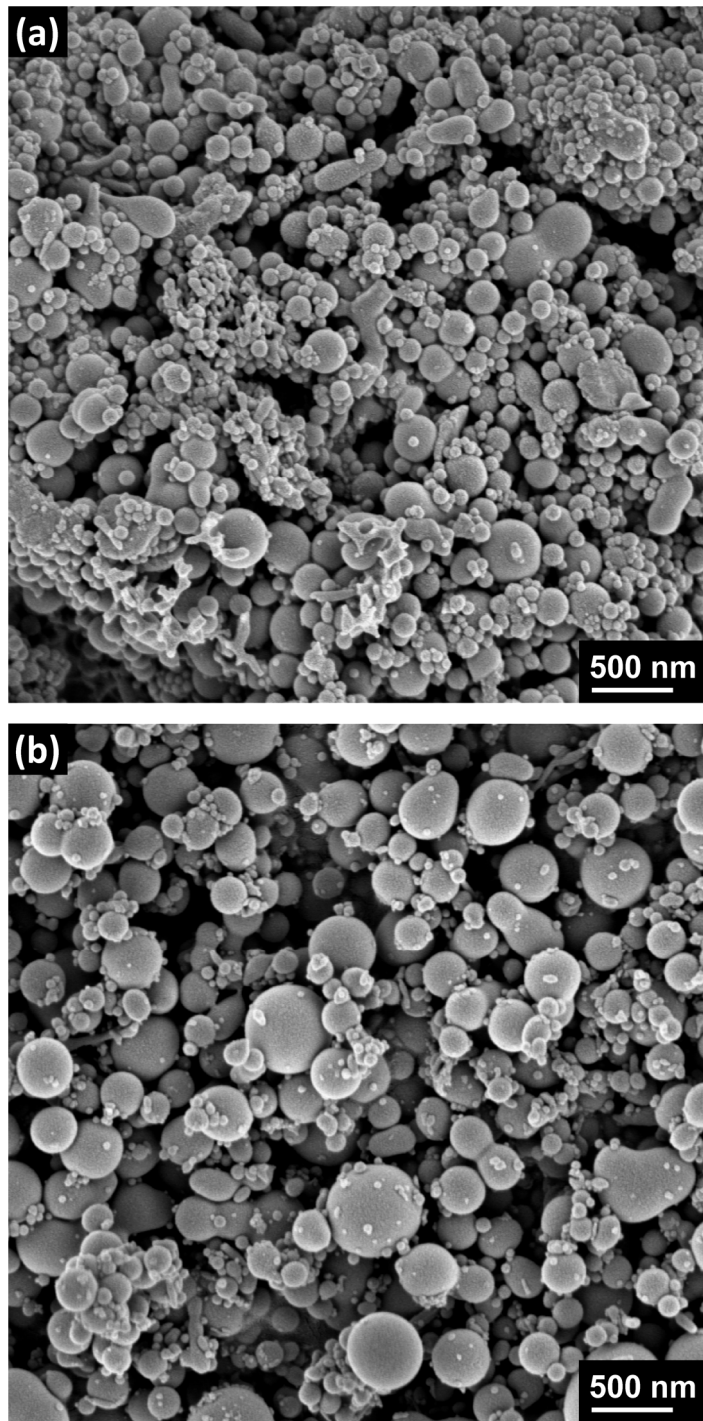


Figure 3.10. Metallic glass nanoparticles fabricated by dealloying process of $\text{Y}_{27.5}\text{Ti}_{27.5}\text{Al}_{25}\text{Co}_{20}$ (a) and $\text{Gd}_{27.5}\text{Ti}_{27.5}\text{Al}_{25}\text{Co}_{20}$ (b) precursor PS-MG alloys.

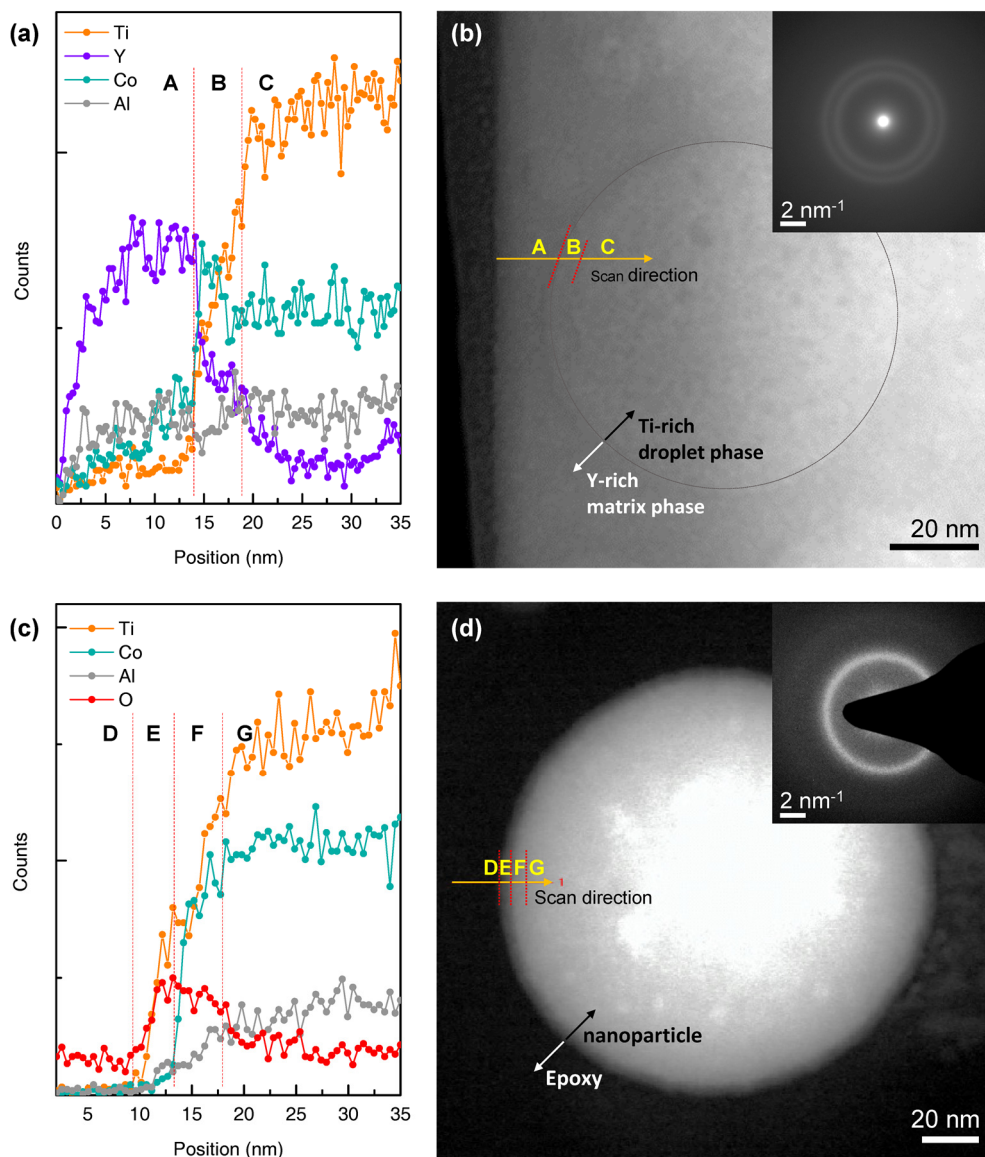


Figure 3.11. EDS line profile with HAADF-STEM imaging. **(a,b)** EDS line profile (a) and HAADF image (b) of $Y_{27.5}Ti_{27.5}Al_{25}Co_{20}$ precursor alloy. **(c,d)** EDS line profile (c) and HAADF image (d) of a nanoparticle fabricated by dealloying of the precursor alloy. A yellow line in (b) and (d) is the direction of EDS line scan (a) and (c), respectively.

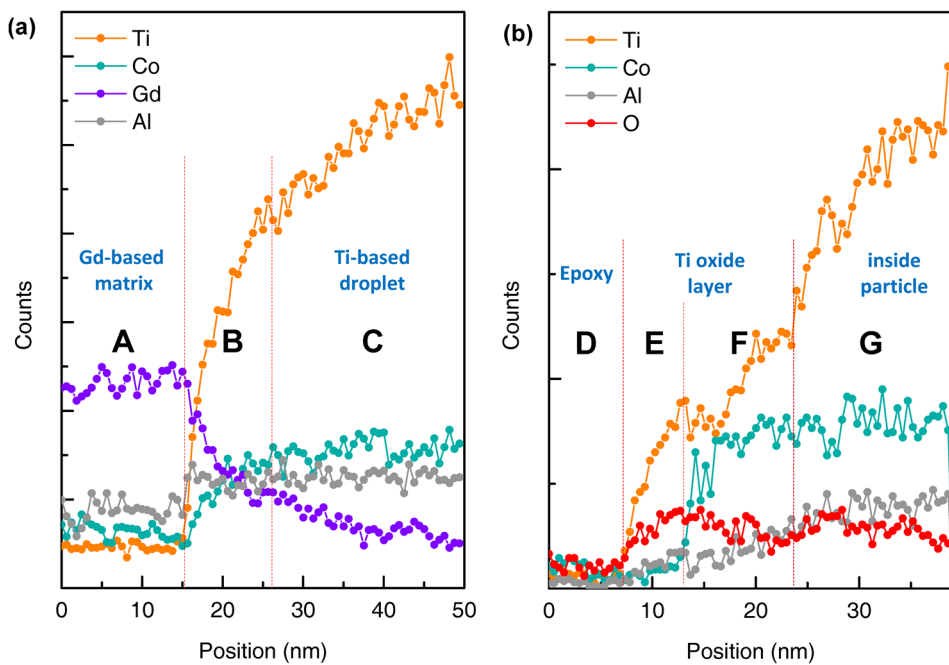


Figure 3.13. EDS line profile across the phase boundary in $Gd_{27.5}Ti_{27.5}Al_{25}Co_{20}$ precursor alloy (a) and at the edge of a particle fabricated by dealloying of the precursor alloy.

3.4. Microstructure of metallic glass nanofoams

Metallic glass nanofoams, similarly with the nanoparticles in the previous section) can be fabricated by dealloying process of PS-MG precursors with interconnected structure (Figure 3.14). As discussed in Section 3.2, the precise control of alloy composition and cooling rate based on thermodynamic assessments enables to fabricate PS-MGs with nanoscale interconnected structure. The precursor alloy with $Y_{19}Ti_{36}Al_{25}Co_{20}$ composition is suitable to form a fine phase-separated structure with nanoscale interconnected phases, as shown in Figure 3.14 (a). By immersion of the precursor alloy in a dilute nitric acid solution (0.1 M), the Gd-rich matrix phase is selectively dissolved and the Ti-rich interconnected phases maintains their morphology as a nanoporous foam (Figure 3.14 (b)). The intensive analysis using STEM and EDS has not performed with the metallic glass nanofoam as the case of Section 3.3. However, a Ti oxide passivating layer and also Ti-Co-enrich layer may exist as well as on the surface of the foam structure, due to the identical dealloying process for the nanoparticle and the nanofoam.

The ligament size (thickness of Ti-rich amorphous phase) in the metallic glass nanofoam is evaluated depending on the distance from the wheel side edge of the dealloyed ribbon (Figure 3.15). The average ligament size was measured with Figure 3.15 (a) by counting the intersect points between the surface edge of ligaments and a line vertically drawn at a certain position. The green line in Figure 3.15 is a fitting curve of measured data point (blue dots) derived by a complex exponential function, which has no physical meaning but suggests the approximate ligament sizes as a function of the distance from the wheel side edge. The largest average ligament size appears near the center of the ribbon cross-section due to the cooling effect by copper

wheel at wheel size and Ar atmosphere at free side during melt-spinning process of the precursor alloy, as discussed in Section 3.2.2. The nanofoam have a ligament size distribution under 300 nm, and the ligament size decreases to a few tens of nanometers at the region close to the wheel side edge of the ribbon. The ligament size distribution in the metallic glass nanofoam sample will be used to investigate the deformation behavior of the nanofoam depending the ligament size in Chapter 6.

In addition, a unique hierarchical nanoporous structure can be fabricated by applying the multi-stage dealloying process. After the formation of the nanofoam structure in Figure 3.14 (b) by selective dissolution of Y-rich phase in nitric acid solution, Ti inside the nanofoam can be also selectively dissolved by hydrofluoric acid (HF) solution. Figure 3.16 shows the morphology of the product after immersing the Ti-based metallic glass nanofoam in 0.1 M HF solution for 30 s. Ti atoms is dissolved relatively faster than Co and Al atoms, then the remaining elements of Co, Al and a small portion of Ti and Y agglomerate to form the other porous structure of smaller scale in the ligament of nanofoam structure in larger scale. This results in the unique hierarchical nanoporous structure as clearly observed in Figure 3.16 (c), while the material may lose the amorphous structure during multi-stage dealloying process. This kind of hierarchical nanoporous materials with a large (electro-)chemical surface area is expected to have advantages to the functional application such as electrochemical catalysts.

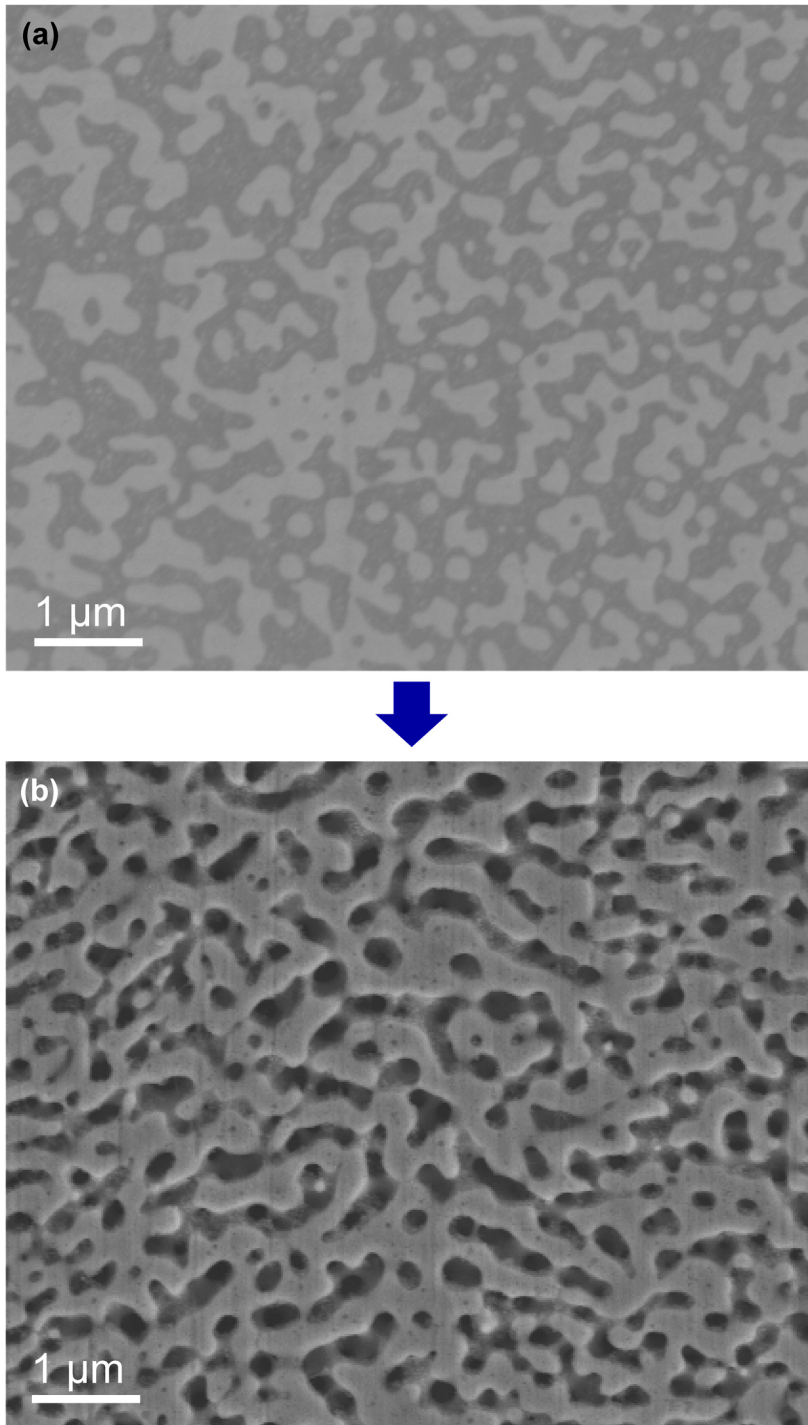


Figure 3.14. SEM image of $Y_{19}Ti_{36}Al_{25}Co_{20}$ precursor alloy before dealloying (a) and a metallic glass nanofoam (b) fabricated by dealloying of the precursor alloy.

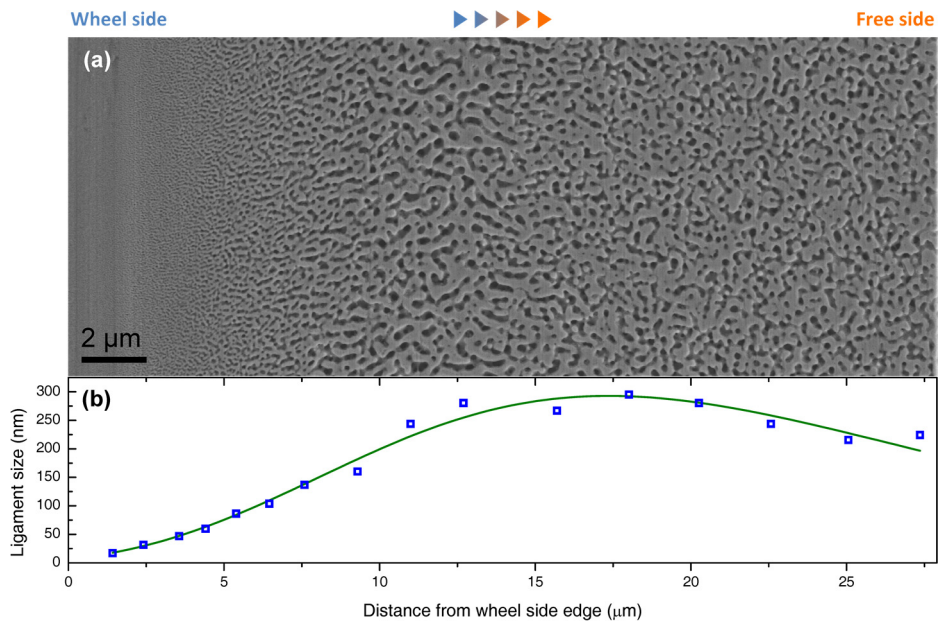


Figure 3.15. (a) Cross-section SEM image of a Ti-based metallic glass nanofoam dealloyed from $Y_{19}Ti_{36}Al_{25}Co_{20}$ precursor alloy. (b) ligament size distribution inside the nanofoam depending as a function of distance from wheel side edge.

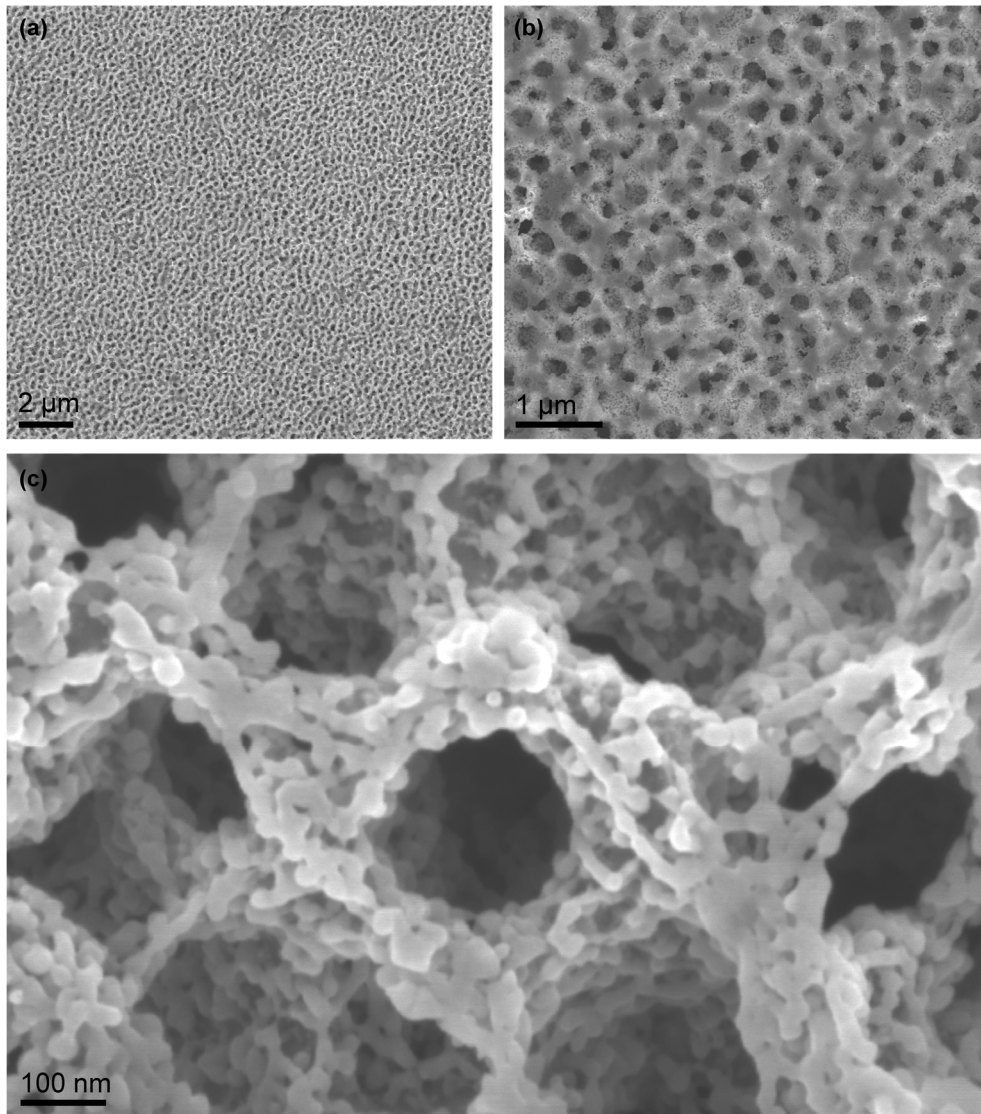


Figure 3.16. Metallic nanofoam with a hierarchical nanoporous structure fabricated by multi-stage dealloying process of $Y_{19}Ti_{36}Al_{25}Co_{20}$ precursor alloy. **(a)** low-magnification image showing the uniform porous structure in large scale (pore size : 200 ~ 300 nm) **(b)** An enlarged part of (a). **(c)** High-magnification image showing the nanoporous structure in smaller scale inside the ligaments in larger scale.

3.5. Summary

The metallic glass nanoparticles and nanofoams handled in this study were prepared through the dealloying process of PS-MG precursors. For fabricating PS-MG precursor alloys, the alloy design considering mixing enthalpy relations among constituent elements was applied for inducing phase separation phenomena into two distinct liquid phase with sufficient glass-forming ability, which can solidify to two different amorphous phases during quenching process. The dealloying process can be applied to dissolve one amorphous phase in a PS-MG selectively while the other remains without reaction, by taking an advantage of the distinct chemical compositions of separated phases. After dealloying the morphology of remaining amorphous phases is completely projected to the product, so the microstructure control of PS-MG precursor alloy is significant to manipulate the product of dealloying process. The precise control of alloy composition and cooling rate based on thermodynamic assessments enables to fabricate PS-MG precursor alloys with a proper size distribution of secondary phases for preparing metallic glass nanoparticles and nanofoams.

Ti-based metallic glass nanoparticles and nanofoam samples were fabricated by dealloying of (Y,Gd)-Ti-Al-Co PS-MG precursors with droplet-structure and interconnected structure, respectively. The surface morphology and size distribution were investigated by SEM observation. Furthermore, by intensive microstructure characterization using STEM-EDS, the thin multi-layer structure of passivating oxide under a few nanometer was confirmed in the Ti-based metallic glass nanoparticles, which is expected to exist also in the nanofoams with the same alloy system.

Chapter 4.

Deformation behavior of metallic glass nanoparticles

4.1. Introduction

The deformation behaviors of nanoscale metallic glasses have been widely investigated since Volkert et al. first reported the unique deformation mode transition in Pd₇₇Si₂₃ metallic glasses by sample size reduction to a few hundred of nanometers⁵⁸. As mentioned in Section 1.2, the researches on the deformation of small scale (from a few micrometer scale to a few tens of nanometer scale) metallic glasses has been mainly interested in the changes of their shear banding nature, the occurrence of homogeneous deformation and strength variation by sample size reduction³⁰.

These size effects on the mechanical behavior of metallic glasses, however, are still controversial subjects due to inconsistent results depending on alloy system and sample preparation history³⁰, and also due to the uncertain origin of the size-dependent behaviors. In regard to the former, the influences of ion irradiation and surface roughness induced by focused ion beam (FIB) are introduced previously in Section 1.2.3. The majority of nanoscale metallic glasses tested in previous studies were fabricated by FIB, which significantly affects the deformation behaviors in nanoscale metallic glasses^{71-73,126}. Nevertheless, the size dependence on the strength and deformation mode transition from FIB-prepared specimens reported in previous studies (summarized in Section 1.2.1 and 1.2.2) cannot be attributed solely to the influence of ion irradiation or pre-existing surface flaws, because a metallic glass

nanorod prepared by a FIB-less electroplating method can also be deformed homogeneously⁷¹ and the yield strength increase of metallic glasses by sample size reduction were observed in FIB-fabricated pillar samples⁵⁴ in contrast to the strength drop in highly-irradiated metallic glasses⁷².

Therefore, in order to probe into genuine size effects on the deformation behaviors of metallic glass, nanomechanical studies using metallic glass specimens with a smooth and clean surface prepared by FIB-less process are necessary. In this aspect, metallic glass nanoparticles prepared by dealloying process of phase separating metallic glass (described in detail in Chapter 3) have great advantages of the exclusion of ion irradiation effect and near-perfectly spherical morphology minimizing surface flaws. A large number of spherical metallic glass particles with a wide size distribution in a few tens ~ hundreds nanometer scale can be prepared by a single dealloying process in a relatively short preparation time, so the metallic glass nanoparticles are useful for investigating the size-dependent deformation behavior of nanoscale metallic glass.

While the occurrence of deformation mode transition from inhomogeneous shear banding to homogeneous deformation in nanoscale metallic glass have been widely reported in diverse results, the origin and characteristics of room-temperature homogeneous deformation of nanoscale metallic glasses have not been not still studied in depth. Especially, the flow characteristic and temperature dependence of the homogeneous deformation in nanoscale metallic glasses at near room temperature (RT) are still in a veil, in contrast to homogeneous flow at a high temperature near glass transition temperature (T_g)²⁸ which has been intensively investigated in previous studies^{9,28,50,127-129}. The homogeneous deformation of a nanoscale metallic glass at room temperature can be considered as a viscous flow of

entire sample volume (in contrast to shear banding as a viscous flow concentrated in a narrow region), and some questions emerges from this; Can the nanoscale metallic glasses at room temperature flow as the high-temperature case close to supercooled liquid state? If there is a difference between the two cases, what does this difference originate from? In order to answer these questions, the flow characteristics of nanoscale metallic glasses at room temperature should be revealed first.

In this chapter, the compressive deformation behaviors of the metallic glass nanoparticles fabricated by the dealloying process of phase separating metallic glass were investigated by *in situ* compression tests inside scanning electron microscope. Due to their spherical morphology generally unfavorable for uniaxial compression test, the unusual analysis procedure to interpret the stress distribution inside a nanoparticle and the deformation stages depending on strain is applied to the compression test results of the metallic glass nanoparticles. Then, the homogeneous deformation of the metallic glass nanoparticles at high-strain condition was confirmed by the evaluation of the critical stress for inhomogeneous shear banding and molecular dynamic simulations. Based on quantitative viscosity evaluations in the compressive deformation of the metallic glass nanoparticles, the viscosity dependence on strain rate suggests the flow characteristics of homogeneous deformation of nanoscale metallic glass at room temperature.

4.2. Analysis on compressive deformation behavior of individual metallic glass nanoparticles

The compression tests of the metallic glass nanoparticles were performed by *in situ* indentation tester (Hysitron PI-85 picoindenter) inside scanning electron microscope. Detailed experimental procedures are described in Section 2.4.1. Metallic glass nanoparticles used in the compression tests were prepared by dealloying from $\text{Gd}_{27.5}\text{Ti}_{27.5}\text{Al}_{25}\text{Co}_{20}$ precursor alloy ribbons and have a diameter in the range of 100 ~ 600 nm. The particles were placed individually, as shown in Figure 4.1 (a), by spraying process of the particle-dispersed ethanol after ultrasonication. The transmission electron microscope observation results of a dispersed single particle clearly show amorphous structure of the particle from a diffuse halo ring in selective area diffraction pattern (Figure 4.1 (b)) and the absence of lattice fringes in bright-field images (Figure 4.1 (c-d)).

The spherical morphology of metallic glass nanoparticles is generally not preferred for uniaxial compression test as compared to cylindrical samples with a uniform cross-sectional area, so the unusual analysis procedure should be applied in order to interpret the stress distribution inside a spherical particle and the deformation stages of elastic/plastic deformation in the particles depending on strain also differ from the normal case of a cylindrical sample. In this section, the acquisition of a contact diameter-strain relation and a contact pressure-strain relation during nanoparticle compression will be described, and the deformation stages based on the contact pressure (or load)-strain relation and stress distribution inside the compressed particle depending on the stages will be also addressed.

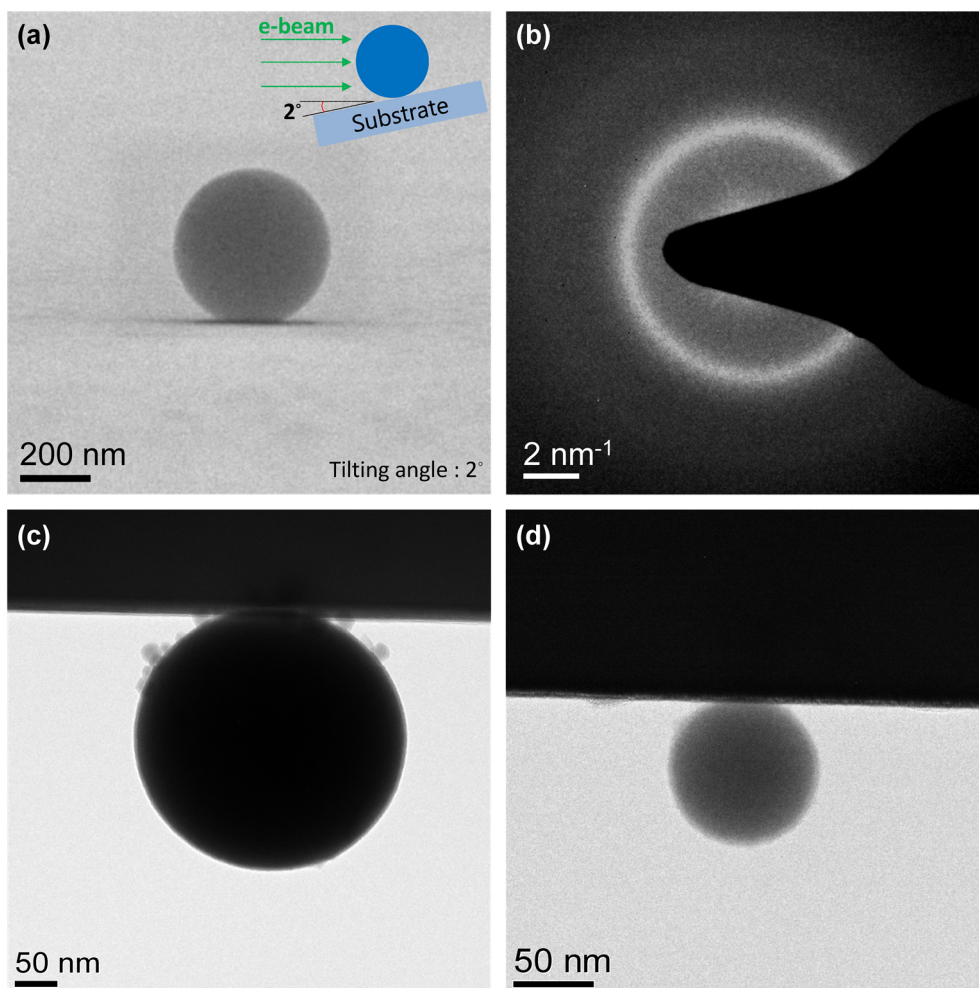


Figure 4.1. (a) SEM image of a single MG-NP observed from the direction nearly-parallel to the surface of the substrate (tilt angle = 2°). (b) Diffraction pattern of a MG-NP obtained by TEM. (c, d) Bright-field TEM images of MG-NPs with different sizes.

4.2.1. Contact diameter-strain relation

During the compression of a spherical particle, the contact area between the particle and a forcing plate changes continuously depending on strain (ϵ), even from the beginning of initial elastic deformation. Since the raw data obtained from *in situ* compression tester is composed of load (F) and compressed depth (displacement; Δh), a contact area-strain relation is necessary in order to convert the raw data set into the form of a stress-strain relation. The shape of contact area is circular if the deformation of the particle is isotropic, then the contact area can be simply estimated from the contact diameter (d_c).

A few particles were tested with in-situ imaging under beam-on condition for the contact diameter measurement, while the majority of the particles (the results in the sections after this) were compressed under beam-off condition. However, the electron beam effect on deformation behavior of MG-NPs is imperceptible in the beam intensity of scanning electron microscope level and for the size range of the tested particles. The contact diameters depending on strain were measured from the video frame data in the compression test of five different particles. Figure 4.2 (a-f) shows an example of frame image series, obtained from SEM video of compression test of a MG-NP with a diameter of 310 nm. The MG-NP does not show the formation of any shear bands or shear steps on the surface observable in SEM resolution, and is plastically deformed continuously even at high strain of ~ 0.7 without fracture. The contact diameters in the lower contact were measured from each image depending on strain, assuming the contact diameter is identical in both the upper and lower contact (Strictly speaking, the contact diameter may be different due to the elastic modulus difference between the upper (diamond) and lower

(silicon), but negligibly small).

The measured values averaged from five different particles were displayed as black dots with the error bars from standard deviation (Figure 4.2 (g)). The data points were fitted considering with the three different contact diameter models. The first model is the Hertzian contact diameter(d_{hertz}) from Hertzian contact theory^{130,131} as

$$d_{hertz} = \sqrt{\varepsilon d^2} \quad \text{Eq. 4-1}$$

where ε and d is strain and particle diameter, respectively. This model can be applied to elastic-dominant deformation state, which is limited in extremely small strain range of initial deformation (case A of Figure 4.2 (h)). For this range, the contact diameter is difficult to be measure experimentally due to the small value and normally the unstable initial contact, but it is considered theoretically to follow the Hertzian model.

The second model is the geometric contact diameter¹³² (d_{geo}), derived from the geometrical relations inside a particle, as described in case B of Figure 4.2 (h). With the assumption of $r' \approx r = d/2$, d_{geo} is estimated as follows.

$$d_{geo} = d\sqrt{2\varepsilon - \varepsilon^2} \quad \text{Eq. 4-2}$$

This model shows a good correspondence to the measured d_c in the range of $\varepsilon < 0.4$, though the model assumes the particle as a purely plastic material. The measured d_c data exhibit a deviation from d_{geo} at the strain over the boundary $\varepsilon \sim 0.4$.

The third is the cylindrical contact diameter¹³² (d_{cyl}), derived by assuming that the particle maintains a constant volume same with initial state and becomes a nearly cylindrical morphology with large deformation, as case C of Figure 4.2 (h). From

the relation of cylindrical volume, d_{cyl} is expressed as,

$$d_{cyl} = \sqrt{\frac{2d^2}{3(1 - \varepsilon)}} \quad \text{Eq. 4-3}$$

However, the morphology of the particle under high strain is not a perfect cylinder and has curvatures on a free surface (the particle surface which does not contact with upper and lower flat plane). This yield the difference (Δd_c) between d_{cyl} and the measured d_c , as described in Figure 4.2 (h). Δd_c is estimated to be equal to $d_{geo} - d_{cyl}$ at $\varepsilon = 0.4$, which is approximately $0.254d$. The solid line with orange color in Figure 4.2 (g) shows that the vertically translated d_{geo} by $0.254d$ well corresponds to the measured d_c at $\varepsilon > 0.4$. As a result, the combination of the three different contact model provide a unified fitting line for the contact diameter variation depending on strain in MG-NPs (The difference between d_{hertz} and d_{geo} become negligibly small in the low strain region of elastic contact, so the contact diameter in region A is assumed to follow also the relation of d_{geo}). This fitting line of $d_c - \varepsilon$ relation enables to convert a load-strain plot into a contact pressure-strain plot, which will be described in the next section.

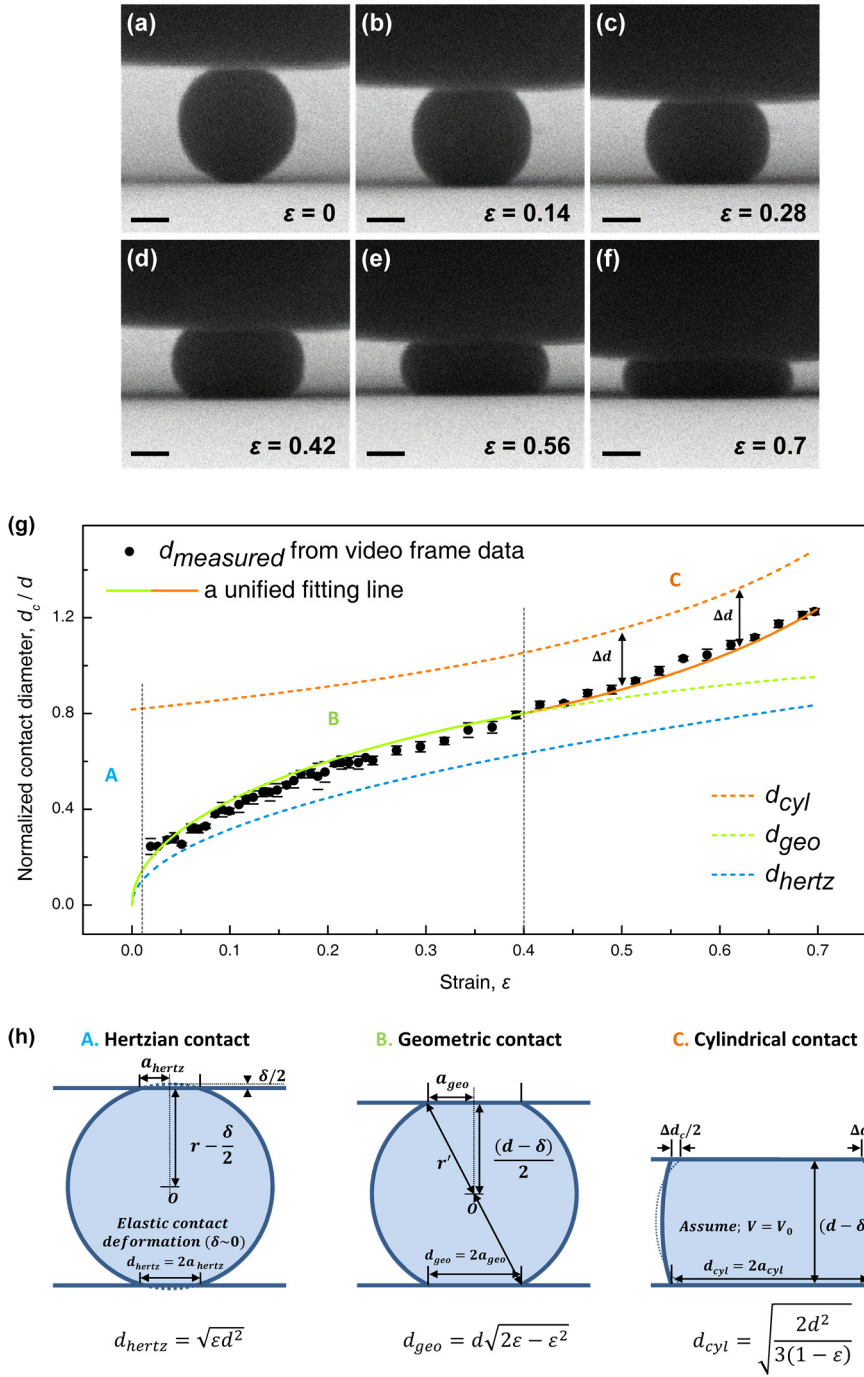


Figure 4.2. (a-f) A series of SEM images of a compressed MG-NP with $d = 310$ nm, at strain of 0 (a), 0.14 (b), 0.28 (c), 0.42 (d), 0.56 (e), 0.7 (f). (g) $d_c - \epsilon$ relation in the compression test of MG-NPs. The black dots with error bars are measured d_c values from SEM video analysis, and the colored solid line is a fitting line obtained by the combination of three different contact diameter models. (h) Schematic illustrations of the geometric relations in the three contact diameter models¹³³.

4.2.2. Contact pressure-strain relation and deformation stages during compression

Figure 4.3 shows a representative result of the compression tests, obtained from a MG-NP with a diameter of 410 nm under beam-off condition. The MG-NP after compression also does not show the formation of any shear bands or shear steps on the surface observable in SEM resolution, and is plastically deformed continuously even at high strain of ~ 0.7 without fracture. The black curve in Figure 4.3 (a) shows the load (F) - strain (ε) curve of the MG-NP compression, where strain is calculated by $\varepsilon = \Delta h/d$. The curve has a nearly-linear part at the initial region and deflection at the end of the linear part, then show load increase on straining with continuously changing slope. Using the contact diameter (d_c) - strain (ε) relation described in previous section, the load- strain curve is converted to the contact pressure (p_c) - ε curve (the navy curve in Figure 4.3 (a)). Note that $p_c = F/(\pi d_c^2/4)$, representing the area-averaged force on circular contact area, is addressed as ‘contact pressure’ rather than ‘stress’ because the stress distribution inside a particle is not uniform (particularly at the initial stage of deformation) due to its spherical morphology. In the p_c - ε curve, the overshoot of p_c accompanied by pop-ins with sharp pressure drop and strain burst appears in the initial part of deformation, while the steady-state flow at nearly constant p_c is observed with further straining.

The deformation process of the spherical particle can be divided into three stages depending on its elastic/plastic-deformation state¹³³ (Figure 4.3 (b)). The first is an elastic-dominant deformation stage (I) before the occurrence of the first pop-in. In this stage, the stress distribution inside the particle follows classical Hertzian contact theory¹³⁰, and that on the contact surface has parabolic distribution with

concentrated stress near the center of contact. After the first pop-in, the highly-stressed region near the contact center preferentially starts plastic deformation and the rest still maintains elastically deformed state under the stress below micro-yield strength (p_y). This elastic-plastic deformation stage (II) exhibits a linear relation in the $F - \varepsilon$ curve¹³³. With the further increase of strain, the plastically-deformed region expands and the internal stress distribution becomes nearly uniform, then the particle enters plastic-dominant deformation stage (III) where the plastic deformation occurs throughout a whole volume.

Figure 4.4 (a) is the enlarged view of Figure 4.3 (a) showing the transition from elastic dominant(I) to elastic-plastic(II) deformation. The pop-ins with rapid strain burst is marked with red arrows. The boundary of the transition is at the first pop-in event, and the elastic dominant part can be fitted by the relation of $F = 4/3 \cdot E_r \sqrt{r} \delta^3$ from Hertzian contact theory, where $r = d/2$, $\delta = \varepsilon d$ and E_r is the reduced elastic modulus^{130,131}. The stress distribution in the elastic dominant deformation stage (stage I) can be also estimated by the relations derived by Hertz^{130,131}. From the center of a contact surface (the origin of x and z axis, where x axis is parallel direction and z axis is perpendicular direction to the contact surface as described in Figure 4.4 (b)), the stress has a parabolic distribution along the x direction (Figure 4.4 (c)) as follows.

$$p_{max} = \frac{3F}{2\pi a^2} \quad \text{Eq. 4-4}$$

$$p = p_{max} \sqrt{1 - \left(\frac{x}{a}\right)^2} \quad \text{Eq. 4-5}$$

Here, a is contact radius ($a = d_c/2$) and F is applied load. Along the z direction, the normal stress (σ_x, σ_z) and maximum shear stress (τ_{max}) inside the particle have the relations as

$$\sigma_x = -p_{max} \left[\left(1 - \frac{|z|}{a} \tan^{-1} \frac{1}{\frac{|z|}{a}} \right) (1 + \nu) - \frac{1}{2(1 + z^2/a^2)} \right] \quad \text{Eq. 4-6}$$

$$\sigma_z = \frac{-p_{max}}{1 + z^2/a^2} \quad \text{Eq. 4-7}$$

$$\tau_{max} = \frac{|\sigma_x - \sigma_z|}{2} \quad \text{Eq. 4-8}$$

where ν is Poisson's ratio of the particle (~ 0.35). Figure 4.4 (d) shows σ_x , σ_z and τ_{max} distribution inside a particle with $\nu = 0.35$. From the relations, the position of $(x, z) = (0, 0.56a)$ is under the maximum τ_{max} ($\sim 0.267 p_{max}$). For the particle with $d = 410$ nm of the results in Figure 4.3 (a) and Figure 4.4 (a), the maximum τ_{max} value at the first pop-in event is estimated to be ~ 3.78 GPa from $F = 14.5$ μN . The value is exceptionally high, close to the ideal shear strength ($\sim \mu/10$ from ref. ¹³⁴, where $\mu = 48$ GPa and $E = 129$ GPa obtained from nanoindentation test of the MG ribbon of the same composition with the MG-NPs)

Figure 4.5 is the enlarged view of the other enlarged part of Figure 4.3 (a) showing transition from elastic-plastic(II) to plastic-dominant(III) deformation. The elastic-plastic region has a linear relation between load and strain¹³³ and the curve has a deflection at the boundary of transition between region II and III. At the stage II the pop-in events with sharp stress drops appear sequentially, while the stress fluctuation becomes moderate with entering the stage III. The first derivative curve ($dp_c/d\varepsilon$) in Figure 4.3 (a) shows the clear alleviation of p_c fluctuation with

approaching plastic-dominant stage (III). Pop-in events in the deformation of MG are generally regarded as the phenomena originated from the activation of individual shear bands¹³⁵. However, if the stress is highly localized close to the ideal strength, the activation of STZ in localized volume can also cause pop-in events without shear banding¹³⁴. This view is supported by the result that the maximum shear stress inside the compressed particle at the moment of the first pop-in event is estimated to be ~ 3.78 GPa from Hertzian theory^{130,131}, which is an exceptionally high value close to the ideal shear strength ($\sim \mu/10$), as mentioned previously. With the progress of deformation in the stage II, the plastically-deformed region under highly-localized stress expands causing a p_c overshoot and the increased amount of activated STZ may percolate to nucleate shear bands. Nevertheless, the driving force for their propagation is still insufficient to propagate them to reach the particle surface due to the non-uniform stress field^{56,136} (decreasing stress gradient towards surface). Thus, despite the pop-in events at the stage II, shear steps by formation of shear bands are hardly observable at the surface of the compressed MG-NP.

At the stage III, on the other hand, the particle exhibits the steady-state plastic flow without obvious pop-in events even at high strain of 0.7 without fracture. The $p_c - \varepsilon$ relation in the stage II has only minor fluctuations, which can be also confirmed in the $dp_c/d\varepsilon - \varepsilon$ curve. In these aspect, the steady-state plastic flow in the stage III can be considered to be related to obvious homogeneous deformation in entire sample volume. The procedure to confirm the occurrence of homogeneous deformation in this stage will be described minutely in the next section.

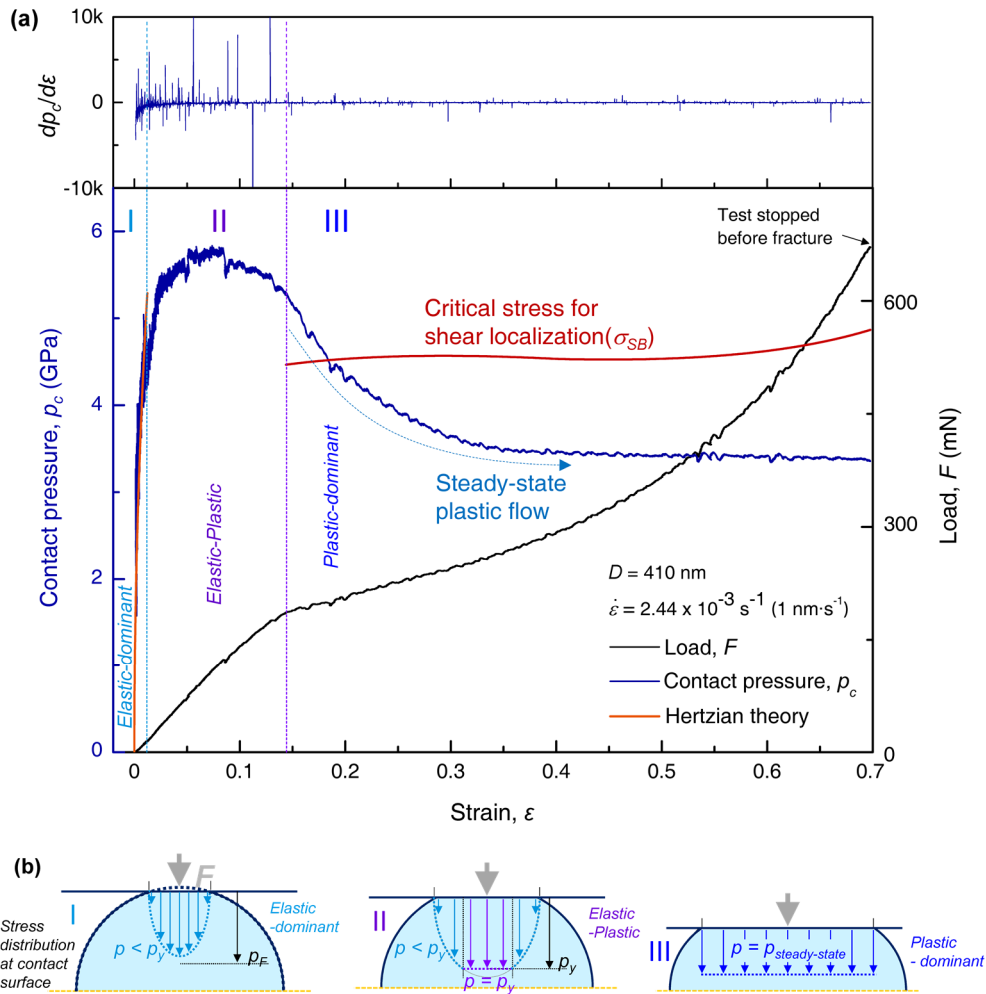


Figure 4.3. (a) F and p_c versus ϵ relations obtained from the compression test of a MG-NP with $d = 410$ nm under beam-off condition. The upper inset is the first derivative curve ($dp_c/d\epsilon$) of the $p_c - \epsilon$ curve. The red solid line is a critical stress for shear localization (σ_{SB}) estimated by Eq. 4-13. (b) Schematic illustrations describing pressure (p) distributions on the contact surface of a compressed MG-NP in the corresponding deformation stages¹³³.

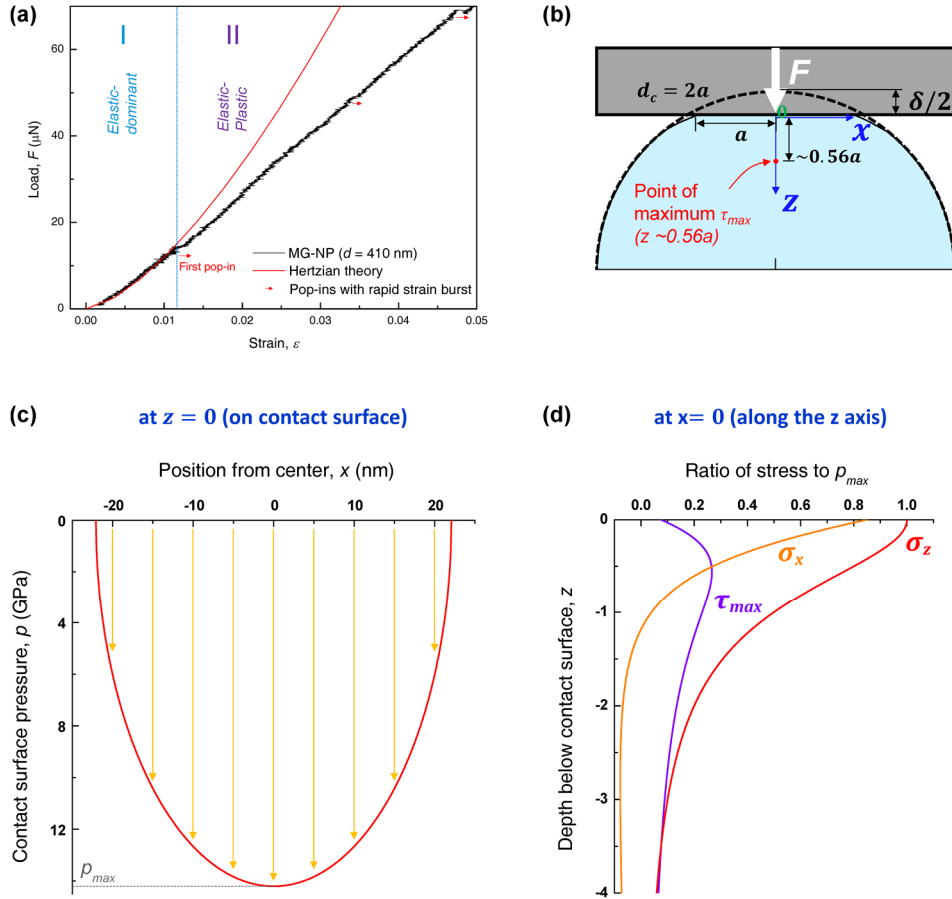


Figure 4.4. (a) An enlarged part of Figure 4.3 (a) showing the transition from elastic dominant(I) to elastic-plastic(II) deformation. (b) Schematic description with axis definitions and the position under the maximum shear stress. (c) Stress distribution along the x direction on the contact surface at the first pop-in event. (d) Distribution of the normal stress (σ_x , σ_z) and maximum shear stress (τ_{max}) along the z axis inside a particle, based on Hertzian contact theory^{130,131}.

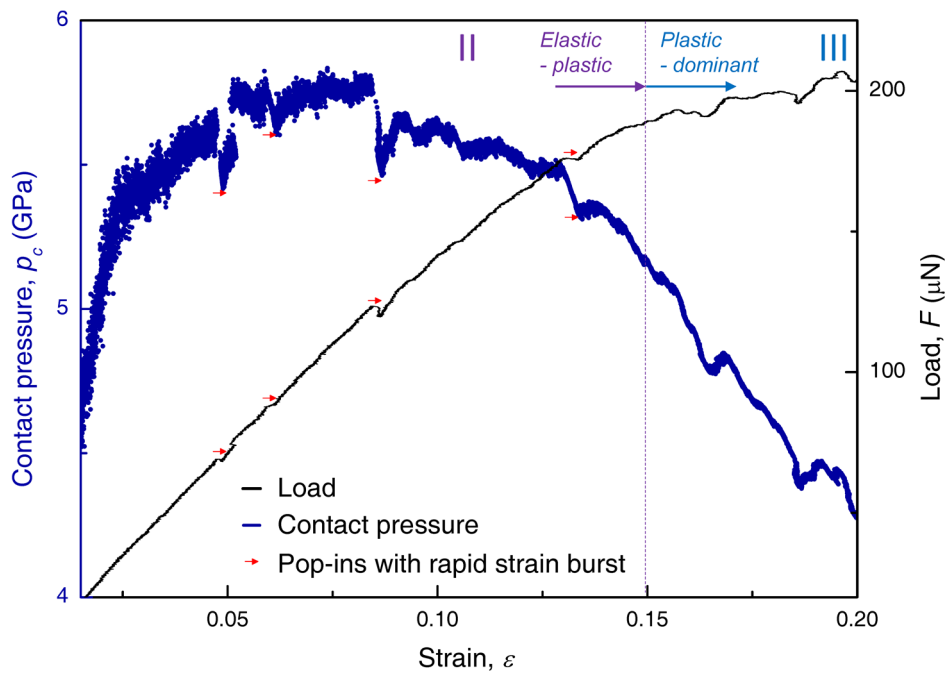


Figure 4.5. The other enlarged part of Figure 4.3 (a) showing transition from elastic-plastic (II) to plastic-dominant (III) deformation. The pop-ins with rapid strain burst are marked with red arrows.

4.2.3. Critical stress analysis for shear banding and homogeneous deformation at high strain condition

At the stage III, as mentioned previously, the compressed particle exhibits the steady-state plastic flow only with some minor fluctuation in $p_c - \varepsilon$ relation, and continuously is deformed without fracture even until a large strain of 0.7. In order to confirm that the steady state flow at the stage III is equivalent to homogeneous deformation without shear banding, one estimate the critical stress for shear band formation (σ_{SB}) in a spherical particle, and compare it with the steady-state flow stress. In previous studies, For the case of a pillar-type MG sample, σ_{SB} can be estimated as $\sigma_{SB} = (\sigma_0^2 + 2^{3/2}E\Gamma/aD)^{0.5}$ derived by relations analogous to the Griffith's crack equation^{54,58}, where σ_0 , E , Γ , a and D are the bulk yield strength, the Young's modulus, the shear band energy per unit area, the aspect ratio and the diameter of the pillar sample, respectively (See Section 1.2.1 for detailed information). The equation reflecting the geometry of pillar has been widely adopted to explain the size-dependent strength of pillar-type MGs^{54,55,58}.

Considering the energy balance relation similarly, σ_{SB} in a spherical MG-NP is estimated. The relation analogous to the Griffith's crack equation^{54,58} represents the conversion of elastic strain energy stored in the entire sample volume into the shear band formation energy related to shear band area. At the moment of shear banding, some portion of stored elastic strain energy will be released and converted to shear band formation energy. Assuming adiabatic conditions, the released elastic energy (U_{el}) from the sample volume by shear band formation is equal to the elastic strain energy difference between the stress state of shear band initiation ($\sim\sigma_{SB}$) and shear band sliding (σ_f), which is expressed as

$$U_{el} = \left(\frac{\sigma_{SB}^2}{2E} - \frac{\sigma_f^2}{2E} \right) \times \frac{4}{3} \pi r^3 \quad \text{Eq. 4-9}$$

where E and r is Young's modulus and radius, respectively, of the particle. If the sample size is large enough to ignore the size effect (i.e. bulk scale), σ_f approaches the bulk strength⁵⁴ (σ_0).

The required energy for shear band formation (U_{SB}) can be estimated from the multiplying the area of shear band (A) and its unit energy per area ($\Gamma = t_{SB} \mu \gamma_c$ (ref. 67), where t_{SB} is the shear band thickness and γ_c is the universal shear elastic limit⁹). The geometric relation for estimating the minimum shear band area penetrating a whole particle is described in Figure 4.6. With the assumption that a shear band with nearly circular area penetrates the particle with an angle of 45° with contact surface, the shear band with the minimum area passes the edge of contact surface and the radius (r_{SB}) of the shear band area is as below from the geometrical relation,

$$r_{SB} = \frac{r - \frac{\delta}{2} + a}{\sqrt{2}} \quad \text{Eq. 4-10}$$

where the compressed depth, δ is equal to εd . If $\varepsilon \leq 0.4$, $a = d_{geo}/2 = r\sqrt{2\varepsilon - \varepsilon^2}$, then r_{SB} can be simplified with applying $\varepsilon' = 1 - \varepsilon + \sqrt{2\varepsilon - \varepsilon^2}$ as follows.

$$r_{SB} = \frac{r}{\sqrt{2}} \varepsilon' \quad \text{Eq. 4-11}$$

The equilibrium condition between U_{el} (Eq. 4-9) and $U_{SB} (=A\Gamma)$ is equal to

$$\left(\frac{\sigma_{SB}^2}{2E} - \frac{\sigma_0^2}{2E} \right) \times \frac{4}{3} \pi r^3 = \pi r_{SB}^2 \Gamma \quad \text{Eq. 4-12}$$

then σ_{SB} for a spherical particle is expressed as below.

$$\sigma_{SB}(d, \varepsilon) = \sqrt{\sigma_0^2 + \frac{3E}{4r}(\varepsilon')^2 \cdot \Gamma} \quad \text{Eq. 4-13}$$

Unlike the case of pillars, the σ_{SB} of MG-NPs depends on not only the sample size but the compressed depth, or the strain as well.

For the MG-NP with a diameter of 410nm the σ_{SB} depending on strain is equal to the red solid line of Figure 4.3 (a). Here, σ_0 (=2.19 GPa) is estimated from a universal relation suggested in ref. ⁹ (this shall be mentioned again later in Section 5.3.3), and $\Gamma = t_{SB}\mu\gamma_c \approx 17 \text{ J/m}^2$ (ref. ⁶⁷), where the shear band thickness $t_{SB} \sim 10$ nm (practically minimum thickness) and the universal shear elastic limit $\gamma_c \approx 0.037$ (ref. ⁹). Figure 4.3 (a) clearly shows that the steady-state flow stress of the particle at high strain over ~ 0.4 remains constant and is lower than σ_{SB} estimated from Eq. 4-13. This indicates that the steady-state plastic flow of the MG-NP in the stage III occurs through homogeneous deformation by the activation of distributed STZ in entire sample volume rather than inhomogeneous shear localization (shear banding).

The homogeneous deformation of the MG-NP is cannot be attributed to the low aspect ratio (width/height) of the largely compressed MG-NP. Figure 4.7 (a-b) are the surface morphology of a bulk metallic glass sample with a low aspect ratio of 0.67 after compression¹³⁷. These images show clear shear steps by the formation of multiple shear bands even in the sample with a small aspect ratio. Figure 4.7 (c) is a schematic illustration the effect of aspect ratio in uniaxial compression test. In the case of a normal sample with large aspect ratio (> 2), the lateral stress (σ_L) acts only close to the upper and lower contact planes, and does not affect the formation and propagation of shear bands far from contact surface. This has only a minor effect on

the yield stress of the sample. In the case of a sample with small aspect ratio (< 1), the initiation of primary shear bands (or the yield stress of the sample) is also not affected largely by the lateral force, while the lateral stress limits the propagation of shear bands due to the strong effect of the friction between the sample and the forcing planes, induces the formation of multiple shear bands and enhance the plasticity of the sample (plastic strain ~ 0.2). In contrast, the MG-NPs in this study have much larger compressive plasticity over $\varepsilon \sim 0.7$ and does not show any clear shear steps on the surface. These differences suggest that the homogeneous deformation behavior of the MG-NPS is not originated from the low aspect ratio in high strain condition.

In the steady state homogeneous deformation region, the $p_c - \varepsilon$ relation has minor and irregular fluctuations. Figure 4.8 (a) shows an enlarged view of the $p_c - \varepsilon$ relation in Figure 4.3 (a). The minor fluctuations may be originated from (i) the friction effect between the particle and forcing plates (upper: diamond tip, lower: silicon substrate), and (ii) the formation of infinitesimal shear transformations (percolated shear transformation zone or immature nuclei of shear bands), as depicted as schematic illustration in Figure 4.8 (b).

The homogeneous deformation of the MG-NPs at room temperature can be regarded as the viscous flow of entire sample volume, comparable with the flow of high-temperature supercooled liquid state. The flow characteristics of the former will be investigated and compared with the latter, in Section 4.3.

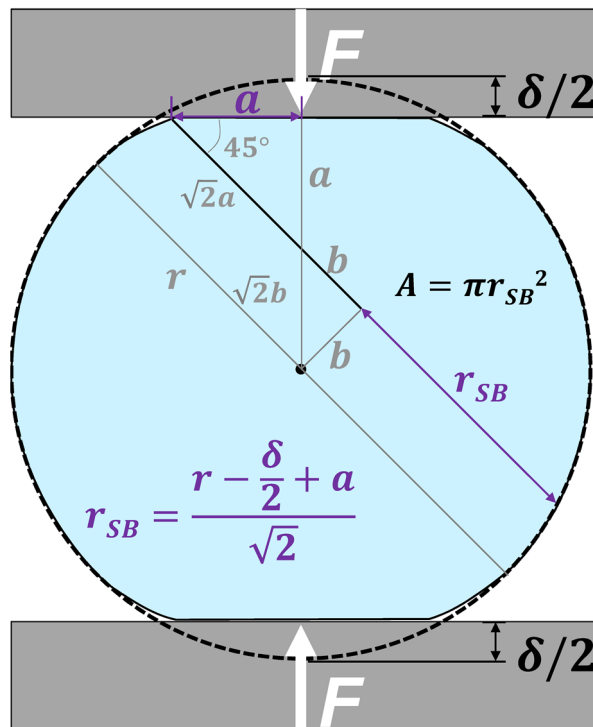


Figure 4.6. Schematic illustration of a geometric relation for the shear banding area which penetrates a whole MG-NP.

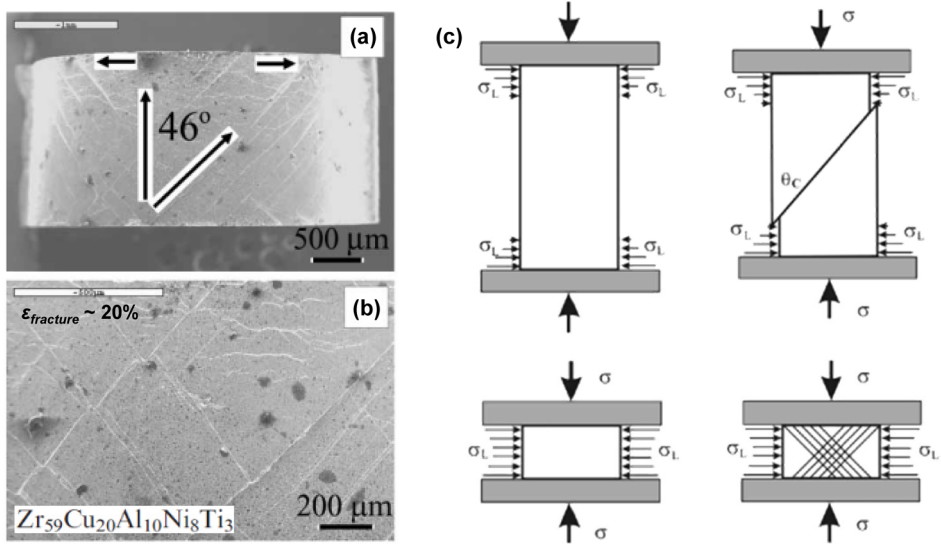


Figure 4.7. (a) Compressive shear deformation patterns of a Zr-based metallic glass sample with an aspect ratio of 0.67. (b) Magnified image of the sample in (a). (c) Schematic illustrations of the confining effect in the region near contact plane and the formation of shear bands depending on the aspect ratio of samples. Reproduced from ref. ¹³⁷ with permission through "Copyright Clearance Center".

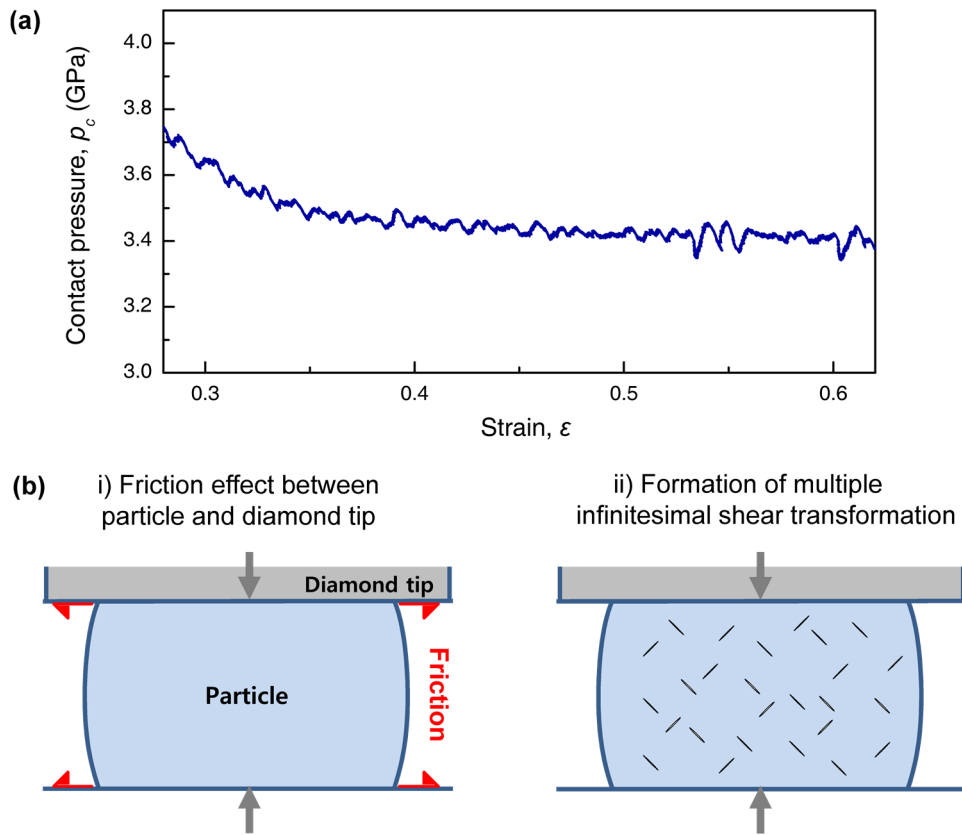


Figure 4.8. (a) an enlarged part of the steady state flow region in the $p_c - \varepsilon$ curve of Figure 4.3 (a). (b) Schematic illustration of the possible origins of minor p_c fluctuations in steady-state flow of a compressed MG-NP.

4.2.4. Molecular dynamic simulations

Molecular dynamics (MD) simulation is also applied to analyze local strain distribution¹³⁸ inside a compressed MG-NP. The basis of potential energy relation for MD simulation is not well-established for Ti-Co-Al-Gd alloy system used in experimental results, so the MD simulation of uniaxial compression is performed using a $\text{Cu}_{64}\text{Zr}_{36}$ MG-NP with the advantage of easiness to handle in atomistic modeling^{138,139}. Figure 4.9 (a) shows the compressive deformation procedure of a tested particle ($d = 20$ nm) with strain rate of 10^8 s⁻¹ in MD simulation. The particle was prepared by rapid cooling following the cooling curve of Figure 4.9 (b), and the radial distribution function (RDF; the inset of Figure 4.9 (b)) analysis shows the amorphous structure of the quenched particle. During compression to $\varepsilon = 0.7$, the particle does not exhibit the formation of shear step or abrupt shear sliding. The $d_c - \varepsilon$ relation of the compression test results in MD simulation well corresponds to that obtained in the experimental results described in Section 4.2.1 (Figure 4.2 (g)).

Due to the alloy system difference the absolute scale of F (or p_c) has the discrepancy between the MD simulation and the experimental results, but the tendencies of F and p_c dependence on ε also correspond thoroughly between both results (Figure 4.10 (a) and (b)). The $p_c - \varepsilon$ relation in Figure 4.10 (b) also reveals a clear transition from the pressure overshoot to the following steady-state plastic flow. The atomic local shear strain analysis during this transition (Figure 4.10 (c, d)) shows that the deformed volume is concentrated in the vicinity of the contact surface and contact center at the moment of the overshoot ($\varepsilon = 0.15$) as predicted in Figure 4.3 and Figure 4.4. In this state, the shear bands can nucleate at the shear strain-concentrated region, while the operation of mature shear bands are still impeded due

to the weak strain (or stress) field of the surrounding. In the following steady-state ($\varepsilon = 0.4$) the local atomic strain distribution becomes uniform into highly-deformed state, then the nearly-whole volume of the particle undergoes the consistent plastic deformation through homogeneous deformation without shear banding, at constant flow stress.

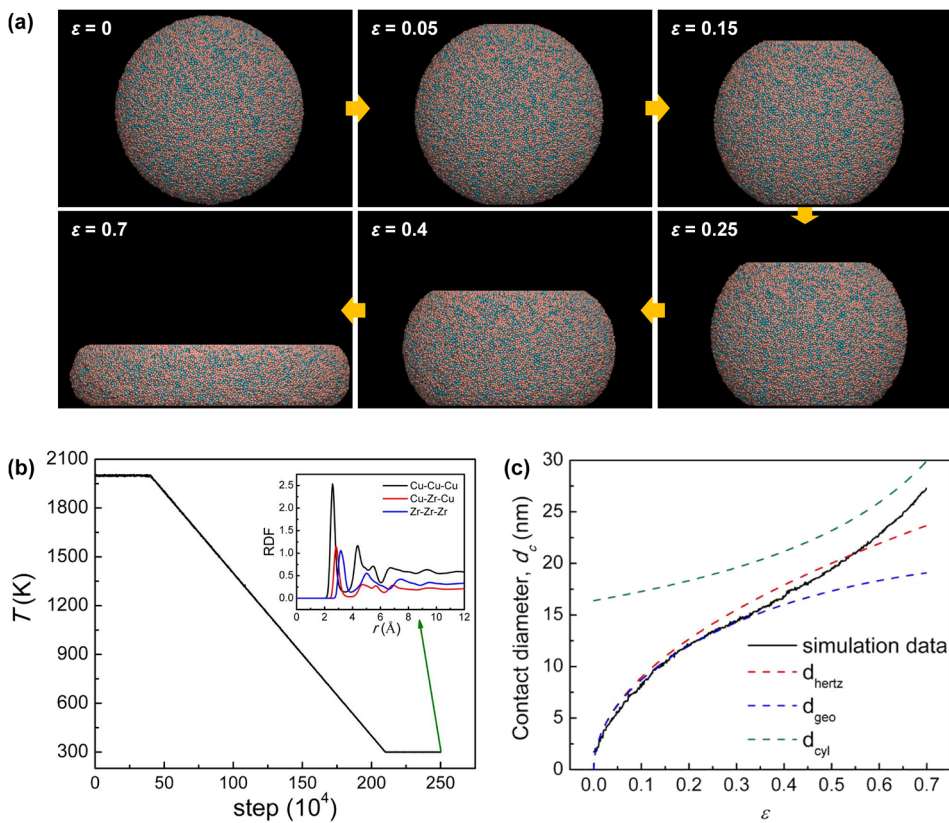


Figure 4.9. (a) A series of images of a compressed $\text{Cu}_{64}\text{Zr}_{36}$ MG-NP with $d = 20$ nm in MD simulation, depending on strain. (b) Cooling curve of solidification for the MG-NP. The inset is a radial distribution function (RDF) curves after solidification. (c) Contact diameter (d_c) versus strain (ϵ) relation in the compression of the MG-NP. The dotted lines correspond to the three different contact diameter models.

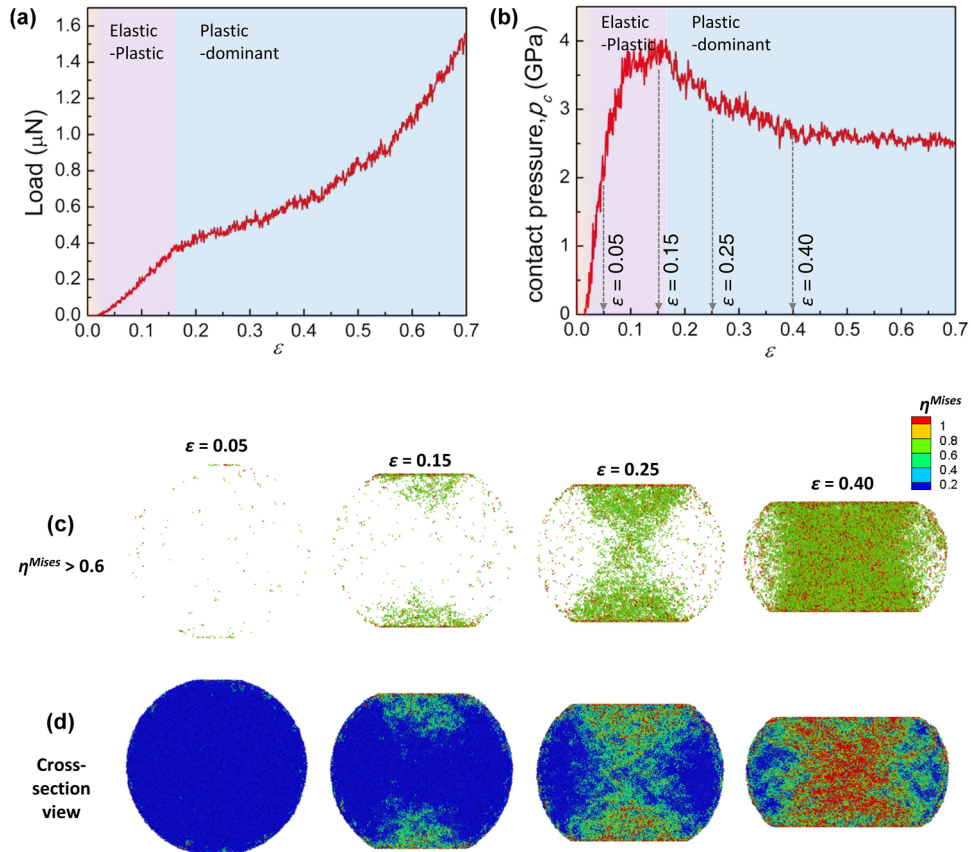


Figure 4.10. MD-simulated compressive deformation of a $\text{Cu}_{64}\text{Zr}_{36}$ MG-NP with $d = 20$ nm. **(a)** $F - \epsilon$ curve of the MG-NP during compression. **(b)** p_c versus ϵ response of the MG-NP. **(c-d)** Atomic local shear strain (η^{Mises}) distribution inside the particle at different strains, showing the atomic position under relatively high strain of $\eta^{Mises} > 0.6$ (c) and on a cross-sectional plane (d).

4.3. Non-Newtonian homogeneous flow behavior of metallic glass nanoparticles

In the previous sections, the analysis procedures for the compression test results of a single MG-NP were described. From these, it is confirmed that the homogeneous deformation can occur in compression of a MG-NP with $d \sim$ a few hundred of nanometers, at high strain condition over $\varepsilon \sim 0.4$. The homogeneous deformation of MGs is equivalent to the viscous flow of whole sample volume with a certain viscosity value, and the characteristics of the viscous flow behaviors can be classified by the strain rate dependence, as described in Figure 4.11 (a) and (b). The viscosity of a material following Newtonian flow behavior is independent on strain rate. Otherwise, a material follows non-Newtonian flow behavior with clear strain rate dependency¹⁴⁰ (Figure 4.11 (a)). In contrast, the flow stress has an opposite correlation; be dependent to strain rate for Newtonian flow, while nearly independent to strain rate in Non-Newtonian flow. The homogeneous flow of bulk MGs at a high temperature near T_g have the clear transition from non-Newtonian to Newtonian flow behavior with increasing strain rate²⁸. Figure 4.11 (c) and (d) shows the high-temperature deformation behavior of La-Al-Ni bulk metallic glass¹²⁷, which have the clear transition in flow characteristics depending on strain rate. The tendencies of flow behavior transitions have been widely reported also in other bulk metallic glass-forming systems with high-temperature mechanical test^{9,28,128}. In the non-Newtonian flow region, they exhibit the propensity of shear thinning, decreasing viscosity with strain rate rise.

Likewise, the viscosity of homogeneously deformable nanoscale MGs can be an indicator to investigate the flow characteristics of the materials, so one checked

the flow stress and viscosity dependence on strain rate in the steady-state deformation of MG-NPs. The multiple compression tests were performed with the MG-NPs of various diameters under different strain rate conditions. Some of the compression test results are shown in Figure 4.12. Figure 4.12 (a) contains the series of $p_c - \varepsilon$ relations obtained from the MG-NPs with different sizes but under same strain rate. Figure 4.12 (b) is the other series obtained under different strain rate conditions with the MG-NPs with similar sizes. In the both series of results, the flow stress of steady-state flow does not show clear dependency on either strain rate or particle size.

Figure 4.13 (a) shows the flow stress of steady-state flow at ($\varepsilon \geq 0.4$) evaluated from overall tested particles. The flow stress of steady-state homogeneous flow does not show a clear trend of the dependence on both strain rate and particle size, and scatters in a narrow stress range under σ_{SB} . The loading condition that the particles undergo continuous viscous flow with the height of compressed particles (h) smaller than the d_c is analogous to the measurement condition of parallel plate viscometry¹⁴¹, where the viscosity (η) is determined by $\eta = 2\pi Fh^5/[3V(dh/dt)(2\pi h^3 + V)]$ especially when the h is larger than $0.05 * d_c$ (ref. ¹⁴²). The calculated viscosity values of the MG-NPs at $\varepsilon = 0.4$ (Figure 4.13 (b)) are below 10^{12} Pa·s which is regarded as a viscosity boundary for glass transition¹⁴³, and clearly decrease with increasing strain rate but are independent of the particle sizes. These results reveal that the homogeneous deformation of MG-NPs at RT follows a clear shear-thinning non-Newtonian flow behavior regardless of sample sizes in the tested range.

During the high temperature deformation near T_g , the non-Newtonian flow behavior of MG is attributed to the structural instability associated with nanocrystallization driven by stress and temperature in supercooled liquid state¹⁴⁴.

However, during the homogeneous deformation of nanoscale MGs at RT, the nanocrystallization may be precluded due to lack of driving force. In this condition, the non-Newtonian flow behavior can be induced by the atomic disordering process originated from non-equilibrated condition between the creation and annihilation of flow defects¹⁷ (i.e. free volumes or STZ). The creation rate of flow defects during homogeneous deformation is proportional to strain rate, while their annihilation rate is not. With increasing strain rate the creation of flow defects overwhelms their annihilation at non-equilibrated state, then the defect concentration at steady-state flow will equilibrate in higher concentration. This results that the sample can be nudged into more dilatated state (or low viscosity state) under higher strain rate condition, leading to the shear-thinning non-Newtonian flow behavior.

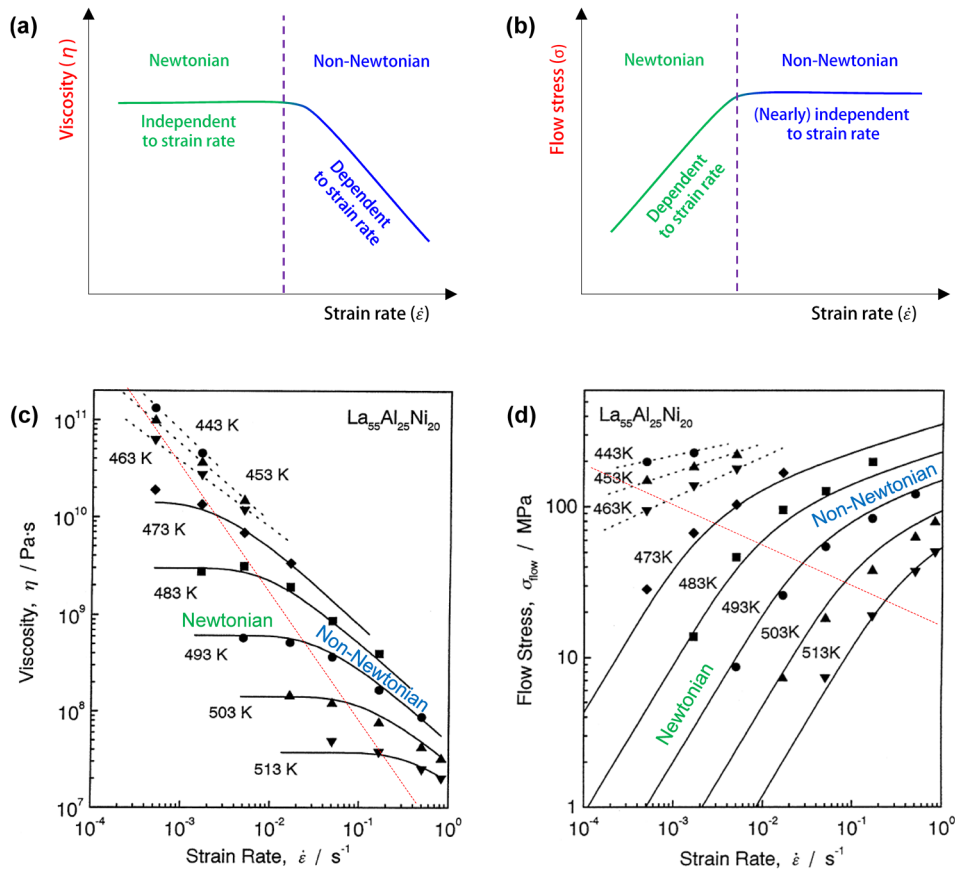


Figure 4.11. (a-b) Schematic description of the difference between Newtonian and Non-Newtonian flow in viscosity (a) and flow stress (b) change depending on strain rate, generally observed in metallic glasses. (c-d) Viscosity change (c) and flow stress variation (d) of La-Al-Ni bulk metallic glass depending on strain rate and temperature. (c) and (d) are recomposed from ref. ¹²⁷ with permission through "Copyright Clearance Center".

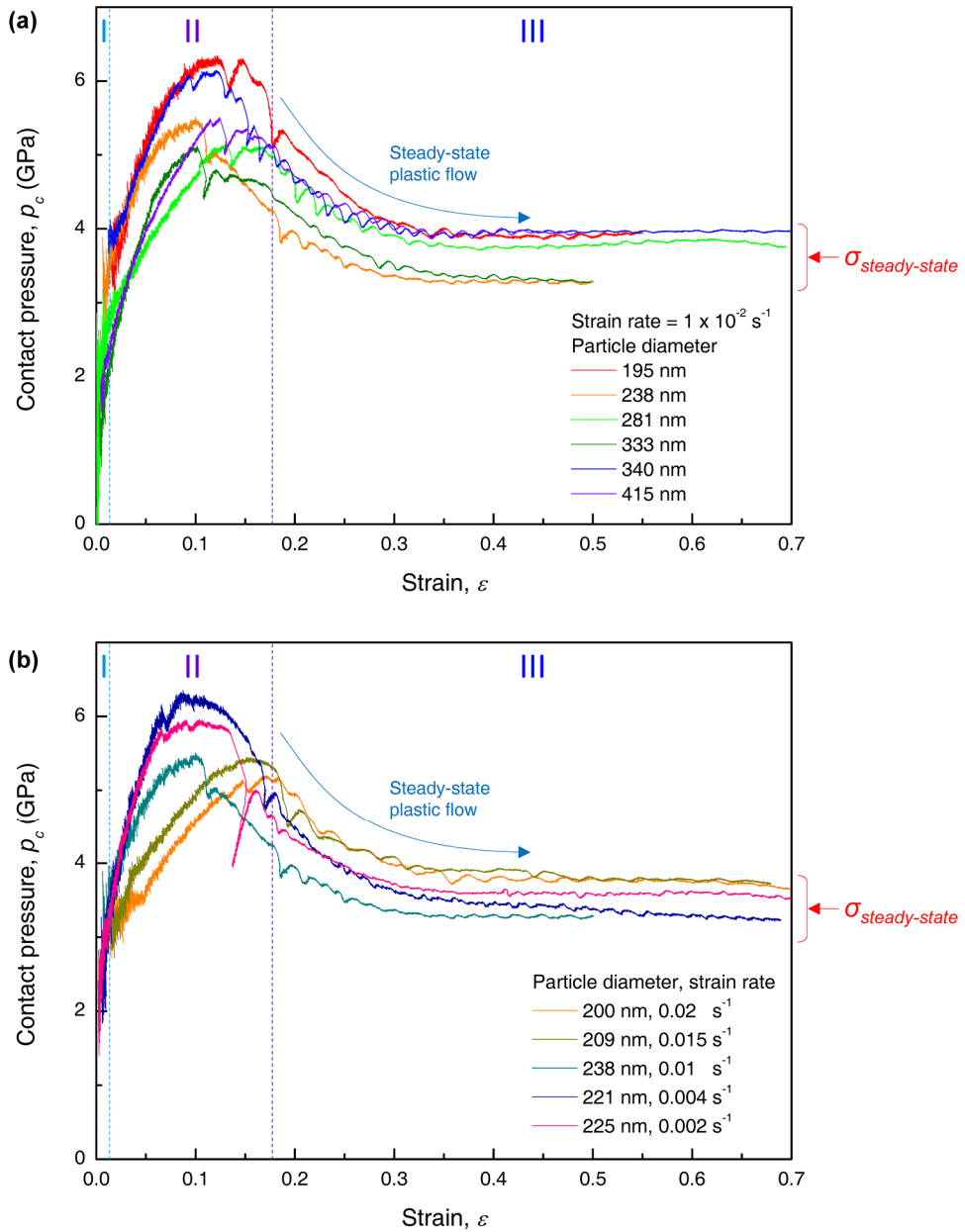


Figure 4.12. Contact pressure (p_c) - strain (ε) curves obtained from the compression tests of MG-NPs. **(a)** p_c - ε curves from the MG-NPs with different sizes but under same strain rate. **(c)** p_c - ε curves from the MG-NPs with similar sizes under different strain rates.

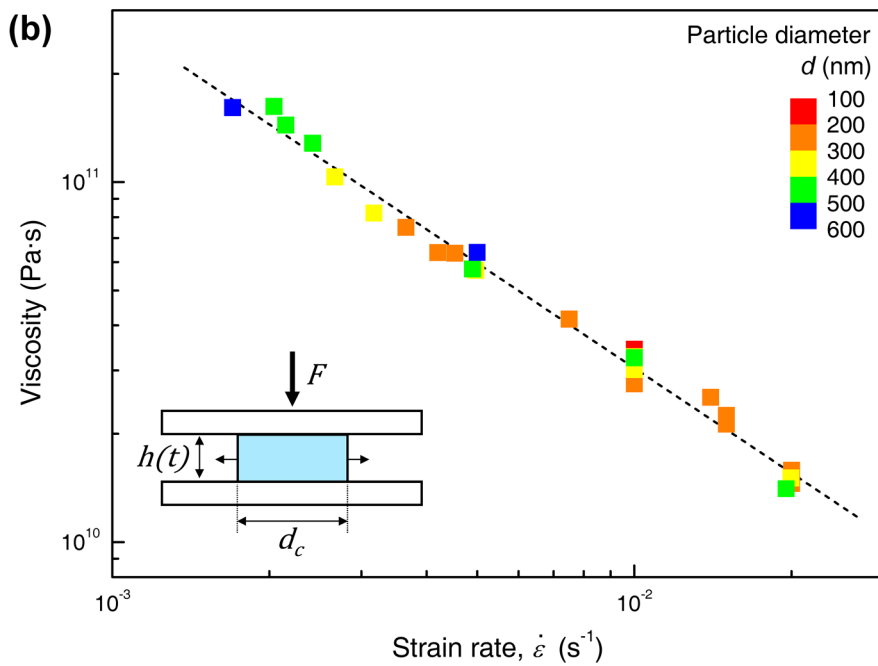
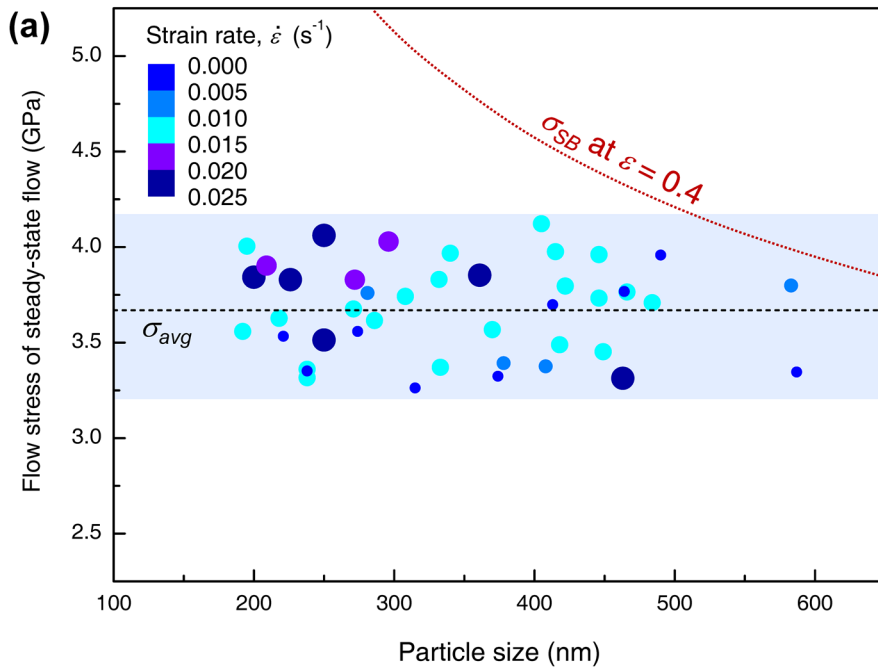


Figure 4.13. (a) Steady-state flow stress at $\epsilon = 0.4$ from the compression deformation of MG-NPs with different diameters under various strain rate conditions. The average stress value is marked as a black dotted line. σ_{SB} at $\epsilon = 0.4$ depending on particle diameter is plotted as a green dotted line based on Eq. 4-13. **(b)** Viscosity versus strain rate relation showing a clear dependency of viscosity on strain rate (non-Newtonian flow behavior).

4.4. Brittle fracture of crystallized nanoparticles

Metallic glass has a limited thermal stability related to crystallization. If a metallic glass is annealed to high temperature over its crystallization onset temperature (T_x), it crystallizes and lose its unique characteristics of amorphous state. Generally, the crystallized alloy from multi-component metallic glass has multiple and complex crystalline phases, exhibiting extremely brittleness.

This transformation behavior also can be applied to MG-NPs. Figure 4.14 shows the compression test result of a crystallized MG-NP. The particle was crystallized by heat treatment over its crystallization temperature in Ar atmosphere using differential scanning calorimeter. The crystallized particle was abruptly fractured after elastic deformation (and also elastic-plastic deformation as described in Section 4.2.2) having a large strain burst at $\varepsilon = 0.15$ as shown in Figure 4.14 (a). The surface morphology of the particle after compression (Figure 4.14 (c)) clearly exhibits the formation of mature shear bands acting as the major cracks at the fracture moment. This results reveals that the particle completely loses the capability of large plastic deformation through the suppression of mature shear bands and homogeneous viscous flow at amorphous state, through crystallization. The result also suggest that the homogeneous deformation of MG-NPs cannot be attributed only to the effect of their unique spherical morphology which is an unusual sample geometry for uniaxial compression test.

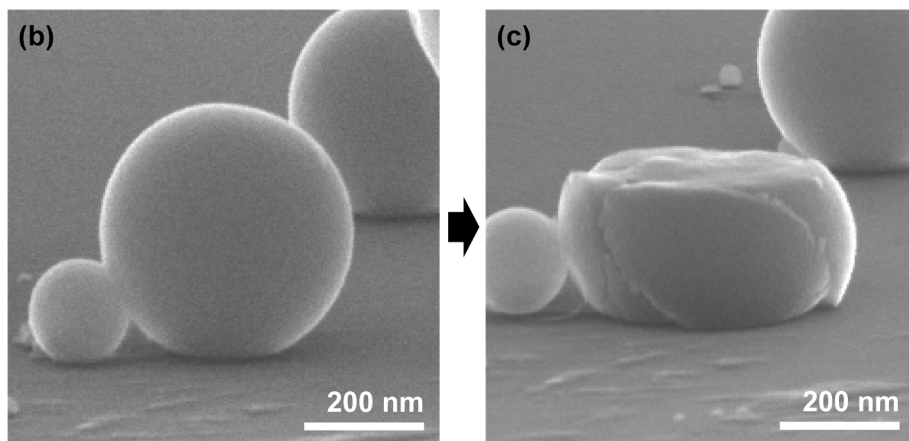
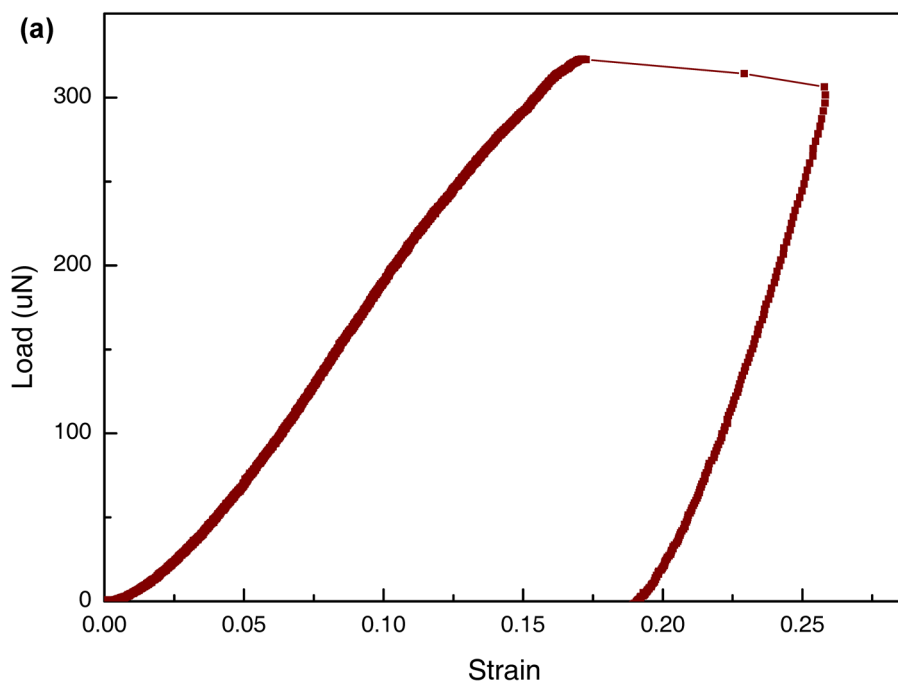


Figure 4.14. Compression test result of a crystallized nanoparticle with $d = 425$ nm. **(a)** Load-strain curve of the crystallized nanoparticle. **(b-c)** SEM images of the particle morphology before (b) and after (c) compression test.

4.5. Summary

In this chapter, the compressive deformation behaviors of the metallic glass nanoparticles prepared by the dealloying process of phase separating metallic glass were systematically investigated by *in situ* compression tests inside scanning electron microscope. As a spherical particle is not preferred sample geometry generally for uniaxial compression test, so the special analysis procedures based on contact mechanics were applied in order to interpret the stress distribution inside an individual spherical MG-NP and elastic/plastic deformation behavior in the compressed particle. Using the contact diameter - strain relation obtained from *in situ* scanning electron microscope video analysis, the pseudo-stress-strain curve (= the contact pressure - strain curve) was attained from the load- strain curve.

Based on the contact pressure - strain curve, the deformation process of the MG-NP can be classified into three stages depending on its elastic/plastic-deformation state and the stress distribution inside the compressed particle changes from highly concentrated state at near contact center to uniformly distributed state during the increase of strain. The formation of mature shear bands was suppressed at the initial plastic deformation stage by the non-uniform stress distribution inside the particle. Then, interestingly, the particle exhibit steady-state plastic flow with nearly-constant flow stress at the plastic-dominant stage with high strain condition. Through the estimation of the critical stress for shear banding in the MG-NPs (using the extended relation analogous to the Griffith's crack equation), the steady-state plastic flow at high strain condition is adjudged to be confirmed to the homogeneous deformation by the activation of distributed STZ in entire sample volume rather than inhomogeneous shear banding. Molecular dynamics simulation analysis also

supports the results of experimental investigation about the stress distribution variation and the occurrence of homogeneous deformation at high strain condition.

In order to check the flow characteristics of the homogeneous deformation of MG-NPs at room temperature, the flow stress and viscosity dependence on strain rate were evaluated in the steady-state deformation of MG-NPs. The multiple compression tests were performed with the MG-NPs of various diameters under different strain rate conditions. The cumulative results reveals that the flow stress of steady-state homogeneous flow of MG-NPs does not show a clear trend of the dependence on both strain rate and particle size, while the viscosity values of them are below the viscosity boundary for glass transition and clearly decrease with increasing strain rate. These results reveal that the homogeneous deformation of MG-NPs at room temperature follows a clear shear-thinning non-Newtonian flow behavior regardless of sample sizes. The origin of this unique deformation behavior of MG-NPs will be discussed in the next chapter, with the aid of a novel deformation map for metallic glass.

Chapter 5.

Deformation map for nanoscale metallic glasses

5.1. Introduction

A deformation-mechanism map for a material are an intuitive guideline for surveying the various deformation mechanisms underlying the deformation of the material⁴⁷. The deformation-mechanism map is composed of transition boundaries among the competing deformation mechanisms, delineated from the rate equations expressing the deformation mechanisms (constitutive models) and the experimental data obtained under external conditions in the ordinates and abscissas of the map^{47,48}. In contrast to various atomistic mechanisms on external conditions underlying the deformation of crystalline materials, the deformation of metallic glass is regarded to be governed by a single mechanism (i.e. diffusive atomic jump¹⁰ or shear transformation zone (STZ) operation¹¹). Thus, for metallic glasses (MGs), the ‘deformation maps’ (without the term ‘mechanism’)⁹ have been suggested representing the deformation mode depending on external conditions. The deformation maps for metallic glasses suggested in precedent studies are summarized in Section 1.1.4. The deformation maps of MGs, comparably to deformation-mechanism maps, provide straightforward information on mechanical behaviors of MG under external conditions.

On the other hand, including the results in Chapter 4, numerous researches have reported that if the size of MG samples is reduced down to a few hundred of nanometer scale, they exhibit unique deformation behaviors³⁰ unexpected from the

existing deformation maps. The interesting changes influenced by size effect on the deformation of MGs includes the tendency of “the smaller is the stronger” under shear banding regime⁵⁴⁻⁵⁶, and the unique mode transition of plastic deformation from brittle-inhomogeneous to ductile-homogeneous manner⁵⁵⁻⁵⁹ as intensively investigated in Chapter 4. In contrast to homogeneous flow at a high temperature near glass transition temperature (T_g)²⁸, however, the origin, flow characteristic and temperature dependence of the homogeneous deformation in nanoscale MGs at near room temperature are still in a veil.

In this chapter, a novel form of deformation map reflecting sample size effect on strength and stress-induced viscosity drop is proposed, which provides illuminating insights on the deformation behavior of nanoscale MGs. Based on the nanocompression test results of MG nanoparticles (MG-NPs) in Chapter 4 and microtensile creep test of ribbon samples having the same composition with the MG-NPs, (i) the boundary between non-Newtonian and Newtonian flow, (ii) iso-viscosity contours and (iii) the critical boundary for shear localization depending on sample size were delineated for consisting a new deformation map for metallic glasses. The implications of the boundary positions in the deformation map will be discussed for understanding nanomechanical behaviors of MGs, with the concept of ‘mechanically-induced’ glass transition^{145,146}.

5.2. Steady-state flow analysis near glass transition temperature

As mentioned in previous section, a deformation(-mechanism) map for a material can be delineated based on the constitutive models (rate equations) and the experimental data under corresponding external conditions. In the case of crystalline materials, each boundary between the deformation mechanisms in the map is delineated from the equilibrium condition between the corresponding rate equations since crystalline solids have a number of alternative (competing) deformation mechanisms depending on stress, temperature and strain rate⁴⁷. On the other hand, a single rate equation is generally applied to the deformation map of metallic glasses for expressing a single mechanism (an elementary plastic unit of shear transformation), while the boundaries in the map is derived from the equilibrium condition between the competing deformation modes (or other expressible components, as iso-viscosity contours), based on the parameters in the rate equation.

The deformation map suggested in this study is based on shear transformation zone (STZ) theory¹¹, which regards an elementary shear transformation unit of metallic glass as a cluster of a few to ~100 atoms undergoing an inelastic shear distortion⁹ (See Section 1.1.1 for the detailed information). In the theory, the steady-state shear strain rate ($\dot{\gamma}$) depending on shear stress (τ) and temperature (T) is expressed as follows.

$$\dot{\gamma} = A \cdot \exp\left(-\frac{Q}{kT}\right) \sinh\left(\frac{\tau V}{kT}\right) \quad . \quad \text{Eq. 5-1}$$

Here, A is the product of numerical factors including the deformed fraction of material via the activated STZs, the fundamental mode vibration frequency and the

characteristic strain (γ_0) for activating the process. Q and k are the characteristic activation energy for the process and the Boltzmann constant, respectively, and the activation volume V is the product of the characteristic STZ volume (Ω) and γ_0 . For the uniaxial mechanical testing condition, Eq. 5-1 can be converted into the following form,

$$\dot{\varepsilon} = A' \cdot \exp\left(-\frac{Q}{kT}\right) \sinh\left(\frac{\sigma V}{\sqrt{3}kT}\right) \quad , \quad \text{Eq. 5-2}$$

where $\dot{\varepsilon}$ and σ are the uniaxial normal strain rate and stress, respectively, and A' is a modified constant from the constant A in Eq. 5-1. Among the factors in Eq. 5-2, $\dot{\varepsilon}$, σ and T are the controllable or the directly-obtainable factors from experimental process. The triple relationship of $\dot{\varepsilon}$, σ and T can be fitted with Eq. 5-2 in order to obtain the parameters of Q and V , which represents the characteristics of STZ (or plastic deformation) in the tested metallic glass sample.

In order to obtain Q and V in the alloy composition of the MG-NPs (tested in Chapter 4), a series of high-temperature tensile creep experiments with the ribbon samples having the same composition with the MG-NPs is designed by setting σ and T as the controllable factors and $\dot{\varepsilon}$ as the dependent variable. The experiments were performed using thermomechanical analyzer (TMA) which enabling the precise temperature-load control and measurement of strain variation (See Section 2.4.2 for the detailed procedures).

The temperature range for the creep tests was determined from the differential scanning calorimetry (DSC) result and isochronal TMA measurement of strain-temperature response. Figure 5.1 shows the DSC trace (navy curve) and TMA result (purple curve) obtained from the ribbon sample. The crystallization onset

temperature (T_x) of the ribbon sample is clearly detected in the DSC result while the glass transition temperature is not. Thus, the softening temperature range by glass transition in the ribbon sample was evaluated approximately from the wide deflection below T_x in the strain-temperature curve. From these, 713 ~ 753 K is selected as the rational temperature range for tensile creep tests (showing observable steady-state flow behavior).

The series of tensile creep tests for the ribbons were performed in the temperature range. Figure 5.2 (a) is a representative result obtained under the condition of $\sigma = 250$ MPa and $T = 723$ K. The strain-time curve (navy) and its first derivative curve (strain rate-time curve, orange) clearly show the four stages of deformation. The initial non-steady-state stage has the clear decrease of strain rate due to the gradual change from unbalanced to balanced state between flow defect creation and annihilation process^{10,17}. After then, the balanced state is achieved and the sample exhibits steady-state flow with a constant strain rate ($\dot{\epsilon}_{steady-state}$) before the obvious crystallization process begins. After a critical timescale for the onset of obvious crystallization (relaxation time), the sample transforms into the rigid crystalline phase accompanying the abrupt decrease of strain rate. This process is also observed as a exothermic event in isothermal DSC trace (black solid curve in Figure 5.2 (a)). The fully crystallized sample only show an extremely small amount of deformation (constant strain, nearly zero strain rate) under the tested condition of constant stress and temperature. In these deformation process, $\dot{\epsilon}_{steady-state}$ is the main concern, in order to obtain the triple relation of $\dot{\epsilon}$, σ and T . The sample tested under the higher temperature exhibit the higher $\dot{\epsilon}_{steady-state}$ values (Figure 5.2 (b)), which is obviously understandable from that the sample at the higher

temperature has the lower equilibrium (steady-state) viscosity. The $\dot{\epsilon}_{steady-state}$ values obtained with $\sigma = 250$ MPa at the different temperatures are listed in the inset table in Figure 5.2 (b).

The triple relationship of $\dot{\epsilon}$, σ and T from the series of tensile creep test of the ribbon samples is summarized in a stress-strain rate ($\sigma - \dot{\epsilon}$) plot of Figure 5.3. Fitting Eq. 5-2 to the experimental data of Figure 5.3 outputs the values of Q and V , which provides the quantitative insight into atomic-scale deformation in the metallic glass system⁹. The value of $A' = 1.97 \times 10^{25} \text{ s}^{-1}$, $Q = 6.99 \times 10^{-19} \text{ J} = 4.36 \text{ eV}$ and $V = 1.03 \times 10^{-28} \text{ m}^3$ provides the best fitting curves (colored solid lines in Figure 5.3) for overall tested temperature conditions. The values of Q corresponds to $\sim 68 kT_g$, which is in the reasonable range suggested in STZ model⁹. By assuming $\gamma_0 = 0.1$, the characteristic volume of STZ in this alloy composition is estimated to be $\Omega = V/\gamma_0 = 1.03 \times 10^{-28} \text{ m}^3 \approx 30 \sim 40$ Ti atoms. Although the uncertainty of Ω arise from the assumption of γ_0 and the atomic packing factor, the estimated size of STZ in this alloy is in the acceptable range of STZ model⁹.

Based on the analysis of steady-state flow (the parameters of Q and V), the boundaries in the deformation map for the metallic glass, especially concerned with the deformation behavior in nanoscale, will be discussed in the next section.

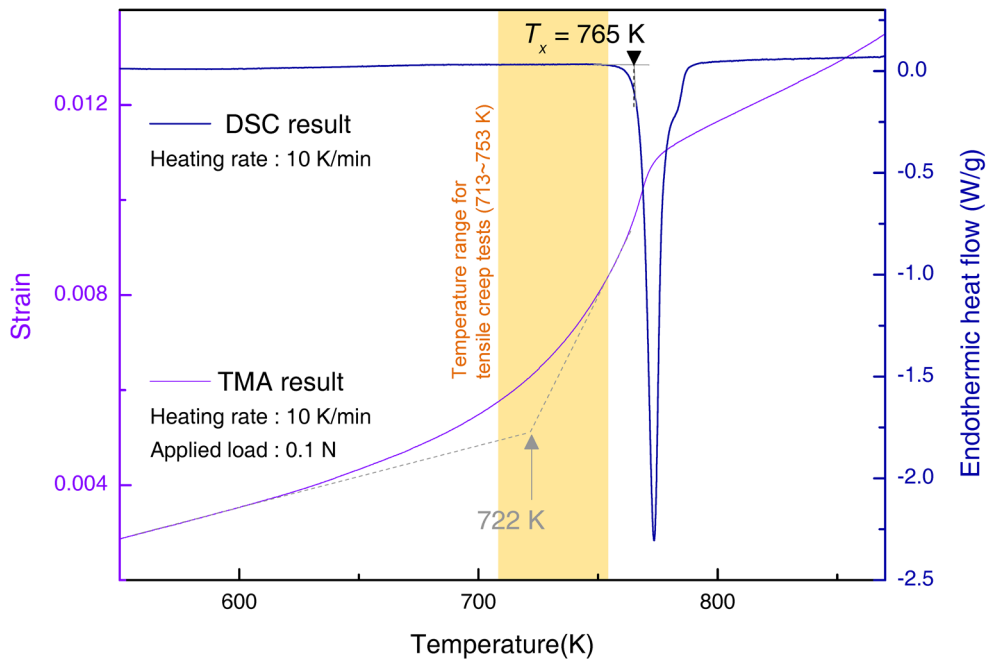


Figure 5.1. Heat flow spectrum in a DSC measurement and strain-temperature response in an isochronal TMA measurement of $\text{Ti}_{55.8}\text{Co}_{30.4}\text{Al}_{11.7}\text{Gd}_{2.1}$ as-spun ribbon sample. The heating rate in the both measurement is 10 K/min.

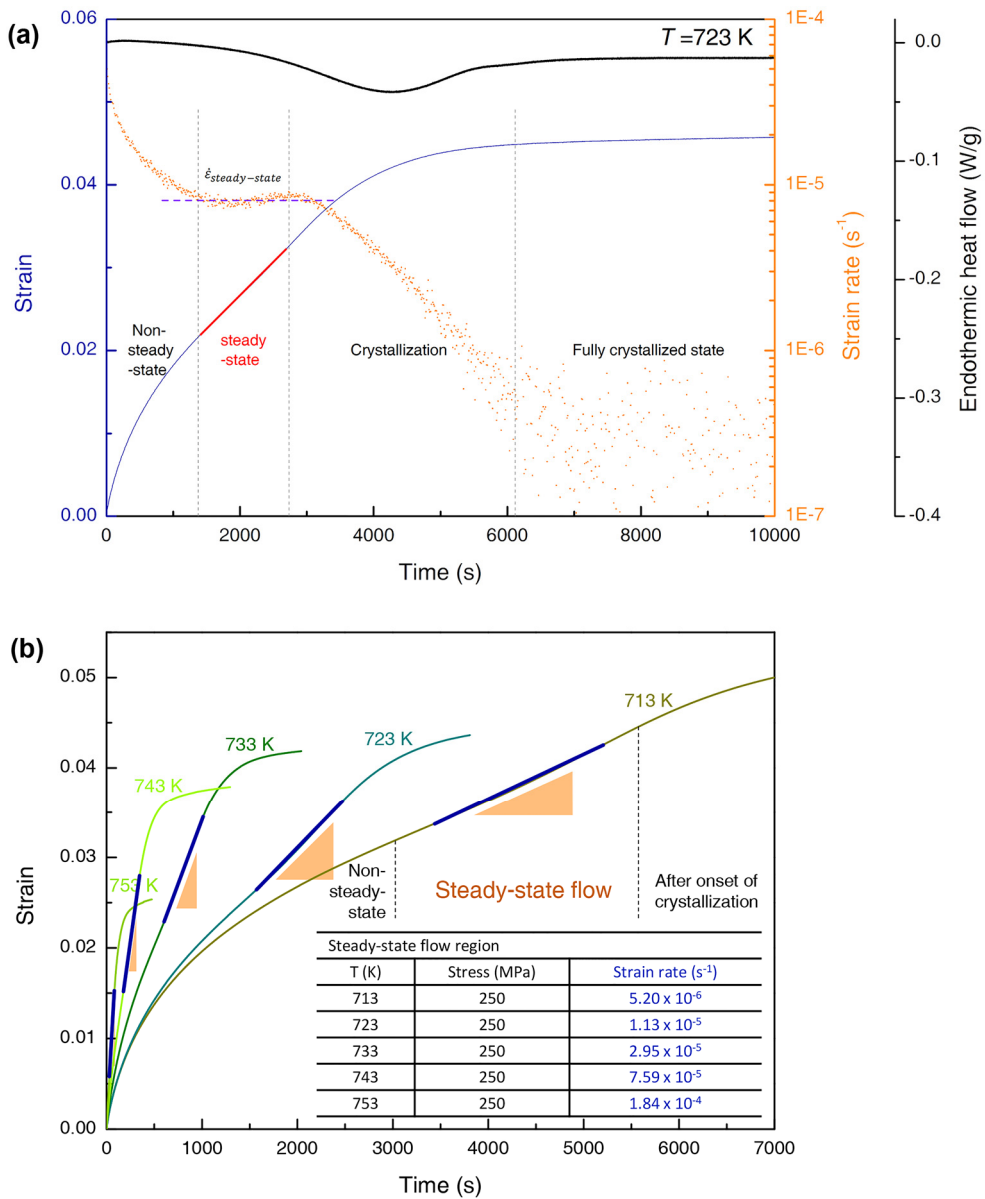


Figure 5.2. High-temperature tensile creep test results of $Ti_{55.8}Co_{30.4}Al_{11.7}Gd_{2.1}$ as-spun ribbon samples. **(a)** Strain, strain rate and heat flow versus time plot from the result under the condition of $\sigma = 250$ MPa and $T = 723$ K. Each colored vertical axis corresponds to the curve with the same color. **(b)** Strain rate versus time curves obtained at the different temperatures under $\sigma = 250$ MPa. The inset table is the list of strain rate in steady-state flow region for each test condition.

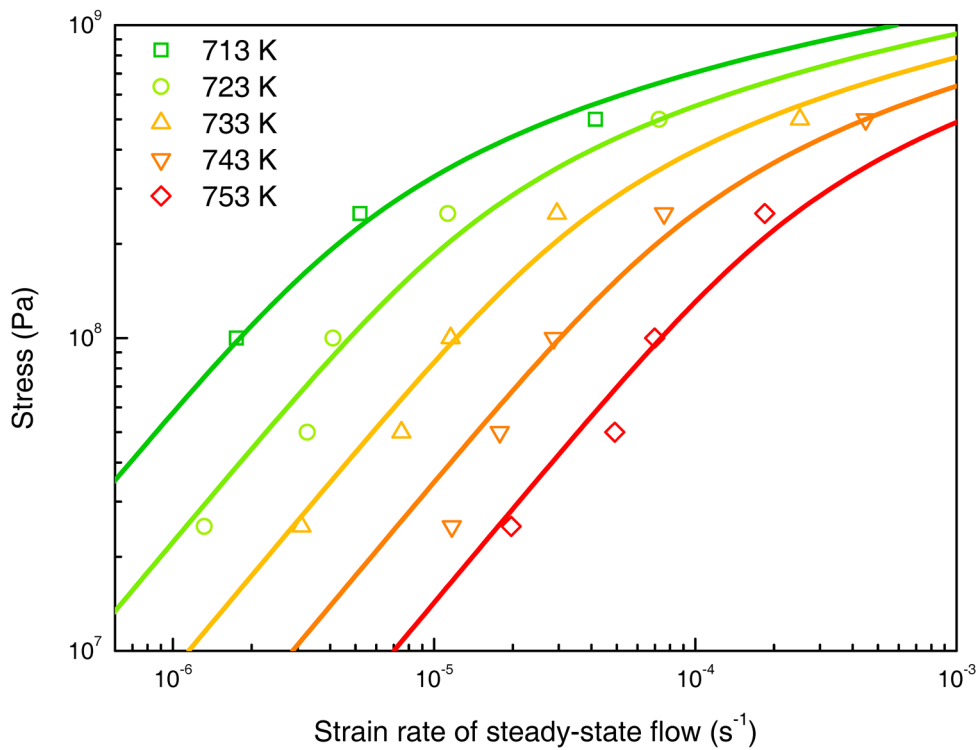


Figure 5.3. Steady-state flow stress versus strain rate relation for $\text{Ti}_{55.8}\text{Co}_{30.4}\text{Al}_{11.7}\text{Gd}_{2.1}$ as-spun ribbon samples, at the temperatures near glass transition temperature (713 ~ 753 K).

5.3. Boundaries constituting the deformation map

The major findings from the compressive deformation studies of MG-NPs in Chapter 4 can be summarized as (1) the steady-state homogeneous plastic flow at high strain condition, of which the flow stress is far below the critical stress for shear localization, (2) its non-Newtonian flow characteristic and (3) the viscosity of the MG-NPs suffering homogeneous flow under 10^{12} Pa·s. In order to elucidate the origin of these findings in the nanoscale metallic glass, the novel deformation map suggested in this study includes following components related to the findings in Chapter 4; (i) the boundary between non-Newtonian and Newtonian flow, (ii) iso-viscosity contours and (iii) the critical boundary for shear localization depending on sample size. The theoretical basis and delineation procedure for each boundary will be described in this section.

5.3.1. Boundary of non-Newtonian and Newtonian flow

The first component which represents the boundary between non-Newtonian and Newtonian homogenous flow is determined based on the extension of STZ model¹¹, similarly with the previous works of Lu²⁸ and Schuh⁹. Depending on the hyperbolic sine term, Eq. 5-1 (and also Eq. 5-2) can be expressed to a Newtonian or non-Newtonian form. For the low stress condition of $\tau \ll kT/V$, Eq. 5-1 and Eq. 5-2 is simplified as follows,

$$\dot{\gamma} = \frac{AV}{kT} \cdot \exp\left(-\frac{Q}{kT}\right) \tau \quad \left(\tau \ll \frac{kT}{V}\right) \quad , \quad \text{Eq. 5-3}$$

$$\dot{\epsilon} = \frac{A'V}{\sqrt{3}kT} \cdot \exp\left(-\frac{Q}{kT}\right) \sigma \quad \left(\sigma \ll \frac{\sqrt{3}kT}{V}\right) \quad , \quad \text{Eq. 5-4}$$

which imply a linear expression between shear strain rate and shear stress of Newtonian flow. On the other hand, for the relatively high stress condition of $\tau \gg kT/V$, the non-Newtonian form of Eq. 5-1 and Eq. 5-2 (non-linear relation between shear strain rate and shear stress) are expressed as,

$$\dot{\gamma} = \frac{A}{2} \cdot \exp\left(-\frac{Q - \tau V}{kT}\right) \quad \left(\tau \gg \frac{kT}{V}\right) \quad , \quad \text{Eq. 5-5}$$

$$\dot{\epsilon} = \frac{A'}{2} \cdot \exp\left(-\frac{Q}{kT} + \frac{\sigma V}{\sqrt{3}kT}\right) \quad \left(\sigma \gg \frac{\sqrt{3}kT}{V}\right) \quad . \quad \text{Eq. 5-6}$$

From the relations, the boundary of non-Newtonian-to-Newtonian transition follows a simple relation of (shear) stress and temperature as follows.

$$\tau = kT/V \quad (\text{general form}) \quad \text{Eq. 5-7}$$

$$\sigma = \sqrt{3}kT/V \quad (\text{uniaxial form}) \quad \text{Eq. 5-8}$$

Using the value of the characteristic activation volume (V) of STZ operation in the alloy composition of the MG-NPs, the boundary of non-Newtonian-to-Newtonian transition is delineated in a stress-temperature relation, as shown in Figure 5.4. The region enabling Newtonian flow is limited to a low stress level under ~ 150 MPa at the temperature range where the sample maintains amorphous structure (under $T_x \sim 765$ K). The implication of this boundary located at low stress level will be discussed in depth in Section 5.5.

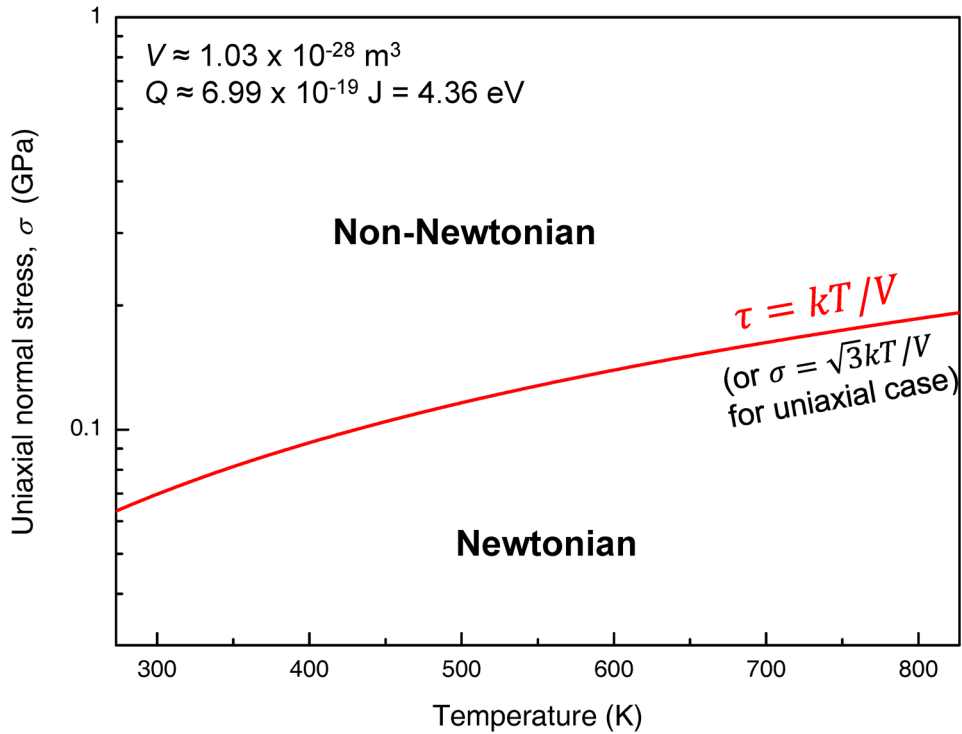


Figure 5.4. The transition boundary between non-Newtonian and Newtonian flow in stress-temperature plot (uniaxial case) for $\text{Ti}_{55.8}\text{Co}_{30.4}\text{Al}_{11.7}\text{Gd}_{2.1}$ metallic glass.

5.3.2. Iso-viscosity contours in a stress-temperature plot

From the work of Guan et al.¹⁴⁵ through molecular dynamic (MD) simulations, a unique stress-temperature scaling equation for viscosity of steady-state flow has been suggested (Figure 5.5). In MD simulation, the temperature of the system can be precisely controlled and the steady-state flow of the sample under the certain shearing condition (shear stress or shear strain rate) stress can be achieved easily². Taking these advantages, they investigated the steady-state flow stress of a model system (Zr-Cu-Al metallic glass) as a function of strain rate and temperature using MD simulation. From the results, the curves for achieving constant viscosity ($\eta = \tau/\dot{\gamma}$) are given by a surprisingly simple expression of normalized stress and temperature as follows¹⁴⁵,

$$\frac{T}{T_0(\eta)} + \left(\frac{\tau}{\tau_0(\eta)} \right)^2 = 1 \quad . \quad \text{Eq. 5-9}$$

$T_0(\eta)$ and $\tau_0(\eta)$ are the temperature and shear stress, respectively, where the viscosity reaches η when the counterpart of each is zero. In other words, $T_0(\eta)$ is the temperature for achieving the equilibrium viscosity value of η without the effect of stress, and $\tau_0(\eta)$ is the shear stress for the same viscosity in athermal condition. The relation implies that the applied shear stress on MGs has the equivalent effect as temperature in reducing the viscosity and inducing mechanical flow. Eq. 5-9 can be slightly modified into the relation of temperature and uniaxial normal stress (σ) by considering the relation, $\tau = \sigma/\sqrt{3}$, for uniaxial tension.

$$\frac{T}{T_0(\eta)} + \left(\frac{\sigma}{\sigma_0(\eta)} \right)^2 = 1 \quad \text{Eq. 5-10}$$

Under uniaxial tension of a Newtonian fluid, the viscosity is determined by¹⁴⁷

$$\eta = \frac{\sigma}{3\dot{\epsilon}} \quad . \quad \text{Eq. 5-11}$$

This relation is applied to calculate the $\sigma - T$ positions for the certain viscosity states in conjunction with Eq. 5-2. The direct combination of Eq. 5-2 and Eq. 5-11 results the complex form of simultaneous equations, so the $\sigma - T$ positions for a constant viscosity were obtained by an indirect way described in Figure 5.6 (a). Using the parameters (A' , Q and V), Eq. 5-2 and Eq. 5-11, the relation of temperature and viscosity under a constant stress can be obtained as colored solid curves in Figure 5.6 (a) depending on stress conditions. Then, the temperature required for certain viscosity values were searched from the intersections between the viscosity-temperature curves and a horizontal line of constant viscosity, as shown in the inset plot of Figure 5.6 (a).

The $\sigma - T$ positions for a constant viscosity value obtained from the procedure described above are shown in Figure 5.6 (b) as the data points with same color and symbol. Assuming that the data points is in the region of Newtonian flow (Strictly speaking, the points at $\sigma = 250$ MPa is in the transition region between non-Newtonian and Newtonian flow.), the data is fitted with Eq. 5-10, which delineates iso-viscosity contours in stress-temperature plot as colored solid curves in Figure 5.6 (b). The fitting parameters ($T_0(\eta)$ and $\sigma_0(\eta)$) for each viscosity state are listed in Table 5.1. As the viscosity is the combination of stress and strain rate, the iso-viscosity contours in the stress-temperature relation imply the strain rate effect on the deformation of MGs.

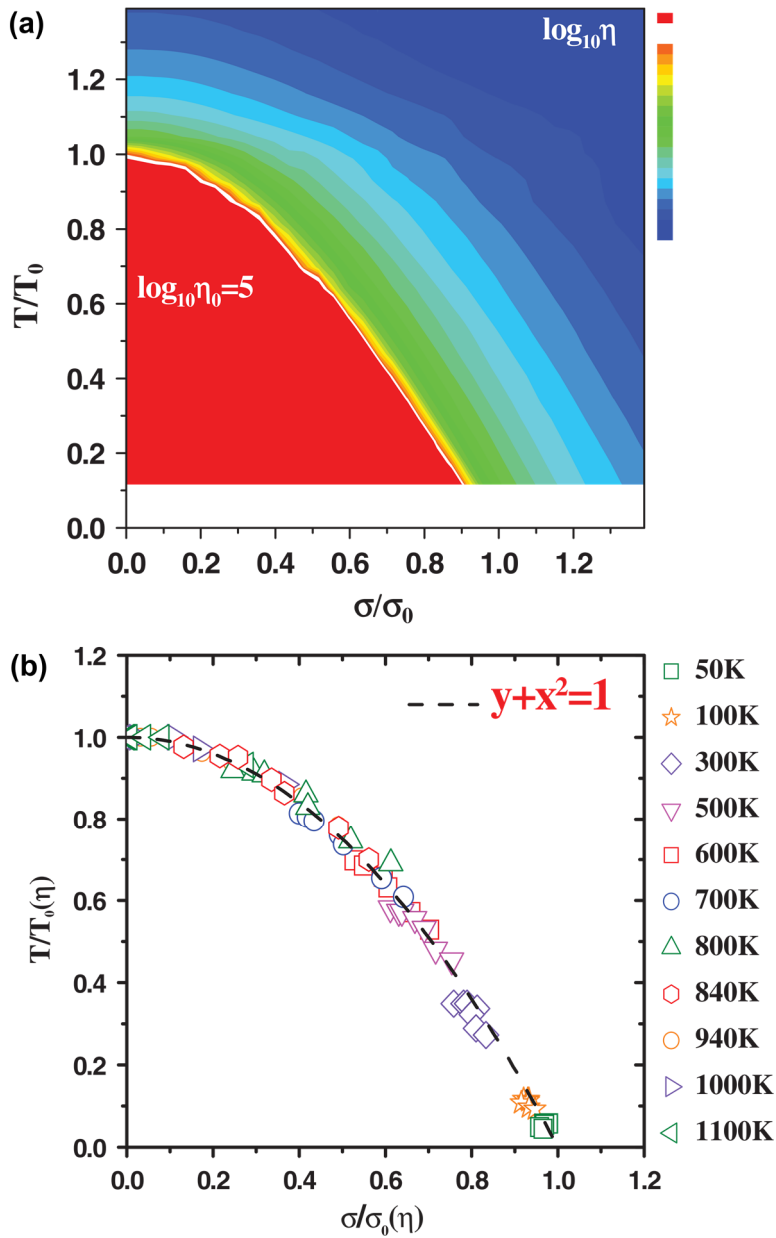


Figure 5.5. Stress-temperature scaling relation for a constant viscosity in steady-state flow. **(a)** Stress-temperature plot normalized by $T_0(\eta_0)$ and $\sigma_0(\eta_0)$, where $\log_{10}\eta_0 = 5$. **(b)** Plot of normalized stress and temperature with various shear strain rate, demonstrating the scaling relationship of Eq. 5-9. Note that σ of horizontal axis in the figures (a) and (b) means shear stress, while the symbol means normal uniaxial stress in the body text. Reprinted from ref. 145 with permission through "Copyright Clearance Center".

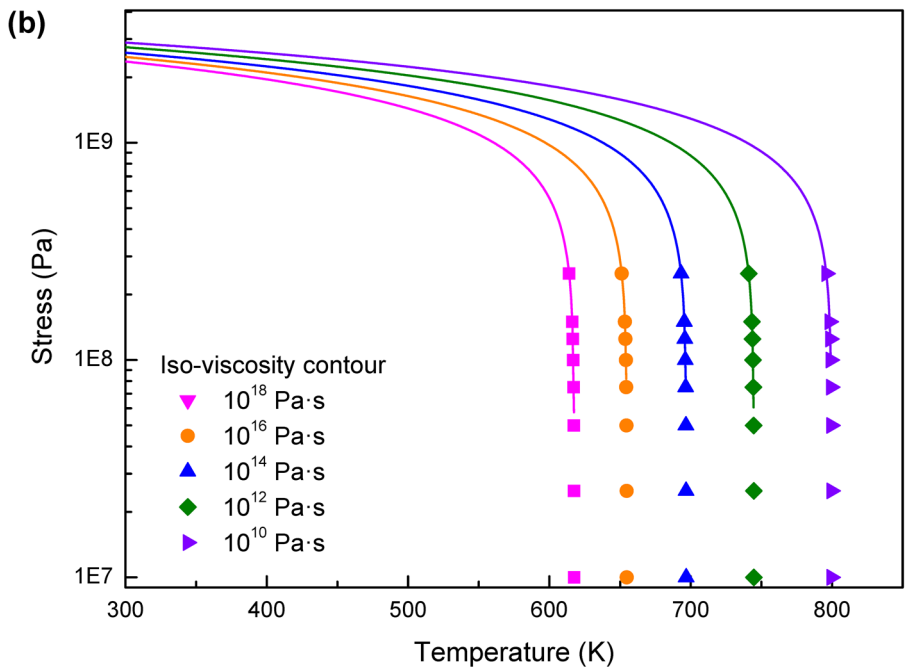
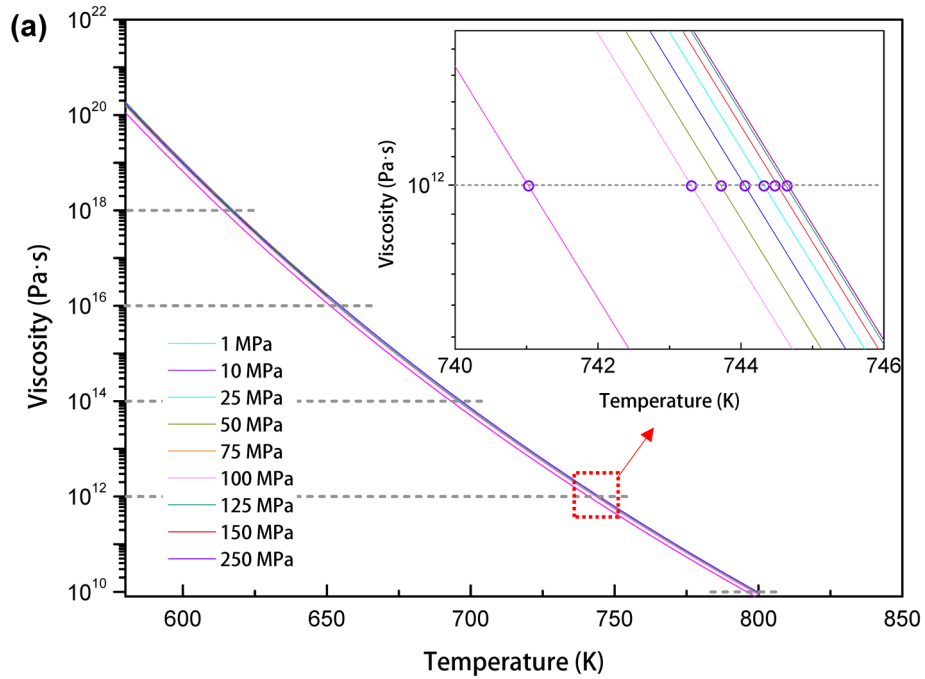


Figure 5.6. (a) Viscosity-temperature plot obtained from the combination of Eq. 5-2 and Eq. 5-11. The inset shows a procedure for searching stress-temperature points for a constant viscosity. (b) Iso-viscosity contours in uniaxial stress-temperature plot, delineated by fitting the positions of same viscosity (obtained from (a)) with Eq. 5-10.

Table 5.1. The parameters of $T_0(\eta)$ and $\sigma_0(\eta)$ corresponding to a viscosity value η , obtained from the fitting process using Eq. 5-10 in Figure 5.6 (b).

η	$T_0(\eta)$	$\sigma_0(\eta)$
10^{18} Pa·s	617.50 K	3.30 GPa
10^{16} Pa·s	654.74 K	3.37 GPa
10^{14} Pa·s	696.79 K	3.44 GPa
10^{12} Pa·s	744.66 K	3.56 GPa
10^{10} Pa·s	799.65 K	3.65 GPa

5.3.3. Critical stress curve for shear localization

The critical stress curves for shear localization (σ_{SB}) in the deformation map represent the temperature dependence of yield stress regulated by shear banding. The universal criterions for yield stress-temperature relation has been proposed by Johnson and Samwer⁵¹ based on cooperative shear model (CSM) for deformation of metallic glass as follows,

$$\frac{\tau_y}{\mu} = \gamma_{c0} - \gamma_{c1} \left(\frac{T}{T_g} \right)^{2/3} \quad , \quad \text{Eq. 5-12}$$

where τ_y and μ is shear strength and shear modulus, respectively. The constants $\gamma_{c0} = 0.036 \pm 0.002$ and $\gamma_{c1} = 0.016 \pm 0.002$ have been suggested by fitting the accumulated experimental data of yield stress depending on temperature and alloy systems (yellow curve in Figure 5.7). On the other hand, the other universal relation based on STZ model¹¹ has been suggested by Schuh and his coworkers⁹.

$$\frac{\tau_y}{\mu} = \gamma_c - \gamma_c D \cdot \ln(\dot{\gamma}_s/\dot{\gamma}) \cdot \left(\frac{T}{T_g} \right)^{\frac{1}{2}} \quad . \quad \text{Eq. 5-13}$$

Here, γ_c is the critical shear strain for shear localization. $\dot{\gamma}_s$ is a characteristic shear strain rate and D is a dimensionless constant. Fitting Eq. 5-13 to the experimental data in Figure 5.7 (navy curve) yields the value of $\gamma_c \approx 0.037$ and $D \cdot \ln(\dot{\gamma}_s/\dot{\gamma}) \approx 0.2$, which also provide a well-fitted relation to the collected data.

The deformation map suggested in this study is fundamentally based on STZ theory, so the σ_{SB} in bulk scale (where the size effect is negligible) for the alloy composition of the MG-NPs is estimated using the universal relation of Eq. 5-13. The glass transition temperature is adopted as $T_g \approx T_g^* = T_0(\eta = 10^{12} \text{ Pa}\cdot\text{s}) = 745\text{K}$,

due to its unclarity in DSC or TMA measurements (see Figure 5.1). With $\mu = 48$ GPa obtained from nanoindentation test of $\text{Ti}_{55.8}\text{Co}_{30.4}\text{Al}_{11.7}\text{Gd}_{2.1}$ as-spun ribbon sample, the σ_{SB} in bulk scale plotted as the thick black solid line of Figure 5.8. The sample size effect on σ_{SB} , as mentioned previously, is quantified using the relation analogous to the Griffith's crack equation considering sample geometry (see Section 4.2.3). The σ_{SB} for the MG-NPs has the relation of Eq. 4-13 depending on particle diameter and strain. At a constant strain the σ_{SB} increases with decreasing the diameter, where the σ_{SB} curve in the σ - T plot shifts to the high stress direction by reducing sample size. The σ_{SB} curve depending on the MG-NP diameter at $\varepsilon = 0.4$ (in the steady-state homogeneous flow region) are delineated as the solid lines with bluish colors in Figure 5.8.

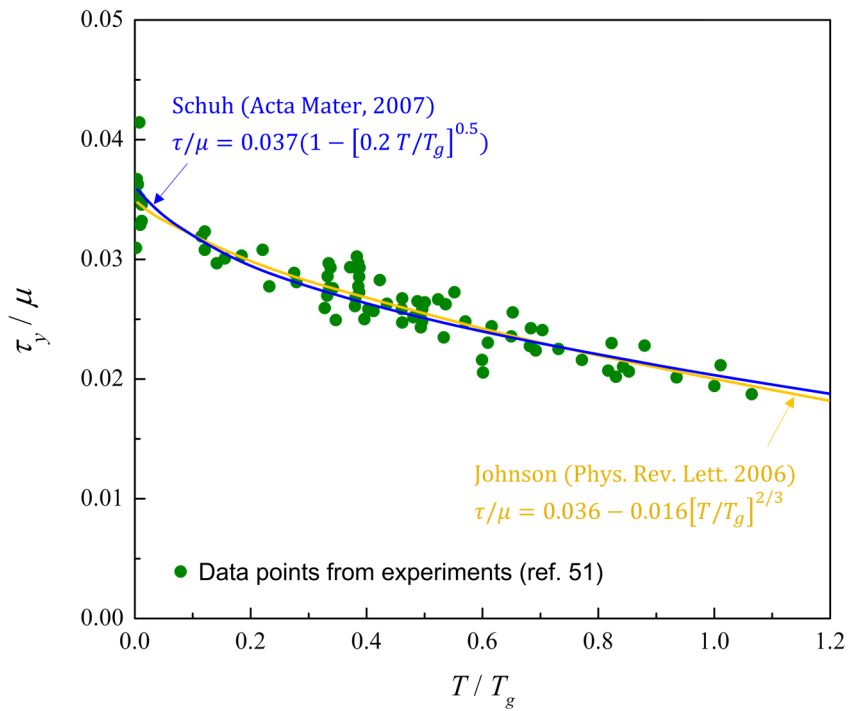


Figure 5.7. Experimental shear strength normalized by shear modulus (or shear strain at yielding) versus temperature normalized by glass transition temperature. The colored solid curves are fitting curves based on the universal relations^{9,51} of Eq. 5-12 (yellow) and Eq. 5-13 (navy). The data points from experiments were collected by Johnson and Samwer in ref. 51 for a variety of metallic glasses.

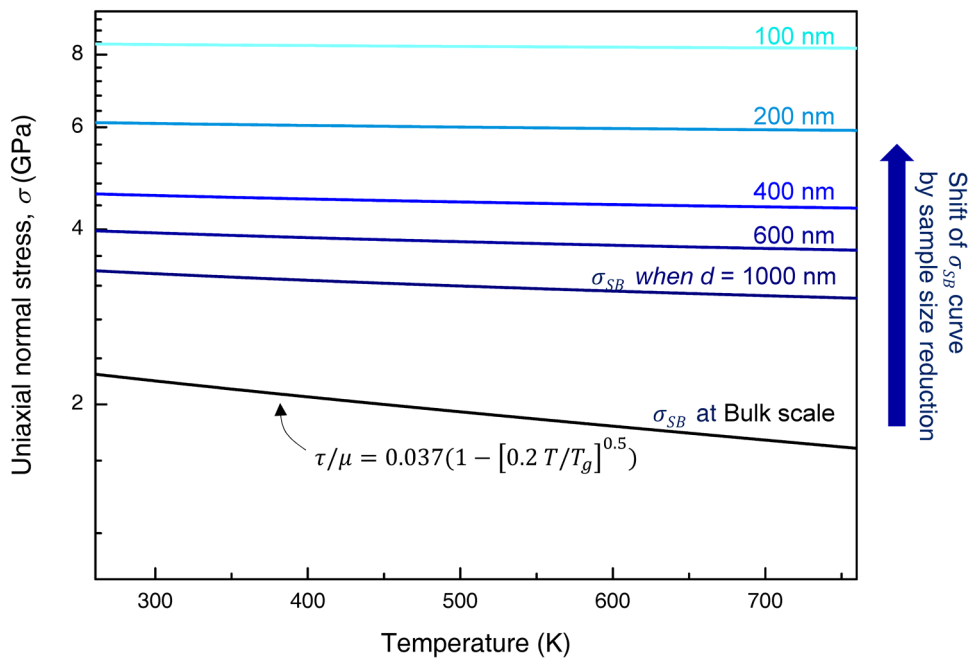


Figure 5.8. The critical stress curves for shear banding in the alloy composition of the MG-NPs ($\text{Ti}_{55.8}\text{Co}_{30.4}\text{Al}_{11.7}\text{Gd}_{2.1}$) depending on the diameter of particle, based on Eq. 4-13 and Eq. 5-13.

5.4. Construction of deformation map

Assembling the three components described in Section 5.3, a new format of deformation map is constructed as shown in Figure 5.9. The left and bottom axes of the map are in the normalized form of stress (τ/μ) and temperature (T/T_g^*), respectively, while the right and top axes are the uniaxial normal stress and temperature, respectively, without normalization which provide the direct quantitative information for the alloy of the same composition with the MG-NPs. The solid lines in Figure 5.9 refer to the critical stress for shear localization (σ_{SB}) for MG-NPs at $\varepsilon = 0.4$ depending on the particle diameter, introduced in Section 5.3.3. The boundary between non-Newtonian and Newtonian homogenous flow is depicted with the red line (and also dotted gray line for extension to elastic deformation region. The extension will be discussed in the next section.) as described in Section 5.3.1. The dotted curves are iso-viscosity contours derived in Section 5.3.2 and the region with a viscosity $> 10^{18}$ Pa·s (having only negligible flowability) is denoted as the elastic deformation region. Each colored region refers to the dominant deformation modes in bulk scale; inhomogeneous (blue), non-Newtonian homogeneous (yellow), Newtonian homogeneous (green). The shift of σ_{SB} curve to the upper direction (higher stress) with sample size reduction leads to the extension of homogeneously deformable region with non-Newtonian flow and the reduction of inhomogeneously deformable (shear banding) region. The implications of the boundary positions in the deformation map for understanding nanomechanical behaviors of metallic glasses will be discussed in depth in the following section.

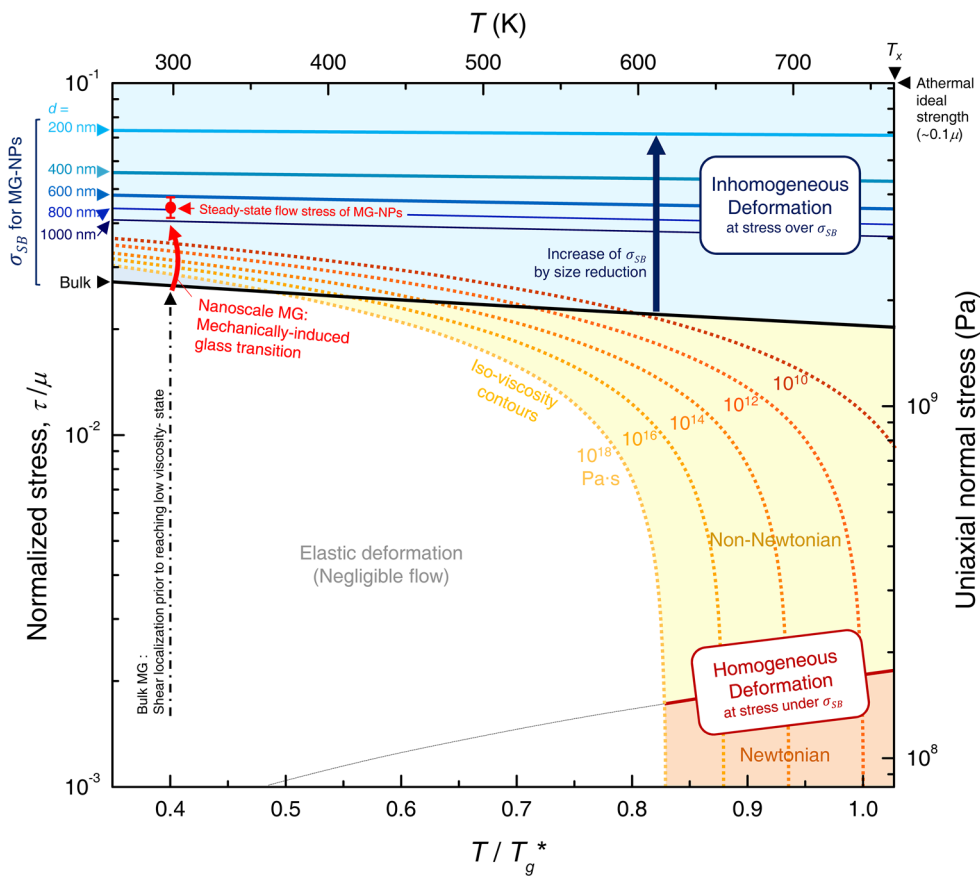


Figure 5.9. Deformation map for metallic glasses in stress-temperature axes encompassing their nanoscale mechanical behavior. The absolute values in the map is based on the metallic glass of the same composition with the MG-NPs ($\text{Ti}_{55.8}\text{Co}_{30.4}\text{Al}_{11.7}\text{Gd}_{2.1}$).

5.5. Interpretation of homogeneous deformation of metallic glass nanoparticles on deformation map

The nanoscale mechanical behavior of metallic glass, especially the findings with the MG-NPs in the Chapter 4, is understandable based on the novel deformation map for metallic glasses of Figure 5.9. First, the region enabling Newtonian homogeneous flow is limited to relatively low stress range under the boundary from Eq. 5-7. In this region, the iso-viscosity contours stand vertically, which corresponds to Newton's hypothesis¹⁴⁰ that the viscosity is independent of stress (or strain rate). On the other hand, non-Newtonian homogeneous flow occurs with stress-dependent viscosity at the stress over the boundary. This reveals that the Newtonian homogeneous flow at room temperature can occur only at extremely low stress condition where the flow is negligibly slow, so the homogeneous deformation at room temperature in the stress of GPa-scale follows only non-Newtonian flow behavior regardless of strain rate, as the results of Figure 4.13.

The viscosity dependence on stress intensifies with decreasing temperature, and the viscosity at room temperature drops drastically even with small increase of stress. The homogeneously deformable region with the viscosity over 10^{18} Pa·s has only negligible flow, so is denoted as the elastic deformation region. However, even in this region the extremely slow homogeneous flow with high viscosity can occur. This view is supported by the anelastic deformation accompanied by atomic reshuffling in atomic-scale simulations^{148,149} and the permanent deformation without shear banding under the stress below yield strength, in the long-period creep test of bulk metallic glasses at room temperature¹⁵⁰. Therefore, the homogeneous flow, strictly speaking, is inevitable in every regime⁹ and the homogeneous deformation

observed in experiments of nanoscale MGs can be specified as a ‘detectable’ homogeneous flow with sufficiently low viscosity (approximately $< 10^{12}$ Pa·s). The continuous viscosity decrease of MGs by increasing the applied stress to the level far below 10^{12} Pa·s is comparable to the thermally-activated glass transition, implied by Eq. 5-9. This ‘mechanically-induced’ (or stress-induced) glass transition¹⁴⁶ arising through a whole sample volume corresponds to the detectable homogeneous flow of nanoscale metallic glasses.

The shift of the σ_{SB} curve implies that the homogeneous deformation can take place even under relatively higher stress condition without shear localization if the sample size decreases. In bulk scale (when the sample size is large enough) the σ_{SB} curve and the iso-viscosity contours of high viscosity state intersect at the temperature over room temperature, which means the inhomogeneous deformation by shear banding occurs preferentially at room temperature before the sample reaches the low viscosity state enabling detectable homogeneous flow. However, if the σ_{SB} curve is shifted to the higher stress condition with sample size reduction the metallic glass can reach the sufficiently low viscosity state ($< \sim 10^{12}$ Pa·s) under the stress below σ_{SB} , then can exhibit the detectable homogeneous flow at room temperature when the sample size is under a critical size which depends on the sample geometry. From the experimental results, the steady-state flow stresses of the tested MG-NPs having the viscosity of $10^{10} \sim 10^{11}$ Pa·s range (a red point in Figure 5.9) exist in the range between the σ_{SB} of bulk scale and that shifted by the size reduction, where the sufficiently low viscosity state can be attained. (The flow stresses in the results are slightly higher than predicted by the iso-viscosity contours, which is attributed to testing mode difference between the compression of the MG-NPs and the tension of the ribbons¹⁵¹.) This results reveals that the mode transition

in nanoscale metallic glasses from inhomogeneous to detectable homogeneous deformation at room temperature is swayed by the competition between the mechanically-induced glass transition of whole sample volume and the formation of shear bands. From Eq. 4-13, the larger E leads to the larger amount of σ_{SB} curve shift to higher stress level by sample size reduction. On the other hand, the smaller V is preferred to activate STZs and dilatate a whole sample volume homogeneously with the lower stress, resulting the shift of iso-viscosity contours to the lower stress level. Therefore, an alloy system with a large elastic modulus and a small activation volume for STZ activation may have a favorable condition for mechanically-induced glass transition without shear banding, relatively at a lower stress and in a larger sample size.

The electron beam effect on the deformation of MG-NPs (especially on the flow stress and the occurrence of mode transition) is not clearly detectable in this study with the beam intensity of SEM-level (> 15 kV, 100 nA). However, it is reported that a strong electron beam on amorphous silica¹⁵² or ion irradiation on MGs^{72,153} can enhance plastic deformability and motivate the deformation mode transition by irradiation-induced structural modification. The enhanced plasticity of MGs from the structural modifications toward a rejuvenated state can be obtained not only by ion irradiation but also severe plastic deformation¹⁵⁴⁻¹⁵⁶ or thermal cycling¹⁵⁷. The influence of the structural rejuvenation³¹ introduced by the pretreatments is expected to translate iso-viscosity contours to the relatively lower temperature and stress direction in the deformation map. Thus, the rejuvenated MGs is envisaged to have a favorable condition for detectable homogeneous deformation at room temperature as compared to the pristine MGs, by reaching the low viscosity state under relatively low stress condition.

5.6. Summary

In this chapter, a novel deformation map which covers the size-dependent mechanical behaviors of metallic glasses is suggested, based on the nanoscale compression test of the MG-NPs and high-temperature tensile creep test of the microscale ribbons having the same composition with the MG-NPs. The quantitative parameters (the characteristic activation energy Q and activation volume V for STZ operation) representing the atomic-scale shear transformation of the metallic glass are evaluated by the series of high-temperature tensile creep test results. Adopting STZ model as a fundamental constitutive model of the novel deformation map, the three boundaries is delineated as the main components of the map; (i) the boundary between non-Newtonian and Newtonian flow, (ii) iso-viscosity contours based on the stress-temperature scaling relation and (iii) the critical boundary for shear localization (σ_{SB}) depending on sample size.

The correlations among the boundaries in the deformation map provide the illuminating insight on the deformation of metallic glass, especially on that in nanoscale. The shift of σ_{SB} curve to the higher stress level with sample size reduction in the deformation map means the extension of region enabling non-Newtonian homogeneous flow without shear banding to the higher stress condition. This results in that the viscosity of nanoscale metallic glass under a critical size can be decreased to the sufficiently low value even under 10^{12} Pa·s at room temperature by stress-induced viscosity drop (i.e. mechanically-induced glass transition), which is supported by the iso-viscosity contours in stress-temperature relation and the experimentally-obtained viscosity values in the compression test of MG-NPs. The boundary of non-Newtonian-to-Newtonian flow transition limits Newtonian

homogeneous flow of metallic glass only at low stress level under a few hundred GPa. Therefore, the detectable homogeneous deformation of nanoscale metallic glass at room temperature with GPa-scale flow stress have only non-Newtonian flow characteristic.

The effects of alloy system and pre-treatment on homogeneous deformation in nanoscale metallic glass can be also considered through the deformation map. An alloy system with a large elastic modulus and a small activation volume for flow defect (STZ) operation has a relatively large amount of σ_{SB} curve shift by sample size reduction and the iso-viscosity contours to the relatively lower stress level, so may have a favorable condition for mechanically-induced glass transition without shear banding, relatively at a lower stress and in a larger critical sample size. The pre-treatment on metallic glass inducing the structural modifications toward a rejuvenated state is expected to translate iso-viscosity contours to the relatively lower temperature and stress direction in the deformation map, also resulting in a favorable condition for detectable homogeneous deformation at room temperature as compared to the pristine MGs.

The systematical investigation on the deformation behavior of nanoscale metallic glass in different alloy systems and also at elevated temperature can strengthen the basis and application of the deformation map, which remains for future works. Notwithstanding, the deformation map for metallic glass suggested in this study is provides extended grasps on the deformation of metallic glass in a novel perspective.

Chapter 6.

Deformation behavior of metallic glass nanofoams

6.1. Introduction

The extrinsic size reduction of metallic glasses into the nanoscale is a unique route for enhancing the plasticity of metallic glasses with avoiding the general propensity of strength-ductility trade-off, as intensively investigated in Chapter 4 and Chapter 5. However, the practical application of the unique mechanical properties in nanoscale metallic glasses, ironically, is limited by their extrinsic size. In order to exploit the excellent mechanical properties emergent at the nanoscale, the strategy to develop metallic glass-based materials with architected (or hierarchical) structures of intrinsic nanoscale components¹⁵⁸ (Figure 6.1 (a)) have been studied. A hollow metallic glass lattice¹⁵⁹ is a representative material of metallic glass-based materials with architected structure. The nanolattice is composed of metallic glass hollow tubes with uniform tube-wall thickness in 20 ~ 120 nm (Figure 6.1 (b) and (c)), which exhibit abnormal deformation mode transitions depending on the tube-wall thickness and temperature (Figure 6.1 (d)), originated from the characteristics of nanoscale metallic glass wall. From this viewpoint in the transference of the properties at nanoscale as an extrinsic scale to the intrinsic properties in larger size scale materials, metallic glass nanofoams with nanoscale ligaments can be a candidate material for extending applications of the excellent mechanical properties of nanoscale metallic glass.

Metallic glass foams have been developed for structural applications by

supplementing poor ductility of metallic glass and achieving high mechanical energy absorption¹¹¹⁻¹¹⁵. The compressive deformation behavior of foam materials can be categorized according to their elastic/plastic characteristic¹⁶⁰, as shown in Figure 6.2. Metallic glass foams prepared by liquid-state methods¹¹¹⁻¹¹⁵ have micro/millimeter-sized ligaments and pores, which results in their compressive deformation behaviors as an elastic-brittle foam shown in Figure 6.2 (c) due to the brittle crushing of metallic glass ligaments. Figure 6.3 shows a Zr-based metallic glass foam prepared by the salt replication method and its compressive deformation behavior¹⁶¹. The micro-sized ligaments in the Zr-based metallic glass foam exhibit obviously brittle crushing behaviors as shown in the images of Figure 6.3 (a-g), and have clear serration behaviors in compressive stress-strain curves regardless of relative density and ligament size in microscale (Figure 6.3 (h) and (i)). Although the large plasticity can be obtained from the porous structure of metallic glass microfoams, the (plastic-collapse) strength of these foam materials are limited to the low stress level (a few tens to hundreds MPa depending on relative density) far below the bulk strength of the corresponding bulk metallic glass (~a few GPa).

From the differentiated size scale of ligaments, nanoporous metallic glass (=metallic glass nanofoam) is expected to exhibit exceptional mechanical properties originated from the nanoscale amorphous ligaments. In this chapter, the compressive deformation behavior of metallic glass nanofoams fabricated by dealloying process will be systematically examined, especially depending on the size of the nanoscale ligaments.

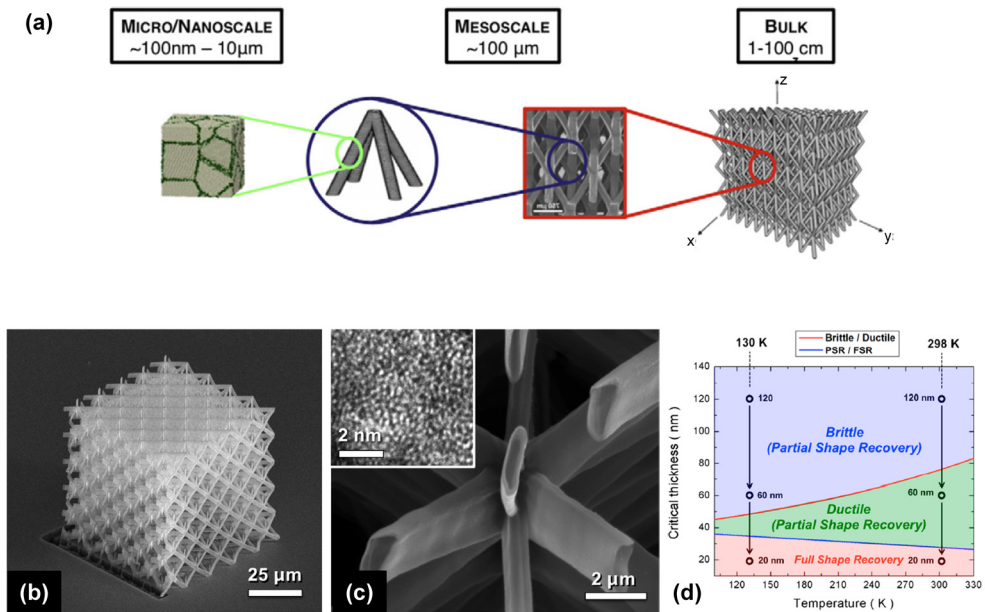


Figure 6.1. (a) Schematic demonstration for the extension of materials properties in micro/nanoscale as a ‘extrinsic size scale’ into the intrinsic properties of large-scale materials (e.g. micro/nano-truss structure). (b) Hollow Cu-Zr metallic glass nanolattice as an example of (a). (c) An enlarged view of the nanolattice (b) showing the hollow structure. (d) Deformation map for the metallic glass nanolattice in the temperature-wall thickness space. Recomposed from ref. ¹⁵⁸ and ¹⁵⁹ with permission through “Copyright Clearance Center”.

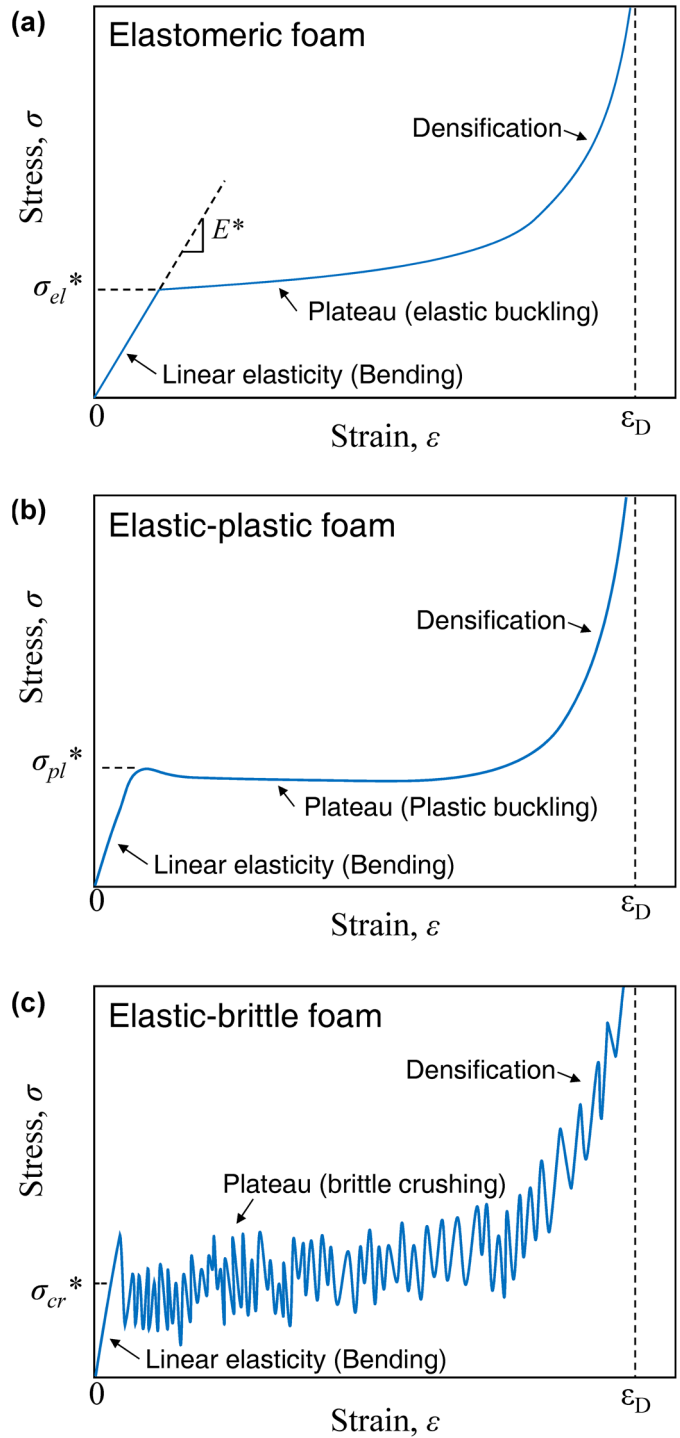


Figure 6.2. Schematic compressive stress-strain curves for foams¹⁶⁰. (a) an elastomeric foam. (b) an elastic-plastic foam. (c) an elastic-brittle foam.

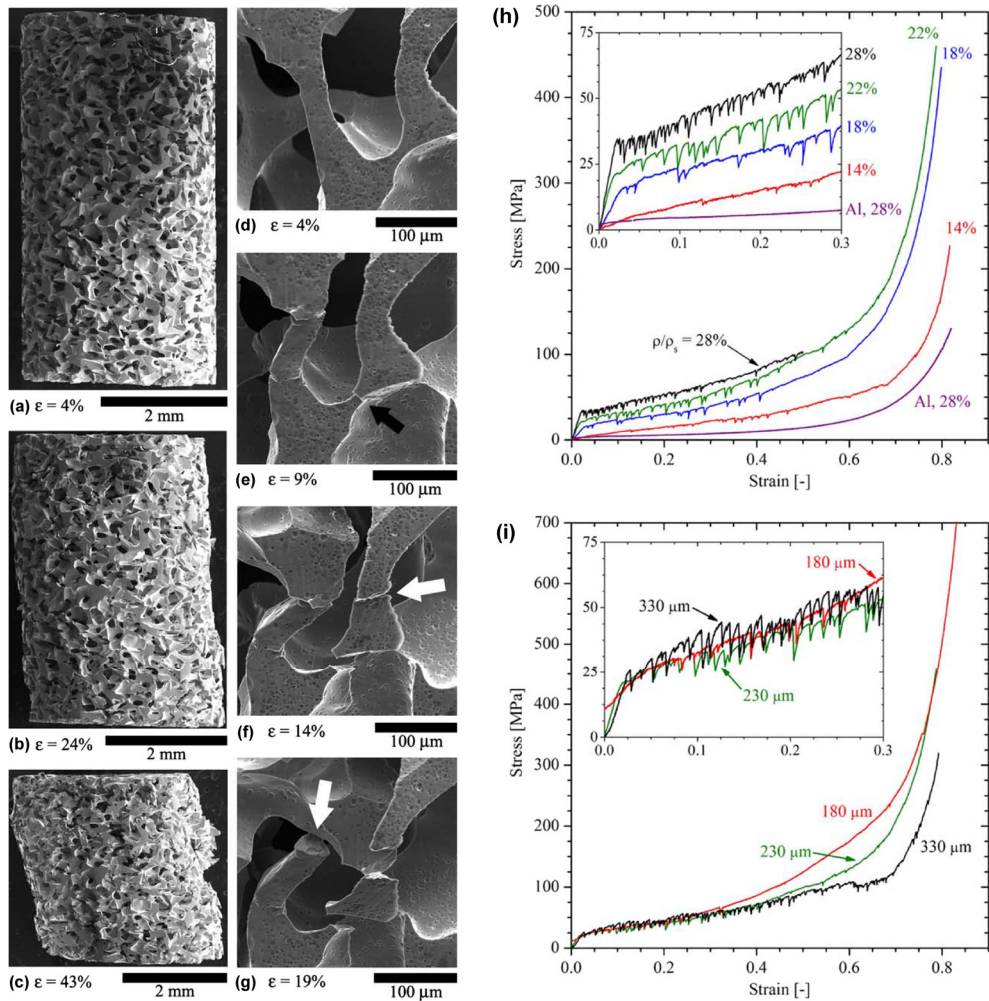


Figure 6.3. Compressive deformation of Zr-based metallic glass foams¹⁶¹. **(a-c)** low-magnification SEM images of the compressed metallic glass foams after unloading from applied macroscopic strains of 4% (a), 24% (b), 43% (c). **(d-g)** SEM images of deformed ligaments in the foam sample, after unloading from the strain of 4% (d), 9% (e), 14% (f), 19% (g). **(h-i)** Engineering stress-strain curves of the foam samples as a function of relative density for a constant pore size 230 μm (h), and as a function of pore size for near-constant relative density ($\sim 23\%$). Recomposed from ref. ¹⁶¹ with permission through “Copyright Clearance Center”.

6.2. Compressive deformation behavior of nanoporous metallic glass micropillar

The compression deformation behavior of the metallic glass nanofoam fabricated by dealloying of $Y_{19}Ti_{36}Al_{25}Co_{20}$ precursor alloy (the fabrication process was discussed in Section 3.4) was investigated through micropillar compression test in SEM. The extrinsic dimension of the metallic glass nanofoam is limited by the size of its precursor alloy. In order to obtain the porous structure with nanometer-scale pores, the interconnected structure in PS-MG precursor alloy should be controlled to have a finely separated structure with an average phase thickness under a few hundred nm. The phase-separated structure and glass formation in the precursor alloy is significantly affected by cooling rate, as discussed in Section 3.2.2. In order to achieve the sufficient cooling rate for nanoscale interconnected structure, the precursor sample is compelled to have dimension under microscale as ribbon samples by melt-spinning technique. Thus, the extrinsic dimension of the metallic glass nanofoam is also limited to microscale. The microscale ribbon-shape sample is not appropriate for conventional compression test, so the micropillar compression test in SEM was performed for investigating the mechanical response of the metallic glass nanofoam sample.

The micropillar sample of the metallic glass nanofoam was prepared by precise ion beam milling using FIB. The influence of Ga ion beam irradiation on the mechanical testing of small-scale metallic glass was discussed in Section 4.1. However, the micropillar samples tested in this study have enough large dimensions over a micron to ignore the influence ion irradiation, and the irradiation effect was minimized in the milling process by step-by-step decrease of beam current condition

with approaching the final milling stage. The micropillar sample was fabricated on a partially-dealloyed precursor, as shown in Figure 6.4 (a) and (b). By controlling immersion time in nitric acid solution, the nanoporous layer with uniform thickness can be formed on the non-reacted PS-MG which can act as a supporting substrate for micropillar. A micropillar was prepared from the ion beam milling from the direction perpendicular to the dealloyed layer, as shown in Figure 6.4 (c-e), in a rectangular parallelepiped-shape with a dimension of $1.9 \mu\text{m} \times 1.9 \mu\text{m} \times 5.5 \mu\text{m}$. The average ligament size in the sample was $\sim 150 \text{ nm}$. The existence of a rigid substrate (non-reacted PS-MG layer) under the relatively soft micropillar enables to obtain solely the mechanical response of the metallic glass nanofoam from a compression test.

The micropillar of Ti-based metallic glass nanofoam was deformed with a series of loading-unloading cycle, as shown in Figure 6.5. The engineering stress-strain curve of the pillar (Figure 6.5(a)) shows a smooth progress without obvious serrations as an elastic-plastic foam (Figure 6.2 (b)), while the bulk metallic glass foam with micro-to-millimeter scale pores (Figure 6.3) shows clear serration behaviors by brittle crushing (Figure 6.2 (c)). The plastic collapse strength (σ_{pl}^*) of the foam pillar is 880 MPa, which is a remarkably high value among cellular materials with similar relative density. Although a slight bending occurs during the compression of the pillar, the Ti-based metallic glass nanofoam was continuously deformed over $\varepsilon \sim 0.65$ (Figure 6.5(c-f)). With the severe compression over $\varepsilon \sim 0.5$, the densification initiates accompanying the drastic increase of engineering stress.

For open-cell foams, the strength of a ligament ($\sigma_{ligament}$) in the foam can be estimated from the plastic collapse strength and relative density of the foam using a following relation¹⁶⁰,

$$\frac{\sigma_{pl}^*}{\sigma_{ligament}} = 0.23 \times (\rho_{rel})^{1.5} (1 + (\rho_{rel})^{0.5}) \quad . \quad \text{Eq. 6-1}$$

ρ_{rel} is relative density and $\rho_{rel} = 1 - \phi$, where ϕ is porosity. The relative density of the tested metallic glass nanofoam was evaluated by image analysis of the precursor alloy (Figure 6.6), to be 0.58. The relative density value also corresponds to the analysis results from 3-D microstructure (Figure 3.9). using the σ_{pl}^* and ρ_{rel} values of the tested sample, the estimated $\sigma_{ligament}$ is ~ 4.9 GPa from Eq. 6-1, which is exceptionally high as compared to the yield strength of bulk-scale Ti-Co-based metallic glass estimated in Section 5.3.3, assuming that the chemical composition of the nanofoam is close to that of the nanoparticles investigated in Chapter 4 and Chapter 5.

The exceptionally high strength of the nanoscale ligament can be understood considering the size-dependent strength of metallic glass. Figure 6.7 shows an enlarged part of the deformation map of Figure 5.9. Note that the critical stress (σ_{SB}) curves for shear banding in Figure 6.7 is estimated for cylindrical samples from the relation⁵⁴

$$\sigma_{SB} = (\sigma_0^2 + 2^{3/2} E \Gamma / a D)^{0.5} \quad . \quad \text{Eq. 6-2}$$

The information of the parameters in Eq. 6-2 is referred to Section 4.2.3. If the strength of the ligaments in the metallic glass nanofoam sample is approximated by that of a cylindrical metallic glass sample, the theoretically predicted strength of the ligament with thickness ~ 150 nm is ~ 5.1 GPa. The predicted value is quite close to the value estimated from experimental results and Eq. 6-1 (~ 4.9 GPa).

However, as discussed in Section 5.5, the homogenous deformation generally

occurs in nanoscale metallic glass under a critical size, by stress-induced glass transition under sufficiently high stress condition over the iso-viscosity contours of low viscosity ($< \sim 10^{12}$ Pa·s). After achieving the steady-state homogeneous flow condition, the sample maintains a nearly-constant flow stress level and the flow stress is difficult to reach σ_{SB} which locates at extremely high stress level by sample size effect. As an exception from the trend, the ligament with considerably small size scale (~ 150 nm) in the metallic glass nanofoam exhibit the exceptionally high strength value and the evidence of local shear banding as shown in Figure 6.8 (a). This is attributed to the non-uniform stress distribution inside the foam structure even under uniaxial macroscopic strain. Figure 6.8 (b) is a finite element analysis¹⁶² result showing von Mises stress distribution at the onset of yielding inside nanoporous gold prepared by electrochemical dealloying which have an analogous ligament structure with the metallic glass nanofoam in this study. This revealed that only a small portion of the ligaments take the sufficiently high stress exceeding the uniaxial yield strength of bulk gold, due to the irregular structure of ligaments, and the stress is concentrated at the ligament necks. Similarly, for the case of the metallic glass nanofoam, the stress is also supposed to be concentrated in local volume of the ligaments. The local region under concentrated stress will be deformed by shear banding and may dominantly influence the (plastic-collapse) strength of the nanofoam, while the other region with less-concentrated stress will be deformed under homogeneous deformation regime resulting in a smooth stress-strain response without obvious serrations. For clarifying the statement above, finite element analysis using the 3-D microstructure model in Figure 3.9 will provide the fruitful information on deformation of the metallic glass nanofoam, which remains for future works.

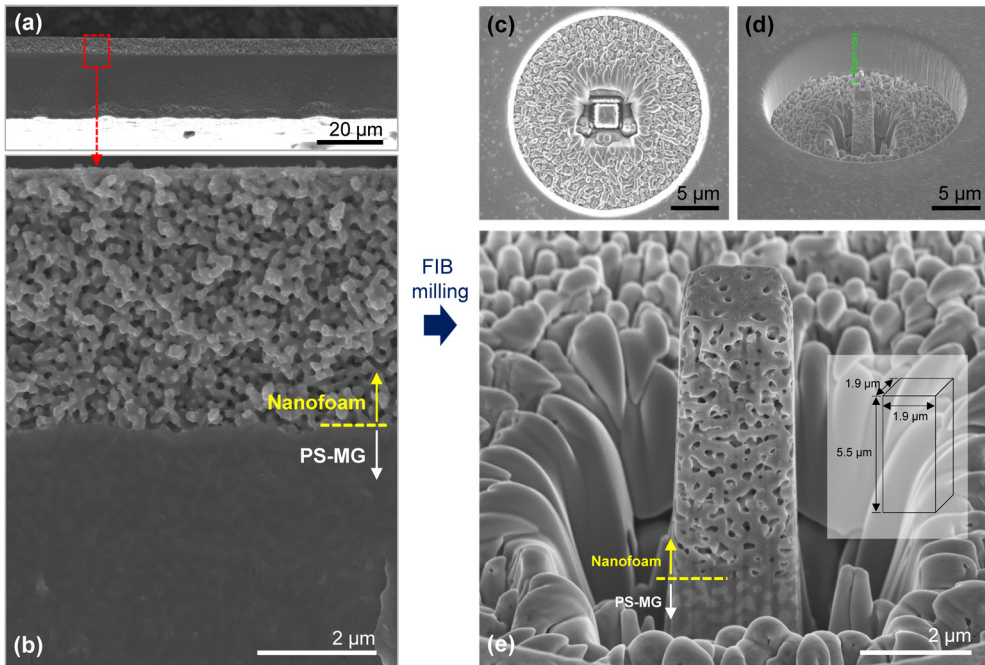


Figure 6.4. Fabrication of a nanoporous metallic glass micropillar from $Y_{19}Ti_{36}Al_{25}Co_{20}$ precursor alloy. **(a-b)** SEM images of the partially-dealloyed precursor alloy for micropillar fabrication. **(c-e)** SEM images after ion beam milling for micropillar fabrication. **(c)** upper view. **(d)** lateral view in low magnification. **(e)** lateral view in higher magnification with tilt angle ~ 52 degrees.

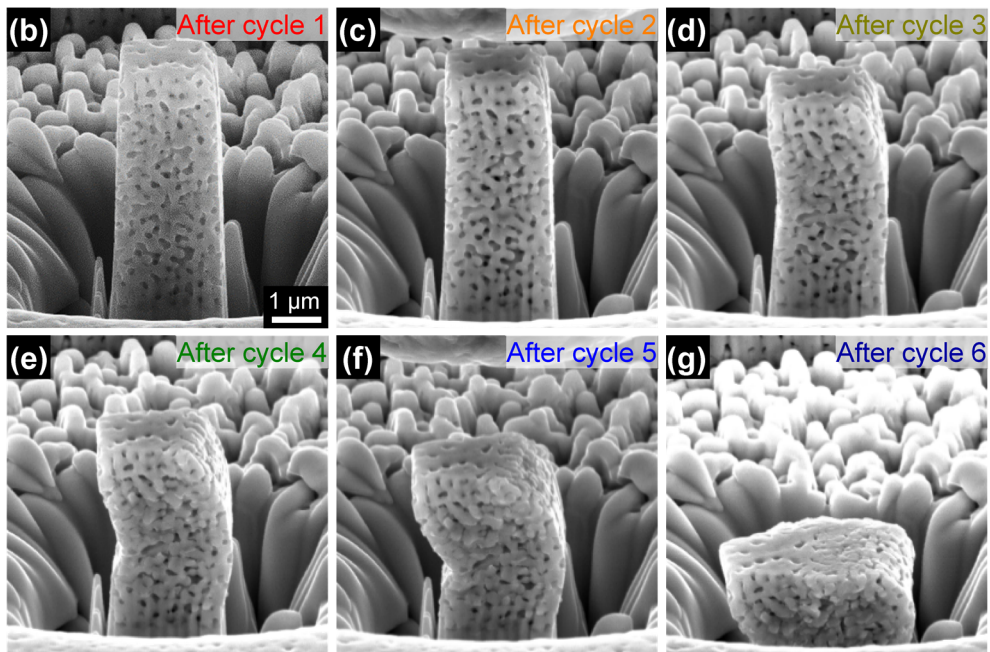
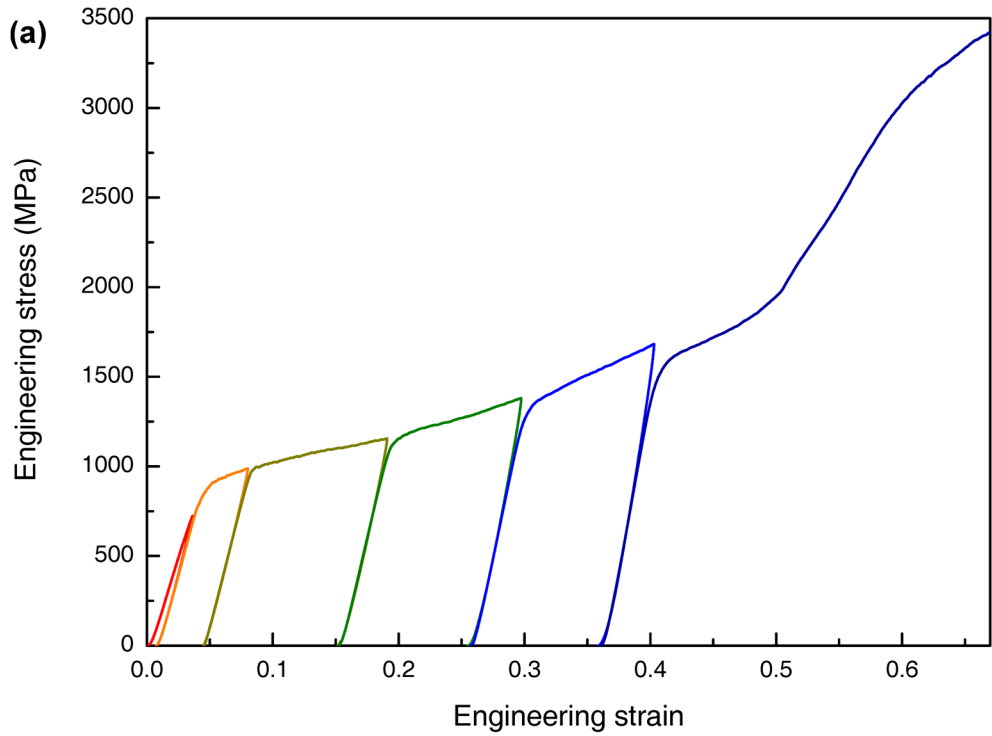


Figure 6.5. Compressive deformation of a nanoporous metallic glass micropillar. (a) Engineering stress-strain curve. (b-g) SEM images observed after each corresponding loading-unloading cycle.

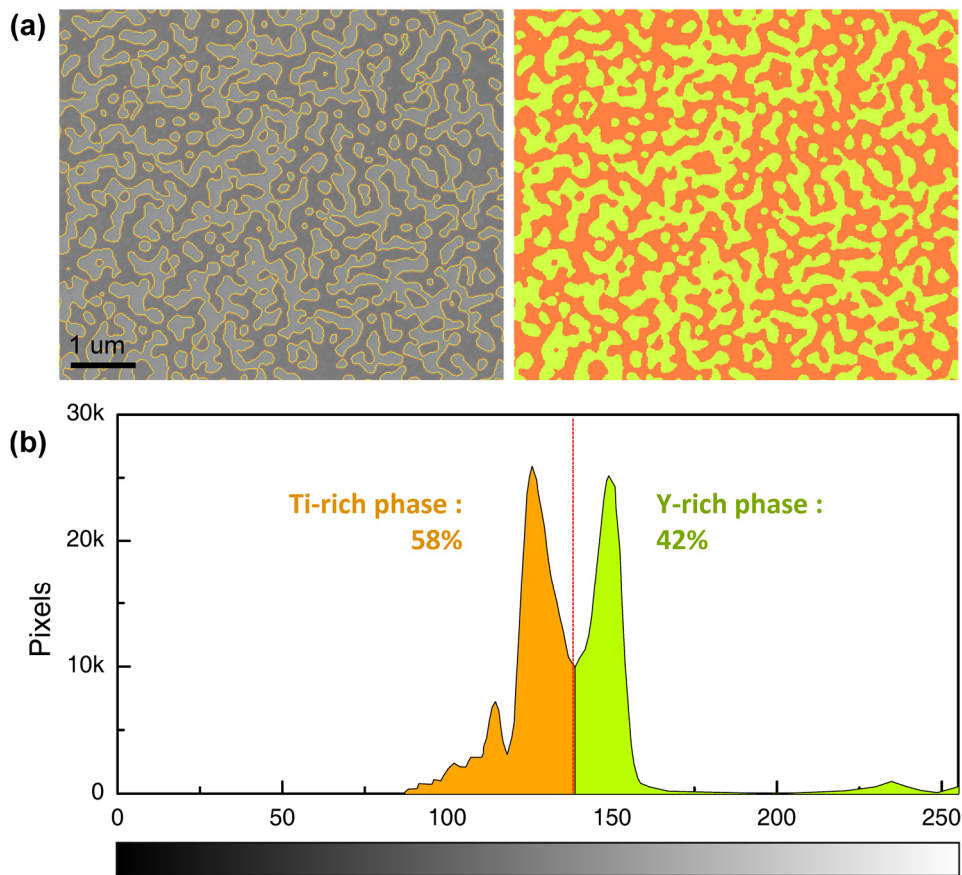


Figure 6.6. Image analysis for the estimation of relative density of metallic glass nanofoam. **(a)** SEM images of $Y_{19}Ti_{36}Al_{25}Co_{20}$ precursor alloy with the boundary of contrast threshold between two amorphous phases. **(b)** Contrast spectrum in the image of (a)

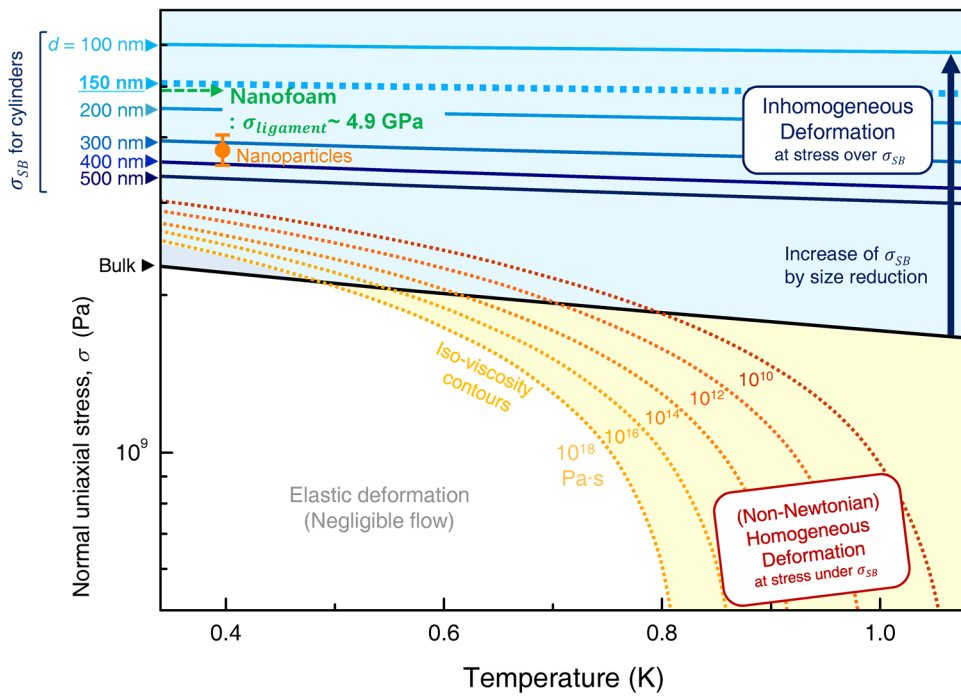


Figure 6.7. An enlarged part of the deformation map for metallic glass, with the critical stress (σ_{SB}) curves for shear banding depending on sample diameter in the case of cylindrical sample.

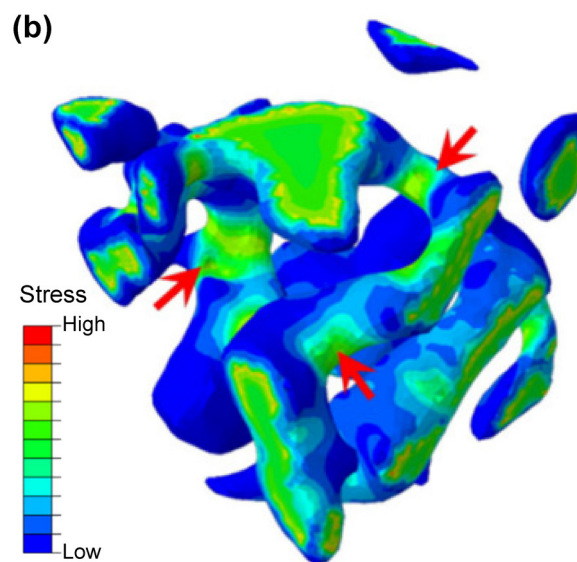
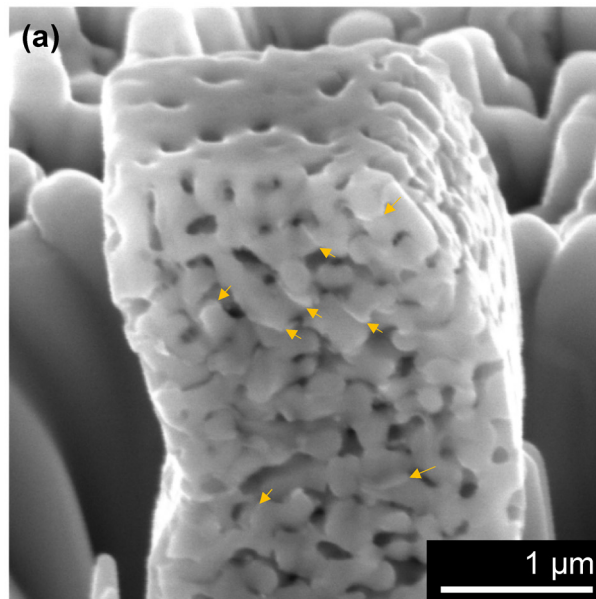


Figure 6.8. (a) SEM image of nanoporous metallic glass pillar after unloading from applied macroscopic strains of $\sim 30\%$. (b) von Mises stress distribution inside nanoporous gold at the onset of yielding, analyzed by finite element modeling. Arrows denotes the region of stress concentration. (b) is recomposed from ref. ¹⁶² with permission through “Copyright Clearance Center”.

6.3. Ligament size effect on hardness of metallic glass nanofoams

The influence of ligament size on the ligament strength in metallic glass nanofoam was indirectly estimated by the size-dependent strength of cylindrical metallic glass samples in previous section. The increase of ligament strength will lead spontaneously to stronger metallic glass nanofoam, as quantitatively expressed in Eq. 6-1. In order to confirm this trend experimentally, the hardness of metallic glass nanofoam depending on its ligament size was investigated by nanoindentation test on the cross-section of the nanofoam ribbon.

Figure 6.9(a) shows a series of indents by nanoindentation tests using Berkovich-type diamond tip, on the cross-section of the ribbon. As discussed in Section 3.4., the ligament size of the nanofoam continuously changes depending on the distance from wheel side edge. Thus, a single indent of nanoindentation does not cover a region with uniform ligament size, but a region with ligament size gradient. The ligament size range in indents and corresponding hardness values are plotted in Figure 6.9 (b). A horizontal bar (orange) for each indentation data point denotes a ligament size range covered by a single indent, calculated from the connection of the result in Figure 3.15 and the image analysis of indent images as Figure 6.9 (a). The hardness of a metallic glass foam with the ligaments having the bulk scale strength (H_{bulk}) is estimated by an analogous relation to Eq. 6-1 assuming the linearity between hardness and strength,

$$\frac{H_{foam}}{H_{ligament}} = 0.23 \times (\rho_{rel})^{1.5} (1 + (\rho_{rel})^{0.5}) \quad . \quad \text{Eq. 6-3}$$

The bulk hardness of ligament ($H_{ligament,bulk} = 7.92$ GPa) was measured by the

nanoindentation test of Ti-Co-based metallic glass ribbon used in Chapter 5. The estimated value of H_{bulk} is 1.41 GPa, expressed with dotted horizontal line in Figure 6.9 (b). Figure 6.9 (b) shows that the hardness values of metallic glass nanofoam exceed the estimated H_{bulk} value, and have a clear trend of the hardness increase with decreasing the ligament size as expected from the deformation map (Figure 6.7) and the relation of Eq. 6-1. The results clearly suggest that the unique mechanical properties of nanoscale metallic glass can be transferred to the intrinsic properties of microscale materials (metallic glass nanofoams).

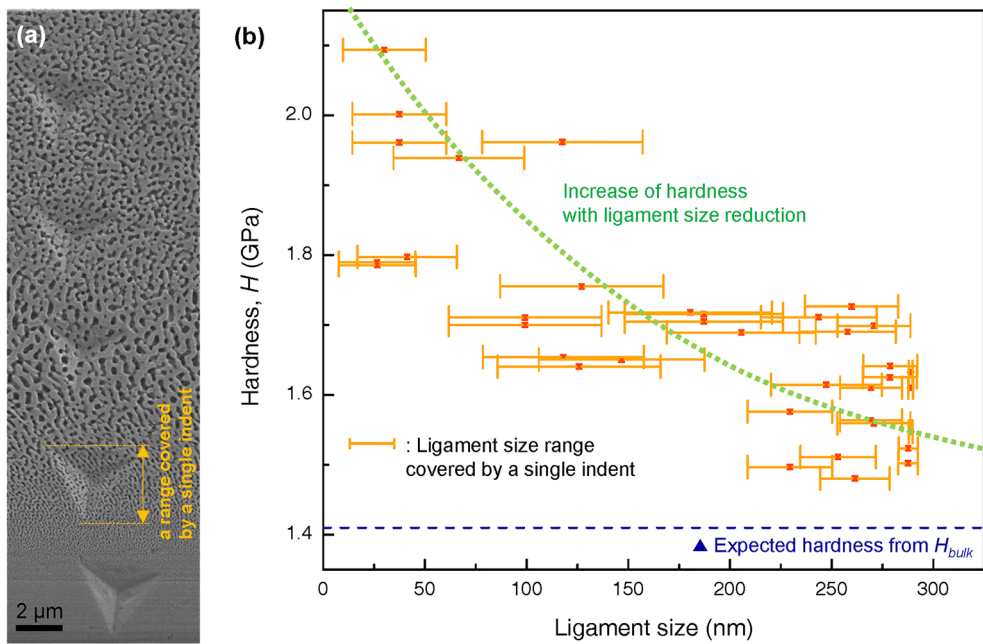


Figure 6.9. (a) SEM image of the indented cross-section of metallic glass nanofoam by nanoindentation technique. (b) Hardness of metallic glass nanofoam depending on the ligament size. Horizontal bars on data points shows the ligament size range covered by a single indent corresponding to each data point.

6.4. Deformation mode transition depending on ligament size

As well as the ligament size dependence on the hardness (or strength) of metallic glass nanofoam, the mode transition in ligament deformation behavior depending on the ligament size was investigated, through the compression tests of nanoporous metallic glass micropillars. Figure 6.10 shows the compression test results of three micropillars with different ligament sizes. Figure 6.10 (a) is the engineering stress-strain curves of the compressive deformation of the pillars. A slight increase of plastic-collapse strength with decreasing the ligament size of the nanofoam was observed, which corresponds to the results in the previous section. The absolute values of plastic-collapse strength in these three pillars are slightly lower than the result of Figure 6.5. This may be originated from the slight misalignment between the top surface of the pillars and the end surface of an indentation tip in the compression tests inside SEM, resulting in tensile strain components in local volume of the samples.

Regardless of the misorientation in compression direction, the surface morphology of the compressed pillars exhibits the difference in the deformation of ligaments. Figure 6.10 (b-d) shows the changes of the entire pillars before and after compression, and Figure 6.10 (e-g) is the enlarged views of the deformed pillars. The compressed pillar with a relatively large average size of ligament ($d_{\text{ligament}} \sim 270$ nm) have a large number of shear-deformed regions with obvious shear banding, marked with yellow arrows in Figure 6.10 (e). By decreasing the ligament size, the number of shear banding region is evidently reduced in Figure 6.10 (f), and disappears in the deformed nanofoam with an average ligament size under ~ 100 nm as shown in Figure 6.10 (g). The trend reveals clear deformation mode transition

from obvious shear banding to dominantly homogeneous deformation manner, with ligament size reduction in metallic glass nanofoams even in microscale samples. The results also suggest that the unique deformation behavior of nanoscale metallic glass can be extended into the larger scale by designing novel metallic glass-based materials consisting of nanoscale metallic glasses as intrinsic scale components.

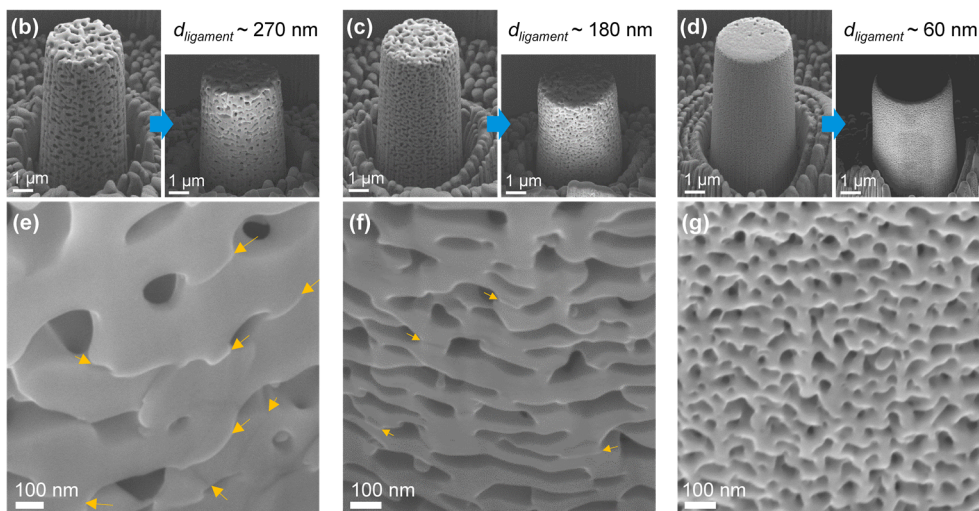
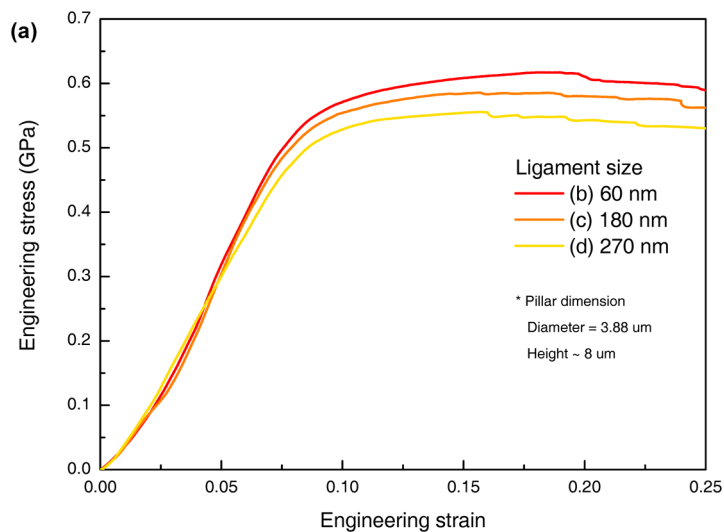


Figure 6.10. (a) Engineering compressive stress-strain curves of nanoporous metallic glass micropillar with different ligament sizes. (b-d) SEM images of the pillars before and after compressive deformation, with average ligament sizes of $\sim 270 \text{ nm}$ (b), $\sim 180 \text{ nm}$ (c), $\sim 60 \text{ nm}$ (d). (e-g) Magnified surface morphology of the compressed pillars with average ligament sizes of $\sim 270 \text{ nm}$ (e), $\sim 180 \text{ nm}$ (f), $\sim 60 \text{ nm}$ (g).

6.5. Summary

The unique mechanical properties of nanoscale metallic glasses have a limitation for structural application due to their extremely small size scale. To overcome this drawback, the strategies of transferring the properties of nanoscale metallic glass to the intrinsic properties of materials with larger scale have been suggested by the developments of metallic glass-based materials with architected or hierarchical structure. As a candidate of the novel metallic-glass-based materials, metallic glass nanofoams is suggested in this study.

In this chapter, the compressive deformation behaviors of metallic glass nanofoams were investigated through the micropillar compression tests and nanoindentation tests of the sample prepared by the dealloying of Y-Ti-Al-Co precursor ribbon. The plastic-collapse strength (σ_{pl}^*) in the compression test results of the nanoporous metallic glass micropillar samples reveals that the nanoscale ligament in the sample have size-dependent strength variation as predicted in the deformation map of metallic glass suggested in Chapter 5. From the increased ligament strength in smaller metallic glass ligaments, the hardness of the metallic glass nanofoam also exhibit a clear trend of hardness increase with ligament size reduction. In addition to the ligament size effect on the strength (or hardness), the metallic glass nanofoam shows clear deformation mode transition from obvious shear banding to homogeneous deformation with ligament size reduction even in microscale nanofoam samples. The results suggest that the unique deformation behavior of nanoscale metallic can be applied to extended scales by designing metallic glass-based materials with multi-scale structure such as nanofoams consisting of nanoscale metallic glasses as intrinsic scale components.

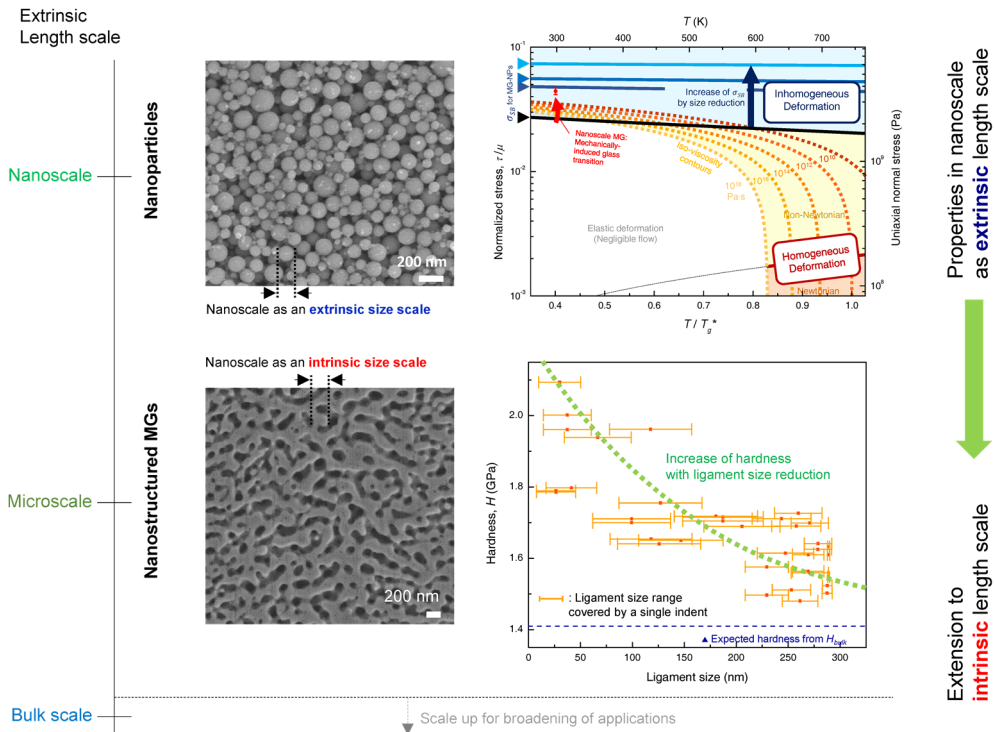


Figure 6.11. A diagram showing the transference of the excellent mechanical properties of nanoscale metallic glass to intrinsic scale properties in the extended scale materials (such as metallic glass nanofoam).

Chapter 7.

Conclusions

The comprehensive investigations on the mechanical response of metallic glass nanoparticles and nanofoams were conducted in this study, in order to clarifying the origin of unique mechanical behaviors of nanoscale metallic glasses and extending their applications. In order to probe into genuine size effects on the deformation behaviors of metallic glass, nanomechanical studies using metallic glass specimens with a smooth and clean surface prepared by FIB-less process are necessary. In this aspect, metallic glass nanoparticles prepared by the dealloying process have great advantages of the exclusion of ion irradiation effect and near-perfectly spherical morphology minimizing surface flaws. Their wide size distribution in a few tens ~ hundreds nanometer scale is also useful for investigating the size-dependent behavior of nanoscale metallic glass.

The metallic glass nanoparticles and nanofoams handled in this study were prepared through the dealloying process of phase-separating metallic glass precursors. The microstructures of the precursor alloys significantly influence the morphology of products extracted by dealloying process. The precise control of alloy composition and cooling rate based on thermodynamic assessments enables to fabricate phase separating metallic glass precursors with a proper size distribution of secondary phases for preparing metallic glass nanoparticles and nanofoams. From this, Ti-based metallic glass nanoparticles and nanofoam samples were fabricated by dealloying of (Y,Gd)-Ti-Al-Co phase separating metallic glass precursors with

droplet-structure and interconnected structure, respectively.

The compressive deformation behaviors of the metallic glass nanoparticles prepared by the dealloying process were systematically investigated by *in situ* compression tests inside scanning electron microscope. The results followed by intensive analysis based on contact mechanics suggests that the stress distribution inside the compressed particle changes from highly concentrated state at near contact center to uniformly distributed state during the increase of strain. Then, interestingly, the metallic glass particle exhibit steady-state plastic flow with nearly-constant flow stress at the plastic-dominant stage with high strain condition. Through the estimation of the critical stress for shear banding using the extended relation analogous to the Griffith's crack equation, the steady-state plastic flow at high strain condition is confirmed to be the homogeneous deformation by the activation of distributed shear transformation zones in entire sample volume rather than inhomogeneous shear banding. The flow stress and viscosity dependence on strain rate in metallic glass nanoparticles reveals the steady-state homogeneous flow of the particles obviously follow non-Newtonian flow behavior regardless of sample sizes.

In order to elucidate the origin of the non-Newtonian homogeneous flow behavior of nanoscale metallic glasses, a new format of the deformation map for metallic glasses is constructed, which covers the size-dependent mechanical behaviors of metallic glasses. The deformation map is composed of the combination of three components; (1) the boundary between Newtonian and non-Newtonian behavior, (2) the iso-viscosity contours based on the stress-temperature scaling relation and (3) the critical stress curves for shear localization depending on the size of metallic glass samples, in a stress-temperature space. The correlations among the boundaries in the deformation map provide the illuminating insight on the

deformation of metallic glass. The notable findings based on the novel deformation maps are (i) the detectable homogeneous deformation of nanoscale metallic glass at room temperature originates from the continuous viscosity decrease induced by shear stress into under $\sim 10^{12}$ Pa·s (“mechanically-induced glass transition”) and (ii) the detectable homogeneous deformation of nanoscale metallic glass at room temperature with GPa-scale flow stress have only non-Newtonian flow characteristic.

These unique mechanical properties of nanoscale metallic glasses have a limitation for structural application due to their extremely small size scale. To overcome this drawback, the properties of nanoscale metallic glasses can be transferred to the intrinsic properties of materials with larger scale, such as metallic glass-based materials with architected or hierarchical structure. As a candidate of the novel metallic-glass-based materials, metallic glass nanofoams is suggested in this study. The results suggest that the unique deformation behavior of nanoscale metallic glass can be applied to extended scales by designing metallic glass-based materials with multi-scale structure such as nanofoams consisting of nanoscale metallic glasses as intrinsic scale components.

Lastly, from the comprehensive investigations on the mechanical response of nanoscale metallic glasses in this study, the comprehensible answers to questions presented in Sections 1.4 are suggested as follow:

Q1) Is the homogeneous deformation of nanoscale metallic glasses at room temperature induced dominantly by the influence of sample preparation methods, such as ion irradiation effect and surface roughness?

► The homogeneous deformation at room temperature can occur in the metallic glass nanoparticles which can exclude the effect of ion irradiation and surface

roughness from their FIB-less preparation method and a nearly-perfect spherical morphology formed by interfacial energy on liquid-liquid interface during cooling from the melt state, respectively. Certainly, the sample preparation methods can significantly affect the mechanical behaviors of nanoscale metallic glass, while those are not neither a sole or dominant origin of the exceptional deformation behavior of nanoscale metallic glass

Q2) Can the nanoscale metallic glasses at room temperature flow as the high-temperature supercooled liquid state, through homogeneous deformation? If there is a difference, what is the main difference in the flow characteristics of both states?

► The homogeneous deformation of nanoscale metallic glass at room temperature and GPa-scale stress follow only non-Newtonian flow characteristic, while the high-temperature supercooled liquid state have the transition between Newtonian and non-Newtonian behavior depending on strain rate.

Q3) How can the internal state of nanoscale metallic glasses suffering homogeneous deformation be described qualitatively or quantitatively?

► The internal state during homogeneous deformation can be expressed quantitatively by viscosity. The viscosity of a nanoscale metallic glass (e.g. metallic glass nanoparticle) undergoing detectable homogeneous deformation is well below $\sim 10^{12}$ Pa·s. Thus, the homogeneous deformation at room temperature can be considered as viscous flow activated by mechanically-induced glass transition.

Q4) What is the scientific signification of the stress required for homogeneous deformation of nanoscale metallic glass at room temperature? Does it remain

constant independent to sample size?

► Strictly speaking, the homogeneous deformation of metallic glass at room temperature initiate even at low stress, but it cannot be detected due to extremely low deformation rate (strain rate). If the sufficiently high stress is given, the nanoscale metallic glass can undergo mechanically-induced glass transition throughout the whole sample volume without shear banding. In this situation, the detectable homogeneous deformation takes place and its steady-state flow stress is investigated to be nearly-independent to sample size and strain rate, related to its non-Newtonian characteristic.

Q5) How can the exceptional mechanical properties of nanoscale metallic glasses be applied to the materials in larger scale for extended applications?

► The unique mechanical properties of nanoscale metallic glasses can be transferred to the intrinsic properties of materials with larger scale, as suggested with metallic glass nanofoams in this study. In other words, the exceptional deformation behavior of nanoscale metallic glass can be applied to extended scales by designing metallic glass-based materials with multi-scale structure consisting of nanoscale metallic glasses as intrinsic scale components.

Bibliography

1. Greer, A. L. & Ma, E. Bulk metallic glasses: At the cutting edge of metals research. *MRS Bull.* **32**, 611-619 (2007).
2. Greer, A. L., Cheng, Y. Q. & Ma, E. Shear bands in metallic glasses. *Mater. Sci. Eng. R* **74**, 71-132 (2013).
3. Klement, W., Willens, R. H. & Duwez, P. O. L. Non-crystalline structure in solidified gold-silicon alloys. *Nature* **187**, 869-870 (1960).
4. Park, E. S., Ryu, C. W., Kim, W. T. & Kim, D. H. A novel parameter to describe the glass-forming ability of alloys. *J. Appl. Phys.* **118**, 064902 (2015).
5. Yavari, A. R., Lewandowski, J. J. & Eckert, J. Mechanical properties of bulk metallic glasses. *MRS Bull.* **32**, 635-638 (2007).
6. Kruzic, J. J. Bulk metallic glasses as structural materials: A review. *Adv. Eng. Mater.*, In press. (2016).
7. Ritchie, R. O. The conflicts between strength and toughness. *Nature Mater.* **10**, 817-822 (2011).
8. Demetriou, M. D. *et al.* A damage-tolerant glass. *Nature Mater.* **10**, 123-128 (2011).
9. Schuh, C. A., Hufnagel, T. C. & Ramamurty, U. Mechanical behavior of amorphous alloys. *Acta Mater.* **55**, 4067-4109 (2007).
10. Spaepen, F. A microscopic mechanism for steady state inhomogeneous flow in metallic glasses. *Acta Metall.* **25**, 407-415 (1977).
11. Argon, A. S. Plastic deformation in metallic glasses. *Acta Metall.* **27**, 47-58 (1979).
12. Bernal, J. D. A geometrical approach to the structure of liquids. *Nature* **183**, 141-147 (1959).
13. Cohen, M. H. & Turnbull, D. Molecular transport in liquids and glasses. *J. Chem. Phys.* **31**, 1164-1169 (1959).
14. Spaepen, F. Homogeneous flow of metallic glasses: A free volume perspective. *Scripta Mater.* **54**, 363-367 (2006).
15. Yang, B., Wadsworth, J. & Nieh, T.-G. Thermal activation in Au-based bulk metallic glass characterized by high-temperature nanoindentation. *Appl. Phys. Lett.* **90**, 061911 (2007).

16. Falk, M. L. & Langer, J. S. Dynamics of viscoplastic deformation in amorphous solids. *Phys. Rev. E* **57**, 7192-7205 (1998).
17. Heggen, M., Spaepen, F. & Feuerbacher, M. Creation and annihilation of free volume during homogeneous flow of a metallic glass. *J. Appl. Phys.* **97**, 033506 (2005).
18. Argon, A. S. & Kuo, H. Y. Plastic flow in a disordered bubble raft (an analog of a metallic glass). *Mater. Sci. Eng.* **39**, 101-109 (1979).
19. Srolovitz, D., Vitek, V. & Egami, T. An atomistic study of deformation of amorphous metals. *Acta Metall.* **31**, 335-352 (1983).
20. Falk, M. L. Molecular-dynamics study of ductile and brittle fracture in model noncrystalline solids. *Phys. Rev. B* **60**, 7062-7070 (1999).
21. Choi, I.-C. *et al.* Estimation of the shear transformation zone size in a bulk metallic glass through statistical analysis of the first pop-in stresses during spherical nanoindentation. *Scripta Mater.* **66**, 923-926 (2012).
22. Choi, I.-C. *et al.* Indentation size effect and shear transformation zone size in a bulk metallic glass in two different structural states. *Acta Mater.* **60**, 6862-6868 (2012).
23. Ma, Y., Ye, J. H., Peng, G. J., Wen, D. H. & Zhang, T. H. Nanoindentation study of size effect on shear transformation zone size in a Ni-Nb metallic glass. *Mater. Sci. Eng. A* **627**, 153-160 (2015).
24. Pan, D., Inoue, A., Sakurai, T. & Chen, M. W. Experimental characterization of shear transformation zones for plastic flow of bulk metallic glasses. *Proc. Natl. Acad. Sci.* **105**, 14769-14772 (2008).
25. Qiao, J. C. & Pelletier, J. M. Dynamic mechanical relaxation in bulk metallic glasses: A review. *J. Mater. Sci. Tech.* **30**, 523-545 (2014).
26. Nieh, T. G. & Wadsworth, J. Homogeneous deformation of bulk metallic glasses. *Scripta Mater.* **54**, 387-392 (2006).
27. Schroers, J. Processing of bulk metallic glass. *Adv. Mater.* **22**, 1566-1597 (2010).
28. Lu, J., Ravichandran, G. & Johnson, W. L. Deformation behavior of the $Zr_{41.2}Ti_{13.8}Cu_{12.5}Ni_{10}Be_{22.5}$ bulk metallic glass over a wide range of strain-rates and temperatures. *Acta Mater.* **51**, 3429-3443 (2003).
29. Steif, P. S., Spaepen, F. & Hutchinson, J. W. Strain localization in amorphous metals. *Acta Metall.* **30**, 447-455 (1982).
30. Tian, L., Wang, X.-L. & Shan, Z.-W. Mechanical behavior of micronanoscaled metallic glasses. *Mater. Res. Lett.*, 1-12 (2016).

31. Sun, Y., Concustell, A. & Greer, A. L. Thermomechanical processing of metallic glasses: extending the range of the glassy state. *Nature Rev. Mater.*, 16039 (2016).
32. Kimura, H. & Masumoto, T. A model of the mechanics of serrated flow in an amorphous alloy. *Acta Metall.* **31**, 231-240 (1983).
33. Qiao, J., Jia, H. & Liaw, P. K. Metallic glass matrix composites. *Mater. Sci. Eng. R* **100**, 1-69 (2016).
34. Shimizu, F., Ogata, S. & Li, J. Yield point of metallic glass. *Acta Mater.* **54**, 4293-4298 (2006).
35. Ogata, S., Shimizu, F., Li, J., Wakeda, M. & Shibutani, Y. Atomistic simulation of shear localization in Cu–Zr bulk metallic glass. *Intermetallics* **14**, 1033-1037 (2006).
36. Klaumünzer, D., Maaß, R. & Löffler, J. F. Stick-slip dynamics and recent insights into shear banding in metallic glasses. *J. Mater. Res.* **26**, 1453-1463 (2011).
37. Matthews, D. T. A., Ocelík, V., Bronsveld, P. M. & De Hosson, J. T. M. An electron microscopy appraisal of tensile fracture in metallic glasses. *Acta Mater.* **56**, 1762-1773 (2008).
38. Liu, C. T. *et al.* Test environments and mechanical properties of Zr-base bulk amorphous alloys. *Metall and Mat Trans A* **29**, 1811-1820 (1998).
39. Lewandowski, J. J. & Greer, A. L. Temperature rise at shear bands in metallic glasses. *Nature Mater.* **5**, 15-18 (2006).
40. Yang, B. *et al.* In-situ thermographic observation of mechanical damage in bulk-metallic glasses during fatigue and tensile experiments. *Intermetallics* **12**, 1265-1274 (2004).
41. Spaepen, F. Metallic glasses: Must shear bands be hot? *Nature Mater.* **5**, 7-8 (2006).
42. Cheng, Y. Q., Han, Z., Li, Y. & Ma, E. Cold versus hot shear banding in bulk metallic glass. *Phys. Rev. B* **80**, 134115 (2009).
43. Maaß, R., Klaumünzer, D., Villard, G., Derlet, P. M. & Löffler, J. F. Shear-band arrest and stress overshoots during inhomogeneous flow in a metallic glass. *Appl. Phys. Lett.* **100**, 071904 (2012).
44. Maaß, R. & Löffler, J. F. Shear-band dynamics in metallic glasses. *Adv. Func. Mater.* **25**, 2353-2368 (2015).
45. Park, E. S. Understanding of the shear bands in amorphous metals. *Applied Microscopy* **45**, 63-73 (2015).

46. Conner, R. D., Johnson, W. L., Paton, N. E. & Nix, W. D. Shear bands and cracking of metallic glass plates in bending. *J. Appl. Phys.* **94**, 904-911 (2003).
47. Frost, H. J. & Ashby, M. F. *Deformation-Mechanism Maps: The Plasticity and Creep of Metals and Ceramics*. (Pergamon Press, Oxford, 1982).
48. Ashby, M. F. A first report on deformation-mechanism maps. *Acta Metall.* **20**, 887-897 (1972).
49. Megusar, J., Argon, A. S. & Grant, N. J. Plastic flow and fracture in Pd80Si20 near T_g. *Mater. Sci. Eng.* **38**, 63-72 (1979).
50. Schuh, C. A., Lund, A. C. & Nieh, T. G. New regime of homogeneous flow in the deformation map of metallic glasses: elevated temperature nanoindentation experiments and mechanistic modeling. *Acta Mater.* **52**, 5879-5891 (2004).
51. Johnson, W. L. & Samwer, K. A universal criterion for plastic yielding of metallic glasses with a $(T/T_g)^{2/3}$ temperature dependence. *Phys. Rev. Lett.* **95**, 195501 (2005).
52. Greer, J. R. & Nix, W. D. Nanoscale gold pillars strengthened through dislocation starvation. *Phys. Rev. B* **73**, 245410 (2006).
53. Weinberger, C. R. & Cai, W. Surface-controlled dislocation multiplication in metal micropillars. *Proc. Natl. Acad. Sci.* **105**, 14304-14307 (2008).
54. Wang, C. C. *et al.* Sample size matters for Al₈₈Fe₇Gd₅ metallic glass: Smaller is stronger. *Acta Mater.* **60**, 5370-5379 (2012).
55. Jang, D. & Greer, J. R. Transition from a strong-yet-brittle to a stronger-and-ductile state by size reduction of metallic glasses. *Nature Mater.* **9**, 215-219 (2010).
56. Jang, D., Gross, C. T. & Greer, J. R. Effects of size on the strength and deformation mechanism in Zr-based metallic glasses. *Int. J. Plasticity* **27**, 858-867 (2011).
57. Guo, H. *et al.* Tensile ductility and necking of metallic glass. *Nature Mater.* **6**, 735-739 (2007).
58. Volkert, C. A., Donohue, A. & Spaepen, F. Effect of sample size on deformation in amorphous metals. *J. Appl. Phys.* **103**, 083539 (2008).
59. Tian, L., Shan, Z.-W. & Ma, E. Ductile necking behavior of nanoscale metallic glasses under uniaxial tension at room temperature. *Acta Mater.* **61**, 4823-4830 (2013).
60. Bharathula, A., Lee, S.-W., Wright, W. J. & Flores, K. M. Compression

- testing of metallic glass at small length scales: Effects on deformation mode and stability. *Acta Mater.* **58**, 5789-5796 (2010).
61. Lai, Y. H. *et al.* Bulk and microscale compressive behavior of a Zr-based metallic glass. *Scripta Mater.* **58**, 890-893 (2008).
 62. Schuster, B. E., Wei, Q., Hufnagel, T. C. & Ramesh, K. T. Size-independent strength and deformation mode in compression of a Pd-based metallic glass. *Acta Mater.* **56**, 5091-5100 (2008).
 63. Tian, L. *et al.* Approaching the ideal elastic limit of metallic glasses. *Nature Commun.* **3**, 609 (2012).
 64. Kuzmin, O. V., Pei, Y. T., Chen, C. Q. & De Hosson, J. T. M. Intrinsic and extrinsic size effects in the deformation of metallic glass nanopillars. *Acta Mater.* **60**, 889-898 (2012).
 65. Dubach, A., Raghavan, R., Löffler, J. F., Michler, J. & Ramamurty, U. Micropillar compression studies on a bulk metallic glass in different structural states. *Scripta Mater.* **60**, 567-570 (2009).
 66. Chen, C. Q., Pei, Y. T. & De Hosson, J. T. M. Apparently homogeneous but intrinsically intermittent flow of taper-free metallic glass nanopillars. *Scripta Mater.* **67**, 947-950 (2012).
 67. Yavari, A. R., Georgarakis, K., Botta, W. J., Inoue, A. & Vaughan, G. Homogenization of plastic deformation in metallic glass foils less than one micrometer thick. *Phys. Rev. B* **82**, 172202 (2010).
 68. Shan, Z. W. *et al.* Plastic flow and failure resistance of metallic glass: Insight from in situ compression of nanopillars. *Phys. Rev. B* **77**, 155419 (2008).
 69. Chen, C. Q., Pei, Y. T. & De Hosson, J. T. M. Effects of size on the mechanical response of metallic glasses investigated through in situ TEM bending and compression experiments. *Acta Mater.* **58**, 189-200 (2010).
 70. Chen, D. Z., Gu, X. W., An, Q., Goddard, W. A. & Greer, J. R. Ductility and work hardening in nano-sized metallic glasses. *Appl. Phys. Lett.* **106**, 061903 (2015).
 71. Chen, D. Z. *et al.* Nanometallic glasses: Size reduction brings ductility, surface state drives its extent. *Nano Lett.* **13**, 4462-4468 (2013).
 72. Magagnosc, D. J. *et al.* Effect of ion irradiation on tensile ductility, strength and fictive temperature in metallic glass nanowires. *Acta Mater.* **74**, 165-182 (2014).
 73. Adibi, S. *et al.* Surface roughness imparts tensile ductility to nanoscale metallic glasses. *Extreme Mech. Lett.* **5**, 88-95 (2015).

74. Kim, D. H., Kim, W. T., Park, E. S., Mattern, N. & Eckert, J. Phase separation in metallic glasses. *Prog. Mater. Sci.* **58**, 1103-1172 (2013).
75. Chou, C. P. P. & Spaepen, F. Some mechanical properties of phase separated Pd_{0.74}Au_{0.08}Si_{0.38} metallic glasses. *Acta Metall.* **23**, 609-613 (1975).
76. Krebs, H. U., Webb, D. J. & Marshall, A. F. Phase separation in amorphous Fe-Zr: Comparison of sputtered and solid-state-reacted films. *Phys. Rev. B* **35**, 5392-5395 (1987).
77. Okumura, H., Inoue, A. & Masumoto, T. Heating rate dependence of two glass transitions and phase separation for a La₅₅Al₂₅Ni₂₀ amorphous alloy. *Acta Metall. Mater.* **41**, 915-921 (1993).
78. Schneider, S., Thiyagarajan, P. & Johnson, W. L. Formation of nanocrystals based on decomposition in the amorphous Zr_{41.2}Ti_{13.8}Cu_{12.5}Ni₁₀Be_{22.5} alloy. *Appl. Phys. Lett.* **68**, 493-495 (1996).
79. Busch, R., Schneider, S., Peker, A. & Johnson, W. L. Decomposition and primary crystallization in undercooled Zr_{41.2}Ti_{13.8}Cu_{12.5}Ni_{10.0}Be_{22.5} melts. *Appl. Phys. Lett.* **67**, 1544-1546 (1995).
80. Hays, C. C., Kim, C. P. & Johnson, W. L. Large supercooled liquid region and phase separation in the Zr-Ti-Ni-Cu-Be bulk metallic glasses. *Appl. Phys. Lett.* **75**, 1089-1091 (1999).
81. Han, J. H., Mattern, N., Kim, D. H. & Eckert, J. Phase separation and microstructure evolution of rapidly quenched Gd-Hf-Co-Al alloys. *J. Alloy Compd.* **509**, Supplement 1, S42-S45 (2011).
82. Mattern, N. *et al.* Phase separation in Cu₄₆Zr_{47-x}Al₇Gd_x metallic glasses. *J. Alloy Compd.* **509**, Supplement 1, S23-S26 (2011).
83. Sohn, S. W., Yook, W., Kim, W. T. & Kim, D. H. Phase separation in bulk-type Gd-Zr-Al-Ni metallic glass. *Intermetallics* **23**, 57-62 (2012).
84. Mattern, N. *et al.* Phase separation in Ni-Nb-Y metallic glasses. *J. Alloy Compd.* **495**, 299-304 (2010).
85. Chang, H. J., Park, E. S. & Kim, D. H. Nano-scale shell in phase separating Gd-Ti-Al-Co metallic glass. *Applied microscopy* **43**, 98-101 (2013).
86. Han, J. H. *et al.* Phase separation in Zr_{56-x}Gd_xCo₂₈Al₁₆ metallic glasses (0 ≤ x ≤ 20). *Acta Mater.* **66**, 262-272 (2014).
87. Park, B. J. *et al.* Phase separating bulk metallic glass: A hierarchical composite. *Phys. Rev. Lett.* **96**, 245503 (2006).
88. Park, E. S. *et al.* In situ formation of two glassy phases in the Nd-Zr-Al-Co alloy system. *Scripta Mater.* **56**, 197-200 (2007).

89. Kündig, A. A., Ohnuma, M., Ping, D. H., Ohkubo, T. & Hono, K. In situ formed two-phase metallic glass with surface fractal microstructure. *Acta Mater.* **52**, 2441-2448 (2004).
90. Park, E. S. & Kim, D. H. Phase separation and enhancement of plasticity in Cu–Zr–Al–Y bulk metallic glasses. *Acta Mater.* **54**, 2597-2604 (2006).
91. Inoue, A. Stabilization of metallic supercooled liquid and bulk amorphous alloys. *Acta Mater.* **48**, 279-306 (2000).
92. Park, B. J., Chang, H. J., Kim, D. H. & Kim, W. T. In situ formation of two amorphous phases by liquid phase separation in Y–Ti–Al–Co alloy. *Appl. Phys. Lett.* **85**, 6353-6355 (2004).
93. Mattern, N. *et al.* Spinodal decomposition of Ni–Nb–Y metallic glasses. *Acta Mater.* **57**, 903-908 (2009).
94. Chang, H. J., Yook, W., Park, E. S., Kyeong, J. S. & Kim, D. H. Synthesis of metallic glass composites using phase separation phenomena. *Acta Mater.* **58**, 2483-2491 (2010).
95. Han, J. H., Mattern, N., Schwarz, B., Kim, D. H. & Eckert, J. Phase separation and magnetic properties in Gd–(Hf,Ti,Y)–Co–Al metallic glasses. *Scripta Mater.* **67**, 149-152 (2012).
96. Jayaraj, J., Fleury, E., Park, B. J., Kim, D. H. & Kim, W. T. Synthesis and characterization of nanometer-sized Ti-based amorphous powders. *J. Mater. Res.* **22**, 1754-1758 (2007).
97. Jayaraj, J., Park, B. J., Kim, D. H., Kim, W. T. & Fleury, E. Nanometer-sized porous Ti-based metallic glass. *Scripta Mater.* **55**, 1063-1066 (2006).
98. Wada, T., Louzguine-Luzgin, D. V. & Inoue, A. Preparation of Zr-based metallic glass nanowires and nanoparticles by selective etching. *Scripta Mater.* **57**, 901-904 (2007).
99. Lupis, C. H. P. *Chemical thermodynamics of materials*. (North-Holland, 1983).
100. Hancock, H. *Theory of Maxima and Minima*. (Ginn, 1917).
101. Redlich, O. & Kister, A. T. Algebraic representation of thermodynamic properties and the classification of solutions. *Industrial & Engineering Chemistry* **40**, 345-348 (1948).
102. Cahn, J. W. Phase separation by spinodal decomposition in isotropic systems. *J. Chem. Phys.* **42**, 93-99 (1965).
103. Perrière, L. *et al.* Spark plasma sintering for metallic glasses processing. *Rev. Metall.* **109**, 5-10 (2012).

104. Liu, L. H. *et al.* Densification mechanism of Ti-based metallic glass powders during spark plasma sintering process. *Intermetallics* **66**, 1-7 (2015).
105. Zhao, M., Abe, K., Yamaura, S.-i., Yamamoto, Y. & Asao, N. Fabrication of Pd–Ni–P metallic glass nanoparticles and their application as highly durable catalysts in methanol electro-oxidation. *Chem. Mater.* **26**, 1056-1061 (2014).
106. Wen, M. *et al.* Soft magnetic Co–Fe–B–P and Co–Fe–V–B–P amorphous alloy nano-particles prepared by aqueous chemical reduction. *J. Alloy Compd.* **417**, 245-249 (2006).
107. Miura, A., Dong, W., Yodoshi, N., Kawasaki, A. & Yanagimoto, K. Preparation of Mono-sized Fe-based Metallic Glass Micro Particles by Pulsated Orifice Ejection Method and Evaluation of the Particles. *J. Jpn. Soc. Powder Metall.* **56**, 9-17 (2009).
108. Kim, T.-S., Lee, J. K. & Bae, J. C. Devitrification behavior and mechanical property of Cu₅₄Ni₆Zr₂₂Ti₁₈ glass powders. *Mater. Lett.* **62**, 323-326 (2008).
109. Yaginuma, S., Nakajima, C., Kaneko, N., Yokoyama, Y. & Nakayama, K. S. Log-normal diameter distribution of Pd-based metallic glass droplet and wire. *Sci. Rep.* **5** (2015).
110. Wu, N. Q., Su, L. Z., Yuan, M. Y., Wu, J. M. & Li, Z. Z. Nano-sized amorphous Cu–Zr alloy particles prepared by mechanochemical reaction. *Mater. Sci. Eng. A* **257**, 357-360 (1998).
111. Brothers, A. H. & Dunand, D. C. Porous and Foamed Amorphous Metals. *MRS Bull.* **32**, 639-643 (2007).
112. Demetriou, M. D., Veazey, C., Harmon, J. S., Schramm, J. P. & Johnson, W. L. Stochastic metallic-glass cellular structures exhibiting benchmark strength. *Phys. Rev. Lett.* **101**, 145702 (2008).
113. Brothers, A. H. & Dunand, D. C. Ductile bulk metallic glass foams. *Adv. Mater.* **17**, 484-486 (2005).
114. Demetriou, M. D. *et al.* High porosity metallic glass foam: A powder metallurgy route. *Appl. Phys. Lett.* **91**, 161903 (2007).
115. Demetriou, M. D. *et al.* Yielding of metallic glass foam by percolation of an elastic buckling instability. *Adv. Mater.* **19**, 1957-1962 (2007).
116. Schroers, J., Veazey, C. & Johnson, W. L. Amorphous metallic foam. *Appl. Phys. Lett.* **82**, 370-372 (2003).
117. Qiu, K. & Ren, Y. Fabrication of porous bulk metallic glass. *J. Mater. Sci. Technol.* **21**, 788-790 (2005).

118. Brothers, A. H. & Dunand, D. C. Syntactic bulk metallic glass foam. *Appl. Phys. Lett.* **84**, 1108-1110 (2004).
119. Xie, G., Zhang, W., Louzguine-Luzgin, D. V., Kimura, H. & Inoue, A. Fabrication of porous Zr–Cu–Al–Ni bulk metallic glass by spark plasma sintering process. *Scripta Mater.* **55**, 687-690 (2006).
120. Takeuchi, A. I., Akihisa; Classification of bulk metallic glasses by atomic size difference, heat of mixing and period of constituent elements and its application to characterization of the main alloying element. *Mater. Trans.* **46**, 2817-2829 (2005).
121. Senkov, O. N. & Miracle, D. B. Effect of the atomic size distribution on glass forming ability of amorphous metallic alloys. *Mater. Res. Bull.* **36**, 2183-2198 (2001).
122. Uchic, M. D., Holzer, L., Inkson, B. J., Principe, E. L. & Munroe, P. Three-dimensional microstructural characterization using focused ion beam tomography. *MRS Bull.* **32**, 408-416 (2007).
123. Chang, H. J. *Plastic deformation behavior of metallic glasses with locally inhomogeneous structure* Ph.D. thesis, Graduate School, Yonsei University (2008).
124. Ellingham, H. J. T. Reciprobility of oxide and sulphides in metallurgical processes. *J. Soc. Chem. Ind.* **63**, 125-133 (1944).
125. Bose, S. *High Temperature Coatings*. (Butterworth-Heinemann, Amsterdam, 2007).
126. Magagnosc, D. J. *et al.* Tunable tensile ductility in metallic glasses. *Sci. Rep.* **3**, 1096 (2013).
127. Kawamura, Y., Nakamura, T., Kato, H., Mano, H. & Inoue, A. Newtonian and non-Newtonian viscosity of supercooled liquid in metallic glasses. *Mater. Sci. Eng. A* **304–306**, 674-678 (2001).
128. Kato, H., Kawamura, Y., Inoue, A. & Chen, H. S. Newtonian to non-Newtonian master flow curves of a bulk glass alloy Pd₄₀Ni₁₀Cu₃₀P₂₀. *Appl. Phys. Lett.* **73**, 3665-3667 (1998).
129. Busch, R., Bakke, E. & Johnson, W. L. Viscosity of the supercooled liquid and relaxation at the glass transition of the Zr_{46.75}Ti_{8.25}Cu_{7.5}Ni₁₀Be_{27.5} bulk metallic glass forming alloy. *Acta Mater.* **46**, 4725-4732 (1998).
130. Hertz, H. Ueber die Berührung fester elastischer Körper. *J. Reine Angew. Math.* **92**, 156–171 (1882).
131. Johnson, K. L. *Contact Mechanics*. (Cambridge University Press, 1987).

132. Mook, W. M. *et al.* Compressive stress effects on nanoparticle modulus and fracture. *Phys. Rev. B* **75**, 214112 (2007).
133. Antonyuk, S. *et al.* Energy absorption during compression and impact of dry elastic-plastic spherical granules. *Granul. Matter* **12**, 15-47 (2010).
134. Cheng, Y. Q. & Ma, E. Intrinsic shear strength of metallic glass. *Acta Mater.* **59**, 1800-1807 (2011).
135. Schuh, C. A. & Nieh, T. G. A nanoindentation study of serrated flow in bulk metallic glasses. *Acta Mater.* **51**, 87-99 (2003).
136. Packard, C. E. & Schuh, C. A. Initiation of shear bands near a stress concentration in metallic glass. *Acta Mater.* **55**, 5348-5358 (2007).
137. Zhang, Z. F., Zhang, H., Pan, X. F., Das, J. & Eckert, J. Effect of aspect ratio on the compressive deformation and fracture behaviour of Zr-based bulk metallic glass. *Phil. Mag. Lett.* **85**, 513-521 (2005).
138. Li, Q.-K. & Li, M. Atomic scale characterization of shear bands in an amorphous metal. *Appl. Phys. Lett.* **88**, 241903 (2006).
139. Li, Q.-K. & Li, M. Free volume evolution in metallic glasses subjected to mechanical deformation. *Mater. Trans.* **48**, 1816-1821 (2007).
140. Malkin, A. Y. & Isayev, A. I. in *Rheology Concepts, Methods, and Applications*, Ch. 3, (Elsevier, Oxford, 2012).
141. Dienes, G. J. & Klemm, H. F. Theory and application of the parallel plate plastometer. *J. Appl. Phys.* **17**, 458-471 (1946).
142. Fontana, E. A versatile parallel-plate viscometer for glass viscosity measurements to 1000 degrees C. *Am. Ceram. Soc. Bull.* **49**, 594-& (1970).
143. Martin, S. W. & Angell, C. A. On the glass transition and viscosity of phosphorus pentoxide. *The Journal of Physical Chemistry* **90**, 6736-6740 (1986).
144. Nieh, T. G., Wadsworth, J., Liu, C. T., Ohkubo, T. & Hirotsu, Y. Plasticity and structural instability in a bulk metallic glass deformed in the supercooled liquid region. *Acta Mater.* **49**, 2887-2896 (2001).
145. Guan, P., Chen, M. & Egami, T. Stress-temperature scaling for steady-state flow in metallic glasses. *Phys. Rev. Lett.* **104**, 205701 (2010).
146. Egami, T. Mechanical failure and glass transition in metallic glasses. *J. Alloy Compd.* **509S**, S82-S86 (2011).
147. Trouton, F. T. On the coefficient of viscous traction and its relation to that of viscosity. *Proc. R. Soc. London A* **77**, 426-440 (1906).

148. Suzuki, Y., Haimovich, J. & Egami, T. Bond-orientational anisotropy in metallic glasses observed by x-ray diffraction. *Phys. Rev. B* **35**, 2162-2168 (1987).
149. Tomida, T. & Egami, T. Molecular-dynamics study of structural anisotropy and anelasticity in metallic glasses. *Phys. Rev. B* **48**, 3048-3057 (1993).
150. Park, K.-W. *et al.* Elastostatically induced structural disordering in amorphous alloys. *Acta Mater.* **56**, 5440-5450 (2008).
151. Schuh, C. A. & Lund, A. C. Atomistic basis for the plastic yield criterion of metallic glass. *Nature Mater.* **2**, 449-452 (2003).
152. Zheng, K. *et al.* Electron-beam-assisted superplastic shaping of nanoscale amorphous silica. *Nature Commun.* **1**, 24 (2010).
153. Heo, J., Kim, S., Ryu, S. & Jang, D. Delocalized plastic flow in proton-irradiated monolithic metallic glasses. *Sci. Rep.* **6**, 23244 (2016).
154. Concustell, A., Méar, F. O., Suriñach, S., Baró, M. D. & Greer, A. L. Structural relaxation and rejuvenation in a metallic glass induced by shot-peening. *Phil. Mag. Lett.* **89**, 831-840 (2009).
155. Meng, F., Tsuchiya, K., II, S. & Yokoyama, Y. Reversible transition of deformation mode by structural rejuvenation and relaxation in bulk metallic glass. *Appl. Phys. Lett.* **101**, 121914 (2012).
156. Dmowski, W. *et al.* Structural rejuvenation in a bulk metallic glass induced by severe plastic deformation. *Acta Mater.* **58**, 429-438 (2010).
157. Ketov, S. V. *et al.* Rejuvenation of metallic glasses by non-affine thermal strain. *Nature* **524**, 200-203 (2015).
158. Greer, J. R. & De Hosson, J. T. M. Plasticity in small-sized metallic systems: Intrinsic versus extrinsic size effect. *Prog. Mater. Sci.* **56**, 654-724 (2011).
159. Lee, S.-W., Jafary-Zadeh, M., Chen, D. Z., Zhang, Y.-W. & Greer, J. R. Size effect suppresses brittle failure in hollow Cu₆₀Zr₄₀ metallic glass nanolattices deformed at cryogenic temperatures. *Nano Lett.* **15**, 5673-5681 (2015).
160. Gibson, L. J. & Ashby, M. F. *Cellular Solids: Structure and Properties*. (Cambridge University Press, 1999).
161. Brothers, A. H. & Dunand, D. C. Plasticity and damage in cellular amorphous metals. *Acta Mater.* **53**, 4427-4440 (2005).
162. Cho, H.-H., Chen-Wiegart, Y.-c. K. & Dunand, D. C. Finite element analysis of mechanical stability of coarsened nanoporous gold. *Scripta Mater.* **115**, 96-99 (2016).

Abstract in Korean

초 록

나노 스케일 비정질 합금의 제조 및 기계적 변형 거동 분석에 대한 연구

김진우

서울대학교 공과대학

재료공학부

비정질 합금의 크기를 나노스케일까지 축소시키면 벌크 크기 수준에서와는 다른 독특한 특성이 나타난다는 것이 최근 다수의 연구로부터 보고되었다. 특히, 비정질 합금은 크기 감소 효과에 의해 확연한 강도의 증가와 더불어 임계 크기 이하의 크기에서는 균일 변형에 의해 향상된 소성 변형능을 나타내는 것으로 알려져 있다. 일반적인 재료에서 강도의 증가는 소성변형능의 저하를 야기하기 때문에, 비정질 합금의 기계적 특성에서 나타나는 이러한 독특한 크기 효과는 활발한 연구의 대상이 되어 왔다. 하지만 기존 보고된 실험 결과들의 비일관성과 더불어 크기 효과에 의해 나타나는 기계적 특성에 대한 근본적 원인이 아직까지 명확히 알려져 있지 않기 때문에, 나노 스케일 비정질 합금의 기계적 특성에 대해서는 현재까지 논란의 여지가 남아 있다. 또한 크기 감소에 의해 나타나는 비정질 합금의 우수한 특성은 모순적으로 그 제한적인 크기로 인해 실제적인 응용이 어렵게 된다.

본 논문에서는, 나노 크기의 비정질 합금에서 나타나는 독특한 기계적 특성의 근원을 밝히고 이들의 응용을 확장할 수 있는 가능성을 제시하기 위하여, 비정질 합금 나노 입자와 나노 다공체를 제조하고 그 기계적 특성을 심도있게 분석하였다. 본 연구에서 시험한 비정질 합금 나노 입자와 나노 다공체는 이상분리 비정질 합금의 선택적 용해법을 통해 제조되었다. 제조 과정에서 전구체의 역할을 하는 이상분리 비정질 합금의 경우, 상분리 과정에 대한 열역학적 요소를 고려하여 합금 조성과 냉각 속도를 정밀 제어함으로써 그 미세구조를 제어할 수 있다. 이로부터, 나노 크기의 비정질 합금 입자와 다공체를 제조하기에 적합한 미세구조를 가지도록 제어된 이상분리 비정질 합금 전구체를 이용하여, 본 연구에서는 타이타늄계 비정질 합금 나노 입자와 나노 다공체를 제조하고 주사 전자 현미경 내에서의 나노 압축 시험을 통해 이들의 기계적 특성을 체계적으로 분석하였다.

표면 결함을 최소화하여 완전한 구형에 가까운 형태로 제조된 비정질 합금 나노 입자는 외적 요인(집속이온빔에 의한 부분 방사화 및 표면 결함 등)을 배제하고 순수하게 크기 효과에 의해 유발된 나노 스케일 비정질 합금의 변형 거동을 분석하기에 최적화된 소재라고 할 수 있다. 구형 입자는 일반적으로 1축 압축 시험을 통한 기계적 특성 분석에 널리 사용되지 않기 때문에, 입자의 압축 시험 결과는 일반적인 경우와 다르게 접촉 역학을 고려하여 면밀히 분석되었다. 실험적 결과와 분자동역학을 이용한 모사 결과로부터, 압축되는 비정질 구형 입자 내부의 응력 분포는 초기에 접촉면의 중심에 집중된 양상에서 점차

변형이 진행됨에 따라 입자 전체에 거의 균일하게 분포되는 양상으로 변화하는 것을 확인하였다. 특히, 흥미롭게도 높은 변형률 하에서의 비정질 합금 나노입자는 급격한 파괴 현상 없이 정상 상태(steady-state)에서의 지속적인 소성 변형을 하는 것이 관찰되었다. 이러한 변형 조건 하에서 전단띠가 형성되기 위한 임계응력을 Griffith crack criterion 에서 확장된 에너지 증가 관계를 통하여 유도된 수식으로부터 계산하였으며, 그 임계응력은 실제 입자가 나타내는 정상 상태 소성 변형에서의 유동 응력보다 더욱 높은 수준에 위치하는 것을 확인하였고, 이로부터 비정질 합금 나노 입자가 고변형률 조건 하에서도 전단띠를 형성하지 않고 시편 전체적으로 균일하게 활성화된 shear transformation zone을 통해 균일 변형 거동을 나타내고 있음을 규명하였다. 또한, 이때의 유동 응력과 점성의 변형 속도에 대한 의존성을 분석함으로써 비정질 합금 나노 입자의 균일 변형은 비뉴턴 유동 거동을 따른다는 것을 확인하였다.

비정질 합금 나노 입자의 압축 변형 거동으로부터 확인한 이러한 현상의 근원을 이해하기 위하여, 본 연구에서는 기존에 제시된 바와 차별화하여 나노 크기 비정질 합금의 기계적 거동까지 내포하는 새로운 형태의 변형 기구 도표(Deformation map)를 제시하였다. 새롭게 제시된 변형 기구 도표를 구성하는, 변형 모드 간 경계선의 위치 관계는 비정질 합금의 변형에 대한 새로운 관점을 제시한다. 특히, 나노 크기의 비정질 합금에서 나타나는 상온 균일 변형은 전단응력에 의한 지속적인 시편의 점성 감소로 인해 야기되는 기계적 유리 천이

거동(Mechanically-induced glass transition)으로부터 발생하며, GPa 수준의 응력 조건에서 발생하는 상온 균일 변형은 비뉴턴 유동 거동만을 따를 수 밖에 없다는 것을 새로운 변형 기구 도표로부터 규명하였다.

이러한 나노 크기 비정질 합금의 독특한 기계적 거동을 더 확장된 크기 수준에서 응용하기 위하여, 이를 더 큰 스케일의 소재의 내재된 특성 요소로 치환하는 방법이 제시된 바 있다. 즉, 나노 크기의 비정질 합금을 기본 구성 단위로서 차용하여 이를 계층 구조화함으로써 더 큰 스케일의 소재를 구성하는 방법이 연구되어 왔으며, 본 연구에서는 이러한 멀티 스케일 소재의 하나로 비정질 합금 나노 다공체를 제시하였다. 나노 크기의 비정질 합금 가지들로 구성된 나노 다공체는 크기 효과에 의한 비정질 합금의 강도 증가 효과와 변형 모드 천이 현상을 모두 내포하고 있는 것을 실험적으로 확인하였다.

이상의 연구결과를 종합할 때, 본 논문에서는 기존에 시도되지 않았던 독특한 실험 방법과 이론적 고찰을 바탕으로 기존에 명확히 이해되지 못하던 나노 크기 비정질 합금의 기계적 변형 거동에 대한 유용하고 새로운 해석을 제시하였다. 이에 더 나아가 나노 크기 비정질 합금의 우수한 특성을 실제로 더 큰 스케일에서 응용할 수 있는 가능성을 보여주는 새로운 소재를 제시하여, 학문적 측면 뿐만 아니라 산업적 측면으로도 중요한 가치가 있는 결과를 도출하였다.

핵심어 : 비정질 합금, 나노 입자, 나노 다공체, 나노 역학,

변형 도표, 응력 유기 유리 천이 거동

학 번 : 2010-20592